Inversion technique for optical remote sensing in shallow water

Dissertation
zur Erlangung des Doktorgrades
der Naturwissenschaften im Fachbereich
Geowissenschaften
der Universität Hamburg

vorgelegt von

Andreas Albert

aus

Mering

Hamburg 2004

Als Dissertation angenommen vom Fachbereich Geowissenschaften der Universität Hamburg

auf Grund der Gutachten von Herrn Prof. Dr. Hartmut Graßl

und Herrn Dr. Peter Gege

Hamburg, den 10. Dezember 2004

Prof. Dr. H. Schleicher
Dekan des Fachbereichs Geowissenschaften

Abstract

In the field of optical remote sensing (400 to 800 nm wavelength) in natural waters, physically based inversion methods can currently be applied only when bottom effects are negligible. In shallow water areas, the remotely sensed signal in the visible range is strongly influenced by the bottom albedo, which must be taken into account for the development of remote sensing algorithms. The aim of this study was to investigate the variability of the remotely sensed signal and the feasibility and uniqueness of inversion model solutions when bottom albedo is not negligible. A well-established and validated forward model (Hydrolight 3.1) was applied to inland waters using measurements of water constituents and light field parameters in deep and shallow water areas from the test site Lake Constance. The shallow water measurements were also used for the derivation of specific bottom reflectance spectra. By using this adjusted forward model, a large number of spectral measurements was simulated, where the optical properties of the water and the bottom were varied within the range of the in-situ values at Lake Constance, but also below and above this range to cover a more general range of concentrations and to extend the study to a wide number of case-2 waters. The dependence of the under water light field on the concentration of phytoplankton and suspended matter, gelbstoff absorption, bottom reflectance, bottom depth, surface wind speed, solar zenith angle, and viewing angle was parameterised. Further parameters including phase functions and specific optical properties of water constituents were kept constant at values typical for Lake Constance. A set of analytical equations for calculating water and bottom properties was developed and implemented in a public-domain software (WASI) to provide a fast and user-friendly tool of forward and inverse modelling of optical data. A new inversion technique based on the analytical parameterisations was developed to estimate the concentrations of the water constituents, the bottom depth, and the coverage of bottom types in shallow water. The errors of the model were studied depending on the water constituent concentrations, bottom depth, and bottom reflectance. The effect of multi-parameter inversion on error propagation was also investigated as well as the influence of sensor characteristics like signal noise, radiometric, and spectral resolution. The new methodology was validated using in-situ data measured in Lake Constance.

Zusammenfassung

Auf dem Gebiet der optischen Gewässerfernerkundung können physikalisch basierte Inversionsmethoden momentan nur angewendet werden, wenn Effekte verursacht durch den Seeboden vernachlässigbar sind. In den Flachwasserbereichen wird das Fernerkundungssignal im sichtbaren Spektralbereich stark beeinflußt durch die Bodenalbedo. Ziel dieser Studie war es, die Variabilität des Fernerkundungssignals sowie die Anwendbarkeit von Inversionsmodellen und ihrer Eindeutigkeit der Lösungen zu untersuchen, wenn die Bodenalbedo nicht vernachlässigbar ist. Zur Untersuchung wurde ein etabliertes und validiertes Vorwärtsmodell (Hydrolight 3.1) angewandt. Messungen der Wasserinhaltsstoffe und Lichtfeldparameter im tiefen und flachen Wasser des Bodensees wurden dazu durchgeführt und in das Modell integriert. Die Flachwassermessungen wurden auch für die Ableitung der spezifischen Bodenreflexionen verwendet. Durch Verwendung dieses angepaßten Vorwärtsmodells wurde eine große Anzahl von Spektren simuliert, wobei die optischen Eigenschaften des Wassers und des Bodens vor allem innerhalb des bodenseetypischen Wertebereiches variiert wurden, aber auch unter- und oberhalb dieses Bereiches, um die Untersuchungen auf eine Vielzahl von Gewässern auszudehnen. Das Unterwasserlichtfeld wurde parametrisiert in Abhängigkeit von Phytoplankton- und Schwebstoffkonzentration, Gelbstoffabsorption, Bodenreflexion, Windgeschwindigkeit, Sonnenzenit- und Beobachtungswinkel. Weitere Parameter einschließlich Phasenfunktion und spezifische optische Eigenschaften der Wasserinhaltsstoffe wurden konstant gehalten bei bodenseetypischen Werten. Ein Satz analytischer Gleichungen zur Berechnung von Wasser- und Bodeneigenschaften wurde entwickelt und in eine frei verfügbare Software (WASI) integriert, um ein schnelles und benutzerfreundliches Werkzeug für die Simulation und Analyse optischer Daten zur Verfügung zu stellen. Basierend auf den analytischen Parametrisierungen wurde eine neue Inversionstechnik entwickelt, um die Konzentrationen der Wasserinhaltsstoffe, die Bodentiefe sowie Typ und Grad der Bodenbedeckung im Flachwasser zu bestimmen. Die Fehler des Modells wurden abhängig von den Konzentrationen der Wasserinhaltsstoffe, der Bodentiefe und dem Reflexionsvermögen des Bodens ermittelt. Der Effekt der Multiparameter-Inversion auf die Fehlerfortpflanzung wurde ebenso untersucht wie der Einfluß von Sensoreigenschaften (Rauschen, radiometrische und spektrale Auflösung). Die neue Methodik wurde validiert anhand von Meßdaten vom Bodensee.

Contents

1 Introduction **1**
- 1.1 Motivation . . . 2
- 1.2 State of the art . . . 4
- 1.3 Test site . . . 7
- 1.4 Concept . . . 9

2 Radiative transfer theory **11**
- 2.1 Radiative transfer equation . . . 11
- 2.2 Absorption . . . 23
  - 2.2.1 Absorption by water . . . 23
  - 2.2.2 Absorption by phytoplankton . . . 25
  - 2.2.3 Absorption by suspended particles . . . 27
  - 2.2.4 Absorption by gelbstoff . . . 28
- 2.3 Elastic scattering . . . 29
  - 2.3.1 Elastic scattering by water . . . 30
  - 2.3.2 Elastic scattering by phytoplankton . . . 33
  - 2.3.3 Elastic scattering by suspended matter . . . 35
  - 2.3.4 Elastic scattering by gelbstoff . . . 37
- 2.4 Inelastic processes and bioluminescence . . . 37
  - 2.4.1 Raman scattering of water . . . 39
  - 2.4.2 Fluorescence by chlorophyll . . . 40
  - 2.4.3 Fluorescence by gelbstoff . . . 42
  - 2.4.4 Bioluminescence . . . 43
- 2.5 Bottom effects . . . 43
- 2.6 Effects at the water surface . . . 49

3 Analytical parameterisations **55**
- 3.1 Radiative transfer model . . . 56
  - 3.1.1 Absorption and scattering . . . 57
  - 3.1.2 Depth profiles . . . 59
  - 3.1.3 Bottom reflectance, water surface, and sky conditions . . . 61

3.2 Result: set of parameterisations . . . 62
  3.2.1 Irradiance reflectance of deep water . . . 63
  3.2.2 Remote sensing reflectance of deep water . . . 65
  3.2.3 Diffuse attenuation coefficient . . . 68
  3.2.4 Irradiance reflectance of shallow water . . . 69
  3.2.5 Remote sensing reflectance of shallow water . . . 72
  3.2.6 Remote sensing reflectance above water . . . 75
3.3 Comparison with in-situ measurements . . . 77
  3.3.1 Deep water . . . 78
  3.3.2 Shallow water . . . 81
  3.3.3 Above water . . . 82

4 Inversion **87**
4.1 Curve fitting and search algorithm . . . 88
4.2 Determination of initial values . . . 89
  4.2.1 Bottom depth . . . 91
  4.2.2 Concentration of suspended matter . . . 93
  4.2.3 Concentration of phytoplankton and absorption of gelbstoff . . . 104
  4.2.4 Areal fraction of bottom albedo . . . 106
4.3 Pre-calculation and pre-fits . . . 112
  4.3.1 Steps of the initial value calculation . . . 112
  4.3.2 Pre-fit in the blue and near infrared spectra . . . 112
4.4 Main fit . . . 113
  4.4.1 Concentration of phytoplankton . . . 115
  4.4.2 Concentration of suspended matter . . . 115
  4.4.3 Absorption of gelbstoff . . . 117
  4.4.4 Bottom depth . . . 119
  4.4.5 Areal fraction of bottom albedo . . . 123

5 Analysis of inversion accuracy **127**
5.1 Model error . . . 127
5.2 Error propagation . . . 129
5.3 Signal noise, radiometric and spectral resolution . . . 139
5.4 Inversion of measurements . . . 144

6 Conclusion and outlook **153**

A In-situ measurements **157**
A.1 Phytoplankton . . . 157
A.2 Suspended matter . . . 159
A.3 Gelbstoff . . . 160

A.4 HYDRA 161
A.5 RAMSES 165

B WASI: water colour simulator **167**
B.1 Concept 167
B.2 Models 168
B.3 Forward calculation 169
B.4 Invers modeling 170

Acknowledgement **173**

References **175**

List of Figures

1.1 Scheme of the ecosystem of coastal areas and lakes. 3
1.2 Diagrammatic representation of case-1 and case-2 waters. 4
1.3 Map of the location of Lake Constance. 9

2.1 Scheme of radiative transfer in shallow water. 12
2.2 Path of the radiance in a thin layer of water. 13
2.3 Scheme of a detector for radiance measurements. 14
2.4 Scheme of a detector for irradiance measurements. 15
2.5 Scattering of the radiance in forward and backward direction for isotropic scattering and scattering in natural waters. 19
2.6 Absorption coefficient of pure water. 24
2.7 Temperature gradient of absorption of pure water and the variability of the absorption of pure water due to temperature variation. 25
2.8 Normalised specific absorption coefficient of phytoplankton. 26
2.9 Absorption of phytoplankton derived for five concentrations. 27
2.10 Normalised absorption of gelbstoff. 29
2.11 Absorption of gelbstoff derived for five different concentrations. 30
2.12 Refractive index of water. 31
2.13 Scattering phase function of pure water. 33
2.14 Scattering coefficient of pure water. 34
2.15 Normalised scattering phase function of particles. 36
2.16 Schematic graphs of the electronic states during Raman scattering and fluorescence. 38
2.17 Schematic graph of three inelastic processes by natural water when excited at three different wavelengths (Raman scattering, gelbstoff and chlorophyll fluorescence). 39
2.18 Geometry of incident and reflected radiances for the bidirectional reflection of a surface. 44
2.19 Reflectances of several surface substrates: coral sand, green, brown, and red algae. 46
2.20 Mean bottom reflectances of sediment measured in Lake Constance. 47
2.21 Mean values of irradiance reflectance of submerged vegetation measured at Lake Constance. 48

2.22 Fresnel reflection for incident and water leaving radiance. 50
2.23 Scheme of the hexagonal grid and the triangular wave facets used for the simulation of the wind blown surface. 53

3.1 Distribution of the concentration of suspended matter against phytoplankton used for the simulations with Hydrolight. 58
3.2 Frequency distribution of the concentration values of gelbstoff, suspended matter, and phytoplankton used for the simulations with Hydrolight 59
3.3 Depth profiles of phytoplankton and suspended matter for different concentrations. 60
3.4 Seasonal average depth profiles of the temperature measured in Lake Constance. 62
3.5 Bottom reflectance spectra used for the forward simulations in Hydrolight. 63
3.6 Irradiance reflectance for infinitely deep water depending on $\frac{b_b}{a+b_b}$. 64
3.7 Dependency of the irradiance reflectance for infinitely deep water on surface wind and subsurface solar zenith angle. 65
3.8 Analytically calculated irradiance reflectance against simulated values for infinitely deep water and distribution of the relative errors. 66
3.9 Dependence of the remote sensing reflectance for infinitely deep water on the subsurface viewing angle. 67
3.10 Analytically calculated remote sensing reflectance against the simulated values for infinitely deep water and distribution of the relative errors. 67
3.11 Dependence of downward diffuse attenuation coefficient on $\frac{a+b_b}{\cos\theta_s}$ and distribution of the relative errors. 68
3.12 Dependence of the upward diffuse attenuation coefficient on the sum of absorption and backscattering and subsurface solar zenith angle. 70
3.13 Comparison of simulated and estimated values of irradiance reflectance of shallow water and the distribution of the relative errors. 71
3.14 Comparison of simulated and estimated values of irradiance reflectance of shallow water for the spectral range from 400 to 800 nm for three different cases. 72
3.15 Comparison of simulated and estimated values of remote sensing reflectance of shallow water and the distribution of the relative errors. 73
3.16 Comparison of simulated and estimated values of remote sensing reflectance of shallow water for the spectral range from 400 to 800 nm for three different cases and two different viewing angles. 74
3.17 Comparison of the remote sensing reflectance above the water surface derived from three different equations and for four different Q-factors. 76
3.18 Comparison of simulated and estimated values of remote sensing reflectance of water above surface and the distribution of the relative errors. 77
3.19 Comparison of simulated and estimated values of remote sensing reflectance of water above surface for the spectral range from 400 to 800 nm for three different cases and two different viewing angles. 78

3.20 Map of the positions in Lake Constance for the comparison of in-situ measurements and model calculations. 79
3.21 Comparison of in-situ measurements and model calculations of remote sensing and irradiance reflectance in deep water areas of Lake Constance. 84
3.22 Comparison of in-situ measurements and model calculations of remote sensing and irradiance reflectance in shallow waters of Lake Constance. 85
3.23 Comparison of in-situ measurements and model calculations of remote sensing reflectance above the water surface of Lake Constance. 86

4.1 The Simplex and its potential contours in the next step. 89
4.2 Variability of the f-factors. 90
4.3 Analytically estimated bottom depth for varying concentrations of water constituents above sediment and macrophytes. 92
4.4 Relative error of the estimated bottom depth from irradiance reflectance for varying concentrations of water constituents and different bottom types. 94
4.5 Relative error of the estimated bottom depth from remote sensing reflectance for varying concentrations of water constituents and different bottom types. 95
4.6 Relative error of the estimated bottom depth from irradiance reflectance depending on the relative error of the concentrations of water constituents and different bottom types. 96
4.7 Relative error of the estimated bottom depth from remote sensing reflectance depending on the relative error of the concentrations of water constituents and different bottom types. 97
4.8 Relative error of the estimated bottom depth from irradiance and remote sensing reflectance depending on the relative error of bottom albedo. 98
4.9 Analytically calculated values of the concentration of suspended matter using varying concentrations of phytoplankton and gelbstoff above sediment and macrophytes. 99
4.10 Relative error of the estimated concentration of suspended matter from irradiance reflection for varying concentrations of water constituents and different bottom types. 100
4.11 Relative error of the estimated concentration of suspended matter from remote sensing reflectance for varying concentrations of water constituents and different bottom types. 101
4.12 Relative error of the estimated concentration of suspended matter from irradiance reflectance depending on the relative error of the concentrations of water constituents, bottom depth, and different bottom types. 102
4.13 Relative error of the estimated concentration of suspended matter from remote sensing reflectance depending on the relative error of the concentrations of water constituents, bottom depth, and different bottom types. 103

4.14 Relative error of the estimated concentration of suspended matter from irradiance and remote sensing reflectance depending on the relative error of bottom albedo. 104
4.15 Example of the steps of the technique of nested intervals used for the estimation of the absorption of phytoplankton and gelbstoff for four different values (relative units). 105
4.16 Relative error of the estimated concentration of phytoplankton for irradiance reflectance using nested intervals and the Simplex algorithm depending on the relative error of the concentrations of water constituents, bottom depth, and different bottom types. 107
4.17 Relative error of the estimated concentration of phytoplankton for remote sensing reflectance using nested intervals and the Simplex algorithm depending on the relative error of the concentrations of water constituents, bottom depth, and different bottom types. 108
4.18 Relative error of the estimated absorption of gelbstoff for irradiance reflectance using nested intervals and the Simplex algorithm depending on the relative error of the concentrations of water constituents, bottom depth, and different bottom types. 109
4.19 Relative error of the estimated absorption of gelbstoff for remote sensing reflectance using nested intervals and the Simplex algorithm depending on the relative error of the concentrations of water constituents, bottom depth, and different bottom types. 110
4.20 Relative error of the estimated concentration of phytoplankton for irradiance and remote sensing reflectance depending on the relative error of bottom albedo. . . . 111
4.21 Relative error of the estimated absorption of gelbstoff for irradiance and remote sensing reflectance depending on the relative error of bottom albedo. 111
4.22 Scheme of the steps for the initial value calculation of water constituent concentrations, bottom depth, and areal fraction of the bottom types. 113
4.23 Scheme of the entire inversion procedure using the Simplex algorithm. 114
4.24 Relative error of retrieved phytoplankton concentration depending on the relative error of the concentrations of water constituents, bottom depth, and bottom types.116
4.25 Relative error of the retrieved phytoplankton concentration depending on the relative error of bottom albedo. 117
4.26 Relative error of retrieved suspended matter concentration depending on the relative error of the concentrations of water constituents, bottom depth, and bottom types. 118
4.27 Relative error of retrieved suspended matter concentration depending on the relative error of bottom albedo. 119
4.28 Relative error of retrieved gelbstoff absorption depending on the relative error of the concentrations of water constituents, bottom depth, and bottom types. . . . 120

4.29 Relative error of retrieved gelbstoff absorption depending on the relative error of bottom albedo. 121
4.30 Relative error of retrieved bottom depth depending on the relative error of the concentrations of water constituents and bottom types. 122
4.31 Relative error of retrieved bottom depth depending on the relative error of bottom albedo. 123
4.32 Relative error of the retrieved areal fraction of sediment and macrophyte bottom cover depending on the relative error of the concentrations of water constituents and bottom depth. 124
4.33 Absolute error of the retrieved areal fraction of sediment and macrophytes at the bottom depending on the relative error of the concentrations of water constituents and bottom depth. 125

5.1 Relative error of the retrieved suspended matter concentration using Hydrolight spectra, for different values of the bottom depth. 129
5.2 Relative error of the retrieved phytoplankton concentration using Hydrolight spectra, for different values of the bottom depth. 129
5.3 Relative error of the retrieved gelbstoff absorption using Hydrolight spectra, for different values of the bottom depth. 130
5.4 Relative error of retrieved bottom depth using Hydrolight spectra, depending on suspended matter, phytoplankton, and absorption of gelbstoff. 131
5.5 Relative error of the simultaneously retrieved concentrations of phytoplankton and suspended matter. 133
5.6 Relative error of the simultaneously retrieved gelbstoff absorption and bottom depth. 134
5.7 Relative error of the retrieved phytoplankton concentration fitting three parameters simultaneously. 135
5.8 Relative error of the retrieved bottom depth and areal fraction of sediment fitting three parameters simultaneously. 135
5.9 Relative error frequency distributions for the concentration of phytoplankton, suspended matter, gelbstoff absorption, and bottom depth using Hydrolight spectra of the remote sensing reflectance above sediment and fitting all four parameters simultaneously. 137
5.10 Relative error frequency distributions for the concentration of phytoplankton, suspended matter, gelbstoff absorption, and bottom depth using Hydrolight spectra of the remote sensing reflectance above macrophytes and fitting all four parameters simultaneously. 138
5.11 Influence of signal noise and radiometric resolution on the spectrum of the remote sensing reflectance. 139

5.12 Relative error of retrieved phytoplankton concentration depending on signal noise, radiometric and spectral resolution. 140
5.13 Relative error of retrieved suspended matter concentration depending on signal noise, radiometric and spectral resolution. 142
5.14 Relative error of retrieved gelbstoff absorption depending on signal noise, radiometric and spectral resolution. 142
5.15 Relative error of retrieved bottom depth depending on signal noise, radiometric and spectral resolution. 143
5.16 Relative error of retrieved areal fraction of sediment and macrophytes depending on signal noise, radiometric and spectral resolution. 143
5.17 Map of Lake Constance with 51 in-situ stations. 144
5.18 Comparisons between retrieved and in-situ concentration of phytoplankton, suspended matter, gelbstoff absorption, and bottom depth using remote sensing reflectance measured by the HYDRA and RAMSES instruments in Lake Constance. 147
5.19 Comparisons between retrieved and in-situ concentration of phytoplankton, suspended matter, gelbstoff absorption, and bottom depth using irradiance reflectance measured by the HYDRA and RAMSES instruments in Lake Constance. . 148
5.20 Reanalysis of outliers of the phytoplankton concentration retrieval using fixed gelbstoff absorption. 149
5.21 Inversion of the in-situ measurement in Lake Constance of station "r19" from 09/07/2002. 149
5.22 Inversion of the in-situ measurement in Lake Constance of station "t7" from 06/09/1999. 150

6.1 Classification of bottom types in the littoral zone of Reichenau island at Lake Constance using multispectral airborne remote sensing data. 156

A.1 Photograph and scheme of the optical in-situ instrument HYDRA. 162
A.2 Schematic diagram of the spectrometer unit of the HYDRA. 163
A.3 Four different light collectors of HYDRA to measure irradiance and radiance. . . 164
A.4 Photograph and scheme of the optical in-situ instrument RAMSES. 166
A.5 Photographs of the irradiance and radiance sensors of RAMSES. 166

B.1 Graphical user interface of WASI. 168
B.2 Graphical user interface of WASI for the selection of irradiance reflectance models.170
B.3 Graphical user interface of WASI for the fit tuning. 172

List of Tables

2.1 Coefficients for the determination of the isothermal compressibility of water. . . . 32

2.2 Coefficients for the determination of the pressure derivative of the refractive index of water. 32

2.3 Coefficients for the determination of the refractive index of water for zero salinity. 32

2.4 Coefficients for the determination of the quantum efficiency of gelbstoff. 43

3.1 Concentrations of the water constituents for the simulations with Hydrolight. . . 58

3.2 Parameter values for depth profiles of phytoplankton and suspended matter. . . . 60

3.3 Profile of mean temperatures of the four seasons used for the simulations with Hydrolight. 61

3.4 Coefficients for the irradiance reflectance of deep water. 64

3.5 Coefficients for the remote sensing reflectance of deep water. 66

3.6 Coefficients for the irradiance reflectance for shallow water. 70

3.7 Coefficients for the remote sensing reflectance for shallow water. 73

3.8 In-situ parameters in Lake Constance. 79

4.1 Variation of the concentrations of the water constituents for initial values estimation. 90

5.1 Concentrations of the water constituents and bottom depths used for the simulations with Hydrolight and the following inversion. 128

5.2 Mean relative error of the phytoplankton and suspended matter concentration, gelbstoff absorption, and bottom depth estimated by inversion of Hydrolight spectra for the bottom types sediment and macrophytes. 136

5.3 Mean relative error of retrievals of phytoplankton and suspended matter concentration, gelbstoff absorption, and bottom depth depending on signal noise, radiometric and spectral resolution. 141

5.4 Mean relative error of the retrieved fraction of sediment and macrophytes depending on signal noise, radiometric and spectral resolution. 141

5.5 Retrieval of bottom coverage from in-situ measured remote sensing reflectance for stations in Lake Constance from 09/07/2002. 151

6.1 Mean relative error and standard deviation of the phytoplankton concentration, suspended matter concentration, gelbstoff absorption, and bottom depth simultaneously estimated by inversion. 154

A.1 Inherent and apparent optical properties of the water, which can be derived from HYDRA measurements. 165

B.1 Types of spectral measurements for which inverse modeling is implemented in WASI. 169
B.2 Parameter list of WASI. 171

List of Symbols

β		scattering phase function	$(\mathrm{m}^{-1}\mathrm{sr}^{-1})$
	β_W	scattering phase function of pure water	
	β_X	scattering phase function of suspended matter	
	$\beta^{F,chl}$	fluorescence phase function of chlorophyll	
	$\beta^{F,Y}$	fluorescence phase function of gelbstoff	
	β^R	Raman scattering phase function	
$\tilde{\beta}$		normalised scattering phase function, $\frac{\beta}{b}$	(sr^{-1})
δ		relative error, signal noise	(-)
Δ		residual	(-)
η		spectral quantum efficiency	(nm^{-1})
θ		zenith angle	$(^\circ)$
	θ_s	subsurface solar zenith angle	
	θ_s^+	solar zenith angle above water	
	θ_v	subsurface viewing angle	
	θ_v^+	viewing angle above water	
λ		wavelength	(nm)
μ		cosine of zenith angle, $\cos\theta$	(-)
$\overline{\mu}$		mean cosine of the light field under water, $\frac{E}{E_0}$	(-)
	$\overline{\mu}_d$	mean cosine of the downwelling light field, $\frac{E_d}{E_{0d}}$	
	$\overline{\mu}_u$	mean cosine of the upwelling light field$\frac{E_u}{E_{0u}}$	
ρ		depolarisation ratio	(-)
σ		standard deviation	(-)
σ_L		Fresnel reflection of radiance	(-)
	σ_L^+	Fresnel reflection of air incident radiance	
	σ_L^-	Fresnel reflection of water leaving radiance	
σ_E		reflection of irradiance at the water surface	(-)
	σ_E^+	air incident irradiance reflection	
	σ_E^-	water leaving irradiance reflection	

ϕ		azimuth angle	(°)
Φ		quantum efficiency	(-)
ψ		scattering angle	(°)
ω_0		single scattering albedo, $\frac{b}{c}$	(-)
ω_b		backscattering albedo, $\frac{b_b}{a+b_b}$	(-)
Ω		solid angle	(sr)

a		absorption coefficient	(m^{-1})
	a_W	absorption coefficient of pure water	
	a_P	absorption coefficient of phytoplankton	
	a_X	absorption coefficient of suspended matter	
	a_Y	absorption coefficient of gelbstoff	
	a_{chl}	absorption coefficient of chlorophyll-a	
a_P^*		specific absorption coefficient of phytoplankton	(m^2/mg)
a_{chl}^*		specific absorption coefficient of chlorophyll-a	(m^2/mg)
b		scattering coefficient, $b_f + b_b$	(m^{-1})
	b_W	scattering coefficient of pure water	
	b_P	scattering coefficient of phytoplankton	
	b_X	scattering coefficient of suspended matter	
	b_Y	scattering coefficient of gelbstoff	
b_P^*		specific scattering coefficient of phytoplankton	(m^2/mg)
b_X^*		specific scattering coefficient of suspended matter	(m^2/g)
b_b		backscattering coefficient	(m^{-1})
	$b_{b,W}$	backscattering coefficient of pure water, $\frac{1}{2}b_W$	
	$b_{b,P}$	backscattering coefficient of phytoplankton	
	$b_{b,X}$	backscattering coefficient of suspended matter	
	$b_{b,Y}$	backscattering coefficient of gelbstoff	
$b_{b,P}^*$		specific backscattering coefficient of phytoplankton	(m^2/mg)
$b_{b,X}^*$		specific backscattering coefficient of suspended matter	(m^2/g)
b_f		forward scattering coefficient	(m^{-1})
B		normalised bidirectional reflectance distribution function (BRDF)	(sr^{-1})
$\tilde{B}$		(unnormalised) bidirectional reflectance distribution function (BRDF), $B \cdot R_B$	(sr^{-1})
c		extinction coefficient, $a + b$	(m^{-1})
C_P		concentration of phytoplankton	(μg/l)
C_{chl}		concentration of chlorophyll-a	(μg/l)
C_{pheo}		concentration of pheophytin	(μg/l)
C_X		concentration of suspended matter	(mg/l)

E		plane irradiance, vertical component of vector irradiance	(W m^{-2} nm^{-1})
	E_d	downwelling plane irradiance in water	
	E_d^+	downwelling plane irradiance in air	
	E_u	upwelling plane irradiance in water	
	E_u^+	upwelling plane irradiance in air	
$\vec{E}$		vector irradiance	(W m^{-2} nm^{-1})
E_0		scalar irradiance	(W m^{-2} nm^{-1})
	E_{0d}	downwelling scalar irradiance	
	E_{0u}	upwelling scalar irradiance	
f		proportionality factor	(-)
	f°	proportionality factor of irradiance reflectance	
	$f^\uparrow$	proportionality factor of remote sensing reflectance	
f_a		areal fraction of bottom type	(-)
K		diffuse attenuation coefficient	(m^{-1})
	K_d	downward diffuse attenuation coefficient	
	K_u	upward diffuse attenuation coefficient	
	$K_{u,B}$	upward diffuse attenuation coefficient of photons reflected by bottom	
	$K_{u,W}$	upward diffuse attenuation coefficient of photons reflected by water	
l		length	(m)
L		radiance	(W m^{-2} nm^{-1} sr^{-1})
	L_d^+	downwelling radiance in air	
	L_u	upwelling radiance in water	
	L_u^+	upwelling radiance in air	
	L_W^+	water leaving radiance	
n		Ångström exponent	(-)
n_W		refractive index of water	(-)
Q		Q-factor, $\frac{E_u}{L_u}$	(sr)
R		irradiance reflectance, $\frac{E_u}{E_d}$	(-)
	R_∞	irradiance reflectance of infinitely deep water	
	R_B	bottom reflectance	
	R^+	irradiance reflectance above water surface	
	R_W^+	irradiance reflectance of water above surface	
R_{rs}		remote sensing reflectance, $\frac{L_u}{E_d}$	(sr^{-1})
	$R_{rs,\infty}$	remote sensing reflectance of infinitely deep water	
	R_{rs}^+	remote sensing reflectance above water	
	$R_{rs,W}^+$	remote sensing reflectance of water above surface	

s_X	exponent of suspended matter absorption	(nm^{-1})
s_Y	exponent of gelbstoff absorption	(nm^{-1})
S	salinity	(-)
S_0	internal source term	($\mathrm{W\ m}^{-2}\ \mathrm{nm}^{-1}$)
t^l	transmission of water sample in cuvette of lenght l	(-)
T	temperature	(°C)
u	surface wind speed	(m/s)
V	volume	(m^3)
z	depth	(m)
z_B	bottom depth	

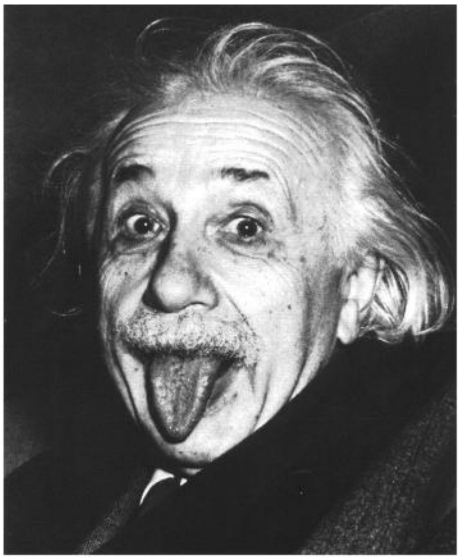

“Was weiß ein Fisch von dem Wasser,
in dem er sein ganzes Leben lang schwimmt?”

Albert Einstein (1879-1955)

Chapter 1

Introduction

Remote sensing is the observation of objects from a distance. This method is as old as animals are living on earth to analyse the environment by their sense organs. Mankind perfected this method by the development of several instruments to study the earth and the space. Researchers and philosophers challenged the structure of organic and inorganic material to understand the origin and formation of nature with the most important substance on earth: water. One of the first philosophers, who manifested this, was the ancient Greek scientist Thales of Miletus (about 624–546 B.C.). Hippolytos of Rome (about 170–235) wrote about him as mentioned by Jaap Mansfeld in "Die Vorsokratiker" (Reclam, 1987):

> «λέγεται Θαλῆν τὸν Μιλήσιον ἕνα τῶν ἑπτὰ σοφῶν πρῶτον ἐπικεχειρηκέναι φιλοσοφίαν φυσικήν. οὗτος ἔφη ἀρχὴν τοῦ παντὸς εἶναι καὶ τέλος τὸ ὕδορ. ἐκ γὰρ αὐτοῦ τὰ πάντα συνίστασϑαι πηγνυμένου καὶ πάλιν διανιεμένου εἲς αὑτὸ διαχεῖσϑαι, ἐπιφέρεσϑαί τε αὐτῷ τὰ πάντα, ἀφ' οὗ καὶ σεισμοὺς καὶ πνευμάτων συστροφὰς καὶ ἄστρων κινήσεις γίνεσϑαι· καὶ τὰ πάντα φέρεσϑαί τε καὶ ῥεῖν τῇ τοῦ πρώτου ἀρχηγοῦ τῆς γενέσεως αὐτῶν φύσει συμφερόμενα. ϑεὸν δὲ τοῦτ' εἶναι, τὸ μήτε ἀρχὴν μήτε τελευτὴν ἔχον.»

Basically, what he wrote is that Thales of Miletus was one of the "Seven Sages" and the father of philosophy. He affirmed that origin and end of all is water. Everything comes from the water and will return to it. All things on earth are floating on water, whereby earthquakes, winds, and stellar movements are caused. The only thing without start and finish is God.

Probably the first scientific experiments to observe the light field under water was conducted by the Italian physicist P.A. Secchi in 1865. He developed a method to measure the penetration depth of visible light. A white disc was immersed in the water and lowered until its disappearance. In our days, this maximum depth of visibility is called "Secchi depth". This value is correlated with the optical properties of the water body and allows statements about the turbidity. Contemporary optical instrumentation is much more complicated. Different methods offer the possibility of estimating properties of water constituents from remotely sensed data. The remote sensing signal is a function depending on different parameters. Generally, the technique of retrieving parameter values of a function is called "inversion". Additionally in shallow water areas, the detected signal is remarkably influenced by the light which is reflected at the bottom. Thus, the interpretation of an optical signal in shallow water can be rather difficult. The objective of this work is the development of a method to determine quantitatively the different effects and to study the feasibility of remote sensing techniques in shallow water.

1.1 Motivation

More than two thirds of the earth's surface are covered with water, and water is the most important substance for life on earth. Thus, monitoring and protecting water resources is a must and a challenge for all countries of the world. The proclamation of the United Nations (UN) of the international year of freshwater 2003 puts this in the spotlight. Furthermore, the UN recommended the proclamation of an international decade on water for life from 2005 to 2015. The supply of water and the sustainable development of water resources were also main topics on the earth summits of Rio de Janeiro, Brasil, 1992 and Johannesburg, South Africa, 2002. The European Community (EC) is already one step further and has passed a directive in October 2000, which is binding on all parties, to establish a framework in the field of water policy (EC, 2000). This focused many activities on surface water including remote sensing as a tool for monitoring of water quality.

Since the launch of the CZCS[1] (Hovis et al., 1980) on Nimbus-7 in 1978, further developments were made on multi- and hyperspectral sensors for ocean colour, for example the airborne sensors AVIRIS[2] and ROSIS[3] (Kunkel et al., 1991; van der Piepen, 1995) and the spaceborne sensors MOS[4] (Zimmermann et al., 1993; Zimmermann and Neumann, 2000) and SeaWiFS[5]. The advantage of remote sensing data is the higher spatial coverage compared to in-situ measurements. Satellites have a fixed repetition rate, therefore, time series can be obtained and changes of environmental conditions can be detected provided that no clouds are in the sensor's field of view. Airborne sensors achieve a higher spatial resolution than satellite sensors due to their lower flight altitude. Thus, their data can be applied for the monitoring of small lakes and rivers as well. Ongoing spaceborne missions with optical sensors like MODIS[6] on the platforms Aqua and Terra or MERIS[7] onboard of Envisat will provide high quality data in the future with the potential to determine ocean colour parameters more accurately than before and will bring forward the development of remote sensing methods.

Wetlands, lakes, and coastal regions including their catchment areas are complex and sensitive ecosystems. Especially littoral zones have a high biodiversity of fish, zooplankton, submersed and emersed macrophytes, epiphytes, and phytoplankton with symbiosis between different species.

---

[1] Coastal Zone Color Scanner

[2] Airborne Visible/Infrared Imaging Spectrometer, `http://aviris.jpl.nasa.gov`

[3] Reflective Optics System Imaging Spectrometer

[4] Modular Optical Scanner

[5] Sea-viewing Wide Field-of-view Sensor, `http://seawifs.gsfc.nasa.gov/SEAWIFS.html`

[6] Moderate Resolution Imaging Spectrometer, `http://modis.gsfc.nasa.gov`

[7] Medium Resolution Imaging Spectrometer, `http://envisat.esa.int/instruments/meris`

The physical variability of littoral zones in space and time is also very high due to changing bottom characteristics and transport processes by inflows, currents, and waves. A schematic view of the ecosystem in coastal regions and lakes adapted from Wetzel (2001) is presented in figure 1.1. Going from the shore line to the deepest point, the zonation is divided into the littoral and the pelagial. The littoral is further subdivided into the epilittoral, which lies entirely above the water level, and the sublittoral, which is below the water surface. The littoral ends at the penetration depth of light, where 1% of the incident light is remaining. Above that depth is the trophogenic or euphotic zone, where the productivity of most species is positive and macrophytes, epiphytes, and phytoplankton use the light for photosynthesis. Moving away from the shore, the sublittoral zone - in the field of remote sensing called shallow water - is followed by the free open water, called pelagial. Below the penetration depth of light lies the tropholytic or aphotic zone, where decomposition of organic matter dominates. The vertical extension of the trophogenic zone in the pelagial is strongly correlated with the Secchi depth.

To improve the understanding of shallow water areas, lakes and coastal regions are intensively under interdisciplinary investigation by geographers, biologists, limnologists, chemists, and physicists as well as by economists. Optical remote sensing is a helpful tool for the observation and assessment of this ecosystem, for example for the determination of water quality parameters and bottom characteristics, especially their spatial distribution. For example, an indicator of the ecosystem's quality is given by the trophic state which can be estimated by the concentrations of water constituents, turbidity, and Secchi depth (Carlson, 1977). The abundance and distribution of macrophytes is also correlated with the trophic state, as for example mentioned by Melzer (1999).

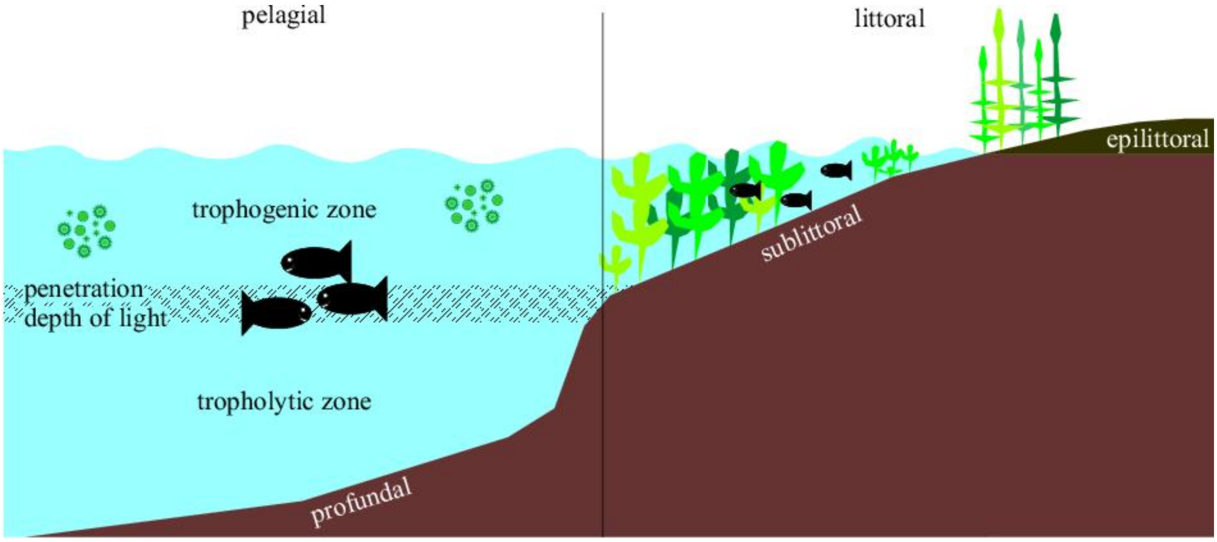

Figure 1.1: Scheme of the ecosystem of coastal areas and lakes.

1.2 State of the art

This work deals with remote sensing of optically complex waters: shallow water in coastal regions and in lakes, where the bottom is visible. Water masses in coastal areas and in lakes are often designated as case-2 waters. The nomenclature arises from a commonly used classification scheme for optically deep water, according to which oceanic waters are partitioned into case-1 and case-2 waters. This was introduced by Morel and Prieur (1977) and refined by Prieur and Sathyendranath (1981) and Gordon and Morel (1983). By definition, case-1 waters are those in which phytoplankton (index P) and its accompanying substances are the principal components for variations in optical properties of the water. Case-2 waters are influenced not only by phytoplankton, but also by other substances, notably suspended material (index X) and gelbstoff (index Y). Other names for gelbstoff are yellow substance, coloured dissolved organic matter (CDOM), and gilvin. A diagrammatic representation of the two cases is adapted from the third report of the International Ocean Colour Coordinating Group (IOCCG, 2000) and is shown in figure 1.2. The classification scheme is based on relative contributions of the three substances and does not depend on the magnitude of each substance. For example, case-1 waters can range from phytoplankton-poor (oligotrophic) to phytoplankton-rich (eutrophic).

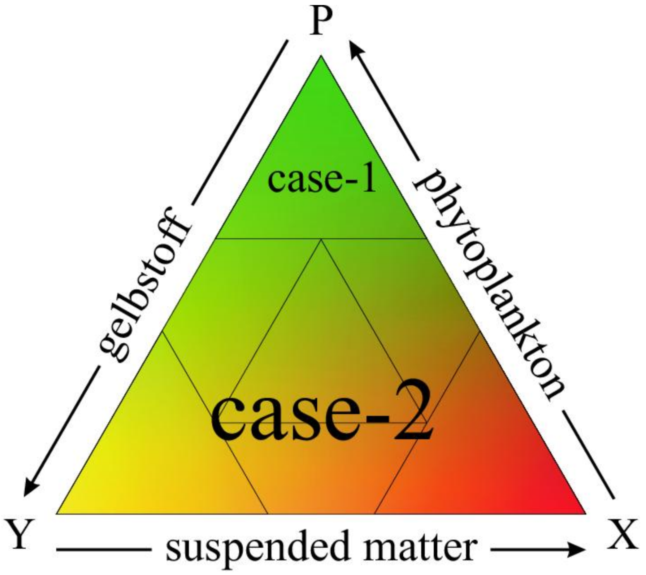

Figure 1.2: Diagrammatic representation of case-1 and case-2 waters after IOCCG (2000).

To make quantitative statements about the light field in the water, the inherent optical properties of the water body must be estimated depending on wavelength by means of specific optical properties of the water constituents - phytoplankton, suspended matter, and gelbstoff - and their concentrations. Together with the absorption and scattering of pure water, the total absorption and scattering can be derived. The sum of absorption and scattering is the extinction, which is a measure for the diffuse attenuation of the light under water. Based on the attenuation, Jerlov (1976) developed a more detailed classification scheme as a function of wavelength. He distinguished between 14 types of water regarding open ocean and coastal waters.

Absorption and backscattering are direct measures for the reflectance of the water column: the higher the backscattering, the higher the reflectance, and the higher the absorption, the lower the reflectance. Additionally, inelastic scattering like fluorescence and Raman scattering affects the reflectance. Before the reflectance of the water can be measured by airborne and spaceborne sensors, the signal is transmitted through the atmosphere, which absorbs and scatters as well. Even in a cloudless atmosphere, the portion of the reflectance coming from the water body and detected by an airborne and spaceborne sensor is only between 5 and 30%. Thus, the correction of atmospheric effects plays an important role for all kinds of remote sensing data, if not measured directly above the water surface. The atmospheric correction is not the task of this work, but the aim was to develop a retrieval in the complex field of shallow water for the determination of water and bottom characteristics from reflectances at the water surface.

At the beginning of airborne and spaceborne optical remote sensing, many algorithms were developed for case-1 waters. Broad spectral channels support simple empirical models of so-called colour ratios. This concept was introduced by Clarke et al. (1970); a summary of early works is given in Gordon and Morel (1983). When dealing with case-2 waters, it is necessary to use physical models based on the radiative transfer, since at least three relevant water constituents can vary independently of each other with a non-linear effect on the measured signals (Prieur and Sathyendranath, 1981; Fischer et al., 1986; Sathyendranath et al., 1989). In shallow water, the bottom reflectance has to be considered additionally. At some wavelengths, two or more substances and the bottom can influence the optical signal in the same manner, making it difficult to distinguish each effect. Thus, attention has to be paid on the choice of wavelengths and the number of wavelengths.

So-called forward models were developed - first for infinitely deep water - based on the physical radiative transfer in the water, i.e. the reflected signal is derived by means of the optical properties of the water and the water constituents. One approach is the Monte Carlo method of the simulation of photon propagation through aquatic environment. The application of the Monte Carlo method in aquatic optics was pioneered by Kattawar and Plass (1972) and Plass and Kattawar (1972) followed by a number of authors, for example Gordon and Brown (1973), Gordon et al. (1975), Morel and Prieur (1977), Kirk (1981; 1984), Stavn and Weidemann (1989), Morel and Gentili (1991), Sathyendranath and Platt (1997). A second model based on the Invariant Imbedding Technique was developed by Preisendorfer (1976) and Mobley (1994). Comparisons with other radiative transfer programs can be found in Mobley et al. (1993). Furthermore, a combined atmosphere-ocean system can be also simulated by the matrix operator method (Fischer and Grassl, 1984; Fell and Fischer, 2001). Recently, the Finite Element Method (FEM) found the way into the method of simulating the radiative transfer (Kisselev et al., 1995; Bulgarelli et al., 1999). All these studies have led to a robust and consistent result of the reflectance at the water surface in deep water. The investigations in shallow water made use of mathematical simplifications of the radiative transfer theory by the two-flow approximation. When the bottom is detectable, the reflectance at the water surface consists of two components: one from the water and the other from the bottom (Joseph, 1950; Lyzenga, 1978; Philpot and Ackleson, 1981; Maritorena et al., 1994; Lee et al., 1998).

Forward models are useful for the study of the light field under different conditions of the optical properties. The determination of optical properties of the water body and, in the case of shallow water, bottom characteristics like depth and submersed vegetation type using remote sensing data is called inversion. To solve this problem, several approaches exist to date:

Empirical approach uses the relationship between optical measurements and the concentrations of water constituents based on empirical data sets. The approach of colour ratios is the most common one. A detailed discussion of such empirical methods is given by Gordon and Morel (1983) and Dekker (1993). The advantage is the easy way of use and the fast computing time. But the disadvantage is that they are valid only for the used data set and therefore restricted to seasonal and regional scale.

Neural network consists of a large number of input values, so-called nodes or neurons, originating from measurements or model simulations of remote sensing signals, and the output consisting of the corresponding values of the optical properties of the water constituents. A number of hidden layers is between the input and output layer. Each neuron of a layer has a link to each neuron of the neighbouring layers connected by logistic or other non-linear functions, for example sigmoid, and weighting factors. Thus, the network can describe almost any non-linear relationship. The determination of the coefficients is called "training" and can be done by different minimisation techniques. The application to remote sensing data was done, for example, by Doerffer and Schiller (1998) and Schiller and Doerffer (1999). Neural networks are useful, if a high processing speed is required for mass production of satellite data, particularly for real-time processing. The disadvantage is that it is relatively expensive to prepare and that the training needs experience and computing time. A trained neural network is only valid for the used data range and can not be extrapolated to other optical properties.

Principal components are linearly transformed original spectral data producing new channels which are uncorrelated, i.e. linear independent. The new channels are chosen to remove the correlation between the former channels, and to maximise the information content and enhance the ability to extract previously defined properties of the data such as water constituent concentrations. The mathematical definition leads to a method for the design of an interpretation algorithm with optimal noise surpressing for multispectral data and is closely related to a multivariate linear regression. The implementation of this approach was done, for example, by Krawczyk et al. (1993) and Neumann et al. (1998). The advantage of the principal component inversion is the linear nature of the algorithm. Thus, it is very simple to implement, fast in calculation, robust and stable, and there are no convergence problems. The disadvantage is that the relation between the radiances and the optical properties of the water and the bottom is non-linear. The principal component algorithm can only be applied for the range of the tested specifical optical properties and must be adapted to other situations.

Non-linear optimisation inverts directly the measured or simulated input data by minimising the differences between calculations and input values. Different methods are available to perform the minimisation, for example the Levenberg-Marquardt and the Simplex algorithm. The calculation can be done by forward models or by analytic equations (Lee et al., 1999; Durand et al., 2000). Forward models are very accurate, but require extensive computing time. The algebraic method of analytical equations is very fast, but with the loss of accuracy. The non-linear optimisation technique has to handle the problem of the convergence between the input values and calculations to avoid non-physical solutions. The convergence is complicated, if the number of unknown parameters is increasing. The advantage of this method is that changes in optical properties can be easily implemented to apply to global and regional conditions.

These different approaches exist for solving the inverse problem. What kind of solution is the best to choose, depends on several factors such as computing time, accuracy, application to regional or global scale, and number of spectral channels and unknown parameters.

1.3 Test site

This work is part of the Collaborative Research Centre SFB 454 “Littoral zone of Lake Constance”[8] in the subproject D3 (van der Piepen and Heege, 2001; Heege, 2004) funded by the German Research Foundation DFG[9]. The SFB 454 performs interdisciplinary research by combining limnologists, biologists, chemists, and physicists with the aim of an improved understanding of the processes in the littoral. The Lake Constance (German: Bodensee) is located in southern Germany at the border to Switzerland and Austria (see figure 1.3) and is the second largest freshwater lake in Central Europe. The lake is situated at 395 m above sea level and covers an area of 571 km^2 with a length of shore line of 273 km (64% in Germany, 10% in Austria, and 26% in Switzerland). The maximum depth is 254 m and the contained volume of water about 48 km^3. The maximum length and width is about 63 and 14 km, respectively. The total catchment area covers about 11500 km^2. The main inflow is the river Rhine in the eastern part of the lake, called Upper Lake Constance (German: Obersee). Due to its alpine origin, the river Rhine carries a lot of inorganic suspended particles into the eastern part of Lake Constance. The Rhine leaves Lake Constance in the west part, called Lower Lake Constance (German: Untersee). Other inflows in the northern part of the lake are influenced by agricultural regions, for example the river Schussen. Thus, these rivers carry significant amounts of dissolved organic substances, nitrates, and phosphates.

---

[8] `http://www.uni-konstanz.de/sfb454`

[9] Kennedyallee 40, 53175 Bonn, Germany, `http://www.dfg.de`

During the last decades the trophic state of Lake Constance changed from eutrophic to mesotrophic due to the reduction of nutrient loads. This process of re-oligotrophication started in the seventies and is still continuing. For example, the content of phosphorus decreased from 80 to 15 mg m^{-3} between 1975 and 2000, and also the annual mean of the phytoplankton biomass in a depth from 0 to 20 m decreased from about 25 g m^{-2} at the end of the seventies to 6.7 g m^{-2} in 2001 (IGKB, 2002). This was the lowest value since 1965 with a maximum of 34 g m^{-2} in 1988. Due to its important role for about 4.5 million people as drinking water reservoir, a high public interest is given, especially on the monitoring of water quality which can be supported by remote sensing techniques. Since 1959, the IGKB[10] is responsible for the protection and observation of the lake. Important tasks are also conducted by the Institute of Lake Research (IfS) in Langenargen[11] and by the Limnological Institute of the University of Konstanz[12]. Important interdisciplinary work on Lake Constance was also performed within the former Collaborative Research Centre SFB 248 "Cycling of matter in Lake Constance" from 1986 to 1997 funded by the German Research Foundation DFG[9]. In terms of optical remote sensing over Lake Constance, the work by Gege (1994) showed the determination of phytoplankton classes from shipborne measurements, followed by investigations by Heege (2000) about the estimation of phytoplankton and suspended matter concentrations from airborne sensors, and by Bochter (2000), who developed a new instrument for in-situ measurement of the optical properties of water. The application of satellite data for the estimation of water constituent concentrations in Lake Constance was investigated by Pulvermüller et al. (1995) and Schneider (1998) using LANDSAT-TM[13] data. Recently, further developments using MERIS[7] were conducted during the projects MAPP (MERIS Applications and Regional Products Project) by Günther et al. (2002) and ENVISAT Oceanography (ENVOC) by (Häse and Heege, 2003).

---

[10] Internationale Gewässerschutzkommission für den Bodensee, `http://www.igkb.de`

[11] Argenweg 50/1, 88085 Langenargen, Germany, `http://www.lfu.baden-wuerttemberg.de/isf`

[12] Mainaustr. 252, 78464 Konstanz, Germany, `http://www.uni-konstanz.de/limnologie`

[13] LANDSAT Thematic Mapper, `http://landsat.gsfc.nasa.gov`

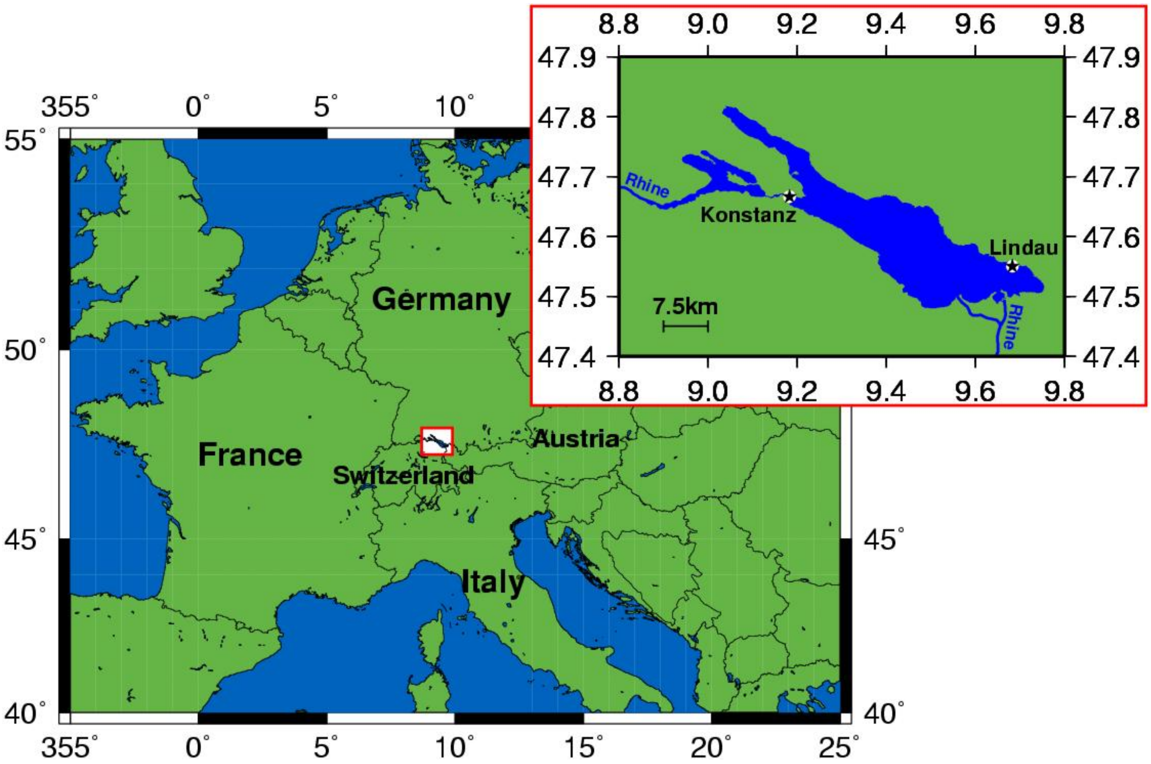

Figure 1.3: Map of the location of Lake Constance.

1.4 Concept

The aim of this study is to develop an inversion technique for shallow water using hyperspectral remote sensing data between 400 and 800 nm to estimate water constituent concentrations and bottom characteristics. The non-linear optimisation combined with analytical equations is chosen, since this technique provides fast calculation, simple adaptation of new optical properties, and the physical interpretation of all steps. The first step is the derivation of a consistent equation system for shallow water based on the radiative transfer theory (chapter 2). Based on these equations new analytical parameterisations are developed for the reflectances and the attenuation of deep and shallow water depending only on inherent optical properties of the water (chapter 3). The new parameteristions are obtained by means of non-linear regression analysis of various simulated spectra. The spectra are calculated by the well-established and validated radiative transfer program Hydrolight (version 3.1) for case-2 waters. The program is described by Mobley et al. (1993) and Mobley (1994). The program code was optimised for the test site Lake Constance by including the optical properties of water and bottom into the source code of Hydrolight. The simulations with Hydrolight were performed not only over the natural range of the concentrations of the water constituents found for Lake Constance, but also below and above this range to cover a more general range of concentrations. This extends the validity of the developed parameterisations to a wide number of case-2 waters.

The analytical equations are the base of retrieving properties of the water and the bottom and are the input of the inversion. For the inversion the non-linear optimisation technique of the Simplex algorithm (Nelder and Mead, 1965; Caceci and Cacheris, 1984) is used. To find the best fit and therefore the best estimates of unknown parameters, a strategy is developed to optimise the starting values of the Simplex algorithm based on the new analytical parameterisations (chapter 4). Both, the new forward model and the inversion technique, are implemented in the software tool WASI (Gege, 2001; 2004) for modeling and analysing optical data measured just below and above the water surface. A sensitivity study is made to investigate the accuracy of the new inversion methodology including a discussion about model errors and error propagation as well as the influence of sensor characteristics like signal noise, spectral, and radiometric resolution. The inversion technique is tested with in-situ measurements from Lake Constance (chapter 5). Finally, the results are summarised with an outlook on the possibilities of remote sensing in shallow water areas (chapter 6).

Chapter 2

Radiative transfer theory

This chapter describes the change of light spectra between 400 and 800 nm wavelength due to several effects in the water. It is explained how these influences can be quantified by equations so that the transfer of the light through the water body can be calculated (chapter 2.1). Figure 2.1 shows the different paths of light from the sun into the water and back to an observer or sensor above the water surface. The source of all light is the sun. This light is scattered in the atmosphere by clouds, aerosols, and air molecules. Thus, the sky radiation is a diffuse light source with angle-dependent intensity and spectral shape. When the light reaches the water surface it is divided into a reflected and a refracted part, as explained in chapter 2.6. The water surface itself is influenced by the wind speed.

In the water the light interacts with water molecules (index W) and water constituents. The constituents are particles like phytoplankton and other organic matter (index P), suspended inorganic particles from inflows and resuspension of sediments (index X), and coloured dissolved organic matter called gelbstoff (index Y) as described by Sathyendranath et al. (1989). Gelbstoff is also known as yellow substance or gilvin. The spectral characteristics of absorption and scattering - elastic and inelastic - is explained in the chapters 2.2 to 2.4 regarding the relevance for the test site Lake Constance. Another important process called fluorescence is also described in chapter 2.4. It is caused by pigments in phytoplankton - mainly chlorophyll - and gelbstoff, when photons are transfered from shorter to longer wavelengths in a short time. In deep water the observed radiances and irradiances are influenced only by the water constituents. But in shallow water the bottom affects the light field remarkably. This influence is represented by the bottom albedo described in section 2.5.

2.1 Radiative transfer equation

The change of the light field under water is due to several processes and can be described by the so called radiative transfer equation. The derivation is explained in the following.

The processes responsible for the variation of the radiance $L(\theta, \phi)$ in any kind of material - water in this study - , are primarily absorption a and scattering b. These processes are explained in

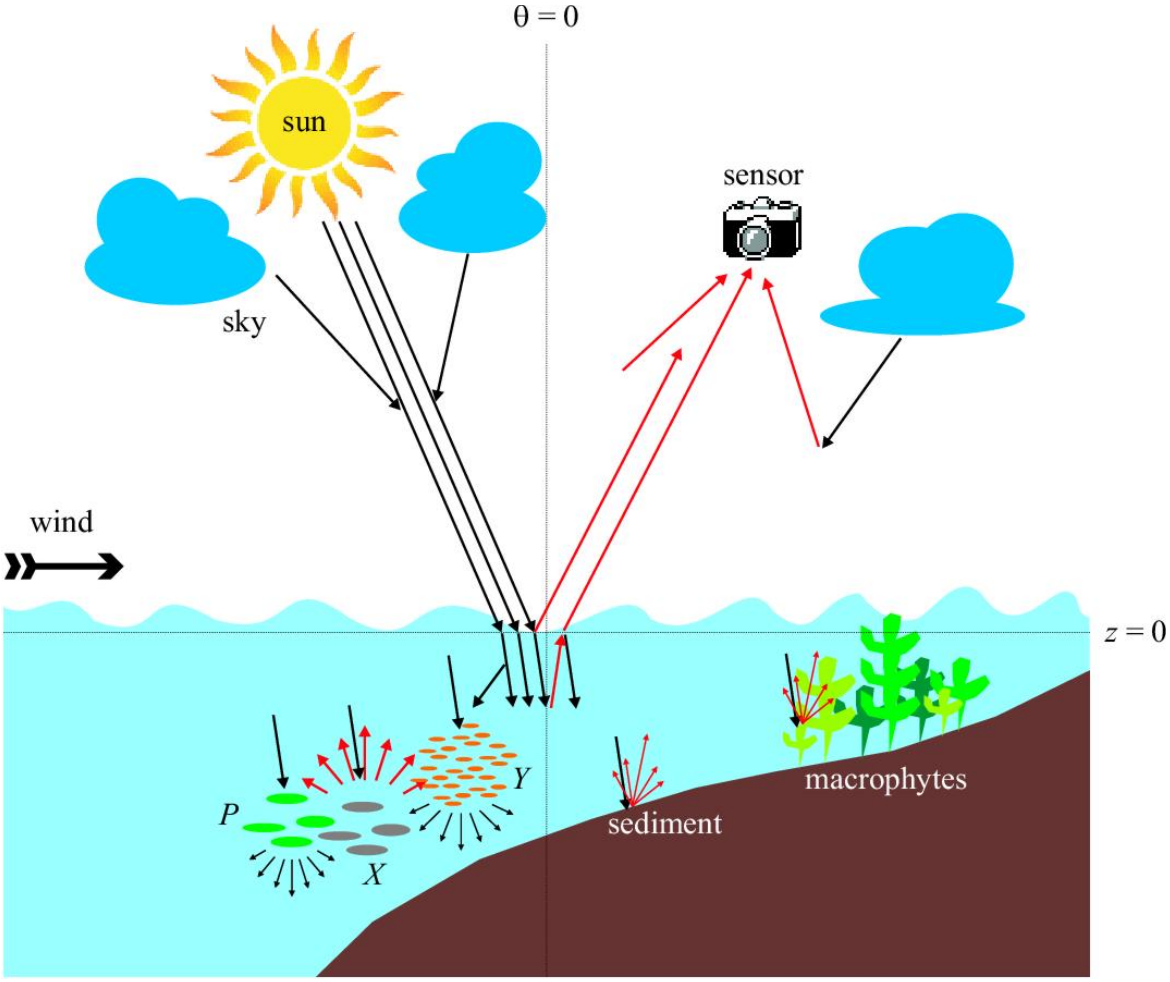

Figure 2.1: Scheme of radiative transfer in shallow water influenced by the surface, phytoplankton (P), gelbstoff (Y), suspended matter (X) and water molecules as well as different bottom types. Downwelling radiances are black arrows, reflected and scattered radiances into the upwelling path are red.

detail in the chapters 2.2 and 2.3. The zenith angle θ and the azimuth angle ϕ denote the direction of the light beam. Radiance is added to the directly transmitted beam, coming from different directions, due to elastic scattering. A further gain of radiance into the direct path is due to inelastic processes (index I) like fluorescence and Raman scattering. These processes are described in chapter 2.4. The elastic and inelastic scattered radiance is denoted as L^E and L^I, respectively. Internal sources of radiances, L^S, like bioluminescence of biological organisms or cells contribute also to the detected radiance. This is included in a so called internal source term S_0, which is explained in chapter 2.4.4. The path of the radiance through a thin layer of water of the thickness $\mathrm{d}z = z_2 - z_1$ is shown schematically in figure 2.2.
The extinction coefficient c is defined as $c = a + b$ and the single scattering albedo ω_0 is $\omega_0 = \frac{b}{c}$. The scattering coefficient is given by the scattering phase function $\beta(\psi)$, which represents the scattering probability into a specific direction of the solid angle $\mathrm{d}\Omega = \sin\theta \mathrm{d}\theta \mathrm{d}\phi$. The incoming

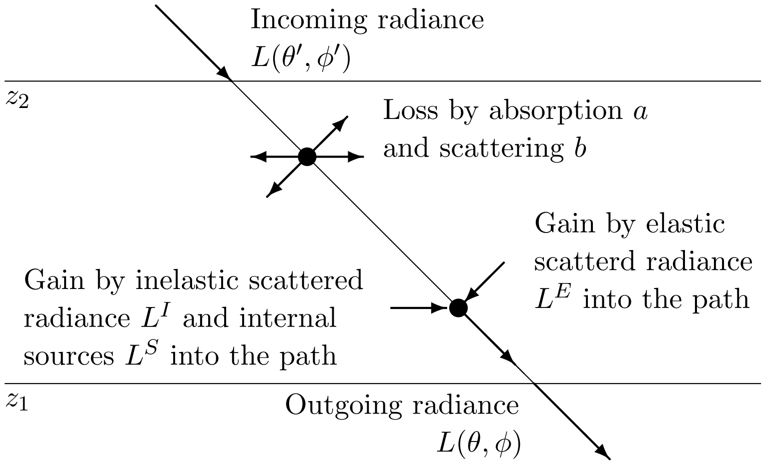

Figure 2.2: Path of the radiance and influences of absorbing and scattering particles in a thin layer of water.

light is thereby scattered by the angle ψ, which is given by the incoming and outgoing zenith and azimuth angles, θ', ϕ', θ, and ϕ, respectively. Since the scattering is azimuthally symmetric about the incident direction, which is valid in natural waters, the volume scattering coefficient b is related to the phase function $\beta(\psi)$ as follows:

$$b = \int_\Omega \beta(\psi) \mathrm{d}\Omega = 2\pi \int_0^\pi \beta(\psi) \sin\psi \mathrm{d}\psi \tag{2.1}$$

The normalised scattering phase function $\tilde{\beta}$ is given by the equation $\tilde{\beta} = \frac{\beta}{b}$ and the relation $\int_\Omega \tilde{\beta} \mathrm{d}\Omega = 1$. The scattering phase function for inelastic scattering is given by β^I, which is the sum of the Raman scattering phase function β^R and the fluorescence phase function β^F. The absorption , scattering , and phases functions are called inherent optical properties, because they depend only on the characteristics of the water constituents themselves and are independent of the light field. Even if not explicitely mentioned for simplification, all values depend on the wavelength λ, depth z, zenith angle θ, and azimuth angle ϕ. If the dependence on θ and ϕ is noted, it is combined by the symbol Ω. The above discussed radiances can be derived by the following equations.

$$\begin{aligned}
L^E(\Omega) &= \int_{\Omega'} L(\Omega')\,\beta(\Omega' \to \Omega)\mathrm{d}\Omega' \;=\; b\int_{\Omega'} L(\Omega')\,\tilde{\beta}(\Omega' \to \Omega)\mathrm{d}\Omega' && (2.2)\\
L^I(\Omega, \lambda) &= \int_{\Omega'}\int_{\lambda'} L(\Omega', \lambda')\,\beta^I(\Omega' \to \Omega, \lambda' \to \lambda)\mathrm{d}\lambda'\mathrm{d}\Omega' && (2.3)\\
\text{with} &\quad \beta^I(\Omega' \to \Omega, \lambda \to \lambda) \;=\; 0 &&\\
L^S &= \frac{S_0}{4\pi} && (2.4)
\end{aligned}$$

Putting all this together, the radiative transfer equation is

$$\mu \frac{\mathrm{d}L}{\mathrm{d}z} = -c \cdot L + L^E + S \tag{2.5}$$

μ is the cosine of the zenith angle θ and S is the total source function given by $S = L^I + L^S$. There exists no exact analytical solution of the radiative transfer equation. Hence it is necessary either to use numerical models or to make approximations and find an analytical parameterisation. A numerical model is for example the Monte Carlo method. The parameters of the light field can be simulated by modelling the paths of photons. For an infinite number of photons the light field parameters reach their exact values asymptotically. The advantage of the Monte Carlo method is the simple structure of the program, and it simulates the nature straightforward. But the disadvantage is the time consuming computation. Details of the Monte Carlo method are explained for example in Mobley (1994). The other way to solve the radiative transfer equation is the development of analytical parameterisations for all needed quantities by making approximations. Therefore, the result is not exact, but the advantage is the fast computing and the analytical equations can be inverted just as fast. In this work the way of developing analytical parameterisations is chosen.

The radiative transfer equation (2.5) is valid for radiance L, which is the collimated beam from one specific direction. Due to the construction radiance detectors can not measure a beam from an infinite solid angle. They have an aperture of typically one or two degrees as shown in figure 2.3. Additional detectors sense light from more than one direction. They measure the entire sphere or hemisphere as shown in figure 2.4. Thus, by integrating over the upward or downward hemisphere one gets the expression of the spectral scalar irradiances E_{0u} or E_{0d} and the spectral plane irradiances E_u or E_d, respectively.

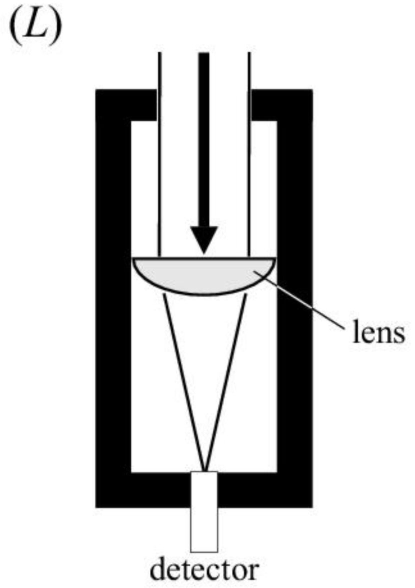

Figure 2.3: Scheme of a detector for measurements of the radiance L.

The spherical shape of the detector of the scalar irradiance ensures that all incoming photons are equally weighted independent of their direction, whereas the detector of the plane irradiance

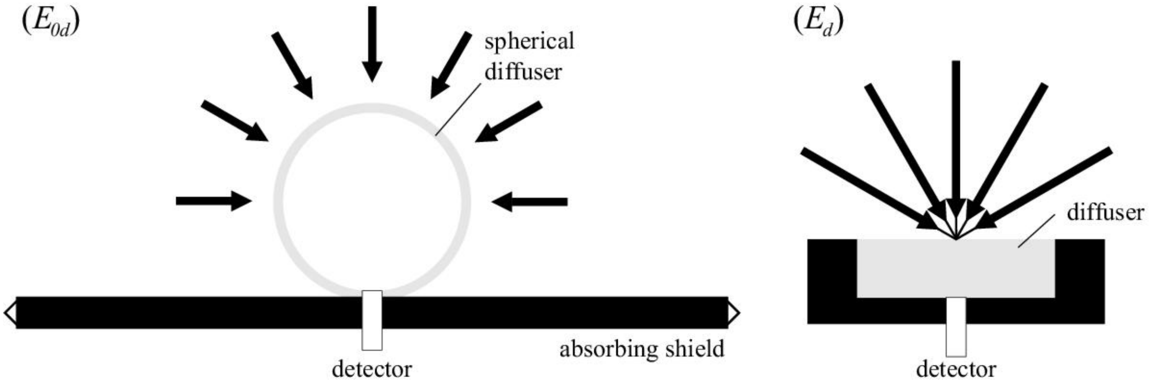

Figure 2.4: Scheme of a detector for measurements of the downward scalar irradiance E_{0d} and plane irradiance E_d.

senses the photons weighted by the cosine of their incoming direction θ. Building the integrals over the upward and downward direction for the radiance, the irradiances are related to the radiances as follows.

$$E_d = \int_{\phi=0}^{2\pi} \int_{\theta=0}^{\pi/2} L(\theta,\phi)\cos\theta\sin\theta \mathrm{d}\theta\mathrm{d}\phi \tag{2.6}$$

$$E_u = -\int_{\phi=0}^{2\pi} \int_{\theta=\pi/2}^{\pi} L(\theta,\phi)\cos\theta\sin\theta \mathrm{d}\theta\mathrm{d}\phi \tag{2.7}$$

$$E_{0d} = \int_{\phi=0}^{2\pi} \int_{\theta=0}^{\pi/2} L(\theta,\phi)\sin\theta \mathrm{d}\theta\mathrm{d}\phi \tag{2.8}$$

$$E_{0u} = \int_{\phi=0}^{2\pi} \int_{\theta=\pi/2}^{\pi} L(\theta,\phi)\sin\theta \mathrm{d}\theta\mathrm{d}\phi \tag{2.9}$$

$$\begin{aligned} E_0 &= \int_{\phi=0}^{2\pi} \int_{\theta=0}^{\pi} L(\theta,\phi)\sin\theta \mathrm{d}\theta\mathrm{d}\phi \\ &= E_{0d} + E_{0u} \end{aligned} \tag{2.10}$$

All radiances and irradiances are positive, the minus sign in equation (2.7) is due to the negative values of the cosine for angles between 90° and 180°. For the hypothetical case that the radiance is isotropically distributed and does not depend on the direction, but only on the wavelength, denoted L_0, the integral over the upward or downward directed hemisphere can be solved and the irradiances are given by: $E_d = E_u = \pi L_0$, $E_{0d} = E_{0u} = 2\pi L_0$ and therefore $E_0 = 4\pi L_0$. The irradiance can also be treated as a vector irradiance $\vec{E} = E_x \cdot \vec{e_x} + E_y \cdot \vec{e_y} + E_z \cdot \vec{e_z}$, which consists of the three parts for the $\vec{x}$-, $\vec{y}$- and $\vec{z}$-direction. The weighting factor of each direction for the integration over the radiance L is given by the expressions of the polar coordinates.

$$\vec{x} \rightarrow \sin\theta\cos\phi\,\vec{e_x} = \sqrt{1-\mu^2}\,\cos\phi\,\vec{e_x} \tag{2.11}$$

$$\vec{y} \rightarrow \sin\theta\sin\phi\,\vec{e_y} = \sqrt{1-\mu^2}\,\sin\phi\,\vec{e_y} \tag{2.12}$$

$$\vec{z} \rightarrow \cos\theta\,\vec{e_z} = \mu\,\vec{e_z} \tag{2.13}$$

Using equations (2.6), (2.7), and (2.13), the vertical component E_z of this vector irradiance is given by

$$\begin{aligned} E_z &= \int_\Omega L\,\mu \mathrm{d}\Omega = \int_{\phi=0}^{2\pi}\int_{\theta=0}^{\pi} L\,\cos\theta\sin\theta \mathrm{d}\theta \mathrm{d}\phi \\ &= E_d\,-\,E_u \end{aligned} \tag{2.14}$$

This is called the net irradiance or vector irradiance, although it is only the vertical component of the entire vector irradiance. In the following the index z of the vertical part of the vector irradiance E_z is omitted and this component is marked as E only. If the light is isotropically distributed the up- and downwelling irradiances are equal and therefore $E = 0$.

Using the irradiances and radiances some useful relations can be defined. The irradiance reflectance R and the remote sensing reflectance R_{rs} are defined as follows:

$$R = \frac{E_u}{E_d} \tag{2.15}$$

$$R_{rs} = \frac{L_u}{E_d} \tag{2.16}$$

As a quantity of the anisotropic light distribution in the water, the Q-factor is defined as the ratio of the upwelling irradiance and radiance,

$$Q = \frac{E_u}{L_u} \tag{2.17}$$

Q has values between 1 and ∞. If the light is totally isotropic, $Q = \pi$, and the Q-factor reaches higher values up to infinity, if the light is collimated. Looking on the equations (2.15) and (2.16) the Q-factor can also be expressed as $Q = \frac{R}{R_{rs}}$. Further, the mean cosines of the upwelling, downwelling, and entire light field, $\overline{\mu}_u$, $\overline{\mu}_d$, and $\overline{\mu}$, respectively, are defined as follows:

$$\overline{\mu}_u \equiv \frac{E_u}{E_{0u}} \tag{2.18}$$

$$\overline{\mu}_d \equiv \frac{E_d}{E_{0d}} \tag{2.19}$$

$$\overline{\mu} \equiv \frac{E}{E_0} \tag{2.20}$$

The mean cosines are measures of the directional behaviour of the light field under water. For a total isotropic distribution the up- and downwelling mean cosines have the value $\overline{\mu}_u = \overline{\mu}_d = \frac{1}{2}$, and the mean cosine of the entire light field is $\overline{\mu} = 0$. If the radiance is collimated in one direction θ_0 and ϕ_0, then the value of the mean cosines is $\cos\theta_0$. The Q-factor and the mean cosines depend on the distribution of the light under water. Parameters with this characteristic are called apparent optical properties.

The above explained calculation of the irradiance from the radiance is the base to derive the radiative transfer equation of the irradiance. This is done by integrating the radiative transfer equation for the radiance (2.5) over all directions:

$$\int_\Omega \mu \frac{\mathrm{d}L}{\mathrm{d}z}\mathrm{d}\Omega = -c\cdot \int_\Omega L\mathrm{d}\Omega + \int_\Omega L^E \mathrm{d}\Omega + \int_\Omega S\mathrm{d}\Omega \tag{2.21}$$

Inserting the results from above the radiative transfer equation of the irradiance can be simplified and one gets the following equation:

$$\begin{aligned}
\frac{\mathrm{d}}{\mathrm{d}z}(E_d - E_u) &= -c \cdot E_0 + \int_\Omega \left[\int_{\Omega'} L(\Omega')\beta(\Omega' \to \Omega)\mathrm{d}\Omega'\right] \mathrm{d}\Omega + \int_\Omega S \mathrm{d}\Omega \\
&= -c \cdot E_0 + \int_{\Omega'} L(\Omega') \left[\int_\Omega \beta(\Omega' \to \Omega)\mathrm{d}\Omega\right] \mathrm{d}\Omega' + \int_\Omega S \mathrm{d}\Omega \\
&= -c \cdot E_0 + b \int_{\Omega'} L(\Omega')\mathrm{d}\Omega' + \int_\Omega S \mathrm{d}\Omega \\
&= -c \cdot E_0 + b \cdot E_0 + \int_\Omega S \mathrm{d}\Omega
\end{aligned}$$

or

$$\frac{\mathrm{d}}{\mathrm{d}z} E = -a \cdot E_0 + \int_\Omega S \mathrm{d}\Omega \tag{2.22}$$

Without any internal light source, $S = 0$, the so called Gershun equation is obtained, which is an exact relation:

$$\frac{\mathrm{d}}{\mathrm{d}z} E = -a\, E_0 \tag{2.23}$$

The internal source term is neglected in the following considerations. To develop the so called two flow equation for the downwelling and upwelling irradiance, the integral of the radiative transfer equation of the radiance over all directions is separated into the upward and downward directed hemisphere, Ω_u and Ω_d, respectively. The integral of equation (2.21) over the upward direction is

$$\int_{\Omega_u} \mu \frac{\mathrm{d}L}{\mathrm{d}z} \mathrm{d}\Omega_u = -c \cdot \int_{\Omega_u} L \mathrm{d}\Omega_u + \int_{\Omega_u} L^E \mathrm{d}\Omega_u$$

which results in

$$-\frac{\mathrm{d}}{\mathrm{d}z} E_u = -c \cdot E_{0u} + \int_{\Omega_u} \left[\int_{\Omega'} L(\Omega')\beta(\Omega' \to \Omega)\mathrm{d}\Omega'\right] \mathrm{d}\Omega_u$$

The integral of the elastic scattered radiance can be transformed into

$$\begin{aligned}
&\int_{\Omega_u} \left[\int_{\Omega'_u} L\beta \mathrm{d}\Omega'_u + \int_{\Omega'_d} L\beta \mathrm{d}\Omega'_d\right] \mathrm{d}\Omega_u \\
&= \int_{\Omega'_u} L \left[\int_{\Omega_u} \beta \mathrm{d}\Omega_u\right] \mathrm{d}\Omega'_u + \int_{\Omega'_d} L \left[\int_{\Omega_u} \beta \mathrm{d}\Omega_u\right] \mathrm{d}\Omega'_d \\
&\equiv b_{uu} \cdot E_{0u} + b_{ud} \cdot E_{0d}
\end{aligned}$$

The first term describes how much of the upwelling radiance is scattered into the upward directed hemisphere. This is the upwelling scalar irradiance E_{0u} diffusely scattered in forward direction, denoted by b_{uu}. The second term specifies how much of the downwelling radiance is scattered into the upward directed hemisphere, which is the downwelling scalar irradiance E_{0d} due to the diffuse backscattering b_{du}. Using the definitions of the mean cosines of equations (2.18) and (2.19) the result is

$$-\frac{\mathrm{d}}{\mathrm{d}z} E_u = -\frac{c}{\overline{\mu}_u} \cdot E_u + \frac{b_{uu}}{\overline{\mu}_u} \cdot E_u + \frac{b_{du}}{\overline{\mu}_d} \cdot E_d \tag{2.24}$$

The extinction coefficient $c = a + b$ and the scattering coefficient can be separated into the scattering from upward to upward and from upward to downward: $b = b_{uu} + b_{ud}$. Inserting this into equation (2.24) the result is

$$-\frac{\mathrm{d}}{\mathrm{d}z}E_u = -\frac{a}{\overline{\mu}_u} \cdot E_u - \frac{b_{ud}}{\overline{\mu}_u} \cdot E_u + \frac{b_{du}}{\overline{\mu}_d} \cdot E_d \tag{2.25}$$

Analogous, the integral of the radiative transfer equation of the radiance over the downward hemisphere Ω_d is

$$\frac{\mathrm{d}}{\mathrm{d}z}E_d = -\frac{c}{\overline{\mu}_d} \cdot E_d - \frac{b_{dd}}{\overline{\mu}_d} \cdot E_d + \frac{b_{ud}}{\overline{\mu}_u} \cdot E_u \tag{2.26}$$

and with $b = b_{dd} + b_{du}$

$$\frac{\mathrm{d}}{\mathrm{d}z}E_d = -\frac{a}{\overline{\mu}_d} \cdot E_d - \frac{b_{du}}{\overline{\mu}_d} \cdot E_d + \frac{b_{ud}}{\overline{\mu}_u} \cdot E_u \tag{2.27}$$

Thereby, the diffuse scattering from downwelling radiance into the downward directed hemisphere is b_{dd}, and from upwelling into downward b_{ud}. To describe the change of the up- and downwelling irradiance with the depth the diffuse attenuation coefficients of the up- and downwelling irradiance, K_u and K_d, are defined as follows:

$$K_d \equiv -\frac{1}{E_d} \cdot \frac{\mathrm{d}E_d}{\mathrm{d}z} \tag{2.28}$$

$$K_u \equiv -\frac{1}{E_u} \cdot \frac{\mathrm{d}E_u}{\mathrm{d}z} \tag{2.29}$$

The diffuse attenuation coefficients depend on the distribution of the light field as mentioned before for the Q-factor and the mean cosines. Thus, they are also apparent optical properties. Inserting these definitions into the equations (2.25) and (2.27) yields

$$K_u E_u = -\frac{a}{\overline{\mu}_u}E_u - \frac{b_{ud}}{\overline{\mu}_u}E_u + \frac{b_{du}}{\overline{\mu}_d}E_d \tag{2.30}$$

$$-K_d E_d = -\frac{a}{\overline{\mu}_d}E_d - \frac{b_{du}}{\overline{\mu}_d}E_d + \frac{b_{ud}}{\overline{\mu}_u}E_u \tag{2.31}$$

Adding the equations (2.30) and (2.31) and using the definition of the irradiance reflectance of equation (2.15) yields

$$R = \frac{K_d - \frac{a}{\overline{\mu}_d}}{K_u + \frac{a}{\overline{\mu}_u}} \tag{2.32}$$

By subtracting the equations (2.30) and (2.31) the result can be compared with equation (2.32) and the following relation is obtained

$$a(a + b_{ud} + b_{du}) = \overline{\mu}_u K_u \overline{\mu}_d K_d + \overline{\mu}_d K_d (a + b_{ud}) - \overline{\mu}_u K_u (a + b_{du}) \tag{2.33}$$

This relation can be simplified by using some assumptions. The scattering coefficient b, which is known from equation (2.1), can be written as

$$\begin{aligned} b &= 2\pi \int_0^{\pi} \beta(\psi) \sin\psi \mathrm{d}\psi \\ &= 2\pi \int_0^{\pi/2} \beta(\psi) \sin\psi \mathrm{d}\psi + 2\pi \int_{\pi/2}^{\pi} \beta(\psi) \sin\psi \mathrm{d}\psi \\ &\equiv b_b + b_f \end{aligned} \tag{2.34}$$

Here b_f denotes the coefficient for forward scattering and b_b for backward scattering. Figure 2.5 shows on the left side the difference between the diffuse scattering functions, b_{dd} and b_{du}, and the forward and backward scattering. Generally, the scattering coefficients are not the same as the diffuse scattering functions because of the incident angle of the radiance: forward scattered radiance contributes to the downwelling light, but also to the upwelling, and backscattered radiance contributes also to both, the up- and downwelling irradiance.

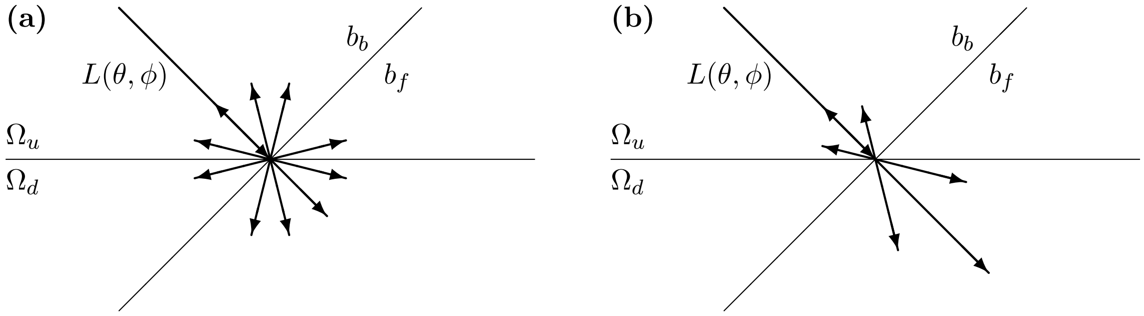

Figure 2.5: Scattering of the radiance $L(\theta, \phi)$ in forward and backward direction, b_f and b_b, and the contribution to the upward and downward looking hemisphere, Ω_u and Ω_d, for isotropic scattering on the left and scattering in natural waters on the right.

In natural waters the scattering is not isotropic. Most light is scattered in forward direction and less is scattered backward or perpendicular to the incoming direction due to the shape and size of the particles in the water (see chapter 2.3). This shows the right side of figure 2.5. Thus, even for greater incident angles, it is assumed that the forward scattered light contributes only to the downward hemisphere and the backward scattered light only to the upward hemisphere. Therefore, b_{ud} and b_{du}, can be substituted by the backscattering coefficient b_b. This yields for the radiative transfer equation (2.25) and (2.27)

$$\frac{\mathrm{d}E_d}{\mathrm{d}z} = -\frac{a}{\overline{\mu}_d}E_d - \frac{b_b}{\overline{\mu}_d}E_d + \frac{b_b}{\overline{\mu}_u}E_u \tag{2.35}$$

$$-\frac{\mathrm{d}E_u}{\mathrm{d}z} = -\frac{a}{\overline{\mu}_u}E_u - \frac{b_b}{\overline{\mu}_u}E_u + \frac{b_b}{\overline{\mu}_d}E_d \tag{2.36}$$

These two differential equations build the two flow equations of the irradiance. They are exact, if internal sources are neglected and the scattering in the water is dominated by forward scattering. To get an analytical solution of the irradiance reflectance and the remote sensing reflectance from these two equations it is further assumed that the diffuse attenuation is nearly the same for up- and downwelling irradiances, $K_u \approx K_d \equiv K$, and also the directionality of the up- and downwelling irradiances represented by the mean cosines is $\overline{\mu}_u \approx \overline{\mu}_d \equiv \overline{\mu}_0$. This results for the two flow equations in

$$\frac{\mathrm{d}E_d}{\mathrm{d}z} = -\frac{a}{\overline{\mu}_0}E_d - \frac{b_b}{\overline{\mu}_0}E_d + \frac{b_b}{\overline{\mu}_0}E_u \tag{2.37}$$

$$-\frac{\mathrm{d}E_u}{\mathrm{d}z} = -\frac{a}{\overline{\mu}_0}E_u - \frac{b_b}{\overline{\mu}_0}E_u + \frac{b_b}{\overline{\mu}_0}E_d \tag{2.38}$$

and the equation (2.33) gives

$$K = \frac{\sqrt{a(a+2b_b)}}{\overline{\mu}_0} \tag{2.39}$$

Therefore, the irradiance reflectance R of equation (2.32) can be transformed to

$$\begin{aligned} R &= \frac{\overline{\mu}_0 K - a}{\overline{\mu}_0 K + a} = \frac{(\overline{\mu}_0 K)^2 - a^2}{(\overline{\mu}_0 K)^2 + a^2 + 2\overline{\mu}_0 a K} \\ &= \frac{b_b}{a + b_b + \sqrt{a(a+2b_b)}} = \frac{1}{1 + \frac{\sqrt{a(a+2b_b)}}{a+b_b}} \cdot \frac{b_b}{a+b_b} \end{aligned}$$

This means that the reflected signal depends in the first order directly on the backscattering and inversely on the sum of absorption and backscattering. Proportionality factors are defined for the irradiance reflectance and the remote sensing reflectance, f° and $f^\uparrow$, and by means of the definitions (2.15), (2.16), and (2.17) the result is

$$R \equiv f^\circ \cdot \frac{b_b}{a+b_b} \tag{2.40}$$

$$R_{rs} \equiv f^\uparrow \cdot \frac{b_b}{a+b_b} = \frac{f^\circ}{Q} \cdot \frac{b_b}{a+b_b} \tag{2.41}$$

The equations (2.40) and (2.41) are valid for situations in deep and shallow water considering the introduced approximations. But the influence of the bottom is not yet included in the equations. To get more accurate relations for shallow water, the differential equations are solved using the following boundary conditions, which introduce the bottom depth z_B and the bottom reflectance or bottom albedo R_B. Another boundary condition is given at the water surface $z = 0$.

$$E_d(z=0) = E_{d0} \tag{2.42}$$

$$E_u(z_B) = R_B \cdot E_d(z_B) \tag{2.43}$$

If the bottom is infinitely deep, there is no influence of the bottom on the remote sensing signal and only reflected light of the water body has to be taken into account by using the reflectance of the infinitely deep water body R_∞.

$$R_\infty \equiv \frac{E_u(z_B \to \infty)}{E_d(z_B \to \infty)} \tag{2.44}$$

With these boundary conditions and the assumption that the irradiances decrease exponentially with increasing depth, the following approach is made to solve the differential equations (2.37) and (2.38):

$$E_d(z) = \mathcal{A}\mathrm{e}^{-Kz} + \mathcal{B}\mathrm{e}^{+Kz} \tag{2.45}$$

$$E_u(z) = \mathcal{C}\mathrm{e}^{-Kz} + \mathcal{D}\mathrm{e}^{+Kz} \tag{2.46}$$

The unknown coefficients $\mathcal{A}$, $\mathcal{B}$, $\mathcal{C}$, and $\mathcal{D}$ can be determined easily. The result is

$$\mathcal{A} = \frac{E_{d0}(1 - R_\infty R_B)}{1 - R_\infty R_B + R_\infty (R_B - R_\infty)\mathrm{e}^{-2Kz_B}} \tag{2.47}$$

$$\mathcal{B} = \frac{E_{d0} R_\infty (R_B - R_\infty)\mathrm{e}^{-2Kz_B}}{1 - R_\infty R_B + R_\infty (R_B - R_\infty)\mathrm{e}^{-2Kz_B}} \tag{2.48}$$

$$\mathcal{C} = \frac{E_{d0} R_\infty (1 - R_\infty R_B)}{1 - R_\infty R_B + R_\infty (R_B - R_\infty)\mathrm{e}^{-2Kz_B}} \tag{2.49}$$

$$\mathcal{D} = \frac{E_{d0}(R_B - R_\infty)\mathrm{e}^{-2Kz_B}}{1 - R_\infty R_B + R_\infty (R_B - R_\infty)\mathrm{e}^{-2Kz_B}} \tag{2.50}$$

Using equation (2.39) of the diffuse attenuation coefficient and the Gershun equation (2.23) with the result for the coefficients $\mathcal{A}$, $\mathcal{B}$, $\mathcal{C}$, and $\mathcal{D}$, the irradiance reflectance of an infinitely deep water body is given by

$$R_\infty = \frac{K - \frac{a}{\bar{\mu}_0}}{K + \frac{a}{\bar{\mu}_0}} \tag{2.51}$$

which was also obtained before and can be transformed into the relation of equation (2.40). Inserting the coefficients of equation (2.47) to (2.50) into the irradiance approach (2.45) and (2.46) and building the ratio to get the irradiance reflectance yields

$$R(z) = \frac{R_\infty(1 - R_\infty R_B) + (R_B - R_\infty)\mathrm{e}^{-2K(z_B - z)}}{1 - R_\infty R_B + R_\infty (R_B - R_\infty)\mathrm{e}^{-2K(z_B - z)}} \tag{2.52}$$

and, therefore, setting $z = 0$ for the reflectance just below the water surface gives

$$R(z=0) = \frac{R_\infty(1 - R_\infty R_B) + (R_B - R_\infty)\mathrm{e}^{-2Kz_B}}{1 - R_\infty R_B + R_\infty (R_B - R_\infty)\mathrm{e}^{-2Kz_B}} \tag{2.53}$$

If the depth dependence of the irradiance reflectance is omitted in the following, R represents the irradiance reflectance below the water surface at depth $z = 0$. Equation (2.53) can be simplified assuming reflectance values within a typical range. The irradiance reflectance of infinitely deep water R_∞ is below 0.1 and the bottom albedo R_B reaches a maximum of about 0.5 in most cases (Ohde and Siegel (2001)). This is ensured by own measurements as well (section 2.5). Thus, quadratic terms or products of the reflectances are small and the denominator of equation (2.52) and (2.53) is close to one. This results in

$$\begin{aligned} R(z) &\approx R_\infty + (R_B - R_\infty)\mathrm{e}^{-2K(z_B - z)} \\ &= R_\infty\,(1 - \mathrm{e}^{-2K(z_B - z)}) \;+\; R_B\,\mathrm{e}^{-2K(z_B - z)} \qquad (2.54) \\ R &\approx R_\infty + (R_B - R_\infty)\mathrm{e}^{-2Kz_B} \\ &= R_\infty\,(1 - \mathrm{e}^{-2Kz_B}) \;+\; R_B\,\mathrm{e}^{-2Kz_B} \qquad (2.55) \end{aligned}$$

The physical range of R_∞, R_B as well as the exponential function including the attenuation and bottom depth is between 0 and 1. Calculations within this range result in a mean relative difference of equations (2.54) and (2.55) to the exact equations (2.52) and (2.53) of 1.4%. Considering the natural range of $R_\infty < 0.3$ and $R_B < 0.7$ in the visible spectrum the maximum difference is about 3%. The advantage of the approximated equations (2.54) and (2.55) is, that the signal is separated into two parts. The first part of the formula represents the signal of the water column and the second the signal coming from the bottom.

The remote sensing reflectance R_{rs} including the shallow water characteristics can be obtained analogously to the irradiance reflectance of equations (2.54) and (2.55):

$$\begin{aligned} R_{rs}(z) &= R_{rs,\infty}\,(1-\mathrm{e}^{-2K(z_B-z)}) + R_{rs,B}\,\mathrm{e}^{-2K(z_B-z)} \qquad (2.56)\\ R_{rs} &= R_{rs,\infty}\,(1-\mathrm{e}^{-2Kz_B}) + R_{rs,B}\,\mathrm{e}^{-2Kz_B} \qquad (2.57)\end{aligned}$$

The remote sensing reflectance of the infinitely deep water $R_{rs,\infty}$ is given by the equation (2.41). $R_{rs,B}$ is the remote sensing reflectance of the bottom and is

$$R_{rs,B} \equiv \frac{L_u(z_B)}{E_d(z_B)} = \frac{L_u(z_B)}{E_u(z_B)} \cdot \frac{E_u(z_B)}{E_d(z_B)} \equiv B \cdot R_B \qquad (2.58)$$

B is the normalised bidirectional reflectance distribution function (BRDF). If the bottom reflects the downwelling radiance equally into all directions, the bottom is called a Lambertian reflector. Thus, using equation (2.7) and solving the integral the normalised BRDF is π^{-1} sr^{-1}.

If the bottom element is a mixture of several bottom types i, $1 \le i \le n$, represented by more than one bottom albedo and BRDF, the reflection of the bottom is given by the sum over all occurring bottom types each weighted by its areal fraction $f_{a,i}$. Thus, the irradiance reflectance and the remote sensing reflectance can be calculated by

$$\begin{aligned} R(z) &= R_\infty\,(1-\mathrm{e}^{-2K(z_B-z)}) + \left(\sum_{i=1}^{n} f_{a,i}\cdot R_B\right) \mathrm{e}^{-2K(z_B-z)} \qquad (2.59)\\ R_{rs}(z) &= R_{rs,\infty}\,(1-\mathrm{e}^{-2K(z_B-z)}) + \left(\sum_{i=1}^{n} f_{a,i}B_i\cdot R_B\right) \mathrm{e}^{-2K(z_B-z)} \qquad (2.60)\\ R &= R_\infty\,(1-\mathrm{e}^{-2Kz_B}) + \left(\sum_{i=1}^{n} f_{a,i}\cdot R_B\right) \mathrm{e}^{-2Kz_B} \qquad (2.61)\\ R_{rs} &= R_{rs,\infty}\,(1-\mathrm{e}^{-2Kz_B}) + \left(\sum_{i=1}^{n} f_{a,i}B_i\cdot R_B\right) \mathrm{e}^{-2Kz_B} \qquad (2.62)\end{aligned}$$

If no depth dependence is mentioned, the irradiance and the remote sensing reflectance represent the values just below the water surface. The equations 2.61 and 2.62 are the commonly used remote sensing parameterisations of shallow water (Joseph, 1950; Lyzenga, 1978; Maritorena et al., 1994; Lee et al., 1998). To derive the depth dependence of the remote sensing reflectance or the irradiance reflectance it is not sufficient to know only the depth z. In addition, the inherent optical properties $a(z)$, $b(z)$ and $b_b(z)$ as well as the apparent optical properties $\overline{\mu}_0(z)$ and $K(z)$ depend also on the depth. Thus, depth profiles of the needed parameters must be available for a proper estimation of $R(z)$ and $R_{rs}(z)$.

More details on the radiative transfer equation and the developement of the analytical equations are given for example in Joseph (1950), Gordon et al. (1975), Preisendorfer (1976), Philpot and Ackleson (1981), Zimmermann (1991), Maritorena et al. (1994), Mobley (1994), Bukata et al.

(1995), Sathyendranath and Platt (1997) and Lee et al. (1998).
With the equations (2.61) and (2.62) it is now possible to investigate the remote sensing signals R and R_{rs} depending on the absorpion, the backscattering, the bottom depth, the bottom albedo, and the anisotropical light distribution due to the sun and viewing geometry. The method to get these informations from a hyperspectral measurement is called inversion and is described in chapter 4.

2.2 Absorption

When light is going through a medium it is weakened by interaction with its atomic and molecular structure. Part of the incoming radiance is scattered away from the incident direction and appears at other directions at the same wavelength (see chapters 2.3.1 to 2.3.4). Another part is absorbed in the sense that a transformation of the radiance takes place into other forms of energy. The light can be absorbed to produce thermal energy by stimulating molecule movement, or can be emitted at another wavelength (see chapter 2.4), or can be used for internal biological or chemical processes. In natural water the absorbed energy is used by biological absorbers, for example, for the photosynthesis of phytoplankton or plants on the sea floor. The molecules which absorb the energy in the visible spectrum are called pigments. Additionally, coloured dissolved organic matter (CDOM) called gelbstoff is an absorber in the water. Inorganic particles like suspended sediment are also present in natural water. Therefore, the absorption coefficient a can be calculated by adding the separate absorption coefficients of the pure water and the water constituents.

$$a(\lambda, T) = a_W(\lambda, T) + a_P(\lambda) + a_X(\lambda) + a_Y(\lambda) \tag{2.63}$$

The individual absorption coefficients of water a_W, phytoplankton a_P, suspended matter a_X, and gelbstoff a_Y are explained in the following.

2.2.1 Absorption by water

The optical properties of the water in the visible and ultra-violet (UV) spectrum are not known in detail. There exists no theoretical model which describes the absorption and scattering of pure water exactly. Therefore, it is necessary to rely on laboratory measurements. Investigations on the absorption of water a_W were done in the last 30 years for example by Morel (1974), Smith and Tyler (1976), Smith and Baker (1981), Pegau and Zaneveld (1993) and most recently by Buiteveld et al. (1994) and Hakvoort (1994). The results of the measurements of Hakvoort (1994) are shown in figures 2.6 and 2.7. He made measurements of the absorption of pure water, but no analytical parameterisation was found to describe the spectral dependence. The dependence on the temperature from 2.5°C to 40.5°C was investigated. Generally, the absorption of water depending on the temperature can be expressed by

$$a_W(\lambda, T) = a_W(\lambda, T = 20°\mathrm{C}) + \frac{\mathrm{d}a_W(\lambda, T)}{\mathrm{d}T} \cdot (T - 20°\mathrm{C}) \tag{2.64}$$

where the temperature T is used in degree Celsius. The data of Hakvoort (1994) of figure 2.6 show that the absorption of water at a temperature of 20°C is below 0.05m^{-1} for wavelengths between 400 to 550 nm. There is a slight increase up to 0.1 m^{-1} till 580 nm, then the absorption increases rapidly to a value of 0.27 m^{-1} at around 610 nm. A second slight increase to 0.4 m^{-1} is at 665 nm before a local maximum is reached at 765 nm with 2.77 m^{-1}.

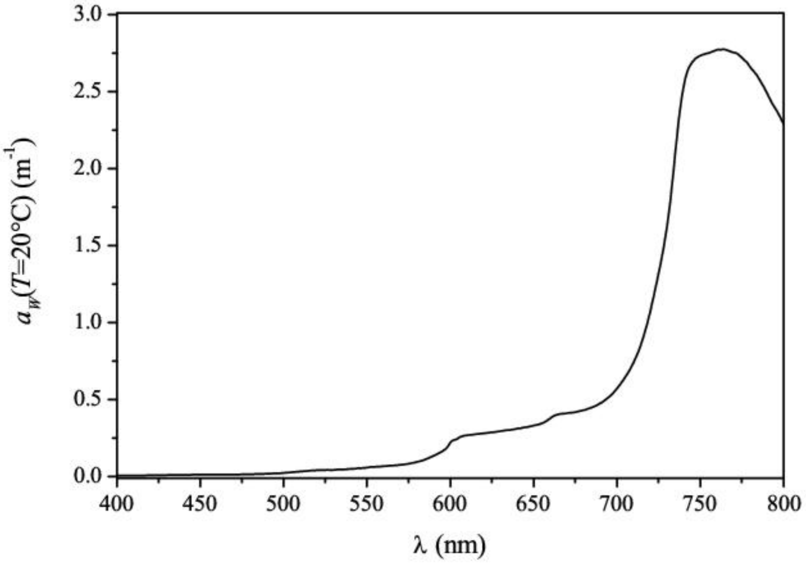

Figure 2.6: Absorption coefficient of pure water at a temperature of $T = 20°\text{C}$ after Hakvoort (1994).

The influence of temperature on the absorption of water is shown in figure 2.7. The temperature gradient $\frac{\mathrm{d}a_W(\lambda,T)}{\mathrm{d}T}$ is on the left of figure 2.7. From 400 to 700 nm the gradient is nearly constant at 0.0012 $\text{m}^{-1}°\text{C}^{-1}$. Small peaks can be observed at 606 and 664 nm with values of 0.0025 and 0.0015 $\text{m}^{-1}°\text{C}^{-1}$, respectively. From 700 nm onwards, the temperature gradient increases to its maximum value at 742 nm with 0.0168 $\text{m}^{-1}°\text{C}^{-1}$. The peak is followed by a strong decrease to negative values from 782 to 800 nm, which means that the absorption of water decreases for increasing temperature. The change of the absolute value of the absorption of pure water is shown on the right of figure 2.7 for four temperatures: 10, 15, 25, and 30°C. Positive values represent a lower absorption compared to the temperature of $T = 20°\text{C}$ and negative values a higher absorption. There is only a little effect due to temperature from 400 to 700 nm. The influence of the peak of the temperature gradient at 742 nm is the largest. It changes the absorption by 0.16 m^{-1} when the water temperature differs by 10°C from 20°C. The difference in the absorption of 0.16 m^{-1} corresponds to a change of the absolute value by 7% around 740 nm for a 10°C temperature difference.

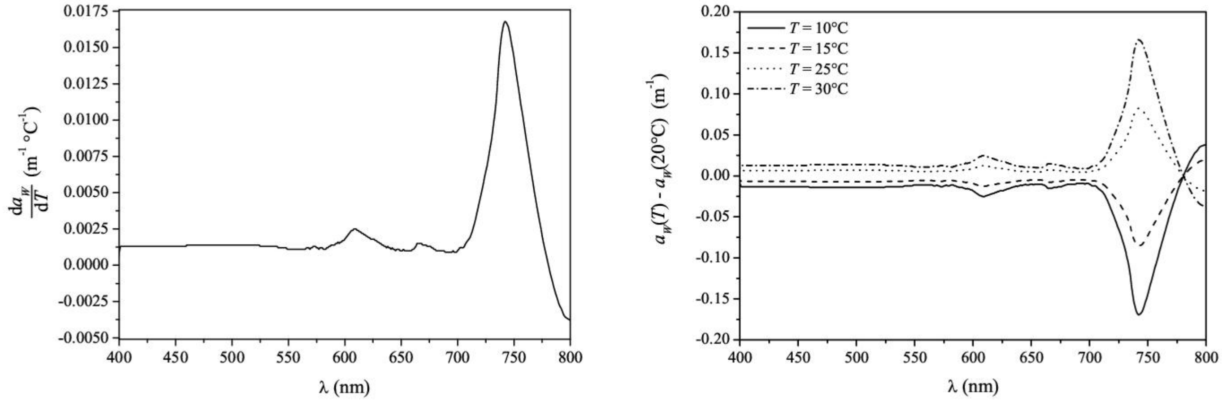

Figure 2.7: The temperature gradient of absorption of pure water (left) after Hakvoort (1994) and the variability of the absorption of pure water due to temperature variation (right) relative to 20°C for temperatures of 10, 15, 25, and 30°C.

2.2.2 Absorption by phytoplankton

Absorption of phytoplankton a_P is due to various photosynthetic pigments under them mainly chlorophyll and pheophytin. These pigments are present in all algae species. Other pigments are for example carotenoids and biliproteins. The absorption is the sum of the specific pigment absorption multiplied each by their concentration. Due to the fact that many species of phytoplankton occur in natural waters and every species contains more than one pigment, it is more practicable to calculate the absorption by mean specific absorption coefficients of the different algae species seperately. This is done for the detection of different species by remote sensing for example by Gege (1994). If no seperation of the species is necessary, the phytoplankton absorption is estimated by the mean specific absorption coefficient of phytoplankton a_P^* multiplied by the total concentration of phytoplankton C_P:

$$a_P(\lambda) = a_P^*(\lambda) \cdot C_P \tag{2.65}$$

The specific absorption coefficient a_P^* was investigated for example by Prieur and Sathyendranath (1981), Sathyendranath et al. (1987) for oceanic and coastal sea water, and Gege (1994) and Heege (2000) for Lake Constance. Figure 2.8 shows the specific absorption coefficient normalised to the value at 440nm as calculated by Prieur and Sathyendranath (1981) as well as Heege (2000), who used measurements of Gege (1994) and Tilzer and Hartig (1994). Absorption bands are in the blue and red part of the visible spectrum, broadly peaked around 440nm and sharply peaked at 675nm, respectively. The absorption of green light is weak, only about 40% at 550nm compared to the value at $\lambda_0 = 440$nm. No absorption by phytoplankton occurs from 750 nm onwards.

The differences between the specific absorption coefficients in figure 2.8 are caused by varying water types with changing composition of phytoplankton. The spectrum of Heege (2000) was

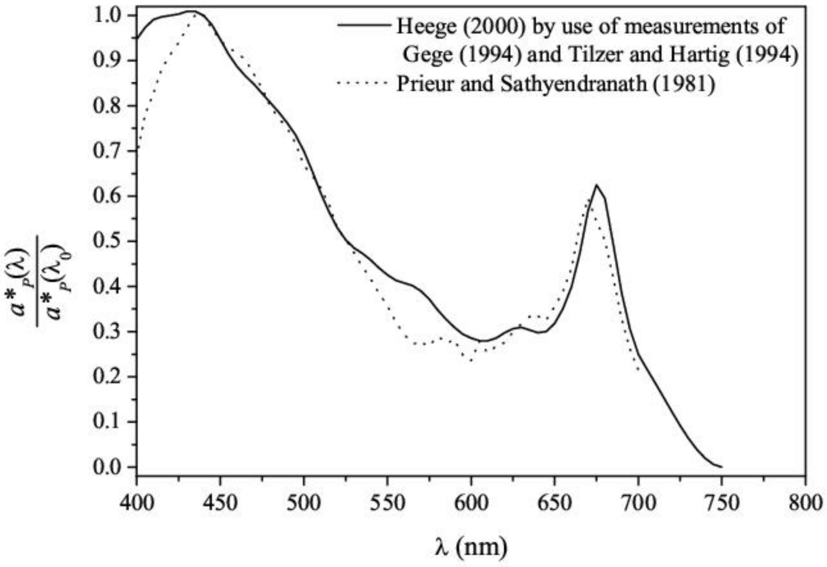

Figure 2.8: Normalised specific absorption coefficient of phytoplankton obtained by spectral optical in situ measurements after Prieur and Sathyendranath (1981) for oceanic and coastal sea water and after Heege (2000) for Lake Constance, who used measurements of Gege (1994) and Tilzer and Hartig (1994).

calculated using in-situ absorption spectra of Gege (1994), which were derived by inversion of spectral reflectance measurements at Lake Constance between 1990 and 1991. Normalisation was performed by the sum of chlorophyll-a and pheophytin measured at the University of Konstanz (Tilzer and Hartig, 1994). The plotted curve is the mean value of 213 measurements. The analysis of Prieur and Sathyendranath (1981) was done in the same way for oceanic and coastal water from 1970 to 1977. 93 observations were investigated.

The absorption coefficient of the phytoplankton can be derived using the values of the normalised specific absorption coefficient plotted in figure 2.8 and known values of $a^*_P(\lambda_0)$. Sathyendranath et al. (1987) found for oceanic and coastal water a variability from 0.0187 to 0.0473 m^2/mg and Heege (2000) found for Lake Constance a mean value of 0.0336 m^2/mg using the measurements of Gege (1994) and Tilzer and Hartig (1994). Figure 2.9 shows the calculated absorption of phytoplankton for Lake Constance for five values of the concentration: 0.5, 1, 3, 7, and 15 μg/l. Besides, there are other models for oceanic waters using the specific absorption and concentration of chlorophyll-a, a^*_{chl} and C_{chl}, respectively. Morel (1991) found that the power law $a_P = 0.06\, a^*_{chl}\, [C_{chl}]^{0.65}$, which was first proposed by Prieur and Sathyendranath (1981), was the best solution to estimate the absorption coefficient for his data set. C_{chl} is the concentration of chlorophyll-a in units of μg/l. The empirical model of Bricaud et al. (1995) uses the parameterisation of the specific absorption coefficient by means of C_{chl}. Their extensive studies of more than 800 spectra results in

$$a_P^*(\lambda) = A(\lambda) \cdot C_{chl}^{-B(\lambda)} \tag{2.66}$$

with positive empirical coefficients A and B depending on the wavelength. The model includes the package effect of phytoplankton cells and the effect of the varying pigment composition.

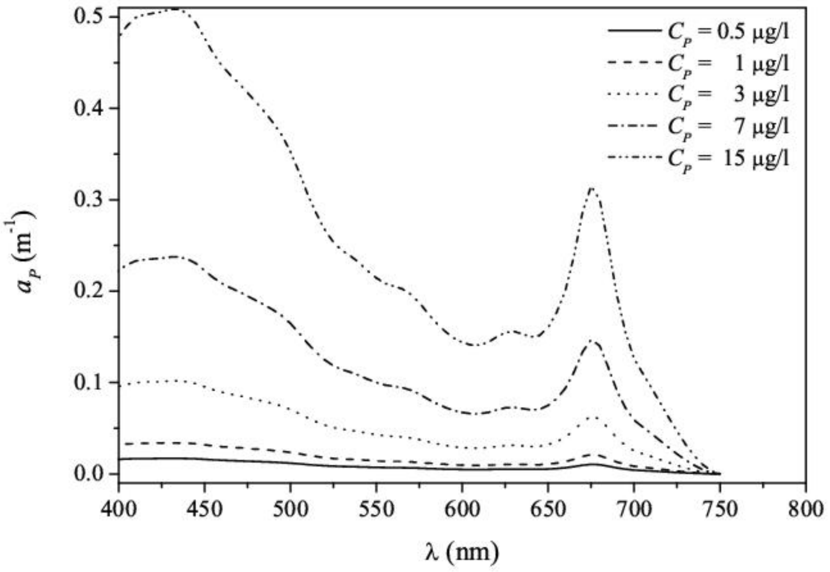

Figure 2.9: Absorption of phytoplankton derived for five concentrations of phytoplankton and the specific absorption coefficient of Gege (1994) for Lake Constance.

2.2.3 Absorption by suspended particles

The origin of particulate matter in natural waters is due to organic and inorganic material. Organic parts are contained in phytoplankton cells or are fragments of dead plankton and faecal pellets of zooplankton. These parts are often called detritus. Inorganic particles are due to suspended minerals coming from inflows or resuspension at coastal regions. They are mainly constisting of quartz, clay, and calcite. Like the absorption of phytoplankton, the absorption of suspended particles a_X can be determined by

$$a_X(\lambda) = a_X^*(\lambda) \cdot C_X \tag{2.67}$$

with the specific absorption coefficient a_X^* and the concentration of suspended particles C_X. There are only few published values of the specific absorption coefficient of suspended particles due to the difficulties of the separation of the individual components in natural waters. A comparison of these values is shown for example in Pozdnyakov and Grassl (2003).

In general, the absorption of the total suspended particles is very low and is negligible for the inorganic particles. For example, Heege (2000) found that the value is zero for Lake Constance.

Due to the close correlation to phytoplankton, the absorption of the organic particulate matter is part of the specific absorption of phytoplankton (Gege (1994), Heege (2000)). Roesler et al. (1989) developed for coastal water the following relation for detritus:

$$a_X(\lambda) = a_X(\lambda_0) \cdot \mathrm{e}^{-s_X(\lambda-\lambda_0)} \tag{2.68}$$

with a mean value of $s_X = 0.011$ nm^{-1} and $a_X(\lambda_0) = 0.09$ m^{-1} at $\lambda_0 = 400$ nm for their data.

2.2.4 Absorption by gelbstoff

Gelbstoff is the result of biological degradation and consists of humic and fulvic acids dissolved in the water. The pigments of the humic and fulvic acids are responsible for the yellow or brown colour of the water, if their concentration is very high. Therefore, Kalle (1937) established the name gelbstoff for these substances. Sometimes the English term yellow substance is used in the literature. Kalle (1966) recognised the exponential variation of gelbstoff absorption a_Y with wavelength in the visible part of the spectra. Following the study of Morel and Prieur (1976), Bricaud et al. (1981) found that gelbstoff absorption shows an exponential decrease for increasing wavelenghts and expressed this in the following relation. For a known absorption at a wavelegth $\lambda_0 = 440$nm, the gelbstoff absorption can be determined by

$$a_Y(\lambda) = a_Y(\lambda_0) \cdot \mathrm{e}^{-s_Y(\lambda-\lambda_0)} \tag{2.69}$$

The exponential coefficient s_Y is variable, but mostly the value $s_Y = 0.014$ nm^{-1} is used. Bricaud et al. (1981) analysed many data sets and found a standard deviation of $\Delta s_Y = \pm 0.003$ nm^{-1} and Roesler et al. (1989) investigated the literature and found similar results. The study of Gege (1999) confirms this value for the case-2 water of Lake Constance. Figure 2.10 shows the spectral absorption of gelbstoff normalised to the absorption at $\lambda_0 = 440$ nm.
First systematic optical gelbstoff measurements at Lake Constance were made by Heege et al. (1998) followed by investigations of Gege (1999), which show that the mean value of $a_Y(\lambda_0)$ was 0.29 m^{-1} in 1998 in the open water of Lake Constance and ranges between 0.22 m^{-1} and 0.47 m^{-1}. High absorption values of about 1 m^{-1} occured in the mouth of rivers, which are transporting high amounts of gelbstoff. Figure 2.11 shows the spectral shape of the gelbstoff absorption for five different values from 0.1 to 1.0 m^{-1} derived by equation (2.69). Even for low amount of gelbstoff, the absorption in the blue from 400 to 450 nm is higher than the absorption of phytoplankton. Exact measurements of the absorption of Gelbstoff show, that the equation (2.69) is only valid approximately. Spectral investigations of Gege (2000) and Schwarz et al. (2002) show that the gelbstoff absorption is a composition of several absorption bands due to the compounds of gelbstoff. The absorption can be fitted by Gaussian curves. This method is relevant especially in the ultraviolet spectrum. In the visible range from 400 nm onwards this method is not necessary in practice and the exponential approach of equation (2.69) is sufficient.

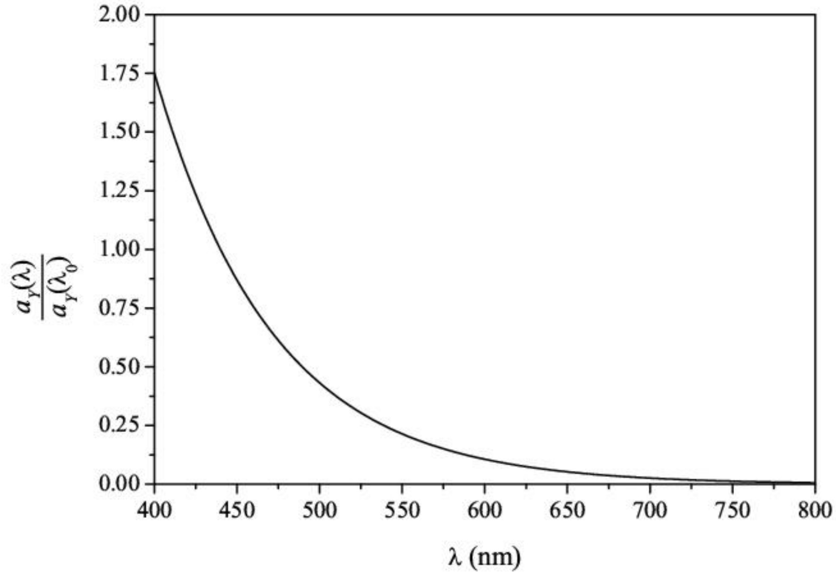

Figure 2.10: Absorption of gelbstoff after Bricaud et al. (1981) normalised to the absorption at $\lambda_0 = 440$ nm with $s_Y = 0.014$ nm^{-1}.

2.3 Elastic scattering

The process of scattering can be described as absorption and simultaneous emission of a photon. Emission at the same wavelength as the incoming radiation is called elastic scattering and emission at another wavelength is called inelastic scattering. The inelastic scattering processes of Raman scattering and fluorescence are explained in chapter 2.4. In these processes, the emitted wavelength is longer than the absorbed and therefore energy is transformed in contrast to elastic scattering, where only the direction of the incident radiation is changed.

Scattering in natural water takes place due to the interaction of photons with water molecules and water constituents. The influence of each constituent on the scattering process depends on wavelength, particle size, concentration, and refractive index. Theoretical details are for example explained in van de Hulst (1981). As for the total absorption coefficient, the total scattering coefficient b is the sum of the scattering coefficient of pure water and the water constituents.

$$b(\lambda, T) = b_W(\lambda, T) + b_P(\lambda) + b_X(\lambda) + b_Y(\lambda) \tag{2.70}$$

As described in chapter 2.1, the backscattering coefficient is the relevant parameter for the reflected radiance and irradiance and therefore for remote sensing. The total backscattering coefficient b_b can be expressed in the same way as the scattering coefficient.

$$b_b(\lambda, T) = b_{b,W}(\lambda, T) + b_{b,P}(\lambda) + b_{b,X}(\lambda) + b_{b,Y}(\lambda) \tag{2.71}$$

The individual scattering and backscattering coefficients of pure water, phytoplankton, suspended matter, and gelbstoff are explained in the following for the elastic scattering occurring

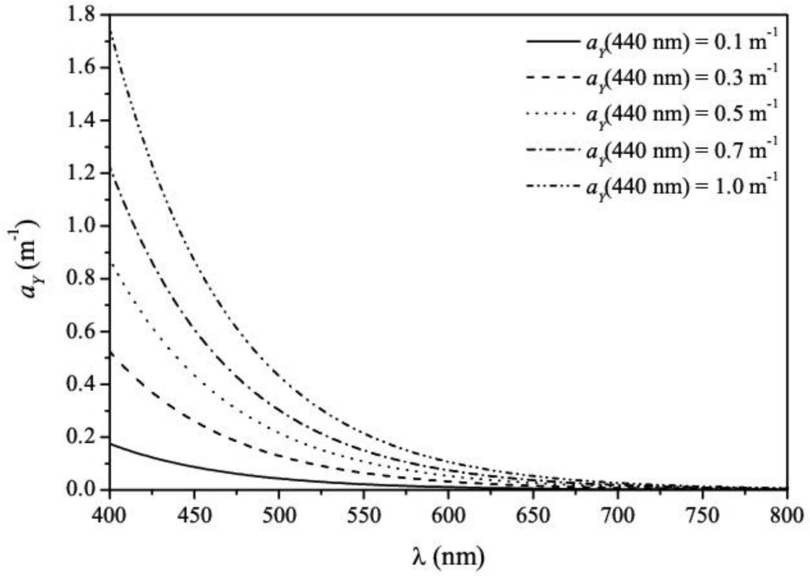

Figure 2.11: Absorption of gelbstoff derived for five different absorptions at 440 nm and for $s_Y = 0.014$ nm^{-1} after equation (2.69).

in equation (2.5) in the term of L^E. Afterwards, the inelastic scattering is described, which is included in the radiative transfer equation (2.5) in the radiance L^I.

2.3.1 Elastic scattering by water

The scattering of light by molecules in liquids is described theoretically by the model of Smoluchowski (1908) and Einstein (1910). Their theory is an approach from the statistical thermodynamics and is called the theory of fluctuation. As for example described by Morel (1974), the volume scattering phase function of water β_W is given by

$$\beta_W(\lambda, T, \psi) = \frac{2\pi^2 k_B T_K}{\lambda^4 \kappa_T} \cdot n_W^2 \cdot \left[\frac{\partial n_W}{\partial p}\right]_T^2 \cdot \frac{6+6\rho}{6-7\rho} \cdot \left(1 + \frac{1-\rho}{1+\rho}\cos^2\psi\right) \tag{2.72}$$

$k_B = 1.38054 \cdot 10^{-23}$ J/K is the Boltzmann constant, T_K the temperature in Kelvin, κ_T the isothermal compressibility in Pa^{-1}, n_W the refractive index of water, $\frac{\partial n_W}{\partial p}$ the pressure derivative of the refractive index of water in Pa^{-1}, and ρ the depolarisation ratio.

Experimental investigations have shown that the phase function does not follow the λ^{-4} law exactly. This is due to the fact that the refractive index of water, the pressure derivative of the refractive index of water, and the depolarisation ratio also depend on the wavelength. Morel (1974) for example proposed a dependence of $\beta_W(\psi = 90°) \propto \lambda^{-4.32}$ using measurements at 366, 405, 436, 546, and 578 nm. More recent investigations on water were performed by Hakvoort (1994) for wavelengths from 300 to 800 nm in 2 nm steps. He suggested the use of equation (2.72) together with empirical relations of the isothermal compressibility, the refractive index,

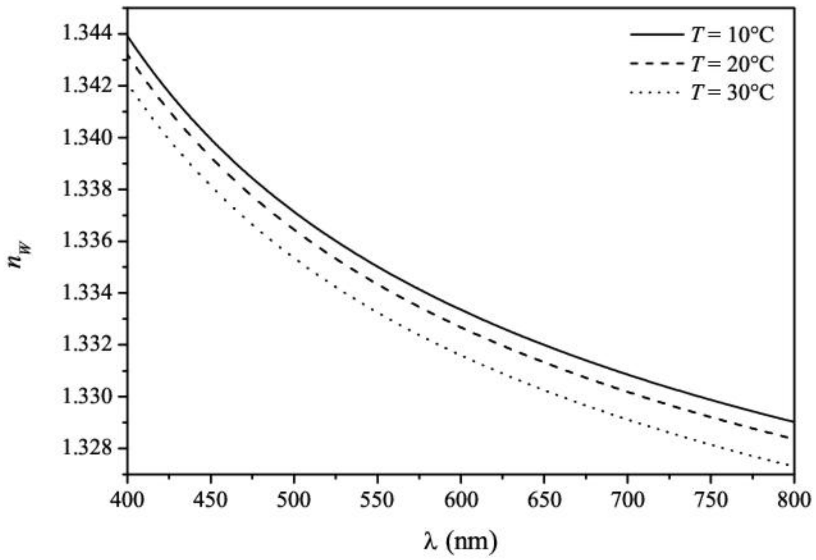

Figure 2.12: Refractive index of water after Quan and Fry (1995) for three different temperatures determined with equation (2.75).

and the pressure derivative based on measurements. The dependence of these relations on wavelength and temperature correct for the measured discrepance of the phase function to the λ^{-4} law found by Morel (1974). The parameterisations of the isothermal compressibility and the pressure derivative are described in Hakvoort (1994) and given by

$$\kappa_T(T) = \kappa_{T,0} - \kappa_{T,1} \cdot T + \kappa_{T,2} \cdot T^2 \tag{2.73}$$

$$\left[\frac{\partial n_W}{\partial p}\right]_T (\lambda, T) = \frac{(\partial_T n_0 \cdot \lambda + \partial_T n_1) \cdot (\partial_\lambda n_0 \cdot T + \partial_\lambda n_1)}{\partial_{\lambda,T} n_0} \tag{2.74}$$

T is the temperature in degree Celsius. The empirical coefficients $\kappa_{T,0}$, $\kappa_{T,1}$, and $\kappa_{T,2}$ are listed in table 2.1 and $\partial_T n_0$, $\partial_T n_1$, $\partial_\lambda n_0$, $\partial_\lambda n_1$, and $\partial_{\lambda,T} n_0$ in table 2.2. The most recent study of the refractive index of water was published by Quan and Fry (1995). They studied the dependence of the refractive index of water on wavelength, temperature, and also salinity and formed an empirical equation. For a salinity value of zero the following equation is obtained

$$n_W(\lambda, T, S = 0) = n_0 + n_1 \cdot T^2 + \frac{n_2 + n_3 \cdot T}{\lambda} + \frac{n_4}{\lambda^2} + \frac{n_5}{\lambda^3} \tag{2.75}$$

The empirical coefficients n_i, $i = 0, ..., 5$, are given in table 2.3. The spectral shape of the refractive index of water is shown in figure 2.12 for three different temperatures of 10, 20, and 30°C. The value decreases with increasing wavelength and ranges between 1.328 and 1.343 for $T = 20$°C.

The influence of the salinity on the scattering of water was investigated for example by Morel (1974). Measurements showed a linear increase of the scattering by water by 34%, if the salinity is increased from zero to 3.5‰. This is due to the change of the density fluctuation in salt water.

$\kappa_{T,0}$	$5.062271 \cdot 10^{-10}$ Pa^{-1}
$\kappa_{T,1}$	$3.179 \cdot 10^{-12}$ °C^{-1} Pa^{-1}
$\kappa_{T,2}$	$4.07 \cdot 10^{-14}$ °C^{-2} Pa^{-1}

Table 2.1: Coefficients for the determination of the isothermal compressibility of water by equation (2.73) after Hakvoort (1994).

$\partial_T n_0$	$-1.56 \cdot 10^{-14}$ nm^{-1} Pa^{-1}
$\partial_T n_1$	$1.5989 \cdot 10^{-10}$ Pa^{-1}
$\partial_\lambda n_0$	$-5.785 \cdot 10^{-13}$ °C^{-1} Pa^{-1}
$\partial_\lambda n_1$	$1.61857 \cdot 10^{-10}$ Pa^{-1}
$\partial_{\lambda,T} n_0$	$1.501511 \cdot 10^{-10}$ Pa^{-1}

Table 2.2: Coefficients for the determination of the pressure derivative of the refractive index of water by equation (2.74) after Hakvoort (1994).

The combined structure of the water molecule dipoles is modified as a result of the inclusion of salt. This has an impact on the refractive index, the isothermal compressibility, the pressure derivative, and the depolarisation ratio.

The scattering coefficient of pure water b_W is obtained by integrating the scattering phase function of equation (2.72) over all directions. This yields

$$b_W(\lambda, T) = \frac{8\pi}{3}\beta_W(\lambda, T, \psi = 90°)\frac{2+\rho}{1+\rho} \tag{2.76}$$

which is approximately $b_W \approx 16 \cdot \beta_W(\psi = 90°)$ assuming a range of the depolarisation ratio of $0.05 < \rho < 0.1$. The scattering phase function of water is plotted in figure 2.13 for a scattering angle from 0 to 180° and for 400, 500, 600, 700, and 800 nm with the specifications after Hakvoort (1994) and the refractive index after Quan and Fry (1995). Due to the cosine in equation (2.72) the phase function is symmetric with the minimum at 90°. Figure 2.14 shows the spectral slope of the scattering coefficient for the model of Morel (1974) and Hakvoort (1994). Morel (1974)

n_0	1.31405
n_1	$-2.02 \cdot 10^{-6}$ °C^{-2}
n_2	15.868 nm
n_3	-0.00423 nm °C^{-1}
n_4	-4382 nm^2
n_5	$1.1455 \cdot 10^6$ nm^3

Table 2.3: Coefficients for the determination of the refractive index of water for zero salinity by equation (2.75) after Quan and Fry (1995).

used a depolarisation ratio $\rho = 0.09$. Hakvoort (1994) found the best agreement for his model with $\rho = 0.051$. The difference between the two models is below 10% from 400 to 500 nm and below 5% from 500 to 680 nm. For a wavelength larger than 680 nm, the results of Hakvoort (1994) are higher than those of Morel (1974) and are lower for wavelengths smaller than 680 nm.

Due to the symmetry of the phase function of water in forward and backward direction the backscatter coefficient of pure water $b_{b,W}$ is half the total scattering coefficient.

$$b_{b,W}(\lambda, T) = \frac{1}{2} b_W(\lambda, T) \tag{2.77}$$

The variability of the scattering and backscattering coefficients due to temperature is in the order of 2%. The coefficients decrease, if the temperature increases from 20°C to 30°C or decreases from 20°C to 0°C. This variability is due to the changes of the temperature dependent quantities of the scattering phase function of equation (2.72). The influence of the water depth due to increasing pressure is below 2% at a temperature of 20°C until a depth of 1000 m. Uncertainties of the depolariasation ratio have also an effect on the scattering and backscattering coefficients. Their values are about 7% higher for $\rho = 0.09$ compared to $\rho = 0.051$.

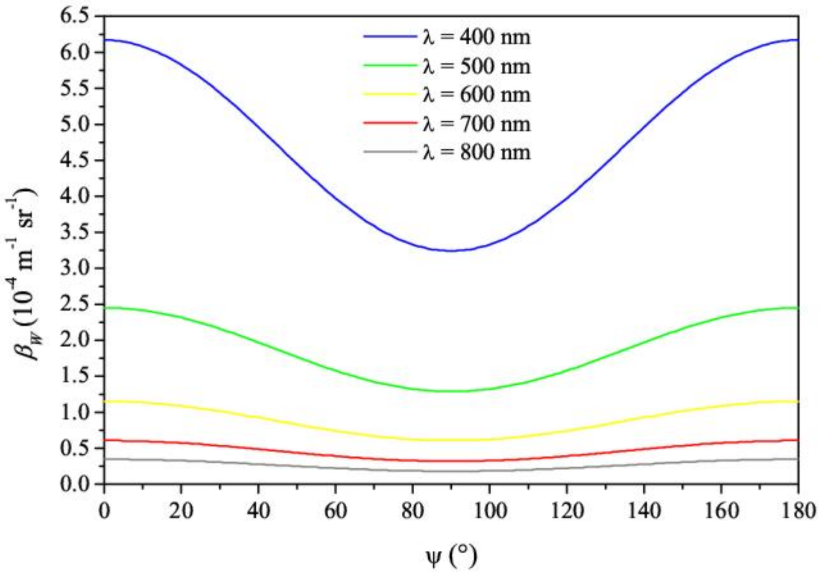

Figure 2.13: Scattering phase function of pure water after Hakvoort (1994) using the parameterisation of the refractive index of water after Quan and Fry (1995) for a temperature of $T = 20$°C.

2.3.2 Elastic scattering by phytoplankton

Scattering by phytoplankton is due to the particulate structure of the cells. The influence of phytoplankton on the total scattering coefficient depends on the water type. For water with low

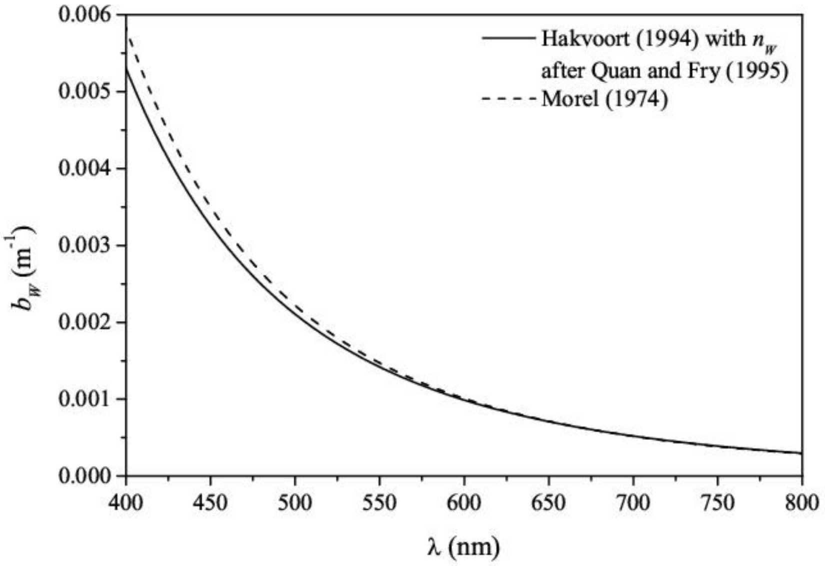

Figure 2.14: Scattering coefficient of pure water after Hakvoort (1994) (solid line) using the parameterisation of the refractive index of water after Quan and Fry (1995) for a temperature of $T = 20°\mathrm{C}$ and the scattering coefficient after Morel (1974) (dashed line).

concentration of inorganic suspended sediment the scattering is driven by the concentration of phytoplankton. This occurs for example in the open ocean. Gordon and Morel (1983) developed an empirical model, where the scattering is correlated directly to the pigment concentration of chlorophyll-a C_{chl} in units of μg/l. The scattering coefficient of phytoplankton b_P in units of m^{-1} is given by

$$b_P(\lambda) = B \cdot C_{chl}^{0.62} \cdot \left(\frac{\lambda_0}{\lambda}\right) \tag{2.78}$$

with $\lambda_0 = 550$ nm and $B = 0.3$ as a mean value for case-1 water dominated by phytoplankton. After Gordon and Morel (1983) the equation (2.78) is valid in the range of phytoplankton concentration from 0.05 to 1 μg/l. Gordon and Morel (1983) found that case-1 water has a value of $B \leq 0.45$. Higher values are used for case-2 water to calculate the scattering coefficient in turbid water for example (Lee et al., 1998).

The backscattering coefficient of phytoplankton $b_{b,P}$ can be determined by using the backscattering to scattering ratio $b_{b,P}/b_P$. Morel (1988) recognised an almost constant ratio of $b_{b,P}/b_P \approx 0.02$ slightly depending on the wavelength and the concentration of chlorophyll-a. He derived the following empirical relation:

$$\frac{b_{b,P}}{b_P} = 0.0021 \cdot \frac{\lambda}{\lambda_0} + 0.021 \cdot \left(\frac{1}{2} - \frac{1}{4}\log C_{chl}\right) \tag{2.79}$$

Ahn et al. (1992) found lower values for phytoplankton cultures grown in the laboratory. Their backscattering to scattering ratio ranges from 0.0004 to 0.0045 at $\lambda_0 = 550$ nm.

For case-2 water, other models were developed. In coastal regions, Sathyendranath et al.

(1989) proposed that the scattering coefficient is indirectly proportional to the absorption of phytoplankton: $b_P(\lambda) \propto 1/a_P(\lambda)$. The proportionality factor depends on the concentration of chlorophyll-a in the same manner as the scattering coefficient of equation (2.78). For the backscattering to scattering ratio Sathyendranath et al. (1989) found a constant value of $b_{b,P}/b_P = 0.005$ in their measurements. Dekker (1993) investigated the contribution of each water constituent in inland water. He observed that the composition of scattering particles is more variable than in the ocean and depends on the trophic state of the water and therefore on the distribution of organic and inorganic particulate matter. The scattering and backscattering coefficient of phytoplankton can be determined by

$$\begin{aligned} b_P(\lambda) &= b_P^*(\lambda) \cdot C_P && (2.80) \\ b_{b,P}(\lambda) &= b_{b,P}^*(\lambda) \cdot C_P = \frac{b_{b,P}^*}{b_P^*} \cdot b_P^*(\lambda) \cdot C_P && (2.81) \end{aligned}$$

with the specific scattering and backscattering coefficient of phytoplankton, b_P^* and $b_{b,P}^*$, respectively. For lakes Dekker (1993) reported that the specific scattering coefficient of phytoplankton ranges from 0.12 to 0.18 $\mathrm{m^2mg^{-1}}$ at a wavelength of 550 nm. Heege (2000) investigated scattering measurements in Lake Constance and found that the pigment specific scattering does not contribute to the total scattering. The scattering of phytoplankton is contained in the scattering coefficient of the total suspended matter, which consists of both inorganic particles and organic particulate matter.

The specific scattering and backscattering coefficients can be obtained by integrating the corresponding scattering phase function. Extensive and commonly used measurements were done by Petzold (1977). Figure 2.15 shows three different phase functions of particles measured in the open ocean, in coastal waters, and in the harbour of San Diego, California at a wavelength of 514 nm. The backscattering to scattering ratio of particles varies from 0.018 to 0.020 for turbid water. Hence most of the incoming light is scattered forward and half of the scattering coefficient is already reached at a scattering angle of 4.7°.

2.3.3 Elastic scattering by suspended matter

In case-2 water the scattering is higher compared to case-1 water due to the additional presence of particles not related to phytoplankton. These particles are due to the amount of suspended inorganic sediment of different size. Scattering of light is caused due to the difference of refractive indices between two materials and due to the ratio of particle size and wavelength. As mentioned by Mobley (1994), Kopelevich has developed a model of particle scattering. He separated the influence of small mineral particles of a size less than 1 μm and an index of refraction of 1.15 relative to water and of large particles larger than 1 μm and an index of refraction of 1.03. The total scattering phase function of particles β_X can then be approximated by

$$\beta_X(\lambda, \psi) = \beta_{X,s}^*(\psi) \cdot \left(\frac{\lambda_0}{\lambda}\right)^{n_s} \cdot C_{X,s} + \beta_{X,l}^*(\psi) \cdot \left(\frac{\lambda_0}{\lambda}\right)^{n_l} \cdot C_{X,l} \qquad (2.82)$$

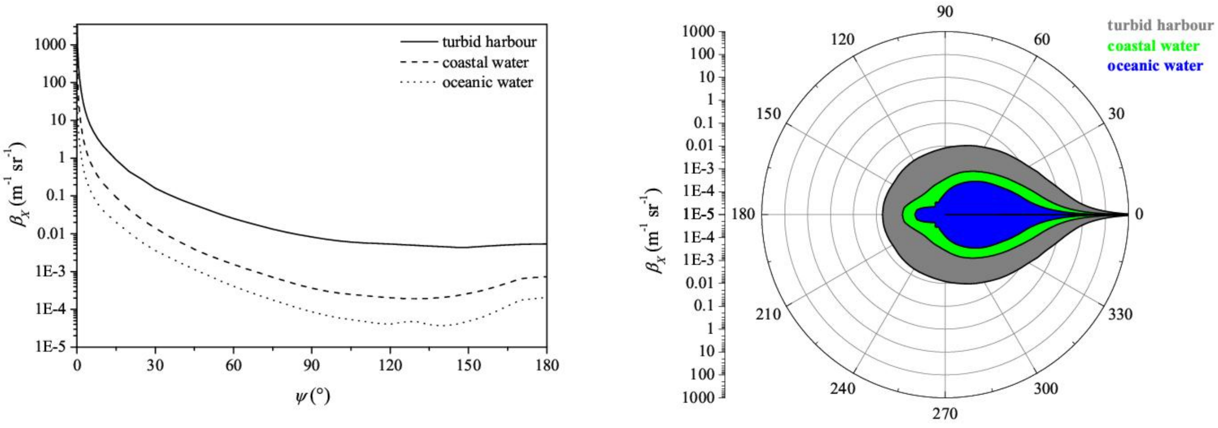

Figure 2.15: Normalised scattering phase function of particles (left) and the correspondent polar diagram (right) after measurements of Petzold (1977) in oceanic water, coastal water, and in the turbid water of San Diego harbour, California, at a wavelength of 514 nm.

with the volume specific phase functions of small and large particles, $\beta^*_{X,s}$ and $\beta^*_{X,l}$ respectively. The exponents n_s and n_l are called the Ångström exponents. Kopelevich found $n_s = 1.7$ and $n_l = 0.3$. The concentrations of small and large particles are given by $C_{X,s}$ and $C_{X,l}$. The measurements of Kopelevich show results for the total scattering phase functions similar to Petzold (1977) in the harbour of San Diego, California. Only at small scattering angles from 0 to 3° the measurements of Petzold (1977) show higher values. The scattering coefficient of suspended matter b_X is obtained by integrating the phase function over all angles. This yields

$$b_X(\lambda) = b^*_{X,s} \cdot \left(\frac{\lambda_0}{\lambda}\right)^{n_s} \cdot C_{X,s} + b^*_{X,l} \cdot \left(\frac{\lambda_0}{\lambda}\right)^{n_l} \cdot C_{X,l} \tag{2.83}$$

with the specific scattering coefficients of small and large particles, $b^*_{X,s}$ and $b^*_{X,l}$, respectively. By integrating over scattering angles from 90° to 180°, the total backscattering coefficient of suspended particles $b_{b,X}$ is given by

$$b_{b,X}(\lambda) = b^*_{b,X,s} \cdot \left(\frac{\lambda_0}{\lambda}\right)^{n_s} \cdot C_{X,s} + b^*_{b,X,l} \cdot \left(\frac{\lambda_0}{\lambda}\right)^{n_l} \cdot C_{X,l} \tag{2.84}$$

If there is no distinction between small and large particles, the equations (2.83) and (2.84) can be simplified to the scattering and backscattering coefficient of total suspended matter

$$b_X(\lambda) = b^*_X \cdot \left(\frac{\lambda_0}{\lambda}\right)^{n} \cdot C_X \tag{2.85}$$

$$b_{b,X}(\lambda) = b^*_{b,X} \cdot \left(\frac{\lambda_0}{\lambda}\right)^{n} \cdot C_X \tag{2.86}$$

with the concentration of the total suspended matter C_X, the specific scattering and backscattering coefficients, b^*_X and $b^*_{b,X}$ respectively, and the Ångström exponent n.

The dominance of large particles in coastal and inland waters yields a negligible wavelength dependence, thus $n = 0$ (Dekker et al., 2001; Heege, 2000). Dekker (1993) found a specific scattering coefficient of 0.23 to 0.79 $\mathrm{m^2/g}$ for different trophic states in lakes. The backscattering to scattering ratio varies from 0.011 to 0.020. For river water with scattering coefficients of 10 to 20 $\mathrm{m^{-1}}$ the ratio can be two to three times higher. Ibelings et al. (2001) reported a specific scattering coefficient of 0.25 to 0.31 $\mathrm{m^2/g}$ in Lake IJssel in the Netherlands with a backscattering to scattering ratio of 0.035 to 0.045. Heege (2000) investigated the scattering of suspended matter in Lake Constance. He found no significant dependence on wavelength, which means $n = 0$. His measurements result in specific scattering and backscattering coefficients of total suspended matter for Lake Constance $b^*_X = 0.45\ \mathrm{m^2/g}$ and $b^*_{b,X} = 0.0086\ \mathrm{m^2/g}$. Thus, the backscattering to scattering ratio is 0.019 and shows the same value as measured by Petzold in San Diego Harbor, California.

2.3.4 Elastic scattering by gelbstoff

Gelbstoff consists of dissolved organic matter as previously mentioned in chapter 2.2 and as described for example by Kirk (1983). The size of all gelbstoff components is smaller than the wavelengths of visible light. Hence, the scattering probability of gelbstoff is described by Rayleigh scattering proportional to λ^{-4}. The scattering and backscattering coefficient of gelbstoff is much smaller compared to the absorption. To date, the scattering probability of gelbstoff is neglected in optical oceanography (Pozdnyakov and Grassl, 2003) and for the investigations at Lake Constance (Gege, 1994; Heege, 2000). Thus, the elastic scattering and backscattering coefficient of gelbstoff is set to $b_Y = 0$ and $b_{b,Y} = 0$.

2.4 Inelastic processes and bioluminescence

Inelastic scattering is a process, where an incident photon excites a molecule to a different quantum state of rotation or vibration. Most molecules exist before in the electronic ground state, thus energy is required to change its state, which is taken from the incoming photon. Consequently, the scattered photon has a longer wavelength (lower frequency) than the incoming photon. The wavelength difference is inversely proportional to the energy, the frequency difference directly. It is also possible that an already excited molecule returns to the ground state and emits a photon of shorter wavelength (higher frequency). Thus, energy is gained. But the probability for this process is very low and can be neglected (Mobley, 1994).
There are two types of inelastic processes: Raman scattering and fluorescence. These are illustrated in figure 2.16.

- Raman scattering: the incoming photon with energy $h\nu$ is absorbed by a molecule, which is in the lowest energy level of the ground state. The molecule reaches an excited energy state and re-emits a photon of the energy $h\nu'$. The molecule returns into a higher vibrational energy level of the ground state than the initial one. The transition into the base level is radiationless and the energy difference $h(\nu - \nu')$ increases rotation and/or vibration.

- Fluorescence: the energy $h\nu$ of an incident photon is absorbed by a molecule. The molecule is excited from the ground state to a higher energy level of the excited quantum state. After a short time ($\sim 10^{-9}$ s) a photon of a wavelength longer than the exciting one with the energy $h\nu'$ is emitted. The reason for the energy difference $h(\nu - \nu')$ here is that the molecules attains first the lowest energy level of the excited state by radiationless transition before a photon is emitted and the molecule returns into the base level.

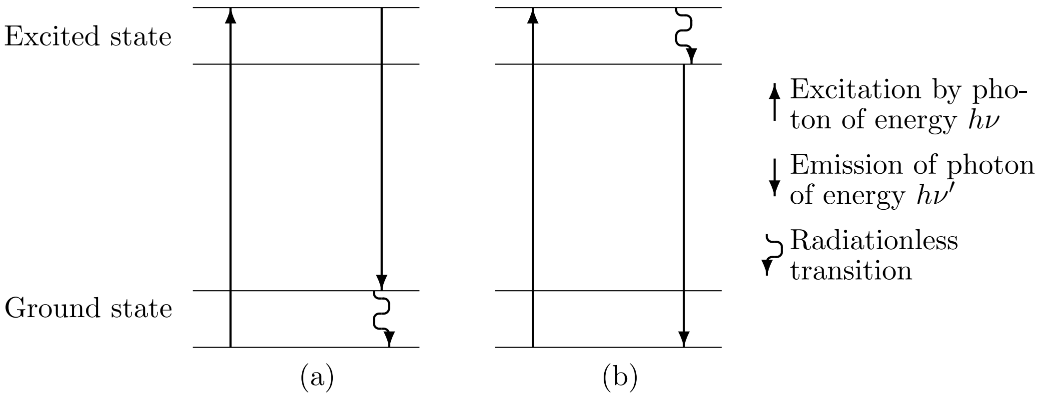

Figure 2.16: Schematic graphs of the electronic states during Raman scattering (a) and fluorescence (b).

Raman scattering in natural water is mainly caused by the water molecules. Fluorescence is the inelastic process occurring in pigments contained in the water constituents of phytoplankton - predominantly chlorophyll - and gelbstoff. The processes are taken into account in the radiative transfer equation by means of the inelastic scattering phase function $\beta^I = \beta^R + \beta^F$ with the Raman scattering phase function β^R and the fluorescence phase function β^F. Fluorescence occurs due to pigments and can be separated into phytoplankton and gelbstoff fluorescence. Thus, β^F is the sum of the fluorescence phase functions of chlorophyll $\beta^{F,chl}$ and gelbstoff $\beta^{F,Y}$:

$$\beta^F = \beta^{F,chl} + \beta^{F,Y} \tag{2.87}$$

The influence of the total inelastic scattering is shown in figure 2.17. The schematic graph shows the response of water, after Reuter et al. (1986), that is excited at the wavelength λ' and the resulting spectrum produced by the Raman scattering and the fluorescence by chlorophyll and gelbstoff. The related impact of Raman scattering and fluorescence of chlorophyll and gelbstoff is indicated in figure 2.17.

Bioluminescence is a process, where light is emitted by organisms in the water. The light is produced by chemical reactions. The quantity of light emitted by this process is very small compared to the sun light, but is the only natural source of light in deep water.

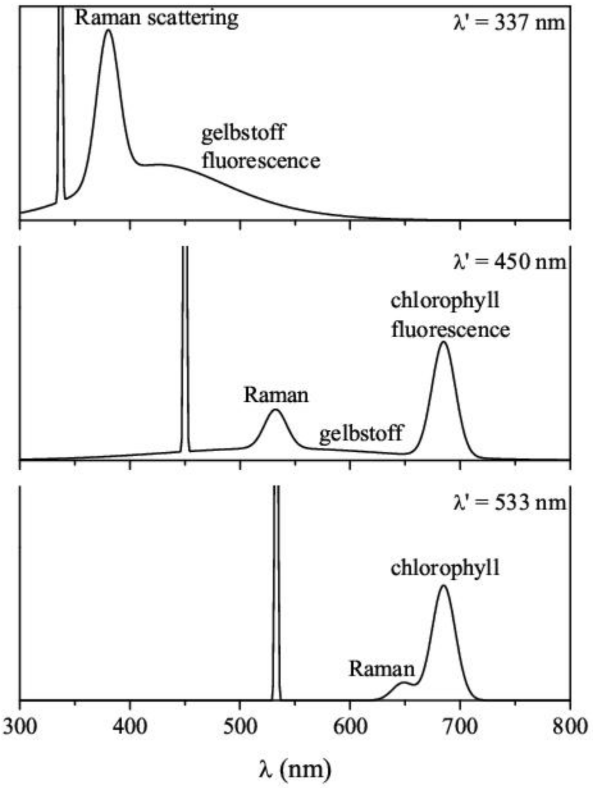

Figure 2.17: Schematic graph of three inelastic processes by natural water when excited at three different wavelengths λ' (Raman scattering, gelbstoff and chlorophyll fluorescence), after Reuter et al. (1986).

2.4.1 Raman scattering of water

The Raman scattering is explained for example by Haltrin and Kattawar (1993) or Mobley (1994). According to chapter 2.1, the Raman scattering phase function β^R is given by the Raman scattering coefficient b^R and the normalised Raman scattering phase function $\tilde{\beta}^R$. Thereby, b^R includes the wavelength dependence and $\tilde{\beta}^R$ the angular dependence:

$$\beta^R(\lambda' \to \lambda, \psi) = b^R(\lambda' \to \lambda) \cdot \tilde{\beta}^R(\psi) \tag{2.88}$$

Due to the fact that photons are absorbed at the incident wavelength λ' and emitted at another wavelength λ, the Raman scattering coefficient can be expressed by the Raman absorption coefficient a^R and the Raman wavelength redistribution function f^R. This results for the Raman scattering phase function in

$$\beta^R(\lambda' \to \lambda, \psi) = a^R(\lambda') \cdot f^R(\lambda' \to \lambda) \cdot \tilde{\beta}^R(\psi) \tag{2.89}$$

As written for example in Mobley (1994) and Pozdnyakov and Grassl (2003), experimental investigations on a^R were made by many authors. The value of a^R is about $2.6 \cdot 10^{-4}$ m^{-1} at

$\lambda' = 488$ nm. The wavelength dependence of a^R can be expressed by

$$a^R(\lambda') = 2.6 \cdot 10^{-4}\ \mathrm{m}^{-1} \cdot \left(\frac{488\ \mathrm{nm}}{\lambda'}\right)^n \tag{2.90}$$

The dependence on the incident wavelength is given by the exponent n. Sugihara et al. (1984) found $n = 5$ for their measurements. Other authors like Haltrin and Kattawar (1993) for example use $n = 4$. This is due to the fact that they use the dependence on the emitted wavelength λ in their studies.

The spectrum of Raman-scattered photons at monochromatic excitation can be approximated by a Gaussian distribution centred at the emitted wavelength and with a full width at half maximum of about 5 to 10 nm. The Raman wavenumber shift given by the energy difference of the quantum states is the base to derive the wavelength shift of f^R. Following investigations of Sugihara et al. (1984), the emitted wavelength is given by

$$\lambda(\lambda') = \frac{\lambda'}{1 - \Delta k \cdot \lambda'} \tag{2.91}$$

with $\Delta k = 3.357 \cdot 10^{-4}\ \mathrm{nm}^{-1}$. Thus, for example, an incident photon of the wavelength $\lambda' = 500$ nm is emitted at about 600 nm. Details of the Raman redistribution function are mentioned in Mobley (1994) and an example of the Raman wavelength shift is shown in figure 2.17.

After Porto (1966) the normalised Raman scattering phase function can be written as

$$\tilde{\beta}^R(\psi) = \frac{3}{16\pi} \cdot \frac{1+3\rho^R}{1+2\rho^R} \cdot \left[1 + \left(\frac{1-\rho^R}{1+3\rho^R}\right)\cos^2\psi\right] \tag{2.92}$$

with depolarisation ratio for Raman scattering $\rho^R = 0.17$. $\tilde{\beta}^R$ is symmetric and is very similar to the elastic scattering phase function of pure water.

The Raman absorption coefficient a^R at 488 nm - and therefore the Raman scattering coefficient - is about one tenth of the scattering coefficient of pure water.

As recently described by Pozdnyakov and Grassl (2003), the influence of Raman scattering on the water leaving radiance decreases with increasing concentrations of the water constituents. The Raman contribution for phytoplankton concentrations below 1 μg/l is larger than 8% and is about 4% for higher concentrations. For concentrations of suspended sediment higher than 1 mg/l the relative contribution of Raman scattering decreases rapidly to 1% and lower. For wavelengths above 500 nm the Raman scattering can be neglected for case-2 water but plays an important role from 400 to 500 nm for the retrieval of concentrations of water constituents. The contribution of Raman scattering to the underwater light field increases with increasing depth as for example reported by Mobley (1994) and Berwald et al. (1998).

2.4.2 Fluorescence by chlorophyll

Figure 2.17 shows a strong emission due to the fluorescence of chlorophyll at 685 nm. This wavelength is fixed, even if the exciting wavelength λ' is changed. But the amplitude of the emission band depends on the excitation wavelength, because the light is specifically absorbed by the phytoplankton. Wavelengths with strong absorption contribute more to the fluorescence peak at 685 nm and wavelengths with weak absorption contribute less. The fluorescence can be taken into account in the radiative transfer equation (2.5) like the Raman scattering using the fluorescence phase function of chlorophyll $\beta^{F,chl}$ (Mobley, 1994), which is given by

$$\beta^{F,chl}(\lambda' \to \lambda, \psi) = a^{F,chl}(\lambda') \cdot f^{F,chl}(\lambda' \to \lambda) \cdot \tilde{\beta}^{F,chl}(\psi) \tag{2.93}$$

with the absorption of the fluorescing substance chlorophyll $a^{F,chl}$, which can be parameterised like the absorption of phytoplankton in equation (2.65).

$$a^{F,chl}(\lambda') = a^{*,F,chl}(\lambda') \cdot C_{chl} \tag{2.94}$$

with the specific absorption of chlorophyll $a^{*,F,chl}$ and the concentration of chlorophyll C_{chl}. The specific absorption of chlorophyll looks similar to the specific absorption of phytoplankton shown in figure 2.8. The second term in equation (2.93), $f^{F,chl}$, is the wavelength redistribution function of fluorescence by chlorophyll and is given by

$$f^{F,chl}(\lambda' \to \lambda) = \eta^{F,chl}(\lambda' \to \lambda) \cdot \frac{\lambda'}{\lambda} \tag{2.95}$$

$\eta^{F,chl}$ is the spectral quantum efficiency function of chlorophyll fluorescence. The integral of $\eta^{F,chl}$ over all wavelengths yields the quantum efficiency or quantum yield of the cholorophyll fluorescence $\Phi^{F,chl}$. For the underwater light field only wavelengths from 370 to 690 nm are important for the fluorescence. This is due to the the specific absorption of chlorophyll, which decreases rapidly for wavelengths longer than 690 nm, and the absorption of water, which increases rapidly for wavelengths longer than 690 nm. The wavelength of the emitted photon is independent on the incident wavelength for cholorophyll fluorescence. The wavelength redistribution function $f^{F,chl}$ can be written as

$$f^{F,chl}(\lambda' \to \lambda) = \begin{cases} \Phi^{F,chl} \cdot h^{chl}(\lambda, \lambda_0, \sigma) \cdot \frac{\lambda'}{\lambda} & \text{, if } 370 \le \lambda' \le 690 \text{ nm} \\ 0 & \text{, otherwise.} \end{cases} \tag{2.96}$$

with a Gaussian function $h^{chl}(\lambda, \lambda_0, \sigma)$, which approximates the fluorescence peak of chlorophyll at $\lambda_0 = 685$ nm with a full width at half maximum of 25 nm yielding $\sigma = 10.6$ nm. The quantum efficiency $\Phi^{F,chl}$ varies between 0.5 and 10% and has typical values of 2 or 3% in natural waters. It depends on the phytoplankton species and their physiological state influenced by the incident radiation intensity as well as the availability of nutrients and pollutants (Mobley, 1994; Pozdnyakov and Grassl, 2003). The emittance of the fluorescence is isotropic and therefore the normalised fluorescence phase function is

$$\tilde{\beta}^{F,chl}(\psi) = \frac{1}{4\pi}\text{sr}^{-1} \tag{2.97}$$

The influence of the fluorescence of chlorophyll on the reflectance spectrum around 685 nm was investigated recently by Pozdnyakov and Grassl (2003). They made simulations with different concentrations of the water constituents. The ratio between the value of the irradiance reflectance just below the water surface estimated with fluorescence and without increases with increasing chlorophyll concentration. Culver and Perry (1997) reported that chlorophyll fluorescence accounts for 10 to 40% of the total upwelling irradiance at the surface in natural waters.

2.4.3 Fluorescence by gelbstoff

In contrast to chlorophyll the position and shape of the fluorescence peak varies for gelbstoff for varying incident wavelength. This is due to the composition of gelbstoff, which contains many kinds of humic and vulvic acids. Each substance produces another fluorescence band. In principle, the fluorescence by gelbstoff can be expressed like the fluorescence of chlorophyll by the fluorescence phase function of gelbstoff $\beta^{F,Y}$ given by

$$\beta^{F,Y}(\lambda' \to \lambda, \psi) = a_Y(\lambda') \cdot f^{F,Y}(\lambda' \to \lambda) \cdot \tilde{\beta}^{F,Y}(\psi) \tag{2.98}$$

with the absorption of the fluorescing substance gelbstoff a_Y given by equation (2.69). The wavelength redistribution function of fluorescence by gelbstoff $f^{F,Y}$ is given by

$$f^{F,Y}(\lambda' \to \lambda) = \eta^{F,Y}(\lambda' \to \lambda) \cdot \frac{\lambda'}{\lambda} \tag{2.99}$$

with the spectral quantum efficiency function of gelbstoff fluorescence $\eta^{F,Y}$, which contains the different wavelength shifts of the fluorescence by gelbstoff due to the different substances of gelbstoff. The spectral quantum efficiency function of gelbstoff was investigated by Hawes et al. (1992). They found a function to describe their measurements between 310 and 490 nm, which is parameterised by

$$\eta^{F,Y}(\lambda' \to \lambda) = A_0(\lambda') \cdot \exp\left\{ - \left[\frac{\lambda'/\lambda - A_1 - B_1\lambda'}{0.6(A_2 + B_2\lambda')} \right]^2 \right\} \tag{2.100}$$

with $A_1 = 0.470$, $A_2 = 0.407$, $B_1 = 8.077 \cdot 10^{-4}$ nm^{-1}, and $B_2 = -4.57 \cdot 10^{-4}$ nm^{-1}. The coefficients A_0 are listed in table 2.4 together with the resulting quantum efficiency of fluorescence by gelbstoff $\Phi^{F,Y}(\lambda') = \int_\lambda \eta^{F,Y}(\lambda' \to \lambda) \mathrm{d}\lambda$. The quantum efficiency ranges from 0.9 to 1.9% depending on the incident wavelength. Pozdnyakov and Grassl (2003) assessed several publications and found similar values regarding the natural variability of different water types. $\Phi^{F,Y}$ can vary from 0.5 to 1.0% for wavelengths around 300 nm, from 0.7 to 2.8% around 390 nm, and from 0.5 to 1.9% around 470 nm.

Like the fluorescence of chlorophyll, also the fluorescence of gelbstoff is emitted isotropically. Thus, the normalised fluorescence phase function of gelbstoff is

$$\tilde{\beta}^{F,Y}(\psi) = \frac{1}{4\pi} \mathrm{sr}^{-1} \tag{2.101}$$

The fluorescence of gelbstoff has the greatest impact in the blue and green spectral region. The influence on the spectral irradiance or remote sensing reflectance varies also with the concentration of phytoplankton and suspended sediment. As investigated by Pozdnyakov and Grassl

λ' (nm)	310	330	350	370	390	410	430	450	470	490
A_0 (10^{-5} nm^{-1})	5.18	6.34	8.00	9.89	9.39	10.48	12.59	13.48	13.61	9.27
$\Phi^{F,Y}$ (%)	0.82	1.04	1.33	1.63	1.50	1.62	1.87	1.92	1.86	1.20

Table 2.4: Coefficients A_0 for the determination of the spectral quantum efficiency function $\eta^{F,Y}$ of equation (2.100) after Hawes et al. (1992) and the resulting quantum efficiency $\Phi^{F,Y}$.

(2003), neglection of fluorescence by gelbstoff causes an error of about 10 to 50% with increasing absorption by gelbstoff from 0.05 to 0.5 m^{-1} at 440 nm for a concentration of phytoplankton and suspended matter of $C_P = 2.0$ μg/l and $C_X = 0.5$ mg/l, respectively. For water with very high amount of gelbstoff, so called “black water”, the error grows up to 70%.

2.4.4 Bioluminescence

Bioluminescence is the only internal source in equation (2.5) and is due to light-emitting organisms. These organisms are bacteria, phytoplankton, and fish in the ocean that produce light by chemical reactions. There were no data available about bioluminescence in freshwater environments for this study. The impact on radiance and irradiance can be neglected at the surface level because the quantity is very small compared to incident sun light. But for deep water near the sea floor bioluminescence is an important light source.
The spectral radiance is emitted isotropically. Thus, the internal source term S_0 for the emitted radiance L_S is given by

$$S_0(\lambda) = 4\pi \cdot L_S(\lambda) \tag{2.102}$$

The dependence on wavelength can be expressed by the sum of several Gaussian peaks at distinct wavelengths, which depend on the species. Lynch (1978) investigated the bioluminescence of 58 marine species and Mobley (1994) made calculations for the intensity of the emitted light. He mentioned that the light produced in a volume of one cubic meter is in the order of 10^{-5} W m^{-2}, which surmounts the irradiance in a clear and starry night (10^{-6} W m^{-2}) but is much less than in a night with bright moonlight (10^{-3} W m^{-2}). For comparison, the typical total irradiance during a sunny summer day can reach 1000 W m^{-2}, depending on the sun zenith angle.

2.5 Bottom effects

In optically shallow water the bottom influences the reflected light in various ways. The magnitude and wavelength dependence is given by the irradiance reflectance of the bottom R_B. As introduced in chapter 2.1, the angular distribution of the reflected radiance is described by the function B - the normalised bidirectional reflectance distribution function (BRDF). Both together give the (unnormalised) BRDF $\tilde{B}$, which is generally defined by the incident and reflected radiances, L_i and L_r, in their solid angle elements, $\mathrm{d}\Omega_i$ and $\mathrm{d}\Omega_r$ respectively.

$$\tilde{B}(\lambda, \theta_i, \phi_i, \theta_r, \phi_r) = R_B(\lambda) \cdot B(\theta_i, \phi_i, \theta_r, \phi_r) \equiv \frac{\mathrm{d}L_r(\lambda, \theta_r, \phi_r)}{L_i(\lambda, \theta_i, \phi_i) \cos\theta_i \mathrm{d}\Omega_i} \tag{2.103}$$

with the incident and reflected zenith and azimuth angles, θ_i, θ_r, ϕ_i, and ϕ_r respectively. The geometry of the incident and reflected radiances for a bidirectional reflecting surface is shown in figure 2.18.

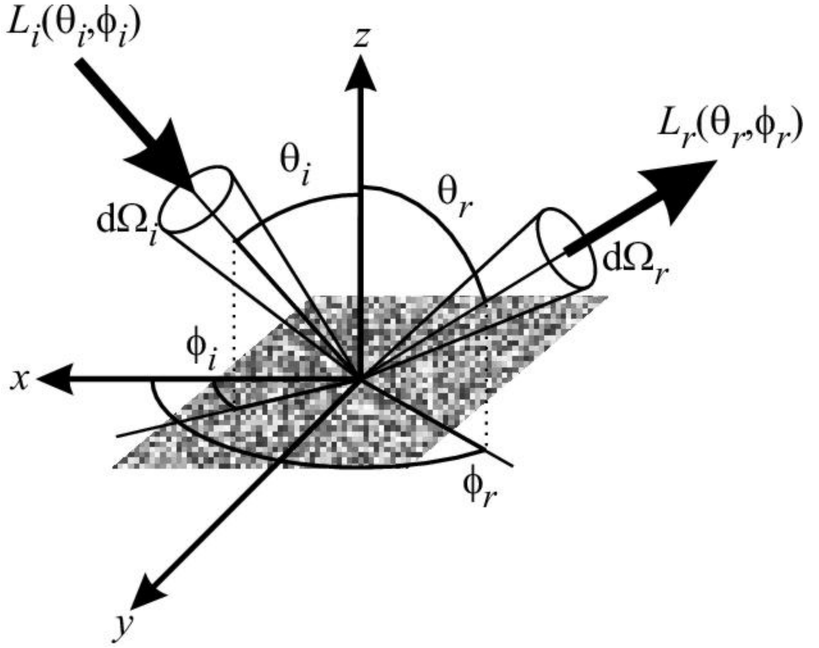

Figure 2.18: Geometry of incident and reflected radiances for the bidirectional reflection of a surface.

The dependence on wavelength is omitted in the following for simplicity. When talking about underwater light field, the incident direction is equal to the downwelling (index d) and the reflected equal to the upwelling direction (index u). Thus, the upwelling radiance directly at the bottom at depth $z = z_B$ is given by

$$L_u(\theta_u, \phi_u) = \int_{\Omega_d} L_d(\theta_d, \phi_d) \tilde{B}(\theta_d, \phi_d, \theta_u, \phi_u) \cos\theta_d \mathrm{d}\Omega_d \tag{2.104}$$

The bottom reflectance R_B is defined as the ratio of the upwelling and downwelling irradiance at the depth $z = z_B$. Using the definitions of the down- and upwelling irradiances of the equations (2.6) and (2.7) yields

$$R_B = \frac{E_u(z_B)}{E_d(z_B)} = \frac{-\int_{\Omega_u} L_u(\theta_u, \phi_u) \cos\theta_u \mathrm{d}\Omega_u}{\int_{\Omega_d} L_d(\theta_d, \phi_d) \cos\theta_d \mathrm{d}\Omega_d} \tag{2.105}$$

Inserting equation (2.104) of the upwelling radiance at the bottom results in

$$R_B = \frac{-\int_{\Omega_u} \left[\int_{\Omega_d} L_d(\theta_d, \phi_d) \tilde{B}(\theta_d, \phi_d, \theta_u, \phi_u) \cos\theta_d \mathrm{d}\Omega_d\right] \cos\theta_u \mathrm{d}\Omega_u}{\int_{\Omega_d} L_d(\theta_d, \phi_d) \cos\theta_d \mathrm{d}\Omega_d} \tag{2.106}$$

Equation (2.105) is the general expression of the bottom reflection, which depends on the surface type itself and on the incident radiance. For the case of a Lambertian reflector, reflecting equally into all directions, $\tilde{B}$ is constant. Thus, the integrals of equation (2.106) can be solved and the result for the Lambertian bottom reflectance is

$$R_B = \pi \cdot \langle \tilde{B} \rangle \tag{2.107}$$

In nature there exists no Lambertian reflector. Thus, it is necessary to find out, if it is possible to calculate the underwater light field in shallow water with negligible errors by using Lambertian bottom reflectance instead of BRDF. It is worth thinking about this because it is very difficult to conduct in-situ BRDF measurements, which was done for an oceanic environment the first time only very recently by Zhang et al. (2003). Many researchers assumed the bottom to be a Lambertian reflector, for example Maritorena et al. (1994), Lee et al. (1998), and Ohde and Siegel (2001). Recent investigastions of Mobley et al. (2003) show that the relative errors are below 10%, if a Lambertian irradiance reflectance is used instead of the BRDF of the same bottom type. This error is less than the error by using a BRDF differing by 10% in comparison to the real BRDF.

They studied different surfaces like sand and benthic vegetation types. Due to the dependence of the bottom reflectance on the incident radiance, the bottom reflectance is also depending on the solar zenith angle. The impact of the sun angle increases with increasing angle and is greatest in very shallow water, where the direct sun light dominates. But owing to Snell's law of refraction at the water surface for upwelling radiance (see chapter 2.6), the effect is negligible, because the underwater sun angle never becomes larger than 48°. The study of Mobley et al. (2003) shows for sandy sediment that the surface reflectance becomes non-Lambertian at an incident angle $\theta_i > 35°$. At higher angles rough surfaces show the so called hot spot or retroreflection at $\theta_r = \theta_i$ and $\phi_r = \phi_i$. Smooth surfaces show specular reflectance like a mirror at $\theta_r = \theta_i$ and $\phi_r = \phi_i + 180°$. Benthic underwater vegetation shows no retroreflection or specular reflection.

Another influence of the bottom on the reflected radiance distribution is the slope of the terrain. Mobley and Sundman (2003) studied the difference of a level bottom instead of a sloping one in a radiative transfer model and found that the relative error is around 10%, if the slope is neglected and the slope angle θ_B is below 20° for an azimuth sun angle ϕ_s of zero (downslope) or 90° (perpendicular to the slope). The solar zenith angle was $\theta_s = 45°$. The error is largest, if the sun is shining upslope ($\phi_s = 180°$). For this case the error is 10% at a slope of 10° and up to 30% at 20°. Mobley and Sundman (2003) developed a simple analytical model to correct the upwelling radiance just below the water surface, which reduces the error below 10% for a slope not more than 20° for overall sun conditions. The radiance upwelling from sloping bottom L_u^{slope} can be estimated by

$$L_u^{slope} = L_u^{level} \cdot \frac{\sin\theta_B \sin\theta_s \cos\phi_s + cos\theta_B \cos\theta_s}{\cos\theta_i^{level}} \tag{2.108}$$

with the upwelling radiance of a level bottom L_u^{level} and the incident angle of the radiance on a level bottom θ_i^{level}.

Measurements of the irradiance reflectance of several bottom types after Maritorena et al. (1994) are shown in figure 2.19. They published the laboratory measurements of bright coral sand and cultures of green, brown, and red algae.

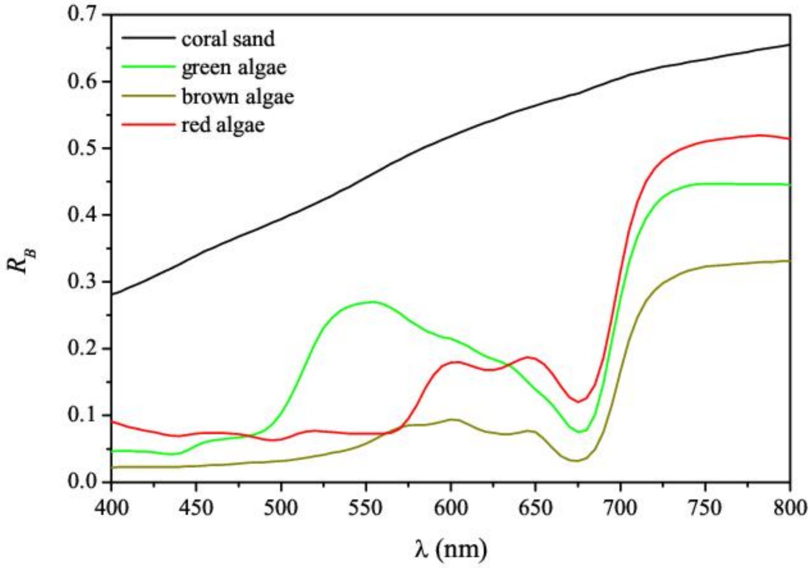

Figure 2.19: Reflectances of several surface substrates: coral sand, green, brown, and red algae measured in the laboratory by Maritorena et al. (1994).

Measurements of typical bottom types at Lake Constance - sediment and submerged vegetation - were conducted during campaigns from 1998 through 2002 and are shown in figures 2.20 and 2.21. The bottom albedo was measured from 1999 through 2001 with the Hydrological Spectral Radiometer HYDRA developed at DLR (Bochter and Wallhäußer, 1997; Bochter, 2000) and from 2001 through 2002 with the hyperspectral radiance and irradiance sensors RAMSES[1]. Both instruments are explained in appendix A. The data were collected from ship placing the sensors above the bottom by means of a sonar. The sensors were between 10 to 20 cm above the sea floor or the benthic vegetation. The bottom reflectances are set constant from about 710 nm onwards, because the absorption of pure water increases rapidly and influences the measurements even if the instrument is placed only a few centimeters above the bottom. Due to the high water absorption in this spectral region, the error of the upwelling radiance is also small assuming a constant bottom albedo.

The sediment is typically a bright gray coloured mud composed of organic and inorganic matter. Investigations on the structure of sediments of Lake Constance were performed by Zahner et al. (1981), Illert et al. (1987), and Wagner et al. (1998). They found an average particle sizes of around 10 μm in the first centimeters. Towards the shore the number of greater particles of one or more millimeters increases up to 15% due to hydrodynamic effects. Thus, the average

---

[1] TriOS Optical Sensors, Werftweg 15, 26135 Oldenburg, Germany, `http://www.trios.de`

particle size increases up to 200 μm (Schmieder, 1998). The water content was between 60 to 80%. The organic matter contains pigment bearing particles composed mainly of carotinoids and chlorophyll, and their degradation products. The amount of pigments varies between 60 and 160 μg/g dry weight. The inorganic matter consists of minerals like calcite (30-50%), dolomite (0-5%), and quartz (5-15%).

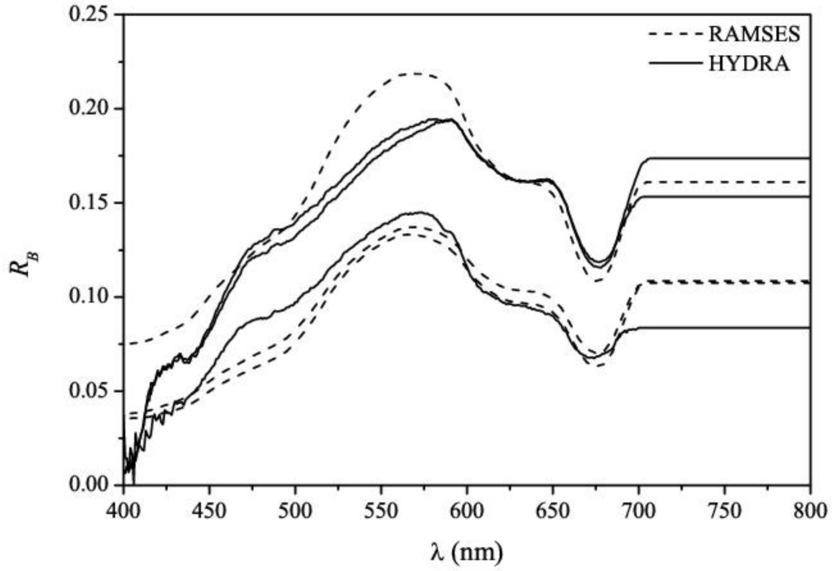

Figure 2.20: Mean bottom reflectances of sediment measured during campaigns in Lake Constance from 1999 through 2002 with the instruments HYDRA and RAMSES. The reflectance is assumed constant for wavelengths longer than 710 nm due to noisy measurements resulting from the high absorption of water.

Figure 2.20 shows the measured sediment reflectances of Lake Constance. The spectral slope of the reflectance shows similar features with a maximum at 550 to 600 nm. The maximum value varies between 13 and 23%. Such variability was also found by Decho et al. (2003) and Stephens et al. (2003). They mentioned the effect of biofilms on the surface, which can reduce the reflectance by 10 to 20%. Stephens et al. (2003) mentioned also that the combined absorption of different substrates, and therefore pigments, on the sediment changes the reflectance. The particle size has also an influence on the bottom albedo. These facts also explain the variability of the reflectance measurements of sediment in Lake Constance shown in figure 2.20.

In addition to bare sediment, three dominant submersed vegetation types were observed in Lake Constance. The irradiance reflectance of *Characeae*, *Potamogeton perfoliatus* L., and *Potamogeton pectinatus* L. were measured. The spectra are shown in figure 2.21. The varability of the albedo is due to the different leaf structures of the macrophytes. *Characeae* grow in clear water and cover often wide areas from a depth of 0.5 m to 15 m (Schmieder, 1998). The plant height of *Characeae* lies between 20 and 40 cm. *P. perfoliatus* and *P. pectinatus* build patches of 1 to 50 m^2 in Lake Constance. They are high growing macrophytes of 0.5 to 4 m height. *P. pectinatus* was observed in depths of 1 to 5 m and *P. perfoliatus* in depths of 1 to 7 m. The irradiance reflectance measurements were recorded during the mature stadium of the submersed vegetation. For *P. pectinatus* also data of the senescent stadium were collected. The difference between the mature and senescent plant and the resulting albedo of figure 2.21 is due to leaf epibionts and fouling processes in the late stadium (Drake et al., 2003; Fyfe, 2003). Drake et al. (2003) observed that the epiphytic biomass on the leafes of macrophytes increases with the age of the macrophytes. The absorption of the epiphytes shows similar features as the chlorophyll absorption. Thus, epiphytes and macrophytes are in a competing situation, whereby the epiphytes can reduce the incoming photons by 49%. This yields to a rapid degradation of the photosynthetic pigments in the leafes, which are bleaching and getting a bright colour. Thus, the irradiance reflectance increases like observed in Lake Constance. Additionally, deposits on the leafs of the macrophytes like calcite can enforce this effect.

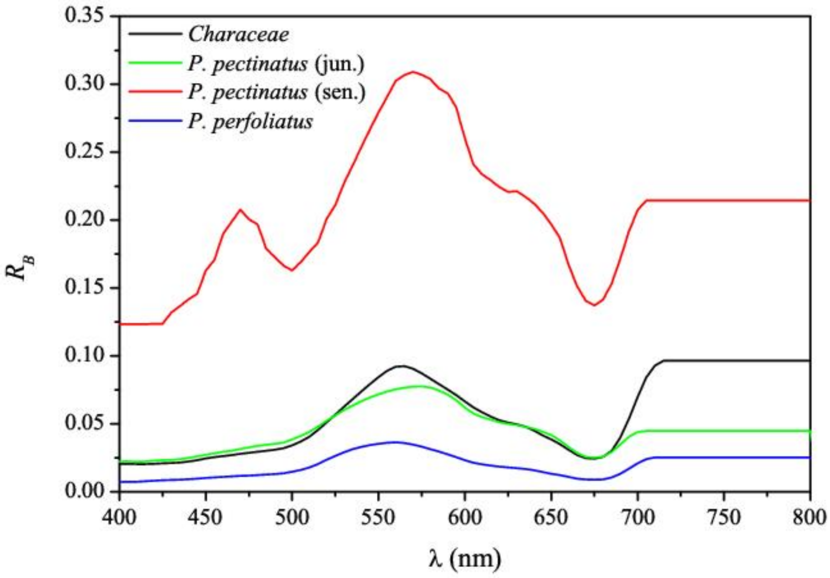

Figure 2.21: Mean values of irradiance reflectance of submerged vegetation measured at Lake Constance. The bottom reflectance is set constant for wavelengths $\lambda > 710$ nm due to noisy measurements resulting from the high absorption of water.

2.6 Effects at the water surface

Before the photons are passing the water body, they first go through the atmosphere and then reach the water surface. Atmospheric effects are not described in this study. The main effects at the water surface are reflection and transmission of light and the surface structure, which is mainly formed by the surface wind. These interaction principles are also relevant for the upward travelling photons.

Reflection and transmission through a plane water surface are exactly determined by Snell's law and Fresnel's formula. Snell's law describes the angular refraction of the incident beam. The light is passing the first medium with refractive index n_1 and then the second medium with refractive index n_2. If the incoming direction of the light is given by the angle θ_1, the beam is refracted to the angle θ_2. Snell's law is

$$n_1 \cdot \sin\theta_1 = n_2 \cdot \sin\theta_2 \tag{2.109}$$

For the case of light coming from the air under the incident angle θ_i and going into the water with the transmitted angle θ_t, this yields for a refractive index of the air of $n_a = 1$ and the water n_W

$$\theta_t = \arcsin\left(\frac{1}{n_W} \cdot \sin\theta_i\right) \tag{2.110}$$

For the equivalent "water leaving" case of light emerging from water to air

$$\theta_t = \arcsin(n_W \cdot \sin\theta_i) \tag{2.111}$$

The radiance is reflected at the water surface with the same angle as the incident angle, $\theta_r = \theta_i$. The reflectance of unpolarised radiance at the water surface, σ_L, is obtained by Fresnel's formula

$$\sigma_L = \frac{1}{2} \cdot \left[\left(\frac{\sin(\theta_i - \theta_t)}{\sin(\theta_i + \theta_t)}\right)^2 + \left(\frac{\tan(\theta_i - \theta_t)}{\tan(\theta_i + \theta_t)}\right)^2\right] \tag{2.112}$$

The dependence of the Fresnel reflection of equation (2.112) on the incident angle is shown in figure 2.22 for both cases, incident and water leaving radiance. For the incident radiance the transmitted angle is determined by equation (2.110) yielding the Fresnel reflectance σ_L^+. The Fresnel reflectance of water leaving radiance σ_L^- is obtained by the use of equation (2.111). The refractive index of water is $n_W = 1.33$. Figure 2.22 shows a nearly constant reflection of 0.02 for both cases till an incident angle of 30°. The water leaving radiance reflectance increases rapidly to $\sigma_L^- = 1$ at about 48°. Incident radiance under greater angles is totally reflected back into the water body. For air incident radiance, reflection increases slowly from 0.02 to 0.13 at 70° and 0.35 at 80° before total reflection is reached at 90°. The unreflected radiance is transmitted following Snells law and the transmittance is given by $(1 - \sigma_L)$.

Analog to the radiance reflection at the water surface, there is also an air incident irradiance reflection σ_E^+ and a water leaving irradiance reflection σ_E^- for the transfer of a irradiance through the water surface. The relations for the downwelling irradiance from the air into the water is

$$E_d = (1 - \sigma_E^+) \cdot E_d^+ + \sigma_E^- \cdot E_u \tag{2.113}$$

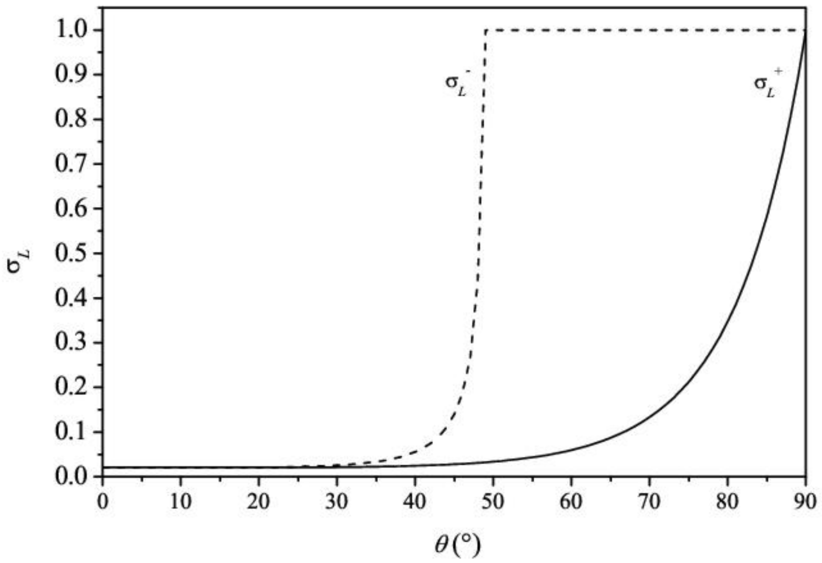

Figure 2.22: Fresnel reflection for incident radiance σ_L^+ (solid line) and water leaving radiance σ_L^- (dashed line) depending on the incident angle after equation (2.112); the transmitted angle is determined by equation (2.110) for incident radiance and by equation (2.111) for the water leaving one.

The first term is the transmitted downwelling irradiance through the water surface and the second term is the upwelling irradiance reflected at the water surface back into the water body. The superscript "+" indicates that the irradiance is related to above water. An analog relation yields the upwelling irradiance above the water surface

$$E_u^+ = (1 - \sigma_E^-) \cdot E_u + \sigma_E^+ \cdot E_d^+ \tag{2.114}$$

The upwelling radiance at the air just above the water surface, L_u^+, is the sum of the water leaving radiance in air, L_W^+, and the reflected downwelling radiance. The upwelling radiance in the water, L_u, is connected with L_W^+ by the n^2 law of radiances, which is estimated from Snell's law (Mobley, 1994). This results in

$$L_u^+ = \frac{1 - \sigma_L^-}{n_W^2} \cdot L_u + \sigma_L^+ \cdot L_d^+ \tag{2.115}$$

Thus, the irradiance and remote sensing reflectance in air just above the water surface, R^+ and R_{rs}^+ respectively, are given by the ratio of the upwelling irradiance and radiance to the downwelling irradiance in the air with the downwelling irradiance in air determined from equation (2.113). This yields

$$R^+ = \frac{E_u^+}{E_d^+} = \frac{(1-\sigma_E^-)(1-\sigma_E^+)}{1/R - \sigma_E^-} + \sigma_E^+ \tag{2.116}$$

$$R_{rs}^+ = \frac{L_u^+}{E_d^+} = \frac{(1-\sigma_L^-)(1-\sigma_E^+)}{n_W^2} \cdot \frac{R_{rs}}{1 - \sigma_E^- \cdot R} + \sigma_L^+ \cdot \frac{L_d^+}{E_d^+} \tag{2.117}$$

The first terms in equation (2.116) and (2.117) are the irradiance and remote sensing reflectance of the water above the surface, R_W^+ and $R_{rs,W}^+$, which are given by

$$R_W^+ = \frac{(1-\sigma_E^-)(1-\sigma_E^+)}{1/R-\sigma_E^-} \tag{2.118}$$

$$R_{rs,W}^+ = \frac{(1-\sigma_L^-)(1-\sigma_E^+)}{n_W^2} \cdot \frac{R_{rs}}{1-\sigma_E^- \cdot R} \tag{2.119}$$

The Fresnel reflection of the upward radiance, σ_L^-, depends on the incident and transmitted angle, which are the viewing angle of an observer or instrument below and above the water surface, θ_v and θ_v^+ respectively. Therefore,

$$\sigma_L^- = \frac{1}{2} \cdot \left[\left(\frac{\sin(\theta_v - \theta_v^+)}{\sin(\theta_v + \theta_v^+)} \right)^2 + \left(\frac{\tan(\theta_v - \theta_v^+)}{\tan(\theta_v + \theta_v^+)} \right)^2 \right] \tag{2.120}$$

whereby the viewing angles are connected by Snell's law

$$\theta_v^+ = \arcsin(n_W \cdot \sin\theta_v) \tag{2.121}$$

The reflection of the downward irradiance at the water surface, σ_E^+, depends on the solar zenith angle θ_s. For a collimated incident radiance distribution, σ_E^+ is given by

$$\sigma_E^+ = \frac{1}{2} \cdot \left[\left(\frac{\sin(\theta_s^+ - \theta_s)}{\sin(\theta_s^+ + \theta_s)} \right)^2 + \left(\frac{\tan(\theta_s^+ - \theta_s)}{\tan(\theta_s^+ + \theta_s)} \right)^2 \right] \tag{2.122}$$

where the sun zenith angle in air and in water, θ_s^+ and θ_s respectively, are connected by Snell's law,

$$\theta_s^+ = \arcsin(n_W \cdot \sin\theta_s) \tag{2.123}$$

Thus, values of σ_E^+ are in the same range as the Fresnel reflection of radiances. Typical values are 0.02 to 0.03 for clear sky and low sun zenith angles and 0.05 to 0.07 for clear sky and solar zenith angles above 45° and for overcast sky (Jerlov, 1976). σ_E^- is smaller than 0.7 (Mobley, 1999). After Jerome et al. (1990) the value is 0.561 for overcast sky, and for a clear sky with direct sun light $\sigma_E^- = 0.271 + 0.249/\cos\theta_s$.

Besides the dependence on the ratio of direct sun to diffuse sky light, the surface reflections depend on the surface waves. In contrast to the plain water surface, there exists no mathematically exact solution for a rough surface with waves. A rough surface is generated by the gravity and the surface wind, which is physically represented by the surface wind speed u. Thus, the surface wind has an impact on the reflection and transmission of the radiance and irradiance. A rough surface reflects and transmits the incoming light beam in more directions and makes the light field more diffuse.

To estimate the effect of the gravity and the surface wind, numerical techniques like the Monte Carlo method are suitable. The characteristics of the water surface is determined by capillary waves due to the surface wind and gravity waves. A possibility how to simulate the gravity-capillary surface is shown in Mobley (1994). He modeled the surface by hexagonal grids and triangular wave facets with a randomly generated elevation. This model is schematically shown in figure 2.23. The variance of slope and elevation of the wave facets follows the wave-slope wind-speed law of Cox and Munk (1954a; b), who made investigations on sun glitter photographs. The position of a surface point varies in horizontal and vertical direction. They found a linear relation between the wind speed u in units of m/s and the variances of the horizontal slopes in alongwind and crosswind direction, σ_a^2 and σ_c^2 respectively.

$$\sigma_a^2 = p_a \cdot u \tag{2.124}$$

$$\sigma_c^2 = p_c \cdot u \tag{2.125}$$

with coefficients $p_a = 3.16 \cdot 10^{-3}$ s/m and $p_c = 1.92 \cdot 10^{-3}$ s/m. If the triangle of a wave facet is defined by the relative width of the baseline α as shown in figure 2.23, the relative length of the triangle γ is

$$\gamma = \alpha \cdot \sqrt{\frac{3p_a}{4p_c}} \tag{2.126}$$

and the variance of the elevation σ_ζ^2 is

$$\sigma_\zeta^2 = \alpha^2 \cdot \frac{p_a}{6} \cdot u \tag{2.127}$$

The optically dominant effect is due to the capillary waves (≤5 mm) forced by the surface wind. Simulations of Mobley (1994) show that the effect of the wind speed for the reflection of the downwelling irradiance is negligible for sun zenith angles above the water surface below 50°. At $\theta_s^+ = 60°$ and a wind speed of 20 m/s, the reflectance is decreased about 10% in comparison to no wind. For a wind speed up to 5 m/s there is no impact for $\theta_s^+ \leq 70°$. For greater wind speed the decrease is up to 50%. The effect increases to 50% and more for low sun elevation, which is equal to great sun zenith angles above the water of 80° and more. The large scale effect of gravity waves (≥100 m) has an impact, if the sun is near the horizon due to shadowing effects. To include this into numerical simulations correctly, the number of hexagonal cells has to be enlarged.

Another effect at the water surface, which occurs at wind speeds above a few meters per second, is the foam and the whitecaps. The latter are due to the dynamics of the waves and are the foamy part of breaking waves. The total foam area has a fraction f_f on the water surface with the reflectance of the foam R_f. Thus, the result is an average irradiance reflection at the surface $\langle\sigma_E^+\rangle$, which is given by

$$\langle\sigma_E^+\rangle = f_f \cdot R_f + (1 - f_f) \cdot \sigma_E^+ \tag{2.128}$$

The value of the foam fraction depends on the wind speed and the difference of the temperature in air T_a and in water T_W. Monohan and O'Muircheartaigh (1986) found the following empirical relation:

$$f_f = \left(\frac{u}{u_0}\right)^{p_{f,1}} \cdot \mathrm{e}^{p_{f,2}(T_W - T_a)} \tag{2.129}$$

with empirical coefficients $u_0 = 70.315$ m/s, $p_{f,1} = 2.55$, and $p_{f,2} = 0.0861$ °C^{-1}. The reflectance of the foam is in the range of about 0.2 to 0.3 (Koepke, 1984). Thus, the average irradiance reflection increases about 10% for a stable condition ($T_W = T_a$) and for a wind speed of 15 m/s.

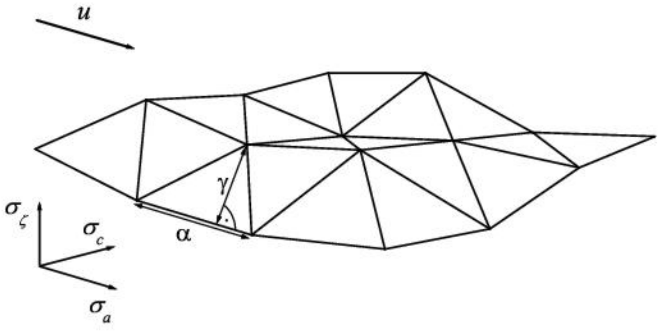

Figure 2.23: Scheme of the hexagonal grid and the triangular wave facets used for the simulation of the wind blown surface causing capillary waves, after Mobley (1994).

Chapter 3

Analytical parameterisations

The theory of chapter 2 describes the radiative transfer in water. Analytical equations were derived for the irradiance reflectance and remote sensing reflectance for deep and shallow water. The inputs of the equations are the inherent optical properties of the water, the characteristics of the bottom and the water surface, and the position of the sun and the observer. Since approximations were used, errors are introduced. This chapter shows, how the errors are reduced and the analytical equations are improved by introducing statistical coefficients.

The irradiance and remote sensing reflectance of deep water just below the water surface, R_∞ and $R_{rs,\infty}$ respectively, are given by the equations (2.40) and (2.41). If the ratio of backscattering to absorption plus backscattering is defined by

$$\omega_b(\lambda) \equiv \frac{b_b(\lambda)}{a(\lambda) + b_b(\lambda)} \tag{3.1}$$

this results in

$$\begin{aligned} R_\infty &= f^\circ \cdot \omega_b & (3.2) \\ R_{rs,\infty} &= f^\uparrow \cdot \omega_b = \frac{f^\circ}{Q} \cdot \omega_b & (3.3) \end{aligned}$$

The dependence on the wavelength is omitted for simplicity. These approximations are valid for infinitely deep water, where only the water body contributes to the reflected signal. For open ocean case-1 waters, constant proportionality factors are commonly used and are sufficient for many applications, for example $f^\circ = 0.33$ (Gordon et al., 1975) and $f^\uparrow = 0.095$ (Gordon et al., 1988). Due to the influences of the sun and surface geometry on the reflectances, a parameterisation of the factors can be developed including these aspects and the inherent optical properties as well (Kirk, 1984; Sathyendranath and Platt, 1997). But in case-2 waters, the factors f° and $f^\uparrow$ are not constant and can vary with time and location (Dekker et al., 1997). Heege (2000) used for his determination at Lake Constance a combination of the models of Kirk (1984) and Bannister (1992).

In addition, if remote sensing data are analyzed including optically shallow waters, the bottom depth z_B and the bottom albedo R_B have to be taken into account as developed in the equations (2.61) and (2.62). These equations also include the diffuse attenuation coefficient of the water column K, which is assumed to represent the downward and upward attenuation equally. However, in reality the diffuse attenuation coefficients of the upwelling and downwelling light are not equal. To get a more accurate expression, the effective attenuation coefficient is divided into an upwelling and a downwelling part, K_u and K_d respectively. The upwelling part distinguishes between radiation reflected in the water column (index W) and from the bottom (index B) (Lee et al., 1998). The viewing angle just below the water surface, θ_v, is included for the remote sensing reflectance in the upward attenuation due to the dependence of the upwelling radiance on the viewing position (Lee et al., 1999). This results in

$$\begin{aligned} R &= R_\infty \cdot \left(1 - \mathrm{e}^{-(K_d + K_{u,W}) z_B}\right) + \left(\sum_{i=1}^{n} f_{a,i} R_B\right) \cdot \mathrm{e}^{-(K_d + K_{u,B}) z_B} \qquad (3.4) \\ R_{rs} &= R_{rs,\infty} \cdot \left[1 - \exp\left\{-\left(K_d + \frac{K_{u,W}}{\cos\theta_v}\right) z_B\right\}\right] \\ &\quad + \left(\sum_{i=1}^{n} f_{a,i} B_i \cdot R_B\right) \cdot \exp\left\{-\left(K_d + \frac{K_{u,B}}{\cos\theta_v}\right) z_B\right\} \qquad (3.5) \end{aligned}$$

Based on these equations new analytical parameterisations were developed for the reflectances of deep and shallow water, the upwelling, and the downwelling attenuation coefficients to obtain an equation for remote sensing data. Simulations were made with the well-established and validated radiative transfer program Hydrolight (version 3.1) (Mobley et al., 1993; Mobley, 1994) for case-2 waters and the results fitted to equations (3.4) and (3.5). The optical properties of Lake Constance were investigated by Gege (1998) and Heege (2000) and were included in the forward simulation program as described in the chapters 2.2 and 2.3. The simulations with Hydrolight were performed not only over the natural range of the concentrations of the water constituents found for Lake Constance, but also below and above this range to cover a more general range of concentrations. This extends the validity of the developed parameterisations to a wide number of case-2 waters.

3.1 Radiative transfer model

For the forward simulation of the underwater light field the radiative transfer program Hydrolight (version 3.1) was used. This program was developed by C.D. Mobley[1] and kindly provided by him. The code bases on the mathematical technique after Preisendorfer (1976) and the solution method called “invariant imbedding theory”. This technique provides an exact method for the solution of the radiative transfer equation (2.5). It uses the radiances of the equations (2.2) to (2.4) and is faster than the conventionally used Monte Carlo method. The model is explained in detail by Mobley et al. (1993), Mobley (1994), and the handling of the program is described in the user guide (Mobley, 1995; 1996).

The optical properties are selected for case-2 waters, such as the test site in Lake Constance,

---

[1] Sequoia Scientific Inc., 2700 Richards Road, Suite 107, Bellevue, WA 98005, USA, `mailto:mobley@sequoiasci.com`

and are given for three kinds of water constituents: phytoplankton (index P), suspended matter (index X), and gelbstoff (index Y). Thus, the total absorption and backscattering coefficients, $a(\lambda)$ and $b_b(\lambda)$, are the sums of all contributions of each water constitutent and pure water (index W) itself as explained in chapter 2. The vertical distribution of the water constituents and the water temperature is included by depth profiles measured in Lake Constance. Inelastic scattering is implemented as described in chapter 2.4.
For shallow water, the influence of the bottom was modeled by the use of measured bottom reflectances in different depths. The simulations were done with bottom reflectances of a bright sand, green algae, sediment, and a high growing macrophyte to cover a wide range of lake floor coverages. The model includes the water surface as mentioned in chapter 2.6. To generate different structures of the water surface, simulations were made with different wind speeds. Altogether, over 1400 spectra were simulated.

3.1.1 Absorption and scattering

Due to the symmetric scattering properties of water, the backscattering coefficient of pure water can be determined from the scattering coefficient b_W: $b_{b,W} = \frac{1}{2} b_W$. The absorption $a_W(\lambda)$ and scattering coefficient $b_W(\lambda)$ of pure water are taken from Buiteveld et al. (1994). The absorption and backscattering coefficients of phytoplankton and suspended matter are the product of the specific absorption and backscattering coefficients and the concentrations. The specific absorption of phytoplankton $a_P^*(\lambda)$ is given after Heege (2000) by the mean value of measurements of Gege (1994) in Lake Constance. Absorption of suspended matter was investigated for Lake Constance by Heege (2000). He found that the absorption of suspended matter does not contribute to the total absorption significantly and therefore a_X is set to zero. The absorption of gelbstoff is approximated by an exponential function (Bricaud et al., 1981) with an exponent $s_Y = 0.014$ nm^{-1} at a reference wavelenght λ_0 of 440 nm after Gege (1999). The scattering in the water is mainly driven by the amount of suspended matter. The influence of the particulate fraction of phytoplankton on the scattering is included in the value of the scattering and backscattering coefficients of suspended matter as investigated by Heege (2000) and therefore, $b_{b,P} = 0$. There was also no wavelength dependence found for the scattering and backscattering coefficients from 400 to 800 nm. Hence, the constant value of the specific backscattering coefficient of suspended matter $b_{b,X}^* = 0.0086$ m^2/g, obtained for Lake Constance, was used. The ratio of the specific scattering to backscattering coefficient is 0.019 (Heege, 2000), which is the same as found by Petzold (1977) in San Diego harbour. Therefore, Petzold's phase function of San Diego harbour was chosen for all simulations. Gelbstoff is assumed not to scatter light. Finally, the following equations are obtained for the absorption and the backscattering coefficients:

$$a(\lambda) = a_W(\lambda) + a_P^*(\lambda) \cdot C_P + a_Y(\lambda_0) \cdot \mathrm{e}^{-s_Y(\lambda-\lambda_0)} \tag{3.6}$$

$$b_b(\lambda) = \frac{1}{2} b_W(\lambda) + b_{b,X}^* \cdot C_X \tag{3.7}$$

C_P (μg/l)	0.5	1.0	1.5	2.0	3.0	5.0	7.0	10.0
	20.0	40.0	60.0	80.0	100.0			
C_X (mg/l)	0.5	1.0	1.5	2.0	3.0	4.0	5.0	6.0
	7.0	9.0	10.0	30.0	50.0			
$a_Y(\lambda_0)(\mathrm{m}^{-1})$	0.05	0.10	0.15	0.20	0.30	0.40	0.50	0.60
	0.70	0.80	0.90	1.00	1.30	2.50	4.00	5.00

Table 3.1: Concentrations of the water constituents for the simulations with Hydrolight.

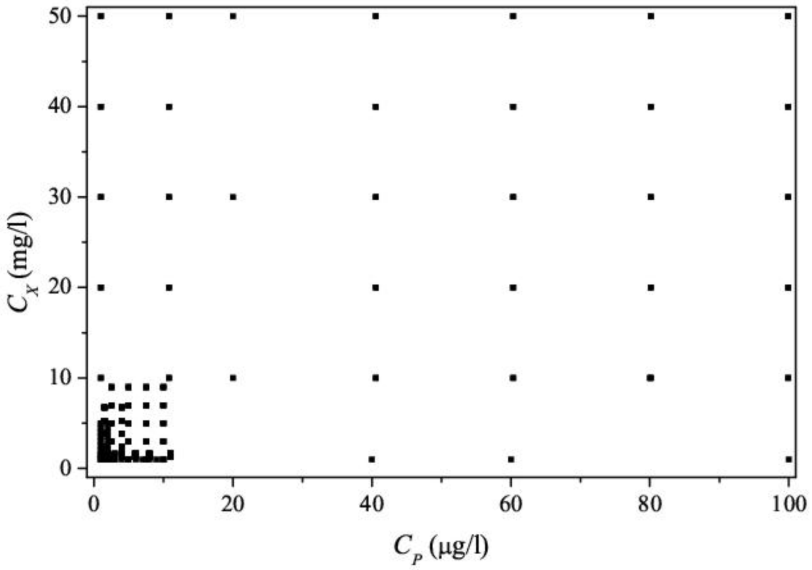

Figure 3.1: Distribution of the concentration of suspended matter against phytoplankton used for the simulations with Hydrolight.

For the simulations from 400 to 800 nm in steps of 5 nm, the concentrations of the water constituents at the surface were varied beyond their natural ranges in Lake Constance (see figures 3.1 and 3.2). The values are given in table 3.1.

The impact of inelastic processes in natural water was described in chapter 2.4. Recent investigations by Pozdnyakov et al. (2002a) show the significant contribution to the irradiance reflectance and remote sensing reflectance. Hence, the fluorescence of chlorophyll and gelbstoff as well as Raman scattering were included in all forward simulations with Hydrolight. The quantum efficiency of chlorophyll fluorescence was set to 2% and the emission function was approximated by a Gaussian function centered at the wavelength 685 nm with 25 nm full width at half maximum (σ = 10.6 nm). The fluorescence of gelbstoff was described by the spectral fluorescence quantum efficiency function defined by Hawes et al. (1992) between 310 and 490 nm. The quantum efficiency took values of about 0.9 to 1.9% in this wavelength interval as

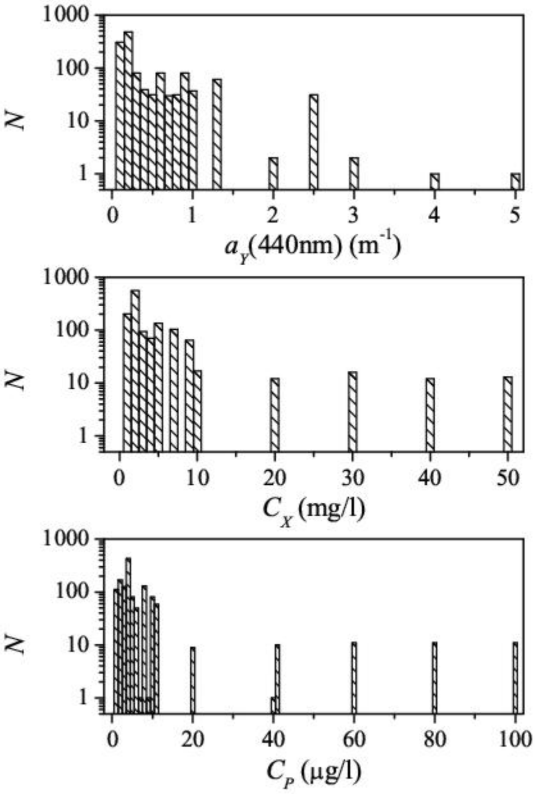

Figure 3.2: Frequency distribution of the concentration values of gelbstoff (top), suspended matter (centre), and phytoplankton (bottom) used for the simulations with Hydrolight.

listed in table 2.4. The Raman scattering was approximated using a wavenumber redistribution function of Gaussian shape at the emitted wavelength as described in chapter 2.4.

3.1.2 Depth profiles

The water constituents are in general not homogeneously distributed with depth in natural waters. Thus, to match on avarage the real situations of the test site Lake Constance, depth profiles of the water constituents were included in all the simulations. More than 500 depth profiles were measured in Lake Constance between 1986 and 1996 within the Collaborative Research Centre SFB 248 “Cycling of matter in Lake Constance” funded by the German Research Foundation DFG (Häse et al., 1998). The data were analysed and mean profiles were determined for phytoplankton and suspended matter (Heege, 2000; Häse and Heege, 2003). The minimum concentration of phytoplankton was 1.0 μg/l used for determining the depth profile. The dependence of concentration on depth z can be expressed as

$$C(z) = C_0 + C_{max} \cdot \exp\left\{-\frac{1}{2} \cdot \left(\frac{|z - z_{max}|}{\sigma}\right)^n\right\} \tag{3.8}$$

where $C(z)$ is the concentration of phytoplankton or suspended matter. For gelbstoff, no depth dependence was found. The values of the coefficients C_0, z_{max}, σ, and n are listed in table 3.2. Although the coefficients have a high variance, better results were obtained by the use of equation (3.8) than by the use of other models. If a constant value of the concentration for all depths was used, the irradiance reflectance was underestimated by 12 to 15% for concentrations of 2 to 5 μg/l phytoplankton and 2 to 5 mg/l suspended matter. To get a suitable depth profile for the lowest concentrations of phytoplankton and suspended matter the coefficient C_0 in table 3.2 was adjusted to 0.5 μg/l and 0.5 mg/l respectively. Figure 3.3 shows the curves of the depth profiles of phytoplankton and suspended matter for different concentrations. The different shapes of the profiles are due to the different behaviour of the constituents in the water: phytoplankton is concentrated at the surface, where maximum sun light is available for photosynthesis, whereas the suspended particles sink to greater depth due to their density.

	C_0	z_{max} (m)	σ (m)	n
Phytoplankton	1.0 μg/l	2.9	9.6	3.0
Suspended matter	0.9 mg/l	12.9	10.7	2.3

Table 3.2: Values of the constant factors of phytoplankton and suspended matter for the depth profile in equation (3.8).

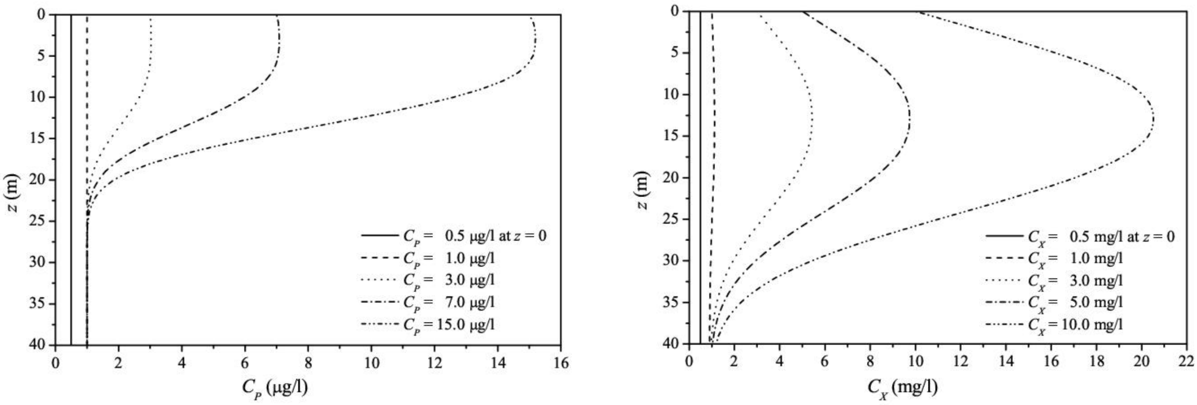

Figure 3.3: Depth profiles of phytoplankton (left) and suspended matter (right) for different concentrations after equation (3.8).

As described in chapter 2.2 and 2.3, the temperature influences the absorption and scattering coefficient of water. Thus, mean depth profiles of the temperature were included into the forward model. Simulations were computed for four seasons: winter (December, January, February), spring (March, April, May), summer (June, July, August), and autumn (September, October, November). The profiles were measured from 1990 through 1996 in Lake Constance within the Collaborative Research Centre SFB 248 "Cycling of matter in Lake Constance" funded by

z (m)	0.5	1.5	2.5	3.5	4.5	5.5	6.5	7.5	8.5	9.5	10.5	20.0	30.0	40.0
$\langle T \rangle_{winter}$ (°C)	5.13	5.13	5.13	5.13	5.12	5.12	5.12	5.11	5.11	5.11	5.11	4.8	4.4	4.0
$\langle T \rangle_{spring}$ (°C)	9.84	9.71	9.52	9.32	9.09	8.76	8.48	8.22	7.94	7.67	7.45	5.0	4.5	4.0
$\langle T \rangle_{summer}$ (°C)	19.78	19.65	19.39	18.91	18.24	17.42	16.54	15.65	14.81	14.05	13.42	10.0	6.0	5.0
$\langle T \rangle_{autumn}$ (°C)	15.12	15.12	15.09	15.03	14.91	14.78	14.62	14.43	14.18	13.85	13.47	10.0	6.0	5.0

Table 3.3: Profile of mean temperatures of the four seasons used for the simulations with Hydrolight.

the German Research Foundation DFG. The measurements were conducted by E. Bäuerle[2] and kindly provided for this study. The mean values and the standard deviations of the depth profiles are shown in figure 3.4 showing clearly the annual cycle. The mean temperatures $\langle T \rangle$ of each season depending on the depth are listed in table 3.3.

3.1.3 Bottom reflectance, water surface, and sky conditions

The bottom types were selected to get a wide natural range of bottom reflectances over all wavelengths. Spectra of sand and green algae included in Hydrolight after Maritorena et al. (1994) were used. Additionally, bottom albedo spectra were used for the simulations for sediment and macrophyte covered beds as described in chapter 2.5. The sediment was gray colored mud consisting of about 50% inorganic particles and 50% organic matter typical for Lake Constance. The average particle size is around 10 μm. The reflectance of the macrophyte was measured above a patch of the species *Potamogeton Pectinatus* L. with senescent leaves. The bottom reflectances used for the simulations are shown in figure 3.5. Additionally to the plotted bottom albedos, a constant reflectance over all wavelengths of R_B =0.1 was used. The bottom depth was set to 1, 3, 6, 10, 20, 30 m, and infinitely deep water. Effects due to BRDF and sloping bottom were neglected. The remote sensing reflectance was simulated with a Lambertian bottom reflector, $\langle \tilde{B} \rangle = R_B/\pi$ sr^{-1}.

For simulating the sun and sky conditions the model of Gregg and Carder (1990) included in Hydrolight was used. Clear sky conditions were chosen with varying subsurface sun zenith angle θ_s. The angles were 8, 14, 21, 27, 34, 39, 43, and 46°. The output of the Hydrolight simulations is given for different subsurface viewing angles θ_v ranging between 8° and 46° in the same manner as the sun zenith angle and for azimuth angles in steps of 15°.

The forward simulations were performed for values of the surface wind speed u of 0, 5, and 10 m/s

---

[2] Moislingen Nr. 4, 21369 Nahrendorf, `mailto:erich.baeuerle@t-online.de`

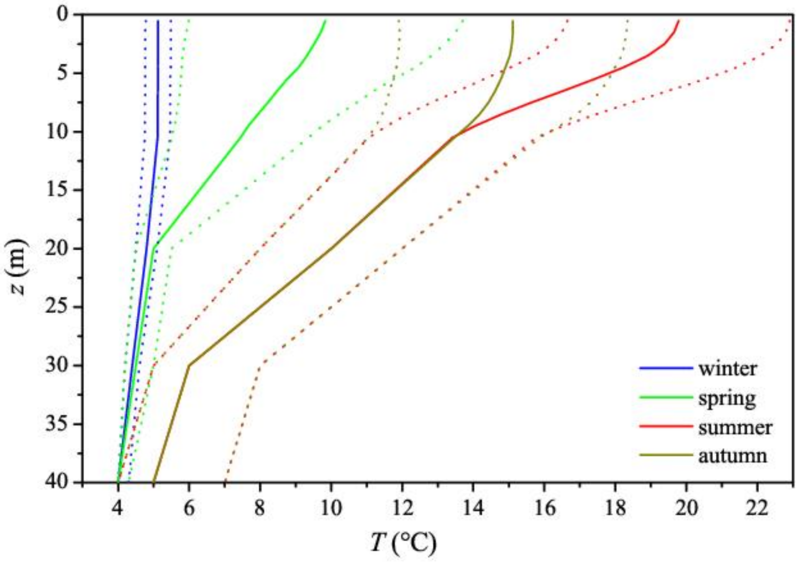

Figure 3.4: Seasonal average depth profiles of the temperature measured in Lake Constance from 1990 through 1996; dotted lines represent the standard deviation.

using the sea surface statistical model incorporated into Hydrolight. This surface representation is based on the wave-slope wind-speed laws of Cox and Munk (1954a; b) and thus includes both gravity and capillary wave effects as explained in chapter 2.6. The impact of whitecaps and foam was neglected.

3.2 Result: set of parameterisations

As published by Albert and Mobley (2003), the Hydrolight simulations of the irradiance reflectance and remote sensing reflectance, R and R_{rs}, were investigated to find parameterisations for the inherent optical properties as well as for the sun and viewing geometry using equations (3.4) and (3.5). The unknown variables in these equations are the irradiance reflectance and remote sensing reflectance of the water body, R_∞ and $R_{rs,\infty}$, and the diffuse attenuation coefficients K_d, $K_{u,W}$, and $K_{u,B}$. For each of these unknown factors new parameterisations were developed based on the inherent optical properties, the solar and viewing angles, and the surface wind speed. Wavelength dependence was included in the inherent optical properties. For all simulations chlorophyll and gelbstoff fluorescence was considered as mentioned above. For the determination of the parameterisations, wavelengths around the strongly peaked fluorescence emission of chlorophyll from 660 to 715 nm were excluded to give a better spectral fit. The parameterisations were generated by fitting the simulated values using the Levenberg-Marquardt multivariate optimization technique yielding regression coefficients. These regression coefficients allow calculation of the reflectances and attenuation coefficients using analytical equations. The

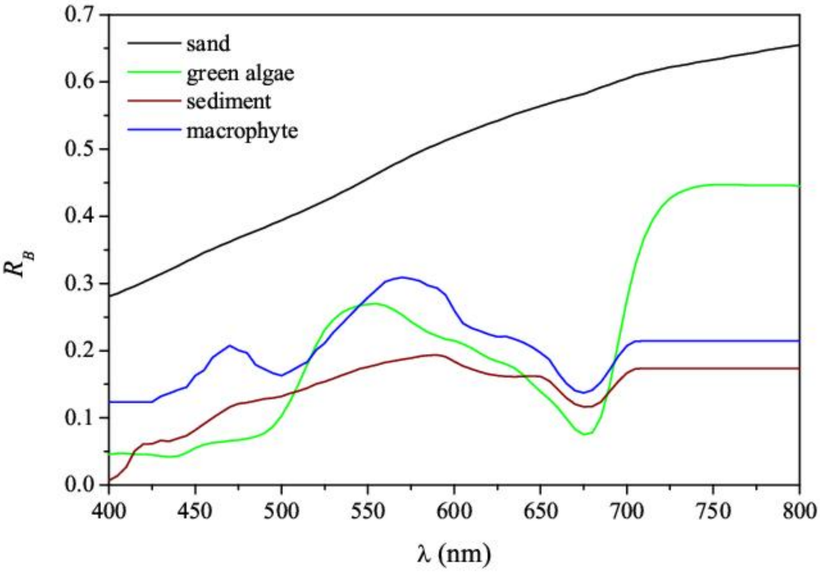

Figure 3.5: Bottom reflectance spectra used for the forward simulations in Hydrolight.

mean relative error $\overline{\delta}$ documents the accuracy of the analytical parameterisations and was estimated by

$$\overline{\delta} = \frac{X - X_0}{X_0} = \frac{\Delta X}{X_0}, \tag{3.9}$$

where X represents the value calculated by the parameterisation and X_0 the value of the simulation.

3.2.1 Irradiance reflectance of deep water

The underwater irradiance reflectance for deep water R_∞ at depth $z = 0$ is parameterized using equation (3.2). The factor f° was analyzed for its dependence on the factor ω_b, the wind speed u, and the subsurface solar zenith angle θ_s. The simulations yield a non-linear dependence on the factor ω_b (figure 3.6) and the subsurface solar zenith angle θ_s (figure 3.7 right) and a linear dependence on the surface wind u (figure 3.7 left). For the investigation of the dependence on surface wind, additional calculations were made for wind speed values ranging from 0 to 30 m/s in steps of 1 m/s. The following parameterisation was found to be suitable:

$$\begin{aligned} R_\infty &= f^\circ(\omega_b, \theta_s, u) \cdot \omega_b = f^\circ(\omega_b) \cdot f^\circ(\theta_s) \cdot f^\circ(u) \cdot \omega_b \\ &= p_1 \cdot \left(1 + p_2 \cdot \omega_b + p_3 \cdot \omega_b^2 + p_4 \cdot \omega_b^3\right) \cdot \left(1 + p_5 \cdot \frac{1}{\cos\theta_s}\right) \cdot (1 + p_6 \cdot u) \cdot \omega_b \end{aligned} \tag{3.10}$$

Using fewer coefficients for the factor ω_b results in a significantly lower correlation. The coefficients p_1 to p_6 were determined using $N = 22184$ model results. The results of the regression are listed in table 3.4. The errors of using a constant factor f° is illustrated in figure 3.6. The dashed line corresponds to the value of $f^\circ = 0.33$ by Gordon et al. (1975). For high values of ω_b, which means high backscattering or high concentration of suspended matter, the error increases up to 100%. With the new parameterisation the error is reduced significantly.

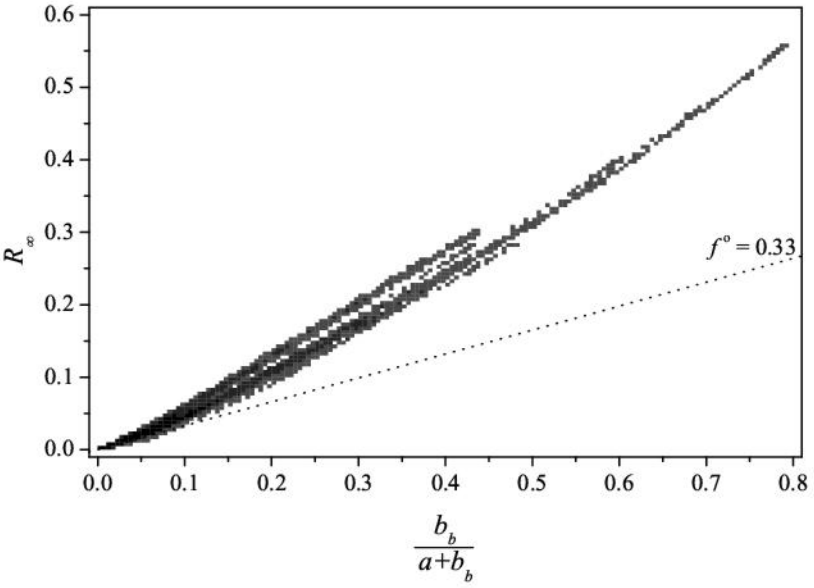

Figure 3.6: Irradiance reflectance for infinitely deep water simulated with Hydrolight ($N = 22184$) depending on $\omega_b = \frac{b_b}{a+b_b}$ and the approximation of Gordon et al. (1975) for a factor $f^\circ = 0.33$ (dotted line).

p_1	0.1034 ± 0.0014
p_2	3.3586 ± 0.0305
p_3	-6.5358 ± 0.0808
p_4	4.6638 ± 0.0649
p_5	2.4121 ± 0.0443
p_6 (s/m)	-0.0005 ± 0.0001

Table 3.4: Coefficients for the irradiance reflectance of deep water for equation (3.10).

Figure 3.8 shows, on the left hand side, the calculated plotted against the simulated values. The black points are the estimated values with equation (3.10) and the blue points are the values derived by the model of Heege (2000). The distribution of the relative error $\overline{\delta}$ between the simulated and predicted values of R_∞ with equation (3.10) (figure 3.8 right) shows a normal distribution with a mean value of 0.04 while the mean error using a constant $f^\circ = 0.33$ is -0.25. The new parameterisation gives also much better results than models of Kirk (1984) and Sathyendranath and Platt (1997) which include the sun zenith angle to estimate the factor f°. The mean relative error of the model of Kirk (1984) is -0.07 and of Sathyendranath and Platt

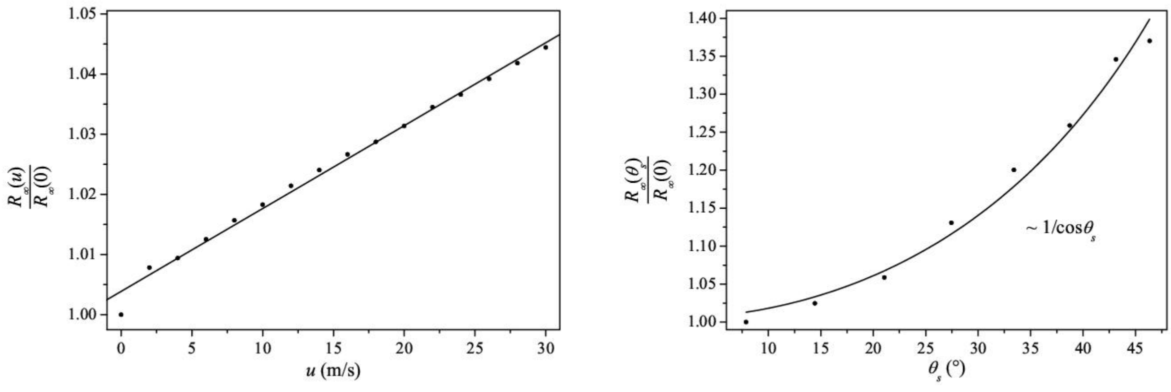

Figure 3.7: Dependency of the irradiance reflectance for infinitely deep water on surface wind (left) and subsurface solar zenith angle (right). The concentrations of the water constituents are $C_P = 3$ μg/l, $C_X = 3$ mg/l, and $a_Y(\lambda_0) = 0.2\text{m}^{-1}$.

(1997) is -0.19. The model of Heege (2000) results in a mean relative error of 0.08 (figure 3.8 right), but for irradiance reflectances larger than 20% the mean relative error is 0.22. For these situations of high backscattering due to high amount of suspended matter, the new parameterisation results in a mean relative error below 1%.

The advantage of the new parameterisation is the separation of the dependences on the inherent optical properties and the sun and surface geometry. This allows the influence of the variables on the remote sensing signal to be analysed separately. The surface wind speed has the weakest influence. If it is neglected, the error is below 1%. The influence of the sun's position is stronger: the irradiance reflectance varies by about 15% for a subsurface solar zenith angle range from 0 to 25° and about 30% for 0 to 40°.

3.2.2 Remote sensing reflectance of deep water

The determination of the remote sensing reflectance from the irradiance reflectance is possible using the Q-factor, $R_{rs,\infty} = \frac{R_\infty}{Q}$ (see equation (3.2) and (3.3)). The Q-factor is determined by the angular distribution of the light field under water. Therefore, a parameterisation of $Q = Q(\theta_s, \theta_v, u)$ seemed to be feasible. All data points were analyzed, but no suitable parameterisation was found. The reason is that the angular distribution of Q is controlled also significantly by the inherent optical properties of water constituents and their concentrations: $Q = Q(\theta_s, \theta_v, u, \omega_b)$. Thus, an equation for the remote sensing reflectance in deep water was established that is similar to the equation for the irradiance reflectance, but with different values of the coefficients. The factor $f^\uparrow$ is derived as a function of separated variables. In addition to the dependences on ω_b, θ_s, and u the remote sensing reflectance varies with the subsurface viewing angle θ_v. Simulations using different values of θ_v are shown in figure 3.9. The data points can be fitted with a function proportional to $\frac{1}{\cos\theta_v}$. The variation of the remote sensing reflectance is about 10% for a subsurface viewing angle from 0 to 25°. This is accounted for by

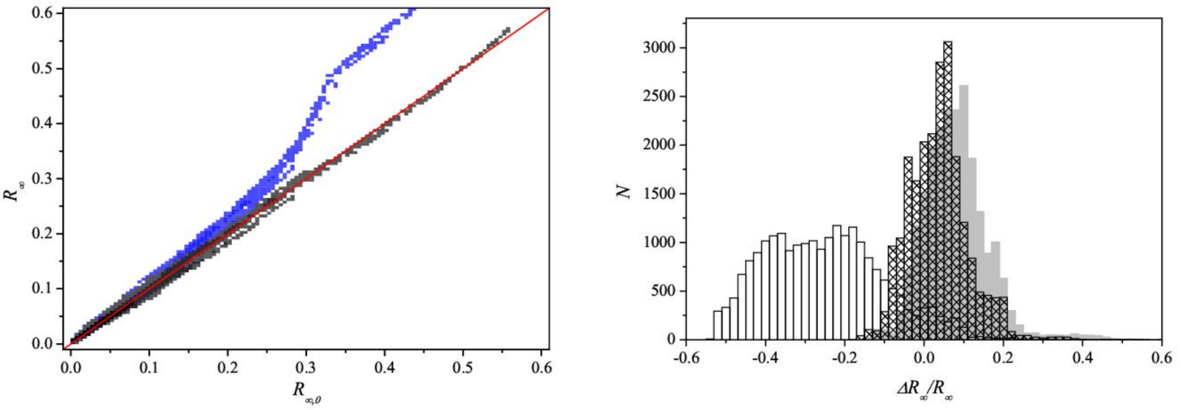

Figure 3.8: Left: irradiance reflectance R_∞ calculated by equation (3.10) (black) and by the model of Heege (2000) (blue) against the simulated values $R_{\infty,0}$ for infinitely deep water. The 1:1 line is plotted in red. Right: distribution of the relative errors for the approximation of Gordon et al. (1975) (white bars), Heege (2000) (gray bars), and of the new parameterisation of equation (3.10) (cross hatched bars).

using the following parameterisation:

$$\begin{aligned} R_{rs,\infty} &= f^{\uparrow}(\omega_b, \theta_s, u, \theta_v) \cdot \omega_b \;=\; f^{\uparrow}(\omega_b) \cdot f^{\uparrow}(\theta_s) \cdot f^{\uparrow}(u) \cdot f^{\uparrow}(\theta_v) \cdot \omega_b \\ &= p_{rs,1} \cdot \left(1 + p_{rs,2} \cdot \omega_b + p_{rs,3} \cdot \omega_b^2 + p_{rs,4} \cdot \omega_b^3\right) \\ &\quad \cdot \left(1 + p_{rs,5} \cdot \frac{1}{\cos\theta_s}\right) \cdot (1 + p_{rs,6} \cdot u) \\ &\quad \cdot \left(1 + p_{rs,7} \cdot \frac{1}{\cos\theta_v}\right) \cdot \omega_b \end{aligned} \tag{3.11}$$

The results of the regression are listed in table 3.5. $N = 177472$ model results were used to calculate the coefficients of the equation. Figure 3.10 shows the calculated values plotted against the simulated. The mean relative error is about 0.02.

$p_{rs,1}$ (sr^{-1})	0.0512 ± 0.0001
$p_{rs,2}$	4.6659 ± 0.0174
$p_{rs,3}$	-7.8387 ± 0.0434
$p_{rs,4}$	5.4571 ± 0.0345
$p_{rs,5}$	0.1098 ± 0.0018
$p_{rs,6}$ (s/m)	-0.0044 ± 0.0000
$p_{rs,7}$	0.4021 ± 0.0020

Table 3.5: Coefficients of equation (3.11) for the remote sensing reflectance of deep water.

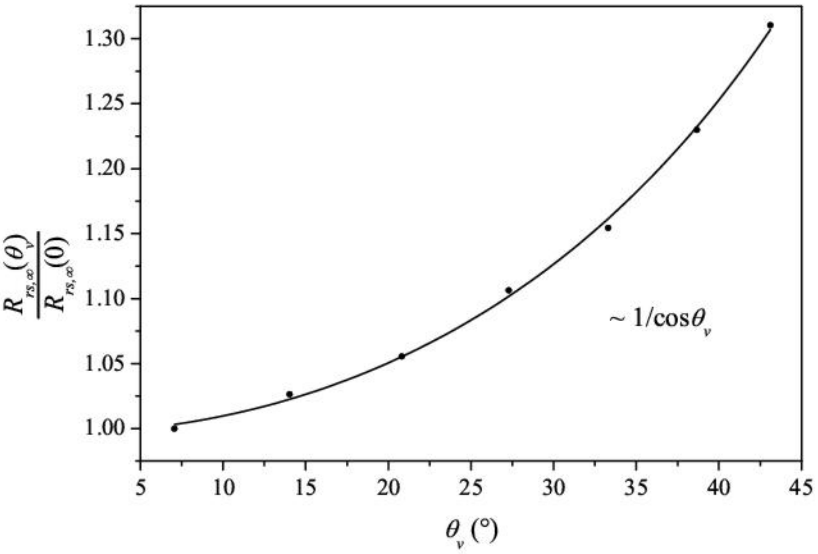

Figure 3.9: Dependence of the remote sensing reflectance for infinitely deep water on the subsurface viewing angle θ_v. The concentrations of the water constituents are $C_P = 3$ μg/l, $C_X = 3$ mg/l, and $a_Y(\lambda_0) = 0.2\text{m}^{-1}$.

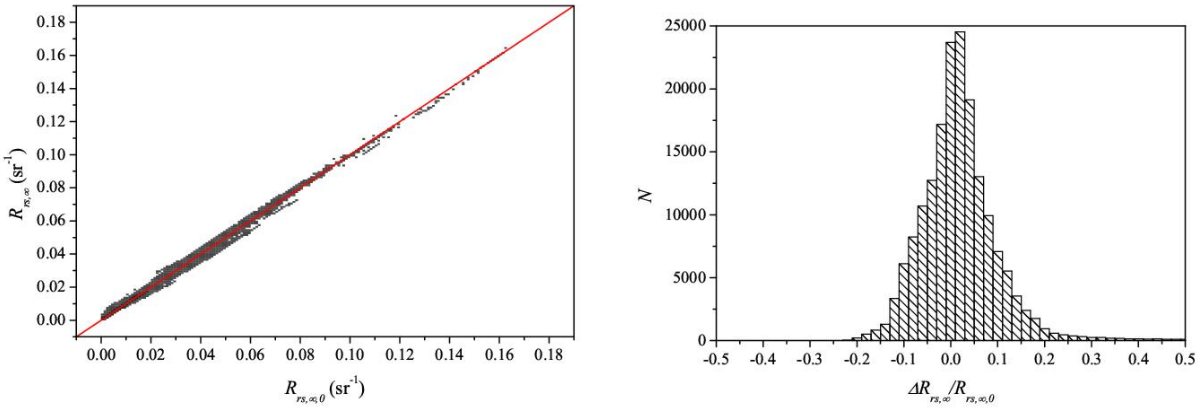

Figure 3.10: Left: remote sensing reflectance $R_{rs,\infty}$ calculated by equation (3.11) against the simulated values $R_{rs,\infty,0}$ for infinitely deep water. The 1:1 line is plotted in red. Right: distribution of the relative errors.

3.2.3 Diffuse attenuation coefficient

The reflectances of deep water are the input for the shallow water equations (3.4) and (3.5). To apply these equations it is necessary to estimate the diffuse attenuation coefficients. The attenuation describes the loss of up- and downwelling irradiance within a thin layer in the water. This loss depends on absorption, scattering, and the isotropy of the light field. The latter is parameterised by the mean cosine. This was explained in chapter 2.1 for the development of equation (2.39). Transforming equation (2.39) yields

$$K = \frac{\sqrt{a(a+b_b)} \cdot \sqrt{1 + \frac{b_b}{a+b_b}}}{\overline{\mu}_0} \tag{3.12}$$

At clear sky conditions, the distribution of the light just below the water surface is mainly affected by the direct beam of the sun. Thus, the mean cosine is approximately the cosine of the subsurface solar zenith angle θ_s in the upper water layers.

Downward diffuse attenuation

K_d depends on the absorption and backscattering as well as on the solar zenith angle as shown in figure 3.11 (left). After Gordon (1989), the parameterisation for K_d is

$$K_d = \kappa_0 \cdot \frac{a+b_b}{\cos\theta_s} \tag{3.13}$$

The simulated values of K_d range from about 0.1 m^{-1} to 10.6 m^{-1} with a mean value of 0.7 m^{-1}. The regression of $N = 72558$ data points gives a value of $\kappa_0 = 1.0546 \pm 0.0001$. The mean relative error is $\overline{\delta} = -0.01$. The distribution of the relative errors is shown in figure 3.11 (right).

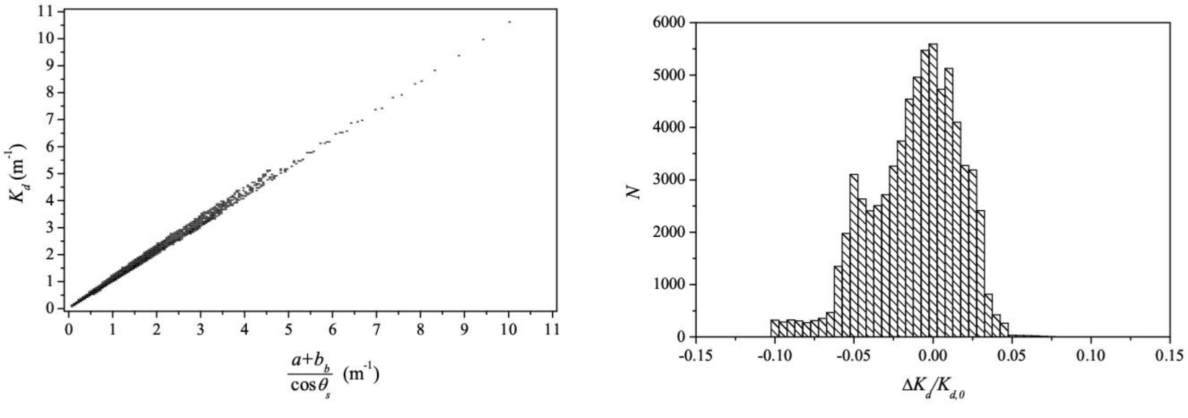

Figure 3.11: Downward diffuse attenuation coefficient of 72558 simulations with Hydrolight. Left: dependence on $\frac{a+b_b}{\cos\theta_s}$. Right: distribution of the relative errors between calculated and simulated values.

Upward diffuse attenuation

Figure 3.12 shows the dependence of K_u on absorption and backscattering (left) and on the subsurface solar zenith angle (right). The graph on the right hand side indicates the following dependency of K_u on the subsurface solar zenith angle θ_s: $K_u \propto \frac{1}{\cos\theta_s}$. On the left hand side the dependence on absorption and backscattering is plotted. The colors indicate the concentration of suspended matter C_X which is directly linked to the backscattering coefficient as described by equation (3.7). Generally, a linear dependence on the sum of absorption and backscattering can be assumed: $K_u \propto (a + b_b)$. However, for concentrations of suspended matter of $C_X < 3.0$ mg/l the relationship differs increasingly from a linear dependence. The upward diffuse attenuation coefficient takes higher values for a lower amount of scattering particles in the water. This is because few photons are scattered upwards, resulting in an anisotropic light field (Kirk, 1989). To correct for this effect an additional term is included depending on $\omega_b = \frac{b_b}{a+b_b}$. The following equation for the upward diffuse attenuation coefficient shows the best fit when used in equations (3.4) and (3.5).

$$K_u = (a + b_b) \cdot (1 + \omega_b)^{\kappa_1} \cdot \left(1 + \kappa_2 \frac{1}{\cos\theta_s}\right) \tag{3.14}$$

For the simulations of an infinitely deep water body the mean relative error was $\overline{\delta} = 0.13$ for $N = 22184$ points. Other parameterisations using more coefficients or the scattering coefficient b instead of b_b did not improve the results. To separate the influence of photons reflected by the water column and the bottom, two different upward diffuse attenuation coefficients, $K_{u,W}$ and $K_{u,B}$, are used for shallow water applications. Thus, four coefficients $\kappa_{i,W}$ and $\kappa_{i,B}$ with $i = 1, 2$ were determined by fitting the entire equations (3.4) and (3.5). The results of the regression are given in table 3.6 and 3.7 for the irradiance and remote sensing reflectance of shallow water, respectively. Since the output of Hydrolight is the total upward diffuse attenuation coefficient, which is not the sum of $K_{u,W}$ and $K_{u,B}$, no mean relative errors can be specified.

3.2.4 Irradiance reflectance of shallow water

Putting all the above results together the shallow water reflectances can be calculated using equations (3.4) and (3.5). Additional coefficients A_1 and A_2 are introduced to adapt the equations to the simulated situations.

With the new parameterisations of the diffuse attenuation coefficients and the factors A_1 and A_2, the irradiance reflectance can be expressed by

$$\begin{aligned} R \;=\; & R_\infty \cdot \left[1 - A_1 \exp\left\{-\left(\frac{\kappa_0}{\cos\theta_s} + \left(1 + \frac{b_b}{a+b_b}\right)^{\kappa_{1,W}} \cdot \left(1 + \frac{\kappa_{2,W}}{\cos\theta_s}\right)\right)(a + b_b) z_B\right\}\right] \\ & + A_2 \cdot R_B \cdot \exp\left\{-\left(\frac{\kappa_0}{\cos\theta_s} + \left(1 + \frac{b_b}{a+b_b}\right)^{\kappa_{1,B}} \cdot \left(1 + \frac{\kappa_{2,B}}{\cos\theta_s}\right)\right)(a + b_b) z_B\right\} \end{aligned} \tag{3.15}$$

The values of A_1 and A_2 were determined by fitting $N = 72558$ simulated data points. The resulting coefficients are listed in table 3.6. In figure 3.13 the estimated irradiance reflectance, R, is plotted against the simulated reflectance, R_0, for all cases. The distribution of the relative

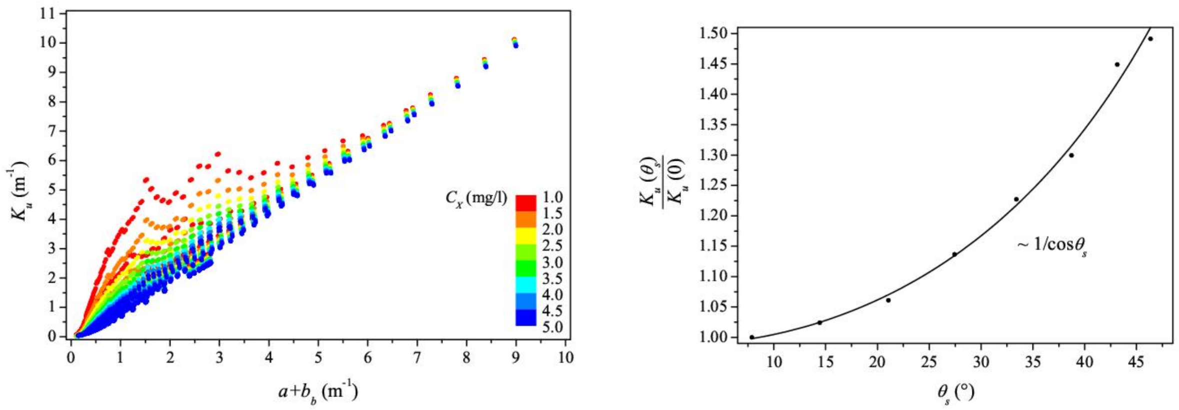

Figure 3.12: Dependence of the upward diffuse attenuation coefficient on the sum of absorption and backscattering (left) and subsurface solar zenith angle (right). The points on the left are valid for $\theta_s = 8°$ with colours representing the concentration of suspended matter and the curve on the right is valid for $C_P = 1$ μg/l, $C_X = 1$ mg/l, and $a_Y(\lambda_0) = 0.2\text{m}^{-1}$.

error - with a mean error of $\overline{\delta} = 0.02$ - is also shown in figure 3.13. For comparison, the original equation (3.4) of Maritorena et al. (1994) using equation (3.10) for the irradiance reflectance of the water column gives a relative mean error of $\overline{\delta} = 0.06$. The simulations were also compared with the recently published model of Pozdnyakov et al. (2002b). They included also Raman scattering and fluorescence of chlorophyll and gelbstoff in the set of analytical parameterisations and estimated the irradiance reflectance of shallow water by the approximation of Maritorena et al. (1994). Their results yield a mean relative error of 0.06 and show better agreement at wavelengths, where chlorophyll fluorescence occurs. But the error increases rapidly for an irradiance reflectance greater than 0.4 from 20% to 100% for $R > 0.5$. This disadvantage is also obvious at the distribution of the relative error, which is flat and ranges between -0.28 and 10.81.

A_1	1.0546 ± 0.0038
$\kappa_{1,W}$	1.9991 ± 0.0305
$\kappa_{2,W}$	0.2995 ± 0.0122
A_2	0.9755 ± 0.0013
$\kappa_{1,B}$	1.2441 ± 0.0209
$\kappa_{2,B}$	0.5182 ± 0.0036

Table 3.6: Coefficients for the irradiance reflectance for shallow water of equation (3.15).

The green points in figure 3.13 are the values for wavelengths from 660 to 715 nm. Although these wavelengths were excluded for algorithm development due to the influence of chlorophyll fluorescence, the estimation with equation (3.15) using the parameters of table 3.6 is in fair

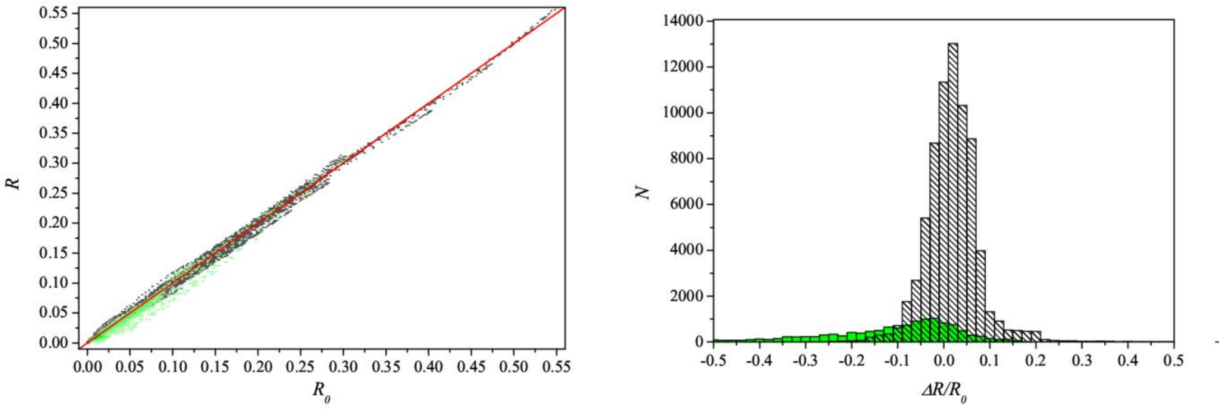

Figure 3.13: Irradiance reflectance of shallow water. Comparison of simulated values R_0 and estimated values R (left) with the 1:1 line in red; the green points are the values for wavelengths from 660 to 715 nm. Distribution of the relative error between simulated and estimated irradiance reflectances (right).

agreement with the simulated values. The mean relative error for these wavelengths is $\overline{\delta} = -0.12$. Hence the new parameterisation can be applied also to these wavelengths, however, leading to an underestimation of about 12%. In other words: the chlorophyll fluorescence contributes on average about 12% to the reflectance.

The spectral shape of reflectance for three examples is shown in figure 3.14 for the range from 400 to 800 nm together with the relative errors compared to the simulations of Hydrolight. The numbers in the figure correspond to the following conditions:

1. Bottom type sediment at a depth of $z_B = 5$ m; the concentration of phytoplankton $C_P = 10.8$ μg/l, suspended matter $C_X = 50.0$ mg/l, and gelbstoff $a_Y(440\text{nm}) = 0.2\text{m}^{-1}$; the subsurface solar zenith angle is $\theta_s = 27°$; the wind speed is $u = 1$ m/s.

2. Macrophytes at $z_B = 6$ m; $C_P = 2.5$ μg/l, $C_X = 7.0$ mg/l, and $a_Y(440\text{nm}) = 0.3\text{m}^{-1}$; $\theta_s = 33°$; $u = 0$ m/s.

3. Sediment at $z_B = 5$ m; $C_P = 1.0$ μg/l, $C_X = 1.0$ mg/l, and $a_Y(440\text{nm}) = 0.05\text{m}^{-1}$; $\theta_s = 27°$; $u = 1$ m/s.

The agreement between simulation and calculation with equation (3.15) is very good in each case. The relative error (figure 3.14: right) is below 5% over the entire spectral range, except for wavelengths around 685 nm and above 700 nm, where the error can be 10%. This is due to the fluorescence of chlorophyll which is not parameterized in these analytical equations. The differences in the other parts of the spectra are mainly caused by the fluorescence of gelbstoff which affects mostly the green part of the visible spectrum (Pozdnyakov et al., 2002a).

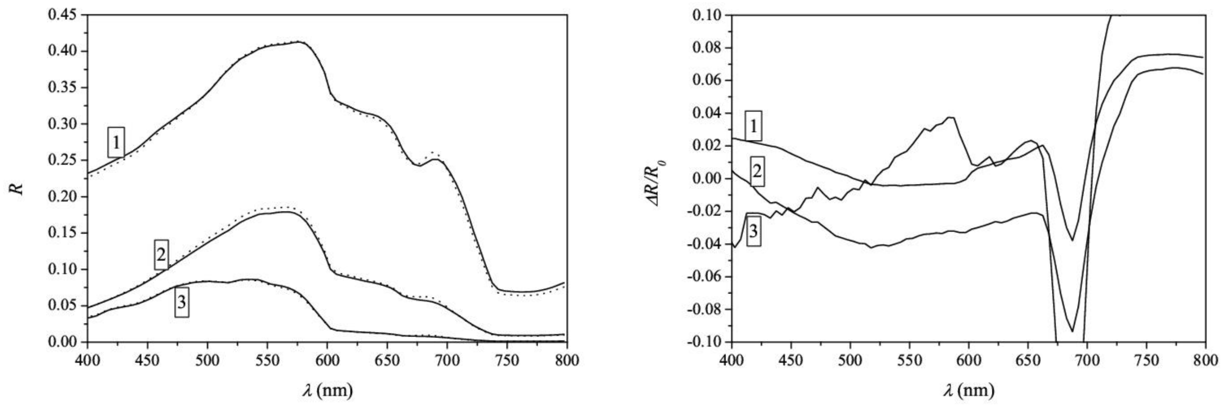

Figure 3.14: Irradiance reflectance of shallow water for the spectral range from 400 to 800 nm for three different cases. Left: comparison of simulated (dotted lines) and estimated values (solid lines); right: relative errors. The numbers refer to the explanation in chapter 3.2.4.

3.2.5 Remote sensing reflectance of shallow water

The remote sensing reflectance R_{rs} can be expressed with a similar approximation as the irradiance reflectance, but with an additional dependence on the subsurface viewing angle θ_v.

$$\begin{aligned} R_{rs} &= R_{rs,\infty}\cdot\left[1 - A_{rs,1}\exp\left\{-\left(\kappa_0\frac{\cos\theta_v}{\cos\theta_s} + \left(1+\frac{b_b}{a+b_b}\right)^{\kappa_{rs,1,W}}\cdot\left(1+\frac{\kappa_{rs,2,W}}{\cos\theta_s}\right)\right)\frac{a+b_b}{\cos\theta_v}z_B\right\}\right] \\ &+ A_{rs,2}\cdot\frac{R_B}{\pi}\cdot\exp\left\{-\left(\kappa_0\frac{\cos\theta_v}{\cos\theta_s} + \left(1+\frac{b_b}{a+b_b}\right)^{\kappa_{rs,1,B}}\cdot\left(1+\frac{\kappa_{rs,2,B}}{\cos\theta_s}\right)\right)\frac{a+b_b}{\cos\theta_v}z_B\right\} \quad (3.16) \end{aligned}$$

The results of the regression analysis of $N = 580464$ numbers of observations are listed in table 3.7. Figure 3.15 shows the estimated against the simulated values and the relative error, with a mean relative error of $\overline{\delta} = 0.03$. For comparison, the equation of Lee et al. (1998) gives a mean relative error of -0.09.

As mentioned for the case of the irradiance reflectance, the green points in figure 3.15 are the values for wavelengths from 660 to 715 nm. The correlation between the estimated and simulated values are very good here as well. The mean relative error for these wavelengths is $\overline{\delta} = -0.13$. Thus, the new parameterisation can be applied also to these wavelengths with an underestimation of about 13%.

The spectral shape of the remote sensing reflectance is shown in figure 3.16 in the same way as explained for the irradiance reflectance in chapter 3.2.4 before. Two graphs are included in the figure, one for a subsurface viewing angle of $\theta_v = 7°$ and one for $\theta_v = 27°$. The calculated values of the remote sensing reflectance agree very well with the simulations. The relative error is below 5% except for situation number 3, where the error is about 10% around 600 nm. The reason for the discrepancies is the same as for the irradiance reflectance, namely gelbstoff fluorescence. Above 700 nm the error is between 10 to 15% for low viewing angles. The error decreases with increasing viewing angles to 10% and lower. This is due to the influence of the fluorescence of chlorophyll, which is not parameterised.

The new parameterisations of R and R_{rs} are included in the Windows-based software tool WASI developed by P. Gege[3]. This operational software allows fast modeling of different optical spectra and the analysis of in-situ measured data (Gege, 2001; 2004). More details are described in appendix B.

$A_{rs,1}$	1.1576 ± 0.0014
$\kappa_{rs,1,W}$	3.5421 ± 0.0152
$\kappa_{rs,2,W}$	-0.2786 ± 0.0030
$A_{rs,2}$ (sr^{-1})	1.0389 ± 0.0004
$\kappa_{rs,1,B}$	2.2658 ± 0.0076
$\kappa_{rs,2,B}$	0.0577 ± 0.0009

Table 3.7: Coefficients in equation (3.16) for the remote sensing reflectance for shallow water.

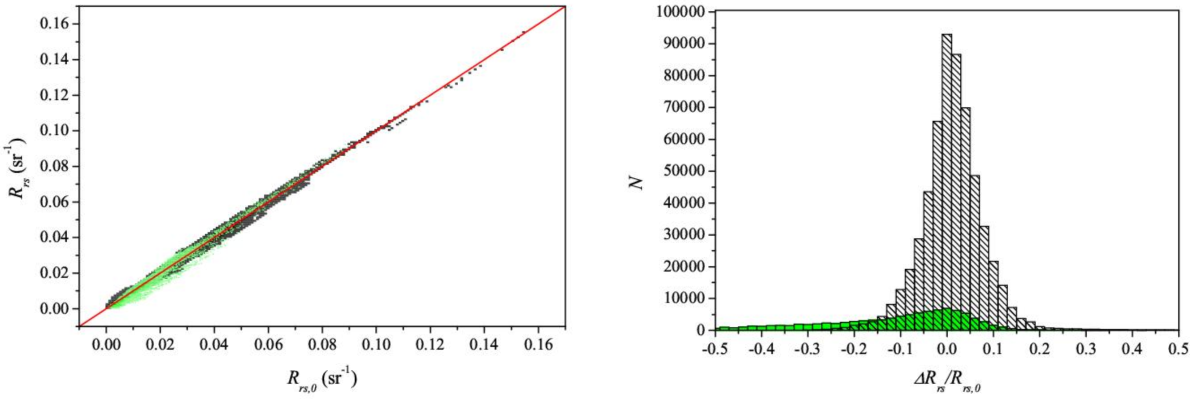

Figure 3.15: Remote sensing reflectance of shallow water. Comparison of simulated values $R_{rs,0}$ and estimated values R_{rs} (left) with the 1:1 line in red; the green points are the values for wavelengths from 660 to 715 nm. Distribution of the relative error between simulated and estimated remote sensing reflectances (right).

---

[3] DLR German Aerospace Center, Remote Sensing Technology Institute, Marine Remote Sensing, Muenchener Str. 20, 82234 Wessling, Germany, `mailto:peter.gege@dlr.de`

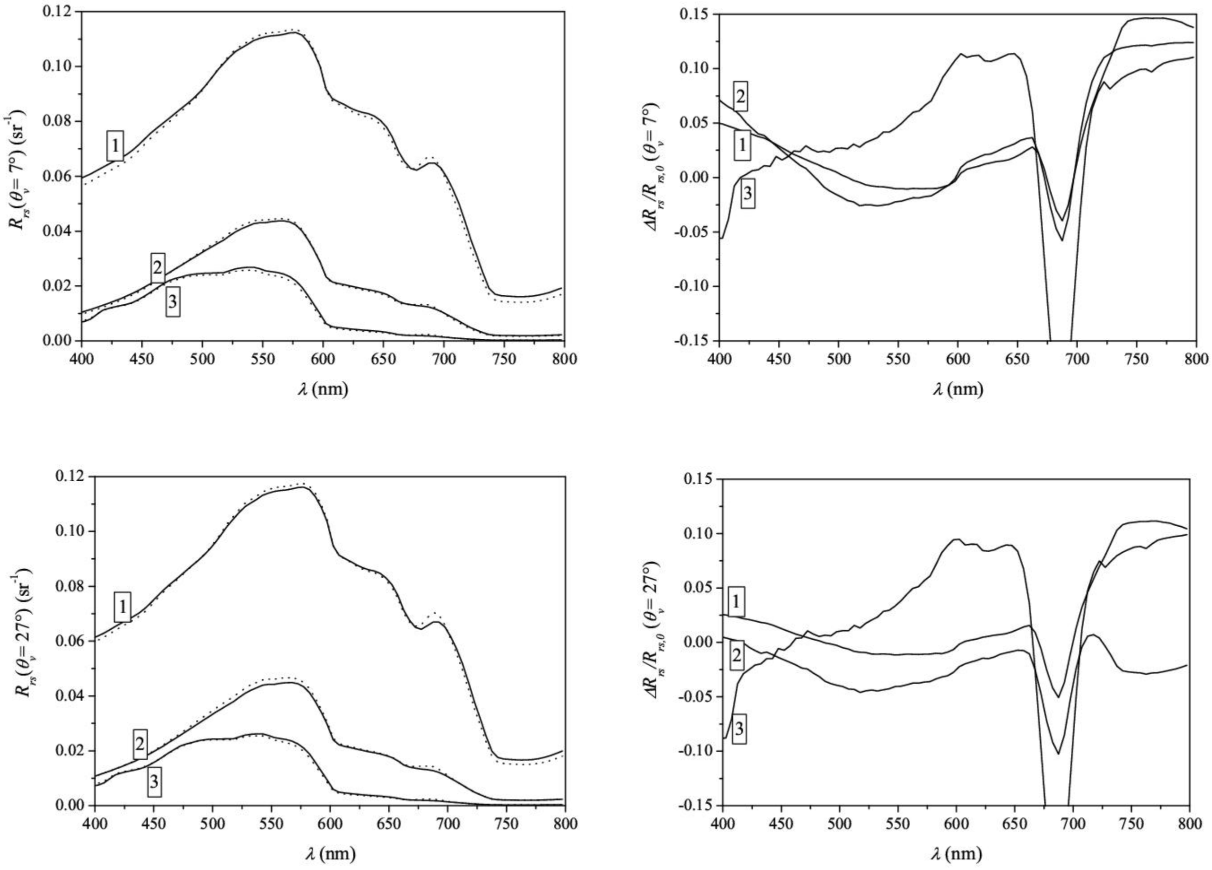

Figure 3.16: Remote sensing reflectance of shallow water for the spectral range from 400 to 800 nm for three different cases and for a subsurface viewing angle of $\theta_v = 7°$ on the top and $\theta_v = 27°$ at the bottom. The left part shows the comparison of simulated (dotted lines) and estimated values (solid lines) and the right side the relative errors. The numbers refer to the explanation in chapter 3.2.4.

3.2.6 Remote sensing reflectance above water

The last two subsections described the development of the analytical parameterisations of R and R_{rs} just below the water surface. As shown in chapter 2.6, it is possible to determine the remote sensing reflectance above the water surface, $R^+_{rs,W}$, by means of R and R_{rs} calculated by equations (3.15) and (3.16):

$$R^+_{rs,W} = \frac{(1-\sigma_L^-)(1-\sigma_E^+)}{n_W^2} \cdot \frac{R_{rs}}{1-\sigma_E^- \cdot R} \tag{3.17}$$

Using the relation of the Q-factor, which is the ratio of R to R_{rs}, two other equations result

$$R^+_{rs,W} = \frac{(1-\sigma_L^-)(1-\sigma_E^+)}{n_W^2} \cdot \frac{R_{rs}}{1-\sigma_E^- \cdot Q \cdot R_{rs}} \tag{3.18}$$

$$R^+_{rs,W} = \frac{(1-\sigma_L^-)(1-\sigma_E^+)}{n_W^2 \cdot Q} \cdot \frac{R}{1-\sigma_E^- \cdot R} \tag{3.19}$$

The factors σ_E^+, σ_L^-, and σ_E^- are the reflection factors for E_d^+, L_u, and E_u, respectively. σ_E^+ depends on the radiance distribution and on surface waves. Typical values are 0.02 to 0.03 for clear sky conditions and solar zenith angles below 45°, and 0.05 to 0.07 for overcast skies (Jerlov, 1976). σ_L^- is calculated by the Fresnel reflection as a function of the viewing angle θ_v. For angles below 30° the value of σ_L^- is 0.02. σ_E^- is in the range of 0.50 to 0.57 with a value of 0.54 being typical (Jerome et al., 1990).

The three equations are formally identical. The total remote sensing reflectance above water, R^+_{rs}, is then estimated by adding the reflection at the surface. Which of the above equations is used, depends on the application:

- Equation (3.17) avoids the use of the Q-factor, which is difficult to assess. The equation is useful, for example, for optical closure experiments, which investigate the consistency of measurements above and below the water surface by measuring simultaneously the spectra of R_{rs}, R, and R^+_{rs}.

- Equation (3.18) links remote sensing reflectance in water to that in air. Since the same spectrum type is used above and below the water surface, it is the most convenient parameterisation.

- Equation (3.19) is useful when R^+_{rs} shall be connected to R, for example if in-situ measurements of R were performed as “ground truth” for a remote sensing instrument.

The influence of the Q-factor on the three different equations of $R^+_{rs,W}$ is shown in figure 3.17. The curves are calculated using a phytoplankton concentration $C_P = 2$ μg/l, suspended matter concentration $C_X = 2$ mg/l, gelbstoff absorption $a_Y(\lambda_0) = 0.3$ m^{-1} at $\lambda_0 = 440$ nm, and a sediment bottom at $z_B = 3$ m. The subsurface solar zenith angle is $\theta_s = 30°$ and the subsurface viewing angle $\theta_v = 0$. The values of the Q-factor are 3, 4, 5, and 6 sr. The different values of Q affect most the spectrum derived by equation (3.19). This is due to the indirect proportionality in the equation: doubling the Q-factor results in half of the value of $R^+_{rs,W}$ and vice versa. The effect is reduced in equation (3.18). The variability is about 5% due to different values of Q. This result implies that the Q-factor in combination with the irradiance reflectance R should only be used in special cases, for example, if the angular distribution of the underwater light field is known.

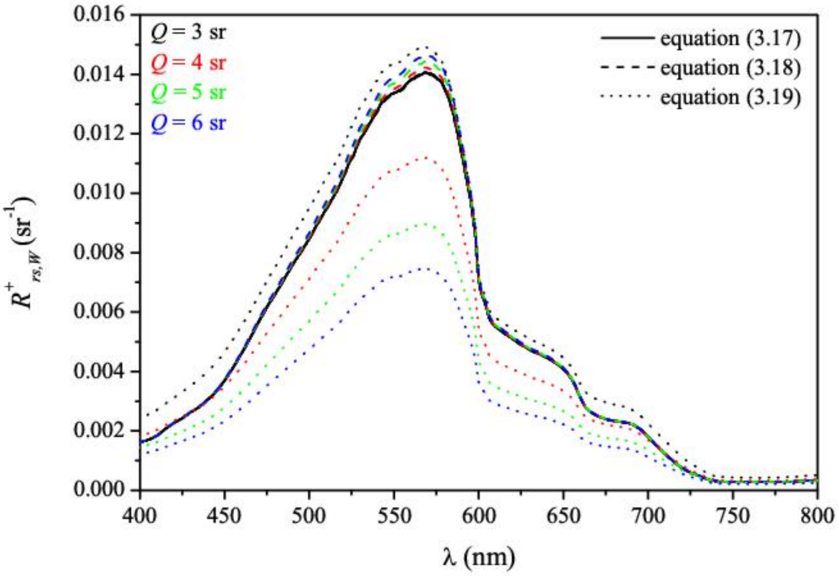

Figure 3.17: Comparison of the remote sensing reflectance above the water surface derived from three different equations and for four different Q-factors. The water constituent concentrations are $C_P = 2$ μg/l, $C_X = 2$ mg/l, and $a_Y(\lambda_0) = 0.3$ m^{-1} at $\lambda_0 = 440$ nm and the sediment bottom depth is $z_B = 3$ m. The subsurface angles are $\theta_s = 30°$ and $\theta_v = 0$.

For remote sensing of case-1 waters, equation (3.17) is often simplified by assuming a low solar zenith angle and a viewing angle near nadir. Then, σ^-_L and σ^+_E are about 0.02. The refractive index of water is around 1.34. The denominator of the second term is near one, if the irradiance reflectance is below 10% and σ^-_E is below 0.7 (Mobley, 1999). These approximations are sufficient for applications in the open ocean and yield

$$R^+_{rs,W} \approx 0.5349 \cdot R_{rs} \tag{3.20}$$

The estimated values of equation (3.17) and (3.20) are plotted against the simulated values and the relative errors of the $N = 580464$ points are calculated. This is shown in figure 3.18. The mean relative error of equation (3.17) is 0.05 and of equation (3.20) 0.06. Although the mean relative error of equation (3.20) is nearly the same as for the exact equation, the disadvantage is clearly seen in figure 3.18 (left): for reflectances of about 0.05 the approximation systematically underestimates by more than 10% and for higher reflectances up to 20%. The green points in figure 3.18 correspond to the values at the excluded wavelengths between 660 and 715 nm. The mean relative bias of these points is -0.13.

The spectral comparison between simulated and calculated values is shown in figure 3.19 for the three cases mentioned in subsection 3.2.4. The curves are plotted for the subsurface viewing angles of 7° and 27°. The spectral error shows the same behaviour as for the irradiance and remote sensing reflectance below the water surface. In the visible range the error is between 0 and 10% and increases to a maximum of about 15% for wavelengths higher than 700 nm. For the fluorescence peak of chlorophyll at 685 nm the error can be higher for high concentrations of phytoplankton.

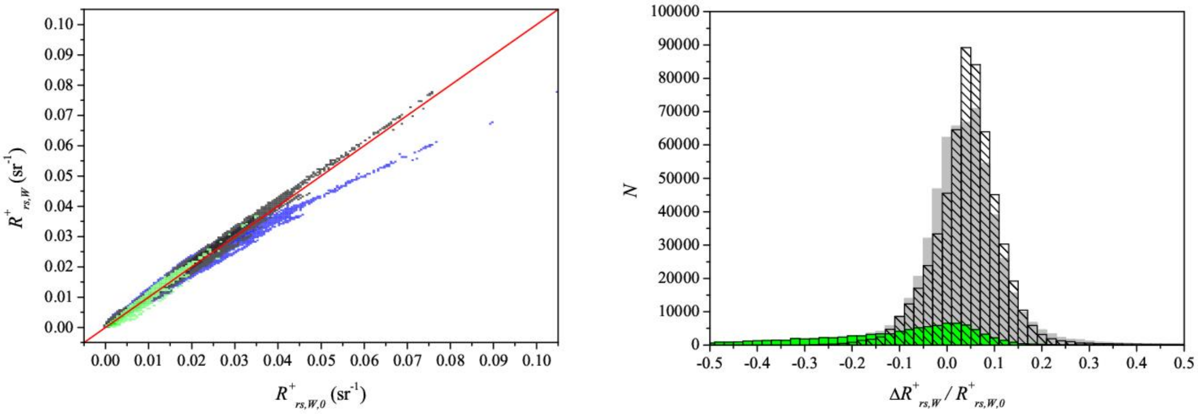

Figure 3.18: Remote sensing reflectance of the water above the surface. Comparison of simulated values $R^+_{rs,W,0}$ and estimated values $R^+_{rs,W}$ (left) with the 1:1 line in red; the green points are the values for wavelengths from 660 to 715 nm. The blue points represent the estimations using the approximation (3.20). Distribution of the relative error between simulated and estimated remote sensing reflectances above water(right); the gray bars represent the relative errors when using equation (3.20).

3.3 Comparison with in-situ measurements

In the preceding sections the parameterisations of the irradiance and remote sensing reflectance below and above the water surface have been developed. Now the calculations are compared with hyperspectral in-situ measurements in and above Lake Constance. During campaigns from 1998 to 2002 irradiance and remote sensing reflectances were measured with the instruments HYDRA (Bochter and Wallhäußer, 1997; Bochter, 2000) and RAMSES[4] from ship. Water samples were taken additionally at a depth of about 0.5 m to determine the concentrations of phytoplankton C_P, suspended matter C_X, the absorption of gelbstoff a_Y at 440 nm, and the gelbstoff exponent s_Y. The methods and instruments of the in-situ measurements are described in detail in appendix A. Measurements were conducted in deep and shallow water, below

---

[4] TriOS Optical Sensors, Werftweg 15, 26135 Oldenburg, Germany, `http://www.trios.de`

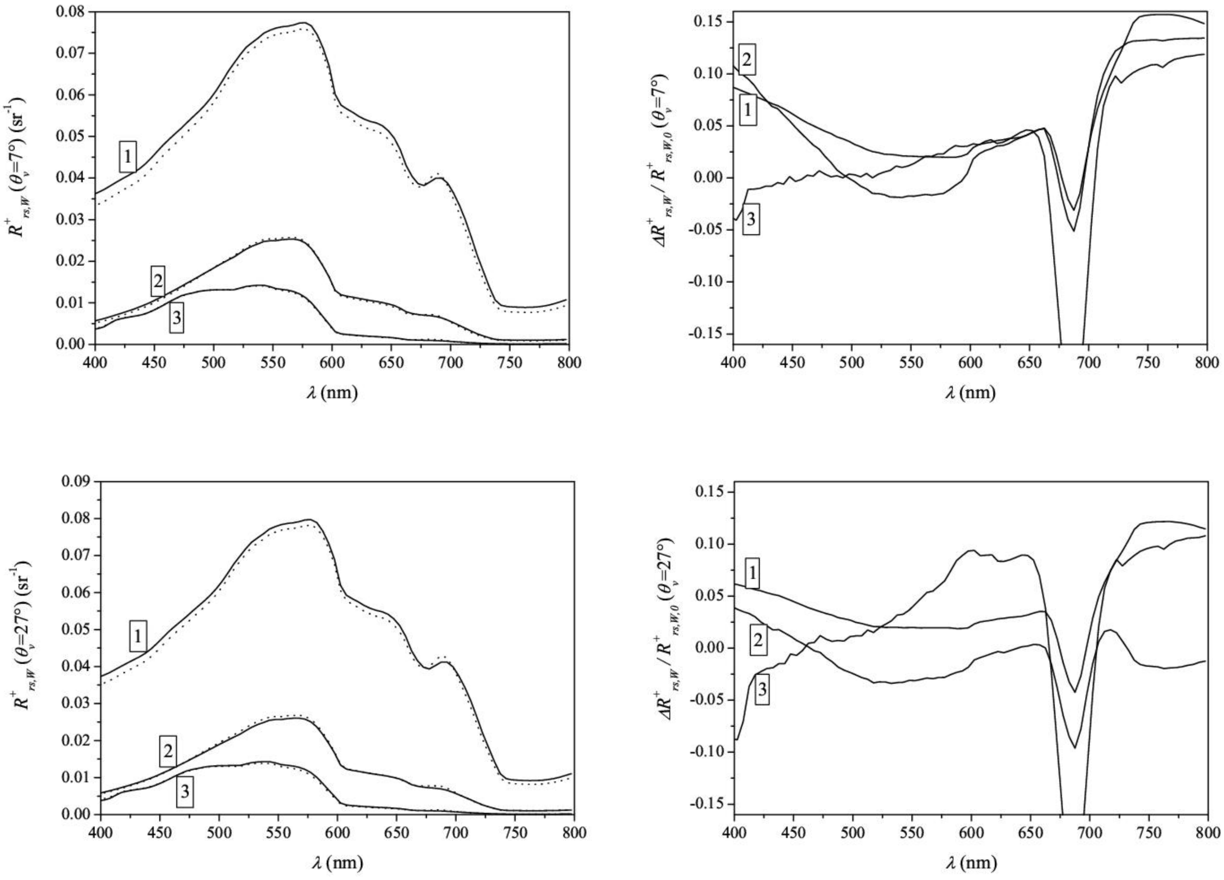

Figure 3.19: Remote sensing reflectance of the water above the surface for the spectral range from 400 to 800 nm for three different cases and for a subsurface viewing angle of $\theta_v = 7°$ on the top and $\theta_v = 27°$ on the bottom. The left part shows the comparison of simulated (dotted lines) and estimated values (solid lines) and the right side the relative errors. The numbers refer to the explanation in chapter 3.2.4.

and above the water surface. A map of the stations in Lake Constance used here is shown in figure 3.20. Table 3.8 lists the estimated values of the in-situ measurements of the water constituents, bottom depth, and bottom type. The points are a selection of more than 50 measurements of HYDRA and RAMSES and are chosen to represent different conditions. The selected examples illustrate the general behaviour of calculations and measurements including a discussion of different error sources. An analysis of all measurements is presented in connection with the inversion in chapter 5.4.

3.3.1 Deep water

Figure 3.21 shows the comparisons of optical in-situ measurements and calculations of the remote sensing and irradiance reflectance in deep water. The calculations are made using the new parameterisations with the values listed in table 3.8 and a subsurface solar zenith angle

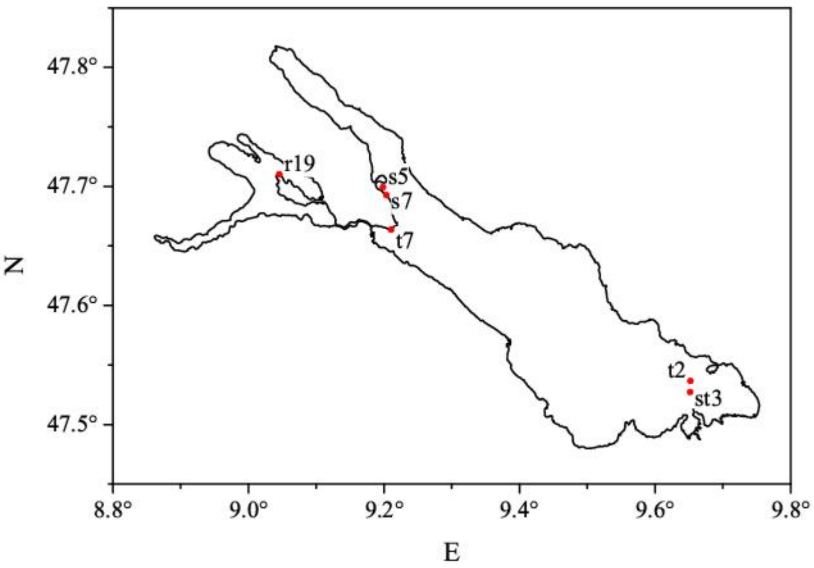

Figure 3.20: Map of the positions at Lake Constance for the comparison of in-situ measurements and model calculations for remote sensing and irradiance reflectance in deep and shallow water.

station	C_P (μg/l)	C_X (mg/l)	a_Y (m^{-1})	s_Y (nm^{-1})	z_B (m)	bottom type
st3	2.1	1.4	0.25	0.0147	∞	-
t2	4.1	4.5	0.31	0.0146	∞	-
t7	3.5	3.3	0.33	0.0125	2.4	sediment
s5	3.6	1.0	0.12	0.0140	∞	-
s7	4.8	2.2	0.14	0.0174	4.5	sediment
r19	3.3	1.5	0.30	0.0140	2.6	*Characeae*

Table 3.8: In-situ parameters in Lake Constance used to calculate spectra of R and R_{rs} by taking the new parameterisations.

of 40°. The error bars of the measurements are due to multiple exposures at the same point. The variances of a calculation are due to uncertainties of the methods determining the water constituent concentrations. An error of 10% is assumed (see appendix A). The remote sensing reflectances match conveniently the calculations considering the inaccuracies of the measurements and additional error sources:

- The optical in-situ data are measured in a variable depth of 10 to 100 cm below the water surface due to waves and ship movements. Also the vertical direction of the sensors varies a few degrees around nadir direction because of the same reasons. This implies a varying influence of the water absorption especially in the red part of the spectrum and causes fluctuations of the signal. Thus, some measurements are omitted at wavelengths longer than 700 nm.

- The sensitivity of the optical sensors is low in the blue part of the spectrum due to the decreasing quantum efficiency of the detector material silicon. Thus, a careful calibration of the detector is necessary and even small deviations cause a high error in this spectral region.
- Stray light in the spectrometer unit of the instrument affects the signal mainly in the blue. The portion of stray light is about 90% of the signal at 400 nm for HYDRA (Bochter, 2000). Thus, the accuracy of the correction of this effect has a high influence on the detected signal.
- Sensor specifications have to be carefully investigated. Effects like non-linearity, temperature, and dark current have a direct influence on the detected signal and can cause relative errors up to 50% (Bochter, 2000).
- Changes of the specific optical properties of phytoplankton and suspended matter are not considered during the measurements. Especially the influence of the specific backscattering of suspended matter affects the detected signal. The particle size distribution near the water surface varies depending on the particle density and origin due to inflows and currents. The variability of the specific backscattering coefficient in Lake Constance is about 10% (Heege, 2000), but can be higher depending on the trophic state of a lake (Dekker, 1993). The standard deviation of the specific absorption of phytoplankton at Lake Constance is between 30 and 40% (Heege, 2000) depending on wavelength due to variations of detritus. Similar variability in other lakes was found by Dekker (1993).
- The estimation of the in-situ concentrations of phytoplankton and suspended matter is done by filtration using glass fibre filters with an effective pore size of about 1 μm. Thus, particulate matter of a size smaller than 1 μm is not considered for the in-situ values. The introduced error depends on the water body, namely the fraction and size distribution of organic and inorganic material. The influence of small suspended particles on the backscattering can be very high and affects the reflectance directly (see appendix A).
- The phytoplankton concentration is determined by adding the chlorophyll-a and pheophytin concentration estimated by filtering the water samples (see appendix A). But there are additional components like for example chlorophyll-b, phycocyanin, phycoerythrin, and carotenoids, which have an influence on the remote sensing signal and are not considered. Besides, the specific optical properties of chlorophyll-a and pheophytin are different. Thus, the physically correct absorption has to be determined by a spectrally weighted sum of both absorptions. No investigations are known, which quantify this influence.
- The optical measurements and the water samples were not taken simultaneously, and not at the same position and depth. The time difference varied from about one minute to

ten minutes. The horizontal distance was between about two and ten meters and the depth dfference was about one meter. These effects are small, if the spatial and temporal variability of the water is small, but can be higher near the shore and inflows depending on currents.

- During the optical measurements, a spectral mismatch of L_u and E_u to E_d leads to spectral noise in the calculated reflectance spectra. This occurs in spectral regions with large gradients of E_d, especially between 400 and 500 nm due to Fraunhofer lines in the solar spectrum.
- Errors of the phytoplankton and suspended matter concentration caused by a wrong handling during filtering, extraction, and weighing are not quantifiable, but may have a great influence on the accuracy of the in-situ data.

The influence of different particle phase functions in deep and shallow water was investigated by Lee et al. (1998) for the remote sensing reflectance at varying solar zenith angles from 0 to 60° and a fixed viewing angle at 0°. They found that the deviation of their analytical model averages about 3% compared to Hydrolight simulations using a particle phase function of a backscattering to scattering ratio $b_{b,X}/b_X$ of 0.037, while the phase function during the development of their analytical equations had a value of $b_{b,X}/b_X = 0.019$.

Comparisons of the irradiance reflectance are shown in figure 3.21 on the right hand side. The calculated spectra are below the measured. Besides the error sources mentioned above, the main reason for this can be due to the influence of suspended particles differing from those of the specific optical properties used for the calculations. Thus, the scattering phase function and the backscattering to scattering ratio of particles can vary and affect the light distribution in the water. Stramska et al. (2000) investigated the effect of different particle phase functions on the backscattering coefficient and the light field for wavelength from 400 to 560 nm. Simulations with $b_{b,X}/b_X = 0.008$ resulted in a deviation of the backscatter coefficient of 40% compared to simulations with $b_{b,X}/b_X = 0.018$. This error has a direct proportional influence on the reflectance.

3.3.2 Shallow water

Hyperspectral measurements in shallow water were first made from ship at Lake Constance in 1999. The results of the estimated water constituent concentrations are listed in table 3.8 together with the bottom characteristics of the sampling points. The measured irradiance and remote sensing reflectances are compared with the calculated in figure 3.22. In addition to the error sources mentioned above for deep water, errors due to the shallow water situation have to be accounted for:

- The bottom albedo used for the calculation may be different to that occuring during the measurements due to a different composition of materials and a sloping bottom. As described in section 2.5, this error affects the reflected signal up to 30%.

- The accuracy of the bottom depth can be reduced due to the sloping bottom and the movement of the ship. The error can be higher than 10% depending on the current at the shore and the duration of the measurement. This error has an high impact: in about 2.5 m depth a variance of the bottom depth of 10% causes an uncertainty of about 20% in the irradiance and remote sensing reflectance for concentrations typical for Lake Constance.
- The specific optical properties of suspended matter can vary near the shore due to the resuspension of all kinds of particles by waves. Various particles are missing in open water due to their shape and density, but are existing in shallow water and therefore increasing the backscattering. A higher backscattering increases the reflectance proportionally.

The main error source is the error in the concentrations of the water constituents. For example, a 10% higher concentration of suspended matter increases the reflectance by 10% over the entire spectrum. Uncertainties in the gelbstoff absorption has a great influence in the blue and phytoplankton concentration mainly in the green. Increasing the gelbstoff absorption at 440 nm from 0.1 to 0.5 m^{-1} decreases the reflectance more than 50%. If the phytoplankton concentration is increased by 50% the reflectance decreases about 10%.

Considering all these error sources, the agreement between calculations and measurements is astonishingly good.

3.3.3 Above water

Measurements above the water surface were made with the instrument HYDRA (Bochter and Wallhäußer, 1997; Bochter, 2000). Sensors for the upwelling radiance and downwelling irradiance were held about 50 to 100 cm above the water surface from the ship. Comparisons of measurements with calculations by the new parameterisations are shown in figure 3.23. It is important to mention that the calculations include only the water leaving radiance and do not include the downwelling radiance reflected at the water surface. The two graphs show the effects, which occur additionally for above surface reflectances and have to be taken into account.

- The downwelling radiance is reflected at the surface. The reflections back into the air depend on the surface structure caused by the wind. The angular distribution of the upwelling radiance depends also on the elevation of the sun. Thus, sun light can be directly reflected into the sensor depending on the viewing angle of the instrument. This effect, called “sun glint”, increases the signal constantly over the entire visible spectrum (figure 3.23 left). Thus, the correction is very important for the retrieval of the suspended matter concentration.
- The upwelling radiance contains the Rayleigh and Mie scattering that is reflected at the water surface. This can be seen in the blue part of the spectrum (figure 3.23 right). Atmospheric scattering correction must be done very carefully to retrieve the phytoplankton concentration and gelbstoff absorption.

The examples of figure 3.23 show good agreement with the calculation taking into account the missing surface reflections. The consideration of surface reflection is very complicated and was not part of this study. Here, the emphasis is on the inversion of the irradiance and remote sensing reflectance of water. Thus, the effects above the water surface are not considered in the following. The inversion of the new parameterisations is developed in the following chapter for the reflectances measured or calculated directly below the water surface.

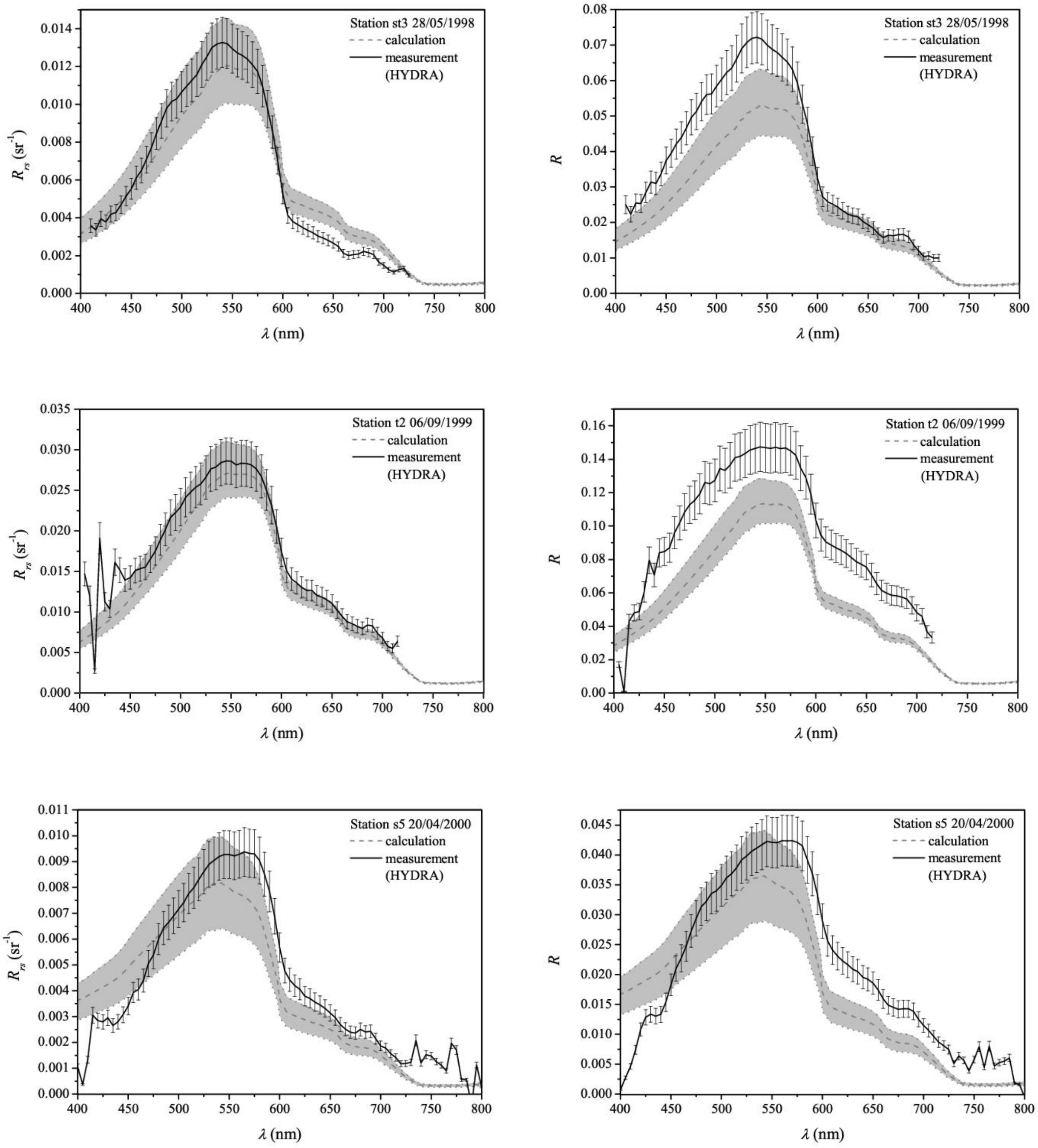

Figure 3.21: Comparison of in-situ measurements and model calculations of remote sensing (left) and irradiance reflectance (right) in deep water areas of Lake Constance. The calculations were made with the water constituent concentrations given in table 3.8 and for a subsurface solar zenith angle of 40°. The gray band represents the range between minimum and maximum of the calculations due to the assumption of 10% error of the water constituent concentrations. The error bars of the in-situ measurements are estimated due to multiple exposures at the sampling points.

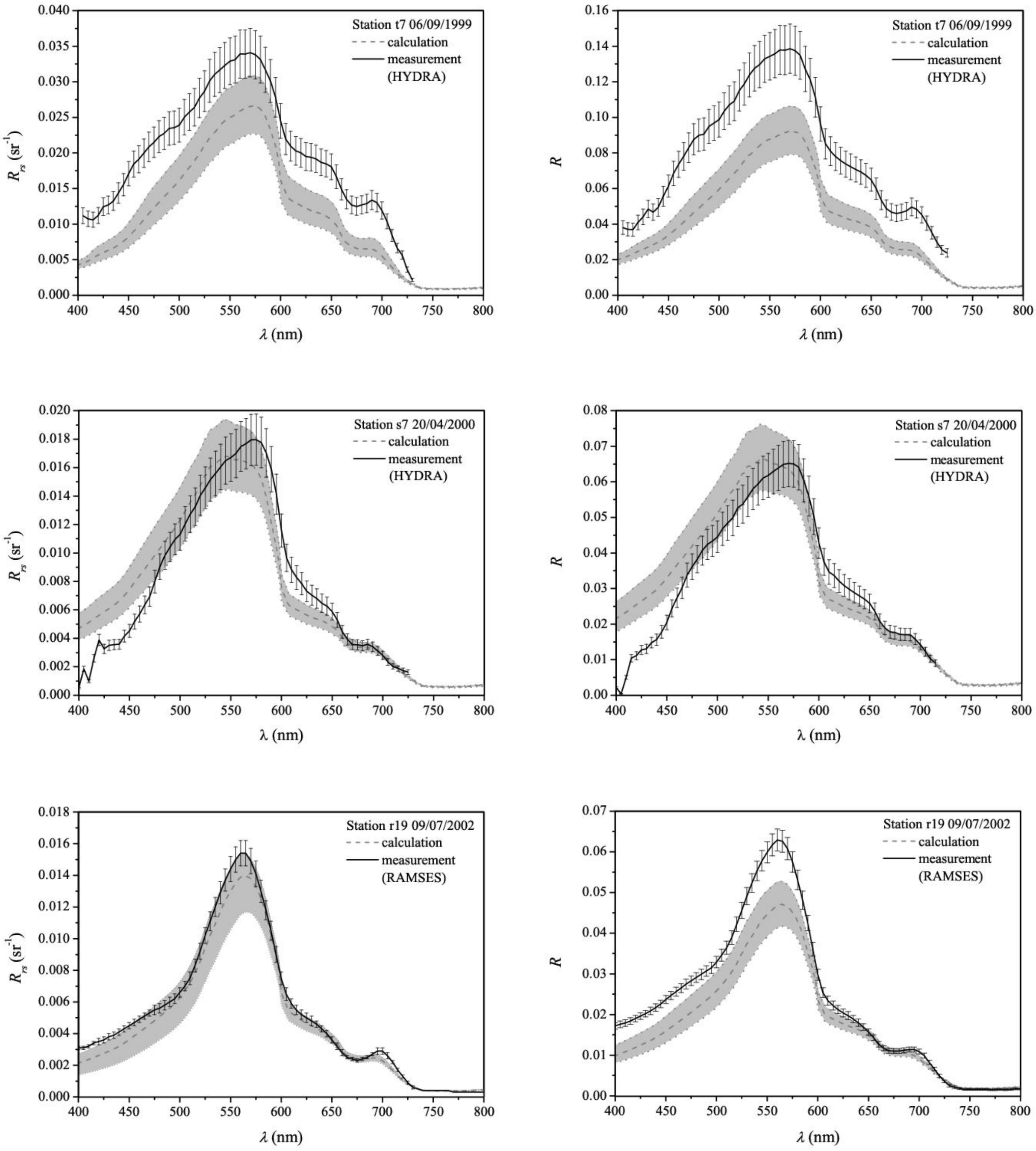

Figure 3.22: Comparison of in-situ measurements and model calculations of remote sensing (left) and irradiance reflectance (right) in shallow waters of Lake Constance. The calculations were made with the water constituent concentrations given in table 3.8 and the subsurface solar zenith angle of 40°. The gray band represents the range between minimum and maximum of the calculations due to the assumption of 10% error of the water constituent concentrations and bottom depth. The error bars of the in-situ measurements are estimated due to multiple exposures at the sampling points.

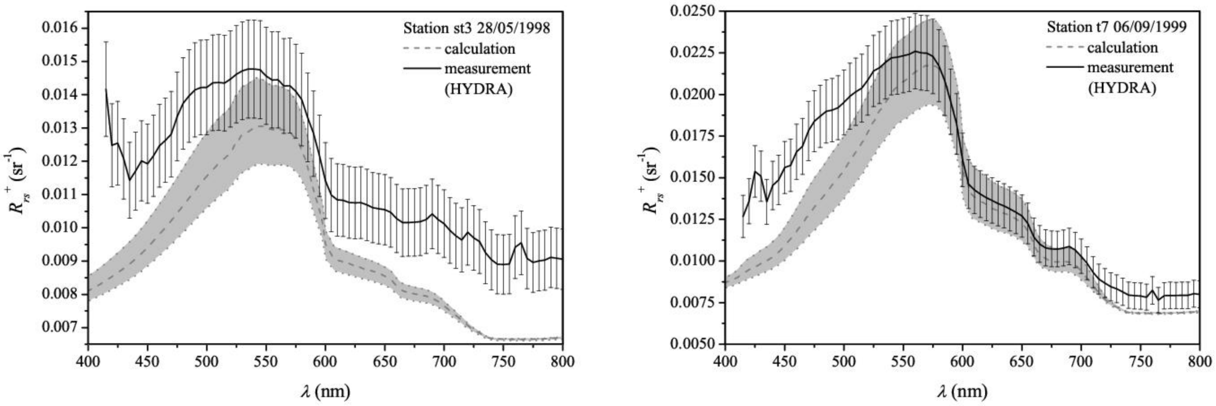

Figure 3.23: Comparison of in-situ measurements and model calculations of remote sensing reflectance above the water surface of Lake Constance. The calculations were made with the water constituent concentrations given in table 3.8 and the subsurface solar zenith angle of 40°. The gray band represents the range between minimum and maximum of the calculations due to the assumption of 10% error of the water constituent concentrations and bottom depth. The error bars of the in-situ measurements are estimated due to multiple exposures at the sampling points.

Chapter 4

Inversion

Analytical equations of the irradiance and remote sensing reflectance, R and R_{rs}, were developed in chapter 3 for deep and shallow water depending on the absorption a, backscattering b_b, surface wind speed u, subsurface solar zenith angle θ_s, subsurface viewing angle θ_v, and the bottom albedo R_B at depth z_B. The parameterisations were the result of simulations of the underwater light field based on the theory of radiative transfer in water described in chapter 2. The following equations were obtained:

$$R = R_\infty \left[1 - A_1 \cdot \mathrm{e}^{-(K_d + K_{u,W}) z_B}\right] + A_2 \cdot R_B \cdot \mathrm{e}^{-(K_d + K_{u,B}) z_B} \tag{4.1}$$

$$R_{rs} = R_{rs,\infty} \left[1 - A_{rs,1} \cdot \mathrm{e}^{-(K_d + k_{u,W}) z_B}\right] + A_{rs,2} \cdot \frac{R_B}{\pi} \cdot \mathrm{e}^{-(K_d + k_{u,B}) z_B} \tag{4.2}$$

with empirical coefficients A_i and $A_{rs,i}$ listed in tables 3.6 and 3.7. The downward and upward diffuse attenuation coefficients K_d, $K_{u,W}$, and $K_{u,B}$ are given in chapter 3.2 by equation (3.13) and (3.14). The attenuation coefficients of the two upwelling radiance components from the water and the bottom are $k_{u,W} = K_{u,W}/\cos\theta_v$ and $k_{u,B} = K_{u,B}/\cos\theta_v$, respectively. $R_\infty = f^\circ \omega_b$ and $R_{rs,\infty} = f^\uparrow \omega_b$ are the irradiance and remote sensing reflectance of infinitely deep water, respectively, with $\omega_b = b_b/(a + b_b)$. The f-factors are given by

$$f^\circ = p_1 \cdot \left(1 + p_2 \cdot \omega_b + p_3 \cdot \omega_b^2 + p_4 \cdot \omega_b^3\right) \cdot \left(1 + p_5 \cdot \frac{1}{\cos\theta_s}\right) \cdot (1 + p_6 \cdot u) \tag{4.3}$$

$$\begin{aligned} f^\uparrow = {} & p_{rs,1} \cdot \left(1 + p_{rs,2} \cdot \omega_b + p_{rs,3} \cdot \omega_b^2 + p_{rs,4} \cdot \omega_b^3\right) \\ & \cdot \left(1 + p_{rs,5} \cdot \frac{1}{\cos\theta_s}\right) \cdot (1 + p_{rs,6} \cdot u) \cdot \left(1 + p_{rs,7} \cdot \frac{1}{\cos\theta_v}\right) \end{aligned} \tag{4.4}$$

The values of the empirical coefficients p_i and $p_{rs,i}$ are listed in tables 3.4 and 3.5 of chapter 3.2. These analytical equations build the basis of the inversion. Inverse modeling is the determination of parameters for a given irradiance reflectance or remote sensing reflectance spectrum. The number of parameters, which are estimated by inversion and called fit parameters in the following, depends on the pre-knowledge about the situation. In the case of shallow water, the determinable parameters are the concentrations of the water constituents phytoplankton, suspended matter, and gelbstoff as well as the bottom depth and the bottom albedo. The technique of getting the unknown parameters for a spectrum is described in the following.

4.1 Curve fitting and search algorithm

The fit parameters are determined iteratively using the method of nonlinear curve fitting. In the first iteration, a model spectrum is calculated using initial values for the fit parameters. This model spectrum is compared with the input spectrum from a measurement or simulation by calculating the residuum as a measure of correspondence. The residuum Δ is calculated as

$$\Delta = \frac{1}{N_\lambda} \sum_{i=1}^{N_\lambda} g_i \cdot \mid X_{0,i} - X_i \mid^2 \tag{4.5}$$

with the number of spectral channels N_λ, the input values $X_{0,i}$, and the fitted values X_i of the spectrum of irradiance or remote sensing reflectance. g_i is the weighing factor of a spectral channel. The classical least square fit is given for $g_i = 1$ at all wavelengths. Then, in the further iterations, the values of the fit parameters are altered, resulting in altered model curves and altered residuals. The procedure is stopped after the best fit between calculated and measured spectrum has been found, which corresponds to the minimum residuum. The values that were used in the step with the smallest residuum are the results.

Since there exists an infinite number of possible parameter combinations, an effective algorithm of the iteration process has to be used to select a new set of parameter values from the previous set. Here, the Simplex algorithm is used (Nelder and Mead, 1965; Caceci and Cacheris, 1984), which is included in the software tool WASI developed by P. Gege[1]. A description of WASI is given by Gege (2001; 2004) and in appendix B. It has two advantages compared to other customary algorithms like Newton-Ralphson and Levenberg-Marquardt: it always converges, and it is fast since no matrix operations are required. The Simplex algorithm can be described as follows. A virtual space of $M+1$ dimensions is constructed, where M dimensions represent the M fit parameters, and one dimension the residuum. Each model curve corresponds to one point in that space. The set of all possible model curves obtained by all combinations of parameter values forms an M dimensional surface. That point on the surface where the residuum is minimal represents the solution of the fit problem. The Simplex can be compared to a spider which crawls on the surface searching for the minimum. It consists of $M+1$ legs, where each leg (vertex) represents a model curve that has already been calculated. The decision regarding which set of parameter values is chosen in the next step (i.e. where the Simplex moves to) is made according to a strategy that is explained using figure 4.1. The triangle WBO represents the Simplex. W corresponds to the worst residuum, B to the best, and O to all others. Four new positions in the next step are considered:

1. Reflection of W at the line OB so that RBO is the new Simplex.
2. Contraction towards this line so that CBO is the new Simplex.
3. Expansion beyond this line to the point E.

---

[1] DLR German Aerospace Center, Remote Sensing Technology Institute, Marine Remote Sensing, Muenchener Str. 20, 82234 Wessling, Germany, `mailto:peter.gege@dlr.de`

4. Shrinkage parallel to the line WO so that SBS' is the new Simplex.

Not all of these positions are always calculated. They are tested in this order, and the first position is taken where the new vertex is better than W. Usually the Simplex is trapped in a minimum after less than $20 \cdot M^2$ iterations (Caceci and Cacheris, 1984). However, if the surface contains local minima, the Simplex may be captured in one of these. In such cases it is important to start the search at a point not too far away from the global minimum. The methodology of the determination of suitable start values is explained next.

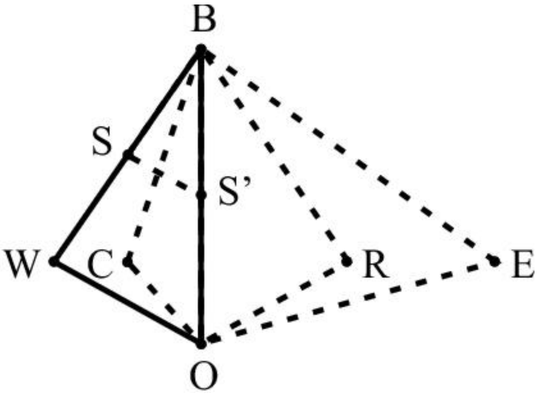

Figure 4.1: The Simplex and its potential contours in the next step after Caceci and Cacheris (1984).

4.2 Determination of initial values

Before the main inversion starts it is necessary to estimate initial values of the unknown parameters. The strategy of finding initial values as accurate as possible is very important for the success of finding the best fit of the input spectra. The following sections explain the determination of the initial values of the bottom depth z_B, the concentration of suspended matter C_X and phytoplankton C_P, and the absorption of Gelbstoff $a_Y(\lambda_0)$ at $\lambda_0 = 440$ nm.

The fastest estimation is realised by using analytical equations. These are obtained by solving the expressions of the irradiance and remote sensing reflectance for the desired parameter. Due to the structure of the equations (4.1) to (4.4) this is only possible using approximations and special wavelengths. The methodology is developed in the following.

A general difficulty is the parameterisation of the f-factors of equation (4.3) and (4.4). They include implicitly the concentrations of the water constituents through the absorption and backscattering coefficients. Thus, the f-factors depend on wavelength. To solve the irradiance and remote sensing reflectance equations for absorption or backscattering a wavelength is chosen, where the f-factors are relatively constant over a wide range of water constituent concentrations. Figure 4.2 shows the variability of the f-factors from 400 to 800 nm for different concentrations of suspended matter and over the range of the concentration of phytoplankton and the absorption of gelbstoff listed in table 4.1. The subsurface solar zenith angle was 30°

and the subsurface viewing angle was zero for $f^{\uparrow}$. The influence of the wind speed was ignored, $u = 0$. The curves show clearly the strong influence of absorption by phytoplankton and gelbstoff in the blue and green below 600 nm. In this spectral region the f-factors vary about 5% for low concentration of suspended matter and more than 12% for concentrations greater than 10 mg/l. Due to the decreasing influence of the absorption of phytoplankton and gelbstoff the variability of f° and $f^{\uparrow}$ decreases to about 3% for wavelengths of 600 nm and larger and is near zero from 700 nm onwards. Thus, the wavelength interval from 600 to 700 nm can be used for inversion with little restriction. The f-factors do not vary between 700 and 800 nm and are nearly constant from 750 to 800 nm for a fixed concentration of suspended matter. This spectral region provides the best choice of determining parameters linked to backscattering (Babin and Stramski, 2002).

C_P (μg/l)	0.50	1.53	2.55	3.58	4.61	5.63	6.66	7.68	8.71	9.73
	10.76	11.79	12.82	13.84	14.87	15.89	16.92	17.95	18.97	20.00
C_X (mg/l)	0.50	1.56	2.61	3.67	4.72	5.78	6.83	7.89	8.94	10.00
$a_Y(\lambda_0)$ (m^{-1})	0.10	1.08	2.06	3.04	4.02	5.00				

Table 4.1: Variation of the concentrations of the water constituents for initial values estimation.

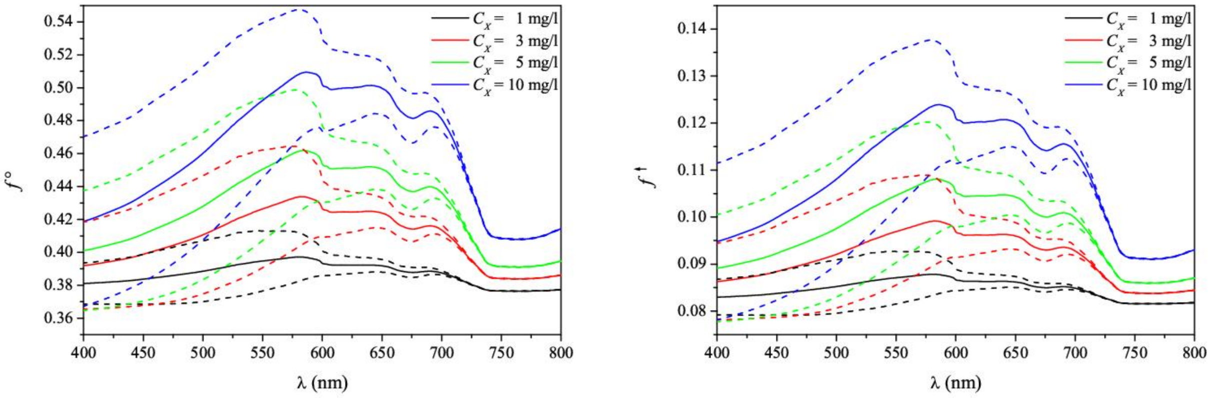

Figure 4.2: Variability of the factors f° (left) and $f^{\uparrow}$ (right). Solid lines represent the average values for the given concentration of suspended matter and all concentrations of phytoplankton and gelbstoff listed in table 4.1. The dashed lines are the mean plus and minus one standard deviation.

4.2.1 Bottom depth

Analytical equations of the bottom depth z_B can be determined from equations (4.1) and (4.2), if no distinction is made between the up- and downward attenuation coefficients. Setting the upward diffuse attenuation coefficients, $K_{u,W}$ and $K_{u,B}$, equal to the downward diffuse attenuation K_d results in an underestimation of the reflectances of about 15% according to Maritorena et al. (1994) for natural waters. But for the estimation of the initial value of the bottem depth, this error is acceptable. Hence, the irradiance and remote sensing reflectance are approximated by

$$\begin{aligned} R &= R_\infty \left[1 - A_1 \cdot \mathrm{e}^{-2K_d z_B}\right] + A_2 \cdot R_B \cdot \mathrm{e}^{-2K_d z_B} && (4.6) \\ R_{rs} &= R_{rs,\infty} \left[1 - A_{rs,1} \cdot \mathrm{e}^{-K_d(1+1/\cos\theta_v) z_B}\right] + A_{rs,2} \cdot \frac{R_B}{\pi} \cdot \mathrm{e}^{-K_d(1+1/\cos\theta_v) z_B} && (4.7) \end{aligned}$$

Like for example shown by Lyzenga (1978), Ohde and Siegel (2001), and Lafon et al. (2002), solving these equations for the bottom depth results in

$$\begin{aligned} z_B &= \frac{1}{2K_d} \cdot \ln\left(\frac{A_1 \cdot R_\infty - A_2 \cdot R_B}{R_\infty - R}\right) && (4.8) \\ z_B &= \frac{1}{K_d\left(1 + \frac{1}{\cos\theta_v}\right)} \cdot \ln\left(\frac{A_{rs,1} \cdot R_{rs,\infty} - A_{rs,2} \cdot \frac{R_B}{\pi}}{R_{rs,\infty} - R_{rs}}\right) && (4.9) \end{aligned}$$

For depths of 1, 3, 6, and 10 m the bottom depth is estimated using these equations for varying concentrations of the water constituents listed in table 4.1. The bottom types of sediment and macrophytes are used and are known during the calculations (see figure 3.5). The results between 400 and 800 nm are shown in figure 4.3. The curves show that the bottom depth is estimated with little error between 600 and 700 nm. Below 600 nm the high absorption of phytoplankton and gelbstoff causes very large errors. For bottom depths lower than 4 m also the wavelenths above 700 nm can be used. But if the bottom depth increases the increasing absorption of the water restricts the estimation to wavelengths below 650 nm, especially for $z_B > 10$ m (not shown). Thus, a wavelength interval is chosen to calculate the initial value of the bottom depth between 600 and 650 nm.

The accuracy of the initial value determination is shown for the irradiance reflectance in figure 4.4 and for the remote sensing reflectance in figure 4.5. The relative error of the bottom depth $\delta_z = \frac{z_B - z_{B,0}}{z_{B,0}}$ is estimated for the bottom types sediment and macrophytes varying either the concentration of phytoplankton, suspended matter, or the absorption of gelbstoff. The sun angle and the viewing angle was fixed at 30° and 0°, respectively. If the concentration is not varied, $C_P = 2\ \mu$g/l, $C_X = 2$ mg/l, and $a_Y(440\mathrm{nm}) = 0.3\ \mathrm{m}^{-1}$. The bottom depth was derived as average between 610 and 650 nm.

The impact of phytoplankton and gelbstoff is low. Up to a depth of 15 m the relative error is below 20%. The error is increasing with increasing concentration. For a greater bottom depth the relative error increases rapidly to 60% and more for R and more than 100% for R_{rs} due to the increasing absorption, which makes it impossible to detect the bottom characteristics optically

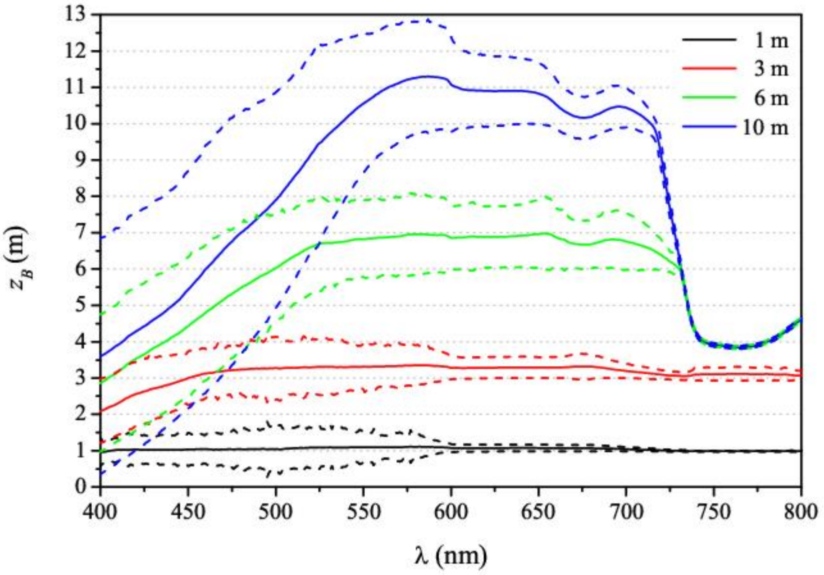

Figure 4.3: Bottom depth estimated by equations (4.8) and (4.9) for varying concentrations of water constituents as listed in table 4.1 above sediment and macrophytes, whose bottom albedos are known during the calculations. Solid lines: mean, dashed lines: intervals given by the standard deviation.

at the surface. The pink areas in the figures are due to the numerical problem of dividing very small numbers, which occur especially for the remote sensing reflectance in equation (4.9). This effect causes also the slight improve of the relative error of z_B in the top left graph of figure 4.4 before the relative error increases rapidly for increasing suspended matter concentration. The largest influence arises from suspended matter. Generally, the higher the concentration, the higher the relative error δ_z, which increases additionally with increasing bottom depth. For a bottom depth up to 10 m the relative error δ_z is 20 to 40% for $C_X < 10$ mg/l and 60% and more for higher concentrations. The relative error of the bottom depth is lower over macrophytes compared to the bottom type sediment. This is due to the used bottom albedo spectra here: the reflectance of sediment is lower than the reflectance of macrophytes. Thus, the detection of the darker bottom causes greater errors.

The figures 4.6 and 4.7 show the relative error of the initial value for z_B ranging from 0.1 to 50.0 m depending on the relative error of the phytoplankton and suspended matter concentration and the gelbstoff absorption. The relative error δ_z is below 40% for $z_B < 4$ m, except for a high underestimation of the concentrations of more than 80%. For larger bottom depths the relative error of the initial value is 40 to 100% and sometimes more. If the phytoplankton concentration and gelbstoff absorption are overestimated, the bottom depth is underestimated. The influence of a wrong suspended matter concentration is the opposite way around: if the concentration is underestimated, the bottom depth is underestimated.

The influence of the relative error of the bottom albedo is shown in figure 4.8. The calculations were made with a spectrally constant bottom albedo of 0.1 for the forward calculations. For a bottom depth greater than 15 m the relative error δ_z is higher than 60%. Underestimation of the bottom albedo does not affect the relative error δ_z as high as overestimation. More than 10% error of the bottom reflectance results in a relative error of the initial bottom depth of 100% and more for $z_B < 10$ m. The reason that an overestimation of the bottom albedo causes a higher error is due to the non-linear influence of the bottom reflectance on the estimation of the bottom depth in equations (4.8) and (4.9). The subtraction of an overestimated bottom albedo results in a very small or even negative value. Thus, the logarithm of this value is negative or not defined and a wrong bottom depth is calculated.
The method of the initial value determination of z_B works well with an acceptable error especially for a bottom depth lower than 10 m. For increasing bottom depth the increasing attenuation of the water body reduces the possibility of detecting bottom depth and therefore bottom type as well.

4.2.2 Concentration of suspended matter

The initial value of the concentration of suspended matter can be also estimated analytically. As already done before for the bottom depth, the analytical equations (4.1) and (4.2) must be simplified to the equations (4.6) and (4.7). As shown in figure 4.2 the f-factors vary only slightly for wavelengths above 750 nm. This is due to the negligible absorption of phytoplankton and gelbstoff in the near infrared, where the total absorption is given by the absorption of water: $a = a_W$. At wavelengths above 750 nm the relative error of f° and $f^\uparrow$ by neglecting the absorption of phytoplankton and gelbstoff is about 1% and lower. Additionally, the absolute value of backscattering b_b is very low in comparison to the total absorption at this wavelength due to high absorption of pure water: $b_b \ll a$. Thus, f° and $f^\uparrow$ are treated as constants estimated using $\omega_b = \frac{\frac{1}{2}b_W}{a_W+\frac{1}{2}b_W}$. Regarding the developments of equation (3.13) in chapter 3.2 the downward diffuse attenuation coefficient K_d is approximated by

$$K_d = \kappa_0 \frac{a_W + \frac{1}{2}b_W}{\cos\theta_s} \tag{4.10}$$

Thus, the equations (4.6) and (4.7) are now

$$\begin{aligned} R &= f^\circ \frac{b_b}{a+b_b}\left[1 - A_1 \cdot \mathrm{e}^{-2K_d z_B}\right] + A_2 \cdot R_B \cdot \mathrm{e}^{-2K_d z_B} && (4.11) \\ R_{rs} &= f^\uparrow \frac{b_b}{a+b_b}\left[1 - A_{rs,1} \cdot \mathrm{e}^{-K_d(1+1/\cos\theta_v)z_B}\right] + A_{rs,2} \cdot \frac{R_B}{\pi} \cdot \mathrm{e}^{-K_d(1+1/\cos\theta_v)z_B} && (4.12) \end{aligned}$$

These equations can be solved analytically for the unknown concentration of suspended matter $C_X = \frac{b_b - \frac{1}{2}b_W}{b^*_{b,X}}$, if the bottom depth z_B is known or initially estimated as described above. The following relations of C_X are derived from the equations (4.11) and (4.12):

$$C_X = \frac{\Re^\circ(a_W + \frac{1}{2}b_W) - \frac{1}{2}b_W}{b^*_{b,X} \cdot (1 - \Re^\circ)} \tag{4.13}$$

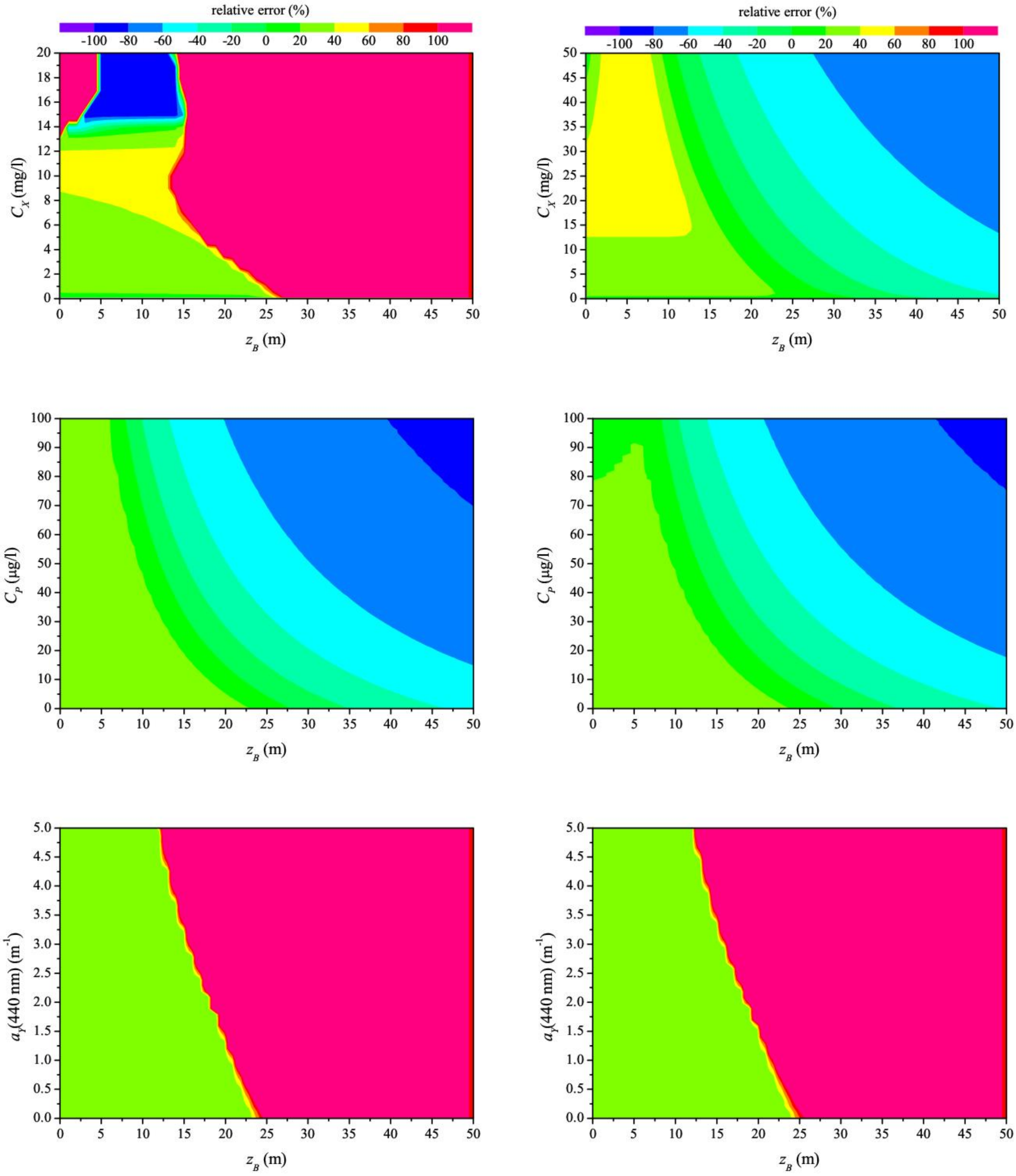

Figure 4.4: Relative error of the estimated bottom depth from equation (4.8) for varying concentrations of water constituents and different bottom types; left graphs are for sediment and right ones for macrophytes. If the concentrations are not varied, $C_P = 2$ μg/l, $C_X = 2$ mg/l, and $a_Y(440\text{nm}) = 0.3$ m^{-1}. Subsurface solar zenith angle is 30°.

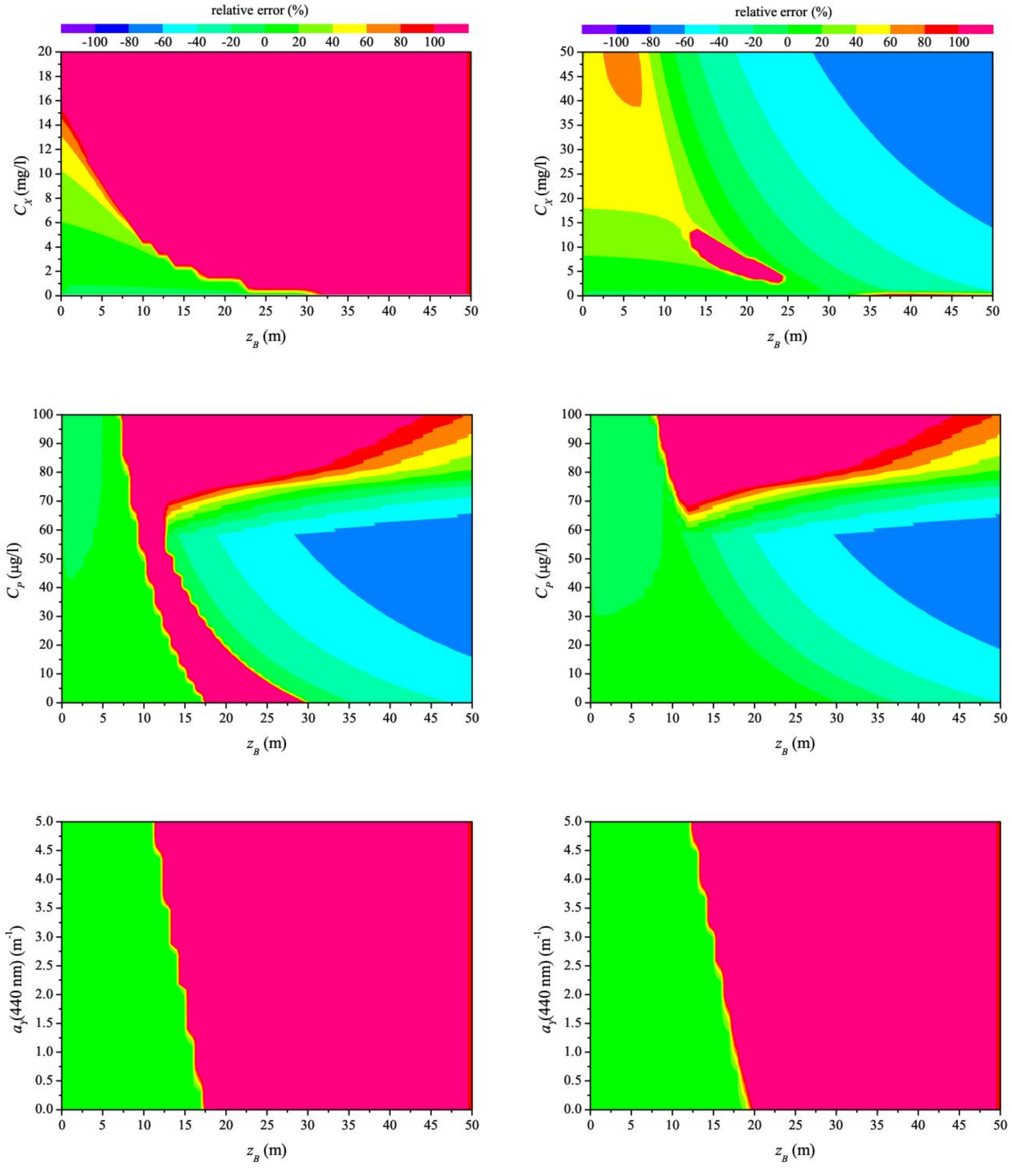

Figure 4.5: Relative error of the estimated bottom depth from equation (4.9) for varying concentrations of water constituents and different bottom types; left graphs are for sediment and right ones for macrophytes. If the concentrations are not varied, $C_P = 2$ μg/l, $C_X = 2$ mg/l, and $a_Y(440\text{nm}) = 0.3$ m^{-1}. Subsurface solar zenith angle is 30° and subsurface viewing angle 0°.

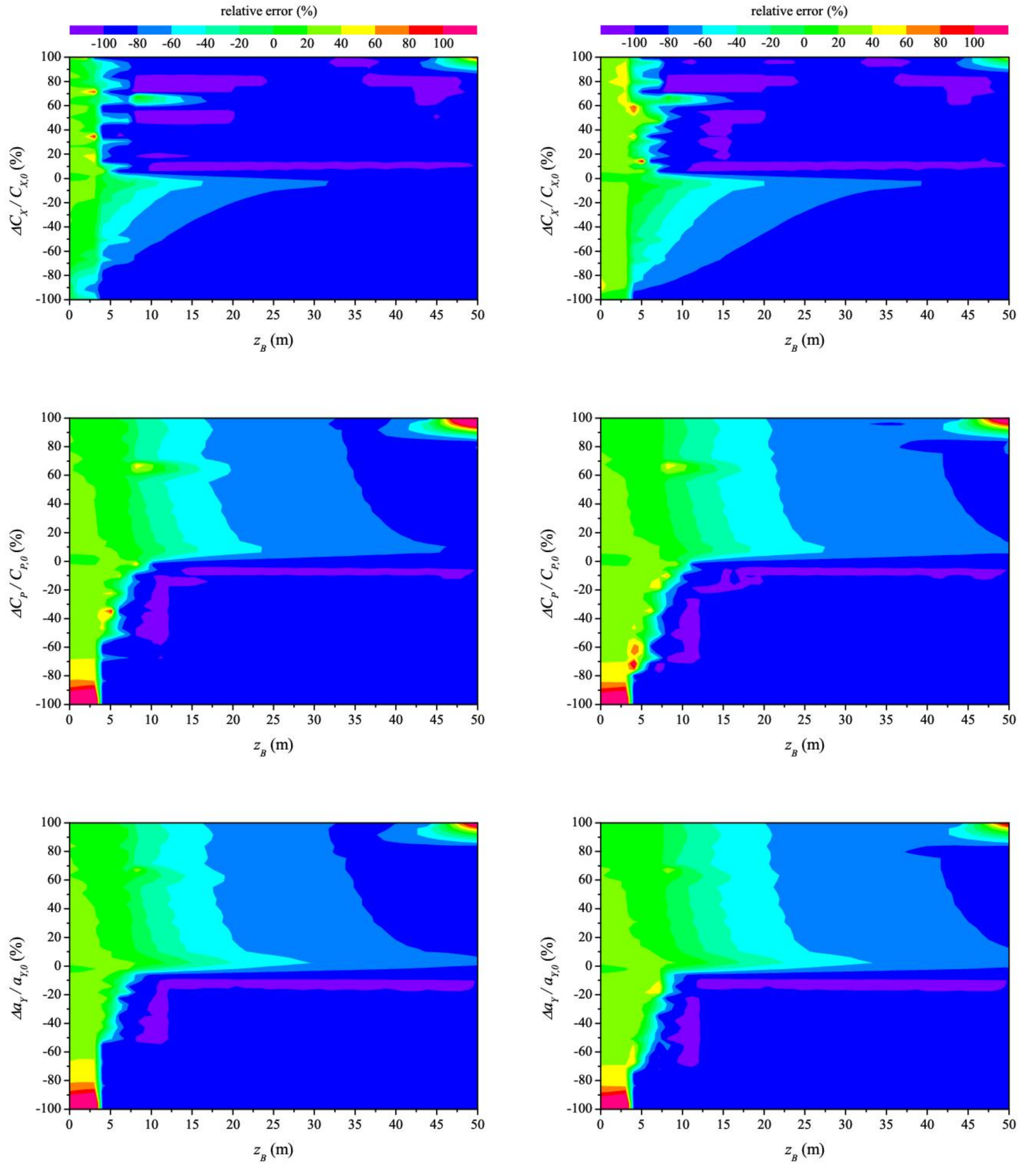

Figure 4.6: Relative error of the estimated bottom depth from equation (4.8) depending on the relative error of the concentrations of water constituents and different bottom types; left graphs are for sediment and right ones for macrophytes. The concentrations are $C_P = 2\ \mu$g/l, $C_X = 2$ mg/l, and $a_Y(440\text{nm}) = 0.3\ \text{m}^{-1}$. Subsurface solar zenith angle is 30°.

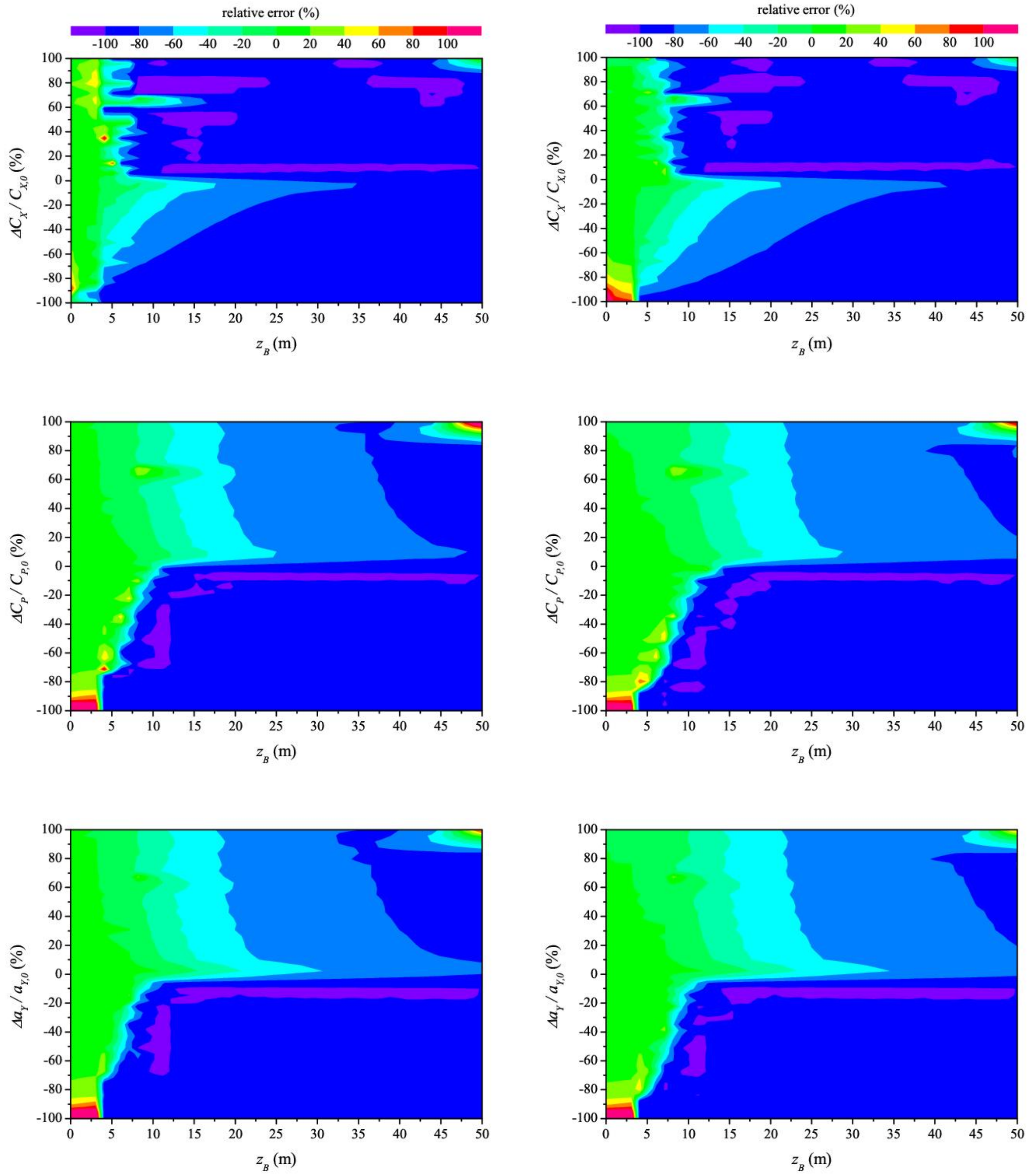

Figure 4.7: Relative error of the estimated bottom depth from equation (4.9) depending on the relative error of the concentrations of water constituents and different bottom types; left graphs are for sediment and right ones for macrophytes. The concentrations are $C_P = 2$ μg/l, $C_X = 2$ mg/l, and $a_Y(440\text{nm}) = 0.3$ m^{-1}. Subsurface solar zenith angle is 30° and subsurface viewing angle 0°.

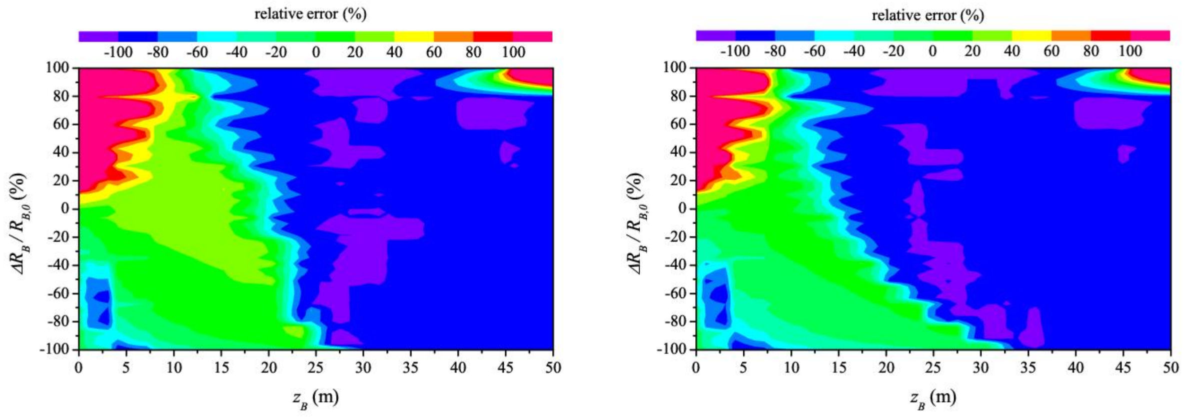

Figure 4.8: Relative error of the estimated bottom depth from equation (4.8) (left) and (4.9) (right) depending on the relative error of bottom albedo. A constant bottom albedo of 0.1 was used for forward calculations. The concentrations are $C_P = 2$ μg/l, $C_X = 2$ mg/l, and $a_Y(440\text{nm}) = 0.3$ m^{-1}. Subsurface solar zenith angle is 30° and subsurface viewing angle 0°.

$$C_X = \frac{\mathfrak{R}^{\uparrow}(a_W + \frac{1}{2}b_W) - \frac{1}{2}b_W}{b^*_{b,X} \cdot (1 - \mathfrak{R}^{\uparrow})} \tag{4.14}$$

with

$$\begin{aligned} \mathfrak{R}^{\circ} &\equiv \frac{R - A_2 \cdot R_B \cdot \exp\{-2K_d z_B\}}{f^{\circ} \cdot (1 - A_1 \cdot \exp\{-2K_d z_B\})} \\ \mathfrak{R}^{\uparrow} &\equiv \frac{R_{rs} - A_{rs,2} \cdot \frac{R_B}{\pi} \cdot \exp\{-K_d(1 + 1/\cos\theta_v)z_B\}}{f^{\uparrow} \cdot (1 - A_{rs,1} \cdot \exp\{-K_d(1 + 1/\cos\theta_v)z_B\})} \end{aligned}$$

Calculations are done with these equations using varying concentrations of the water constituents listed in table 4.1 and different bottom depths of 1, 3, 5, 7, and 9 m. The results are plotted in figure 4.9 for wavelengths from 400 to 800 nm using equation (4.14) for the remote sensing reflectance. The graphs of the equation (4.13) show similar results and are not plotted. For wavelengths below 750 nm the estimation of the concentration of suspended matter is not possible due to the influence of the absorption of phytoplankton and gelbstoff. But above 750 nm the absorption is mainly given by the absorption of the water. The calculations of C_X show a good agreement compared to the real concentration of suspended matter used for the calculated input spectra of R_{rs}. Remaining errors are due to the approximations included in the equations themselves.

The relative error $\delta_X = \frac{C_X - C_{X,0}}{C_{X,0}}$ of the calculated initial values of the suspended matter concentration is shown in the figures 4.10 to 4.11 for C_X from 0.1 to 50.0 mg/l depending on the bottom depth, phytoplankton concentration, gelbstoff absorption, and bottom type. The wavelength for the determination was 760 nm. If the concentration and the bottom depth are not varied, $C_P = 2$ μg/l, $a_Y(440\text{nm}) = 0.3$ m^{-1}, and $z_B = 3$ m. The sun angle and the viewing angle were fixed at 30° and 0°, respectively. Figure 4.10 shows the relative error for calculations using

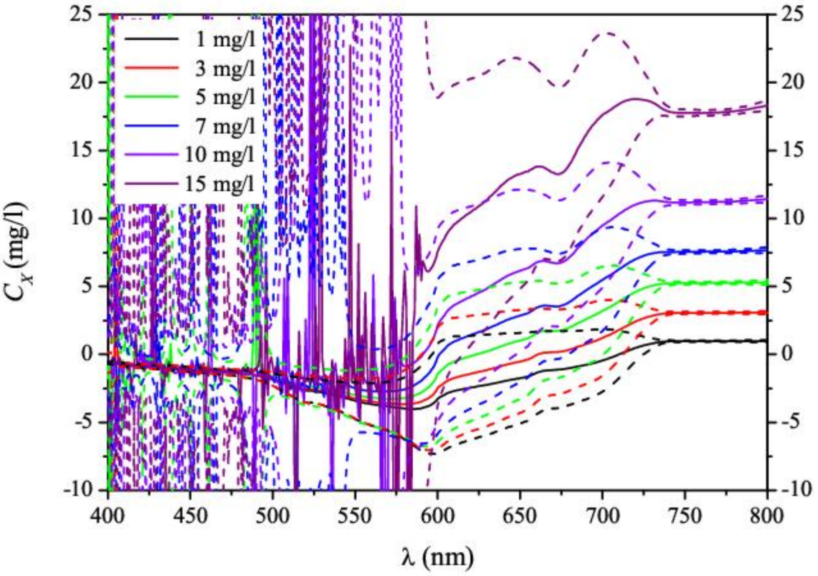

Figure 4.9: Average values of the concentration of suspended matter calculated by equation (4.14) using varying concentrations of phytoplankton and gelbstoff listed in table 4.1 above sediment and macrophytes (solid lines) and the interval given by the standard deviation (dashed lines).

equation (4.13), figure 4.11 using equation (4.14). The relative error is equal for both bottom types, sediment and macrophytes. No dependence on the concentration of phytoplankton was found and only a slight dependence on the gelbstoff absorption. The relative error is below 20% for $C_X \leq 5$ mg/l and increases to 40% at $C_X = 25$ mg/l and more than 60% for $C_X \geq 47$ mg/l. Estimations by equation (4.14) using the remote sensing reflectance result in a little bit higher relative errors: 40% at $C_X = 17$ mg/l, 60% at $C_X = 30$ mg/l, and more than 80% for $C_X \geq 45$ mg/l. The dependence on the bottom depth shows the same results but not for low values of z_B below 2 m. The relative error is constant over the entire range of C_X decreasing from 20% to -40% at a very low bottom depth below 0.5 m.

Figures 4.12 to 4.14 show the dependence of δ_X on the relative error of the bottom depth, phytoplankton concentration, gelbstoff absorption, and bottom albedo. Generally, the same features and the same range of the relative error was obtained as above: no influence of the relative error of phytoplankton concentration; this is also true for the influence of the relative error of z_B, a_Y, and R_B excluding high relative errors of more than 80%, where the relative error of the initial value of C_X increases to more than 100%.

The analysis of the determination of the initial value of C_X shows that C_X can be analytically calculated by the equations (4.13) and (4.14) with sufficient accurracy over a wide range before the main inversion starts using the Simplex algorithm.

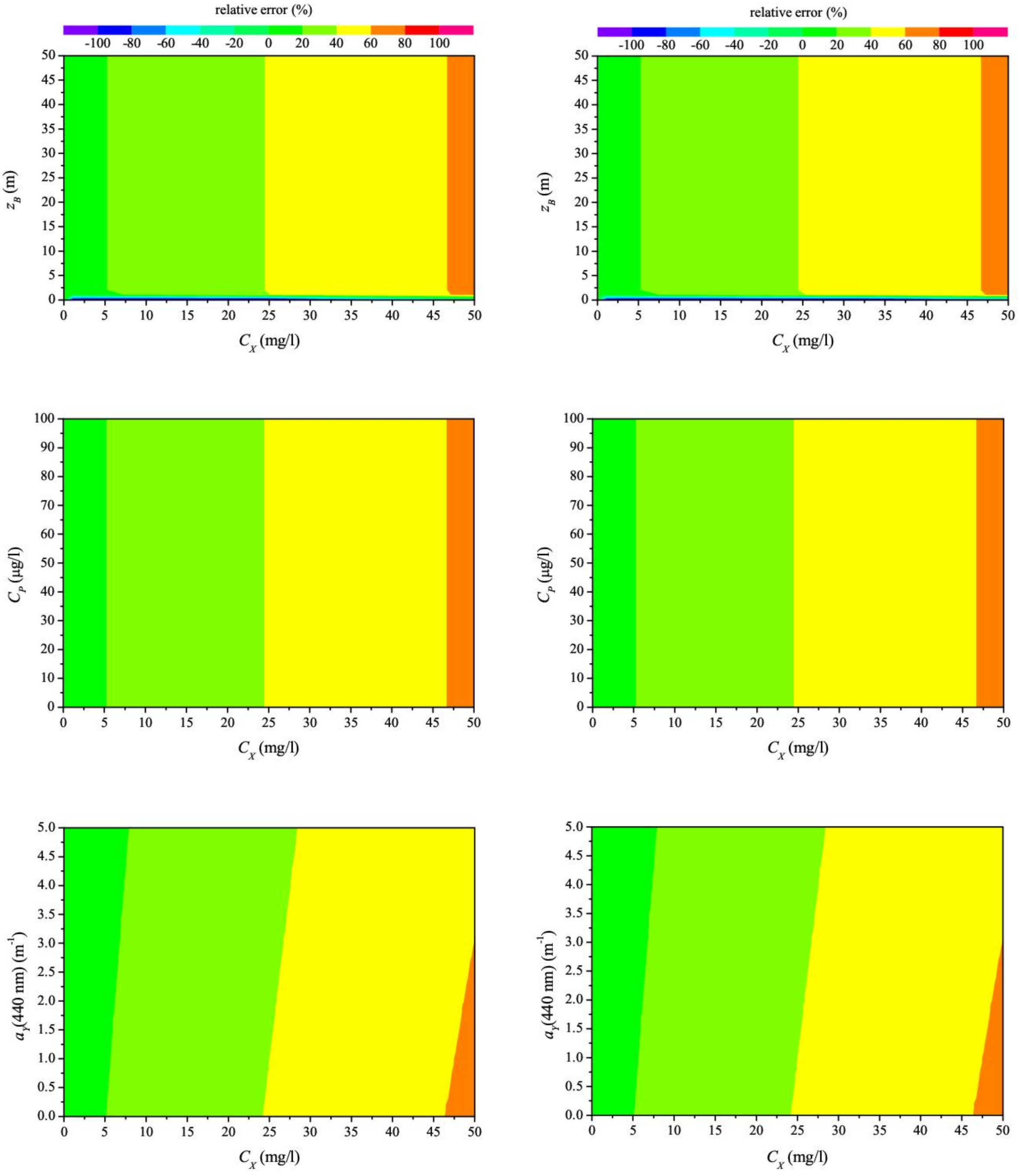

Figure 4.10: Relative error of the estimated concentration of suspended matter from equation (4.13) for varying concentrations of water constituents and different bottom types; left graphs are for sediment and right ones for macrophytes. If the concentrations are not varied, $C_P = 2$ μg/l and $a_Y(440\text{nm}) = 0.3$ m^{-1}. Subsurface solar zenith angle is 30° and $z_B = 3$ m.

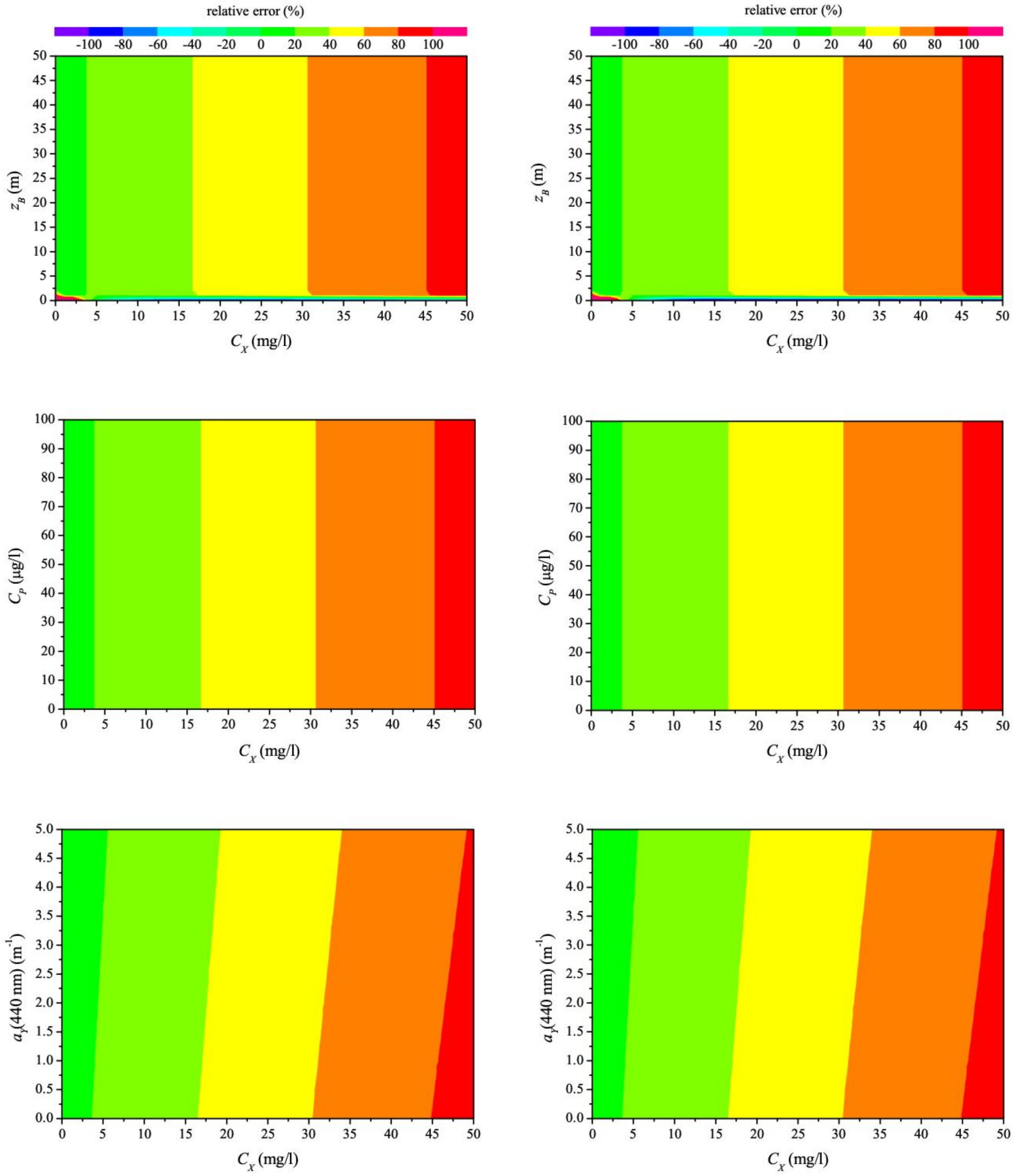

Figure 4.11: Relative error of the estimated concentration of suspended matter from equation (4.14) for varying concentrations of water constituents and different bottom types; left graphs are for sediment and right ones for macrophytes. If the concentrations are not varied, $C_P = 2$ µg/l and a_Y(440nm) $= 0.3$ m^{-1}. Subsurface solar zenith angle is 30° and subsurface viewing angle 0°. The bottom depth is 3 m.

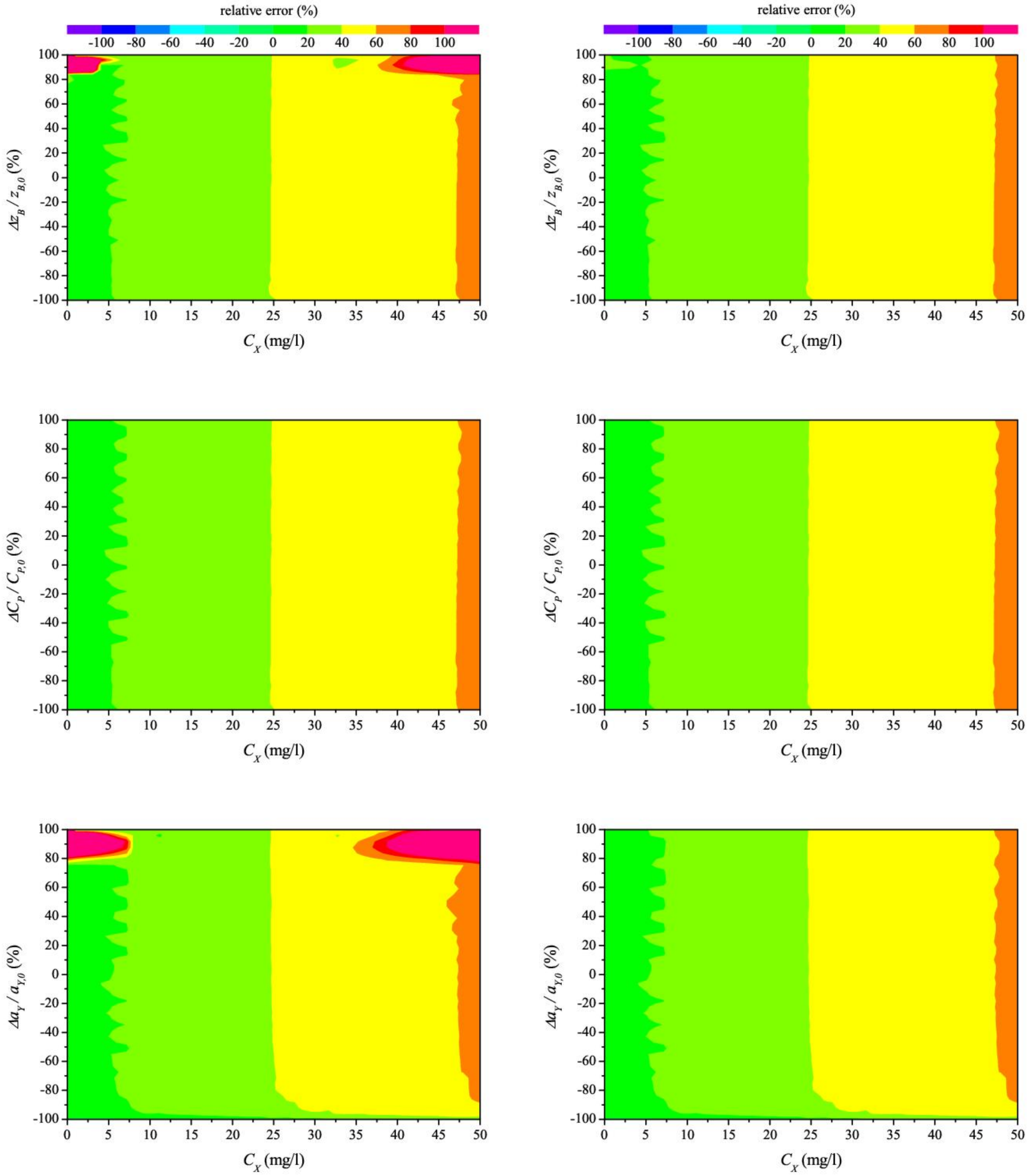

Figure 4.12: Relative error of the estimated concentration of suspended matter from equation (4.13) depending on the relative error of the concentrations of water constituents, bottom depth, and different bottom types; left graphs are for sediment and right ones for macrophytes. The concentrations are $C_P = 2\ \mu$g/l and $a_Y(440\text{nm}) = 0.3\ \text{m}^{-1}$. Subsurface solar zenith angle is 30° and $z_B = 3$ m.

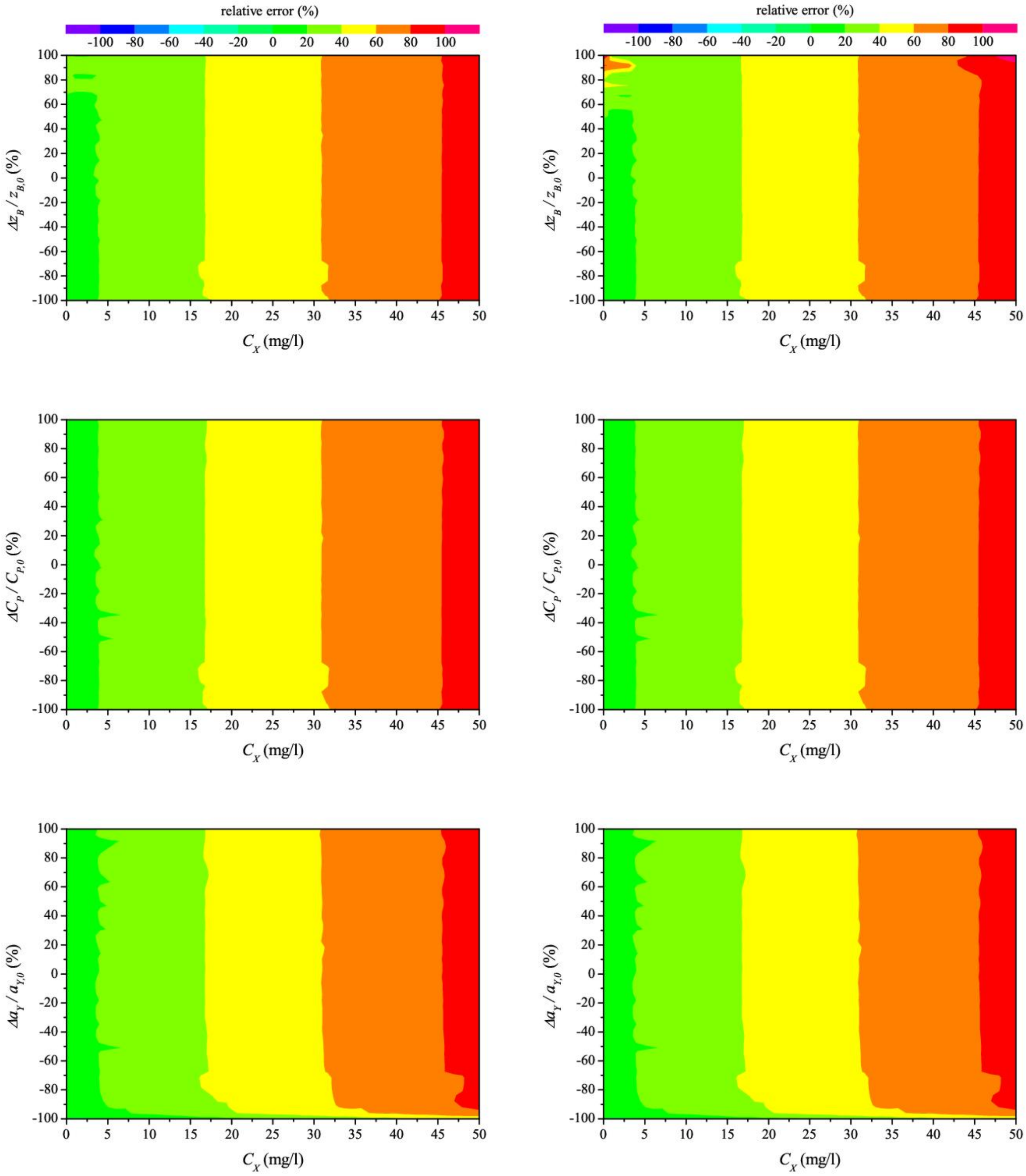

Figure 4.13: Relative error of the estimated concentration of suspended matter from equation (4.14) depending on the relative error of the concentrations of water constituents, bottom depth, and different bottom types; left graphs are for sediment and right ones for macrophytes. The concentrations are $C_P = 2$ μg/l and $a_Y(440\text{nm}) = 0.3$ m^{-1}. Subsurface solar zenith angle is 30° and subsurface viewing angle 0°. The bottom depth is 3 m.

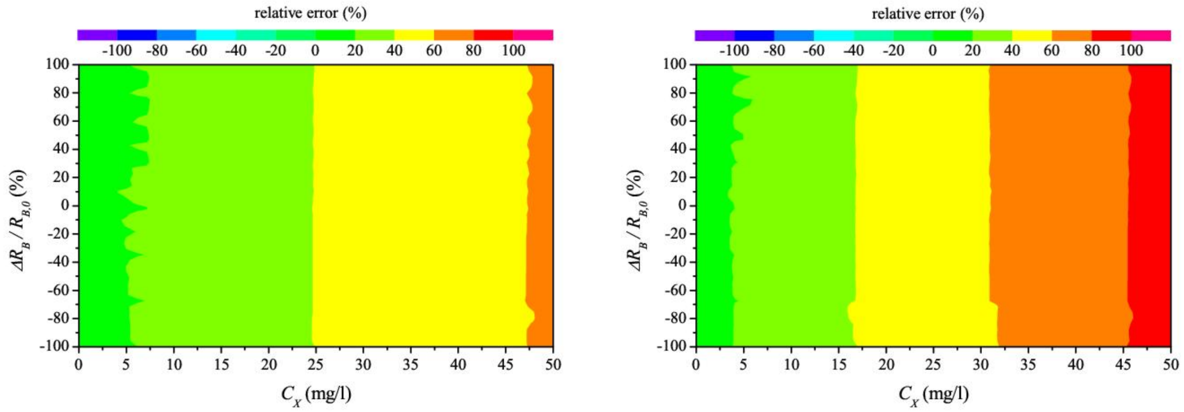

Figure 4.14: Relative error of the estimated concentration of suspended matter from equation (4.13) (left) and (4.14) (right) depending on the relative error of the bottom albedo. A constant bottom albedo of 0.1 was used for forward calculations. The concentrations are $C_P = 2\ \mu$g/l and $a_Y(440\text{nm}) = 0.3\ \text{m}^{-1}$. Subsurface solar zenith angle is 30° and subsurface viewing angle 0°. The bottom depth is 3 m.

4.2.3 Concentration of phytoplankton and absorption of gelbstoff

Considering the results of the initial values of the bottom depth z_B and the concentration of suspended matter C_X the next step is to determine initial values of the concentration of phytoplankton C_P and absorption of Gelbstoff $a_Y(\lambda_0)$, $\lambda_0 = 440$ nm. The problem of the determination of the total absorption $a(\lambda)$ is that the equations (4.1) and (4.2) can not be solved analytically for the absorption of phytoplankton and gelbstoff.

To solve this problem the sum of the absorption of phytoplankton and gelbstoff is defined as

$$\mathfrak{A}(\lambda) \equiv a_P^*(\lambda) \cdot C_P + a_Y(\lambda_0) \cdot \mathrm{e}^{-s_Y(\lambda-\lambda_0)} \tag{4.15}$$

The total absorption is therefore given by $a(\lambda) = a_W(\lambda) + \mathfrak{A}(\lambda)$. By means of the technique of nested intervals it is now possible to find the absorption over the entire spectrum by varying $\mathfrak{A}(\lambda)$ in the equations (4.1) and (4.2) until the value of the relative error $|\delta|$ between the input value of the irradiance and remote sensing reflectance and the estimated one is below a threshold. The iteration starts at $i = 0$ and ends at i_{end}, if the threshold is reached, or at i_{max}. The determination of the $(i{+}1)^{\text{th}}$ value of $\mathfrak{A}$ follows the rules:

$$\mathfrak{A}_{i+1} = \begin{cases} \mathfrak{A}_i + \frac{\Delta}{i} & \text{, if} \quad \delta < 0 \\ \mathfrak{A}_i - \frac{\Delta}{i} & \text{, if} \quad \delta > 0 \end{cases} \tag{4.16}$$

where Δ is the step from i to $i{+}1$. A starting value $\mathfrak{A}_0 = 5\ \text{m}^{-1}$ and a step $\Delta = 1\ \text{m}^{-1}$ is chosen to represent the range of the absorption and to converge before the maximum value of iterations $i_{max} = 100$ is reached. The threshold of $|\delta|$ is set to 0.01. The scheme of figure 4.15 shows the steps of equation (4.16) for four different values of $\mathfrak{A}(\lambda)$.

After the spectrum $\mathfrak{A}(\lambda)$ is determined by nested intervals, the concentration of phytoplankton C_P and the absorption of gelbstoff $a_Y(\lambda_0)$, $\lambda_0 = 440$ nm, are estimated using the Simplex algorithm by fitting the absorption spectra from 400 to 800 nm. The wavelength interval is 5 nm and a maximum number of 10 iterations of the Simplex is chosen, which was found to be sufficient to calculate the initial values of the concentration of phytoplankton and the absorption of gelbstoff.

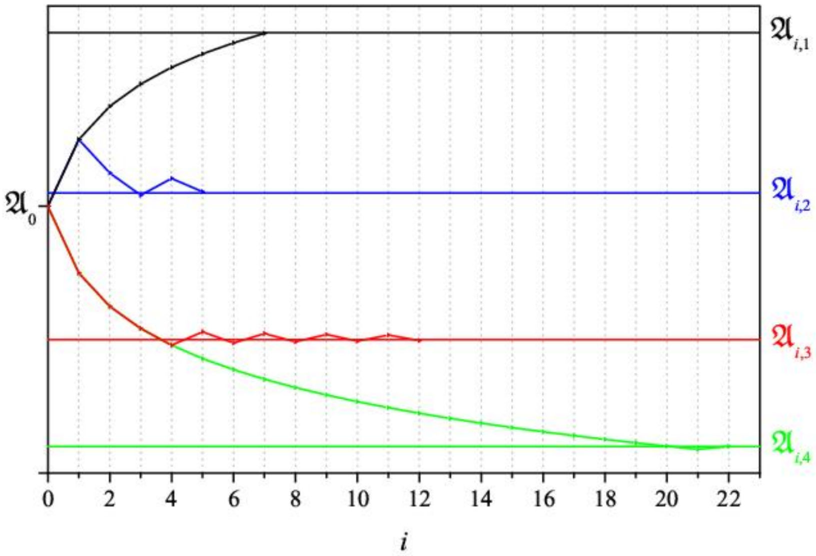

Figure 4.15: Example of the steps of the technique of nested intervals used for the estimation of the absorption of phytoplankton and gelbstoff for four different values (relative units).

This method of determination for the initial values of the phytoplankton concentration and the gelbstoff absorption at 440 nm is very efficient. The investigated range is 0.1 to 100.0 μg/l for C_P and 0.01 to 5.0 m^{-1} for $a_Y(\lambda_0)$, $\lambda_0 = 440$ nm. The relative error $\delta_P = \frac{C_P - C_{P,0}}{C_{P,0}}$ of the initial value of C_P varies for the entire range of $0.1 \leq C_P \leq 100$ μg/l around zero and increases only to about 20% for very low concentrations near 0.1 μg/l. This is true for all varying water constituent concentrations, bottom depths, and bottom types. The same is valid for the relative error $\delta_Y = \frac{a_Y - a_{Y,0}}{a_{Y,0}}$ of the initial value of $a_Y(\lambda_0)$.

The influence of the relative errors of the characteristics of the water body on the accuracy of phytoplankton concentration is shown in the figures 4.16, 4.17, and 4.20. The bottom affects the phytoplankton concentration most for $C_P < 10$ μg/l. An overestimation of z_B results in an underestimation of C_P of -80% and even more. If the bottom depth is underestimated, C_P is overestimated by more than 100%. For increasing phytoplankton concentrations the influence of a wrong bottom depth is decreasing due to the increasing optical thickness. The reverse effect can be seen for the relative error of the bottom albedo. The influence of the relative error of C_X is very strong for $C_P < 10$ μg/l. Only errors below 20% result in an error in C_P of less than

100%, whereby an overestimation of C_X yields an overestimation of C_P, and an underestimation of C_X results in an underestimation of C_P. The effect decreases for higher concentrations of C_P. For $C_P > 20$ μg/l a relative error of 20% in C_X yields about 20% relative error of C_P and 40% relative error of C_X causes a relative error of 50 to 60% in C_P. The error of gelbstoff absorption affects the accuracy of the initial value of C_P most. Below 15 μg/l of C_P even an error of 20% causes a error of C_P of more than 100%. An underestimation of gelbstoff absorption results in an overestimation of phytoplankton concentration. Overestimation of a_Y of about 20% causes an underestimation of C_P of 40 to 50%. The influence of a_Y on C_P decreases with increasing concentration of phytoplankton. The absolute relative error of C_P is about 20% for $C_P > 30$ μg/l and a relative error of 50% in a_Y.

The figures 4.18, 4.19, and 4.21 show the relative error of the initial value of $a_Y(\lambda_0)$. The influence of the error of z_B, C_X, and R_B has the same features as recognised for the phytoplankton concentration, but with lower intensity. The influence of the error of z_B and R_B is higher for macrophytes at the bottom than for sediment due to the spectral shape of the macrophyte albedo, which has an higher impact in the blue wavelengths. The relative error of a_Y is 100% and higher, if the phytoplankton concentration is underestimated by more than 30% and $a_Y(\lambda_0) < 0.75$ m^{-1}. Overestimation of C_P has only a weak impact on the accuracy of $a_Y(\lambda_0)$ below 1.0 m^{-1}.

As already found for the initial values of z_B and C_X, the initial values of C_P and $a_Y(\lambda_0)$ can also be derived by the above described technique with a sufficient accuracy before starting the main inversion.

4.2.4 Areal fraction of bottom albedo

Before the main inversion of the Simplex algorithm starts, the user has to select n bottom types in the sensor's field of view. The i^{th} fraction of the bottom albedo $f_{a,i}$ is equal to the percentage coverage of this bottom type for the observed area. If there is no knowledge about the distribution of the bottom types, the user can select to fit the areal fraction of each bottom type. Up to six bottom types can be fitted simultaneously. The initial values of $f_{a,i}$, $1 \leq i \leq n$, are assigned using the following rule:

$$f_{a,i} = \frac{1}{n} \tag{4.17}$$

Thus, the sum of all fractions is one and it is assumed that all bottom types are equally represented. As the experiences from fitting show, this method of assigning the start values of $f_{a,i}$ is sufficient.

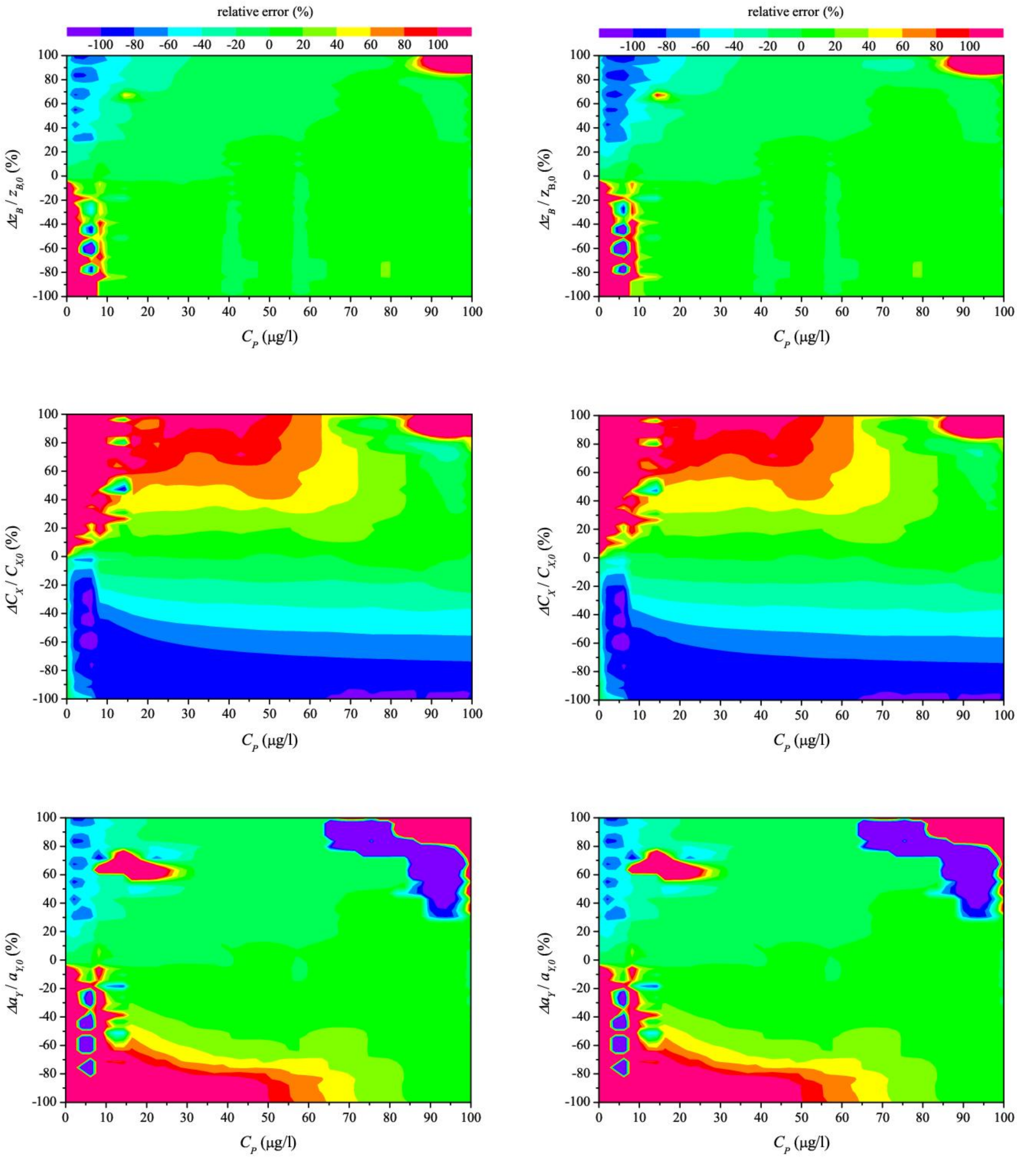

Figure 4.16: Relative error of the estimated concentration of phytoplankton for irradiance reflectance using nested intervals of equation (4.16) and the Simplex algorithm depending on the relative error of the concentrations of water constituents, bottom depth, and different bottom types; left graphs are for sediment and right ones for macrophytes. The concentrations are $C_X = 2$ mg/l and $a_Y(440\text{nm}) = 0.3$ m^{-1}. Subsurface solar zenith angle is 30° and $z_B = 3$ m.

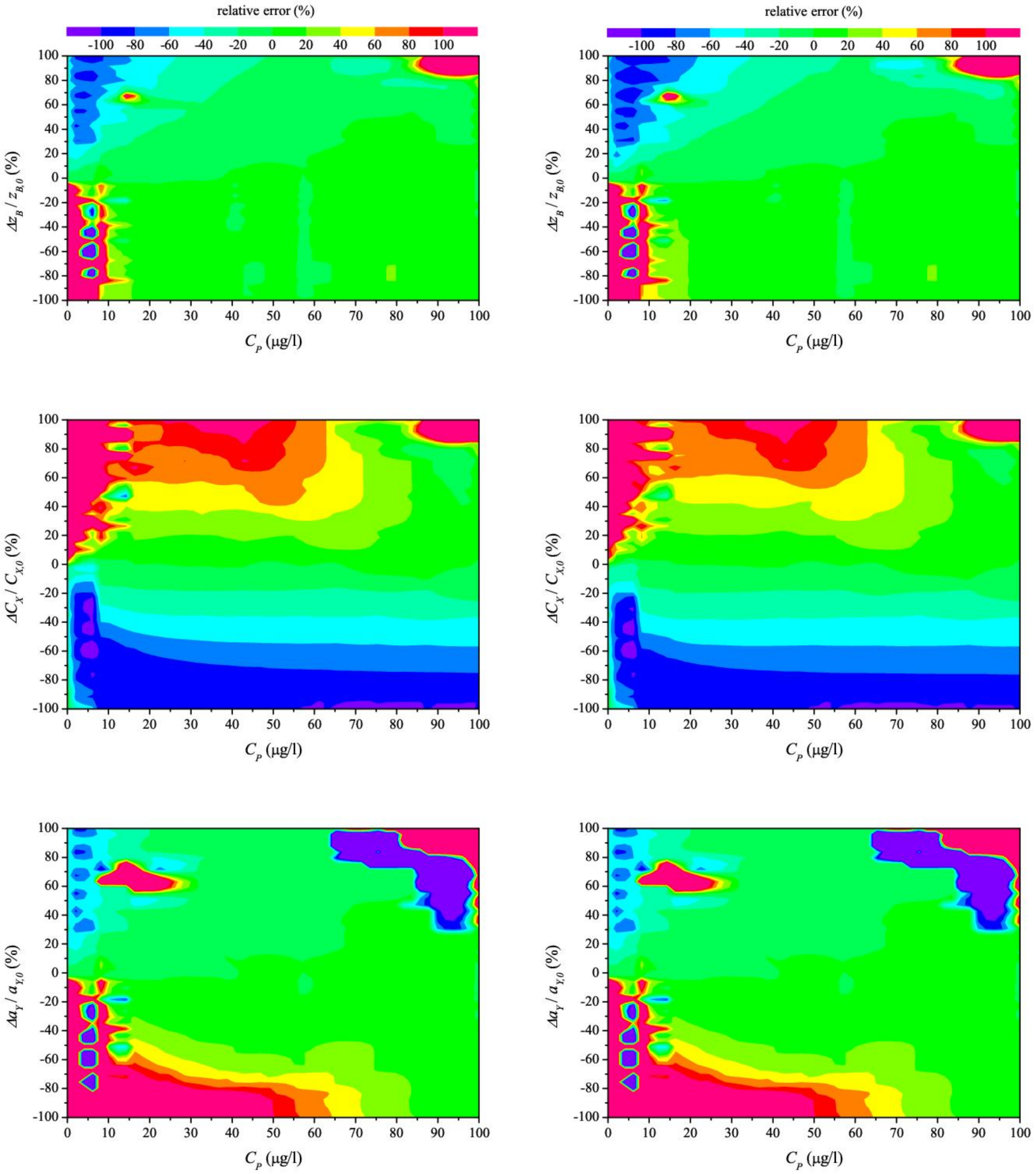

Figure 4.17: Relative error of the estimated concentration of phytoplankton for remote sensing reflectance using nested intervals of equation (4.16) and the Simplex algorithm depending on the relative error of the concentrations of water constituents, bottom depth, and different bottom types; left graphs are for sediment and right ones for macrophytes. The concentrations are $C_X = 2$ mg/l and $a_Y(440\text{nm}) = 0.3$ m^{-1}. Subsurface solar zenith angle is 30° and subsurface viewing angle 0°. The bottom depth is 3 m.

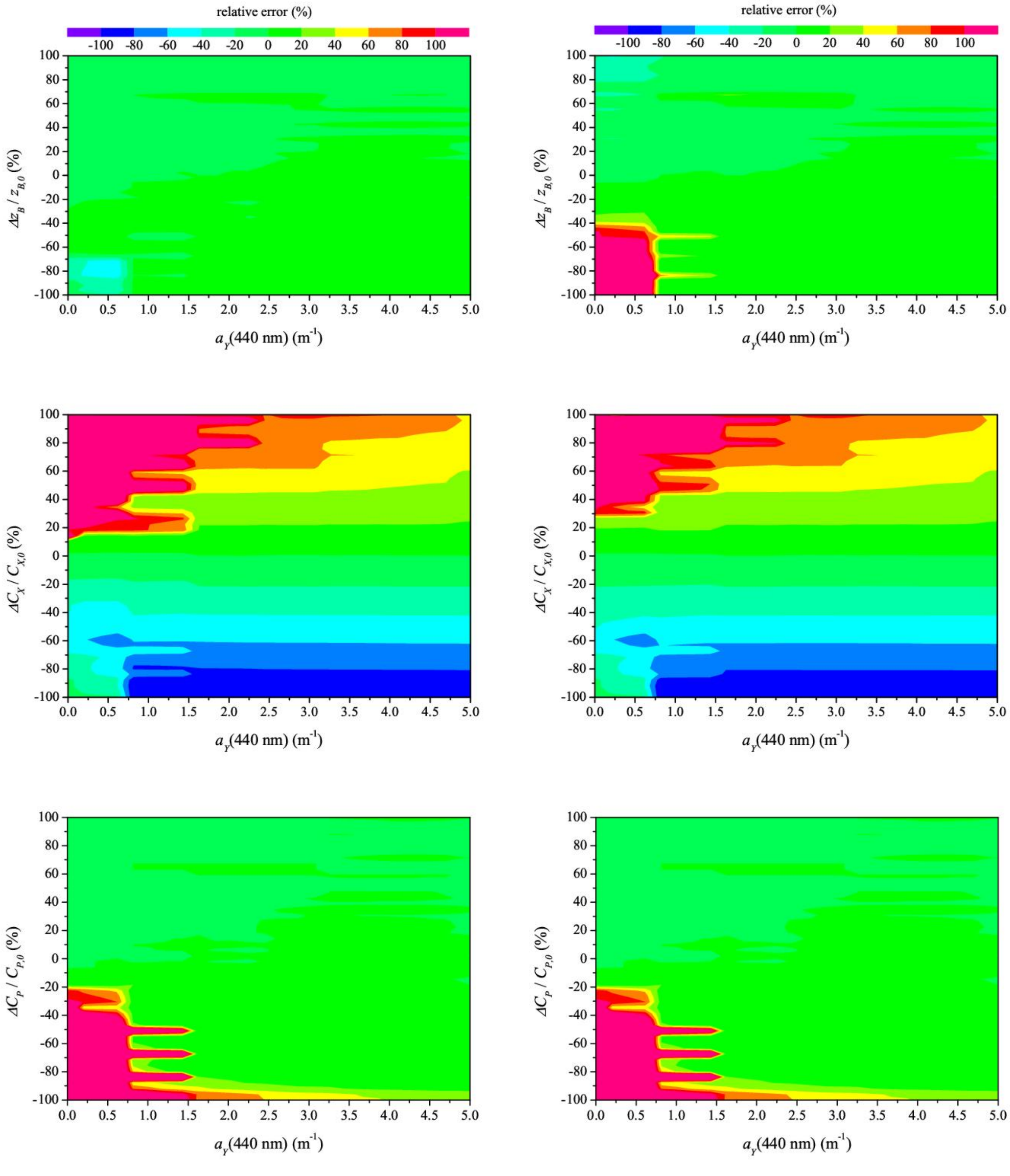

Figure 4.18: Relative error of the estimated absorption of gelbstoff for irradiance reflectance using nested intervals of equation (4.16) and the Simplex algorithm depending on the relative error of the concentrations of water constituents, bottom depth, and different bottom types; left graphs are for sediment and right ones for macrophytes. The concentrations are $C_P = 2$ μg/l and $C_X = 2$ mg/l. Subsurface solar zenith angle is 30° and $z_B = 3$ m.

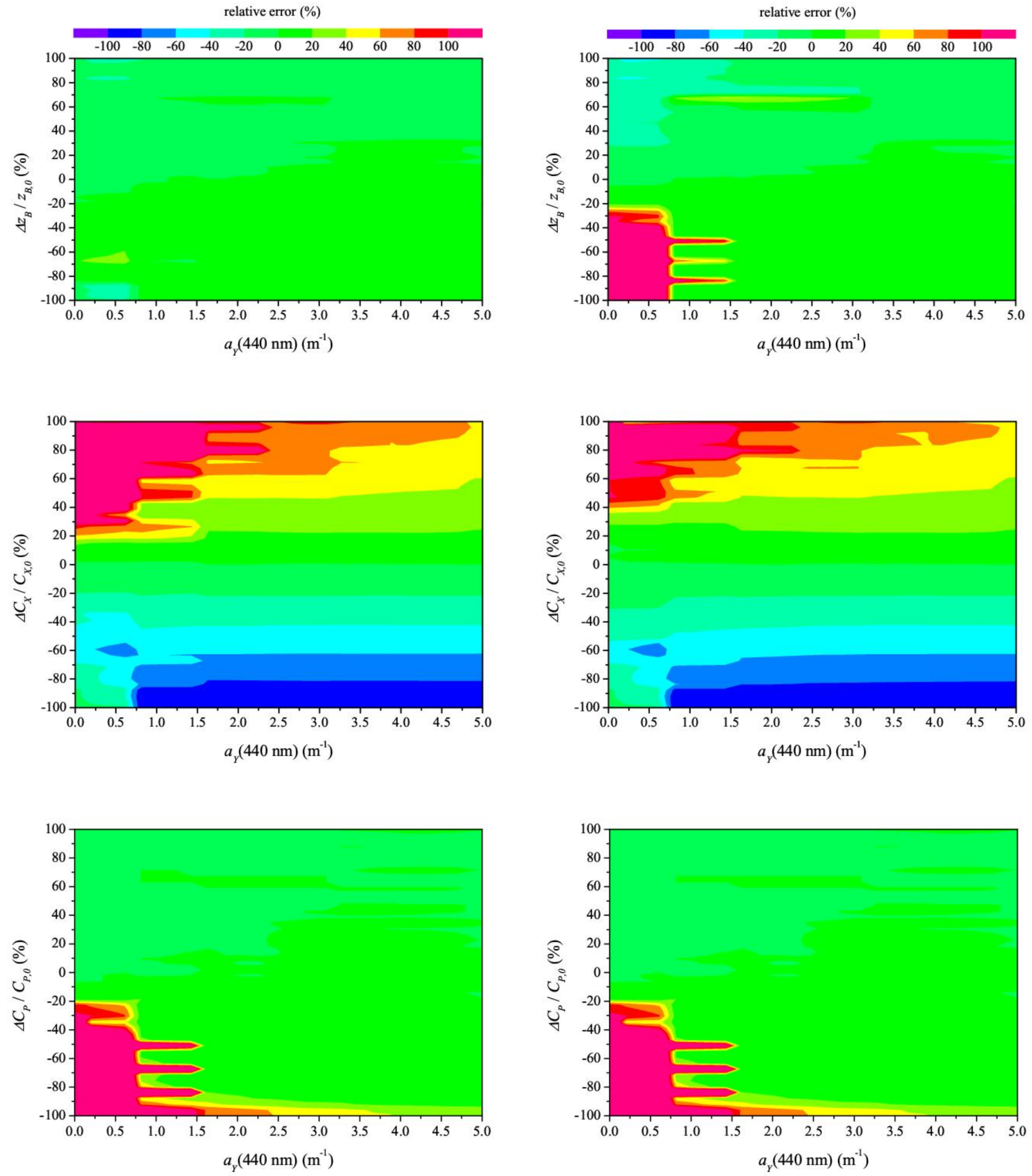

Figure 4.19: Relative error of the estimated absorption of gelbstoff for remote sensing reflectance using nested intervals of equation (4.16) and the Simplex algorithm depending on the relative error of the concentrations of water constituents, bottom depth, and different bottom types; left graphs are for sediment and right ones for macrophytes. The concentrations are $C_P = 2$ μg/l and $C_X = 2$ mg/l. Subsurface solar zenith angle is 30° and subsurface viewing angle 0°. The bottom depth is 3 m.

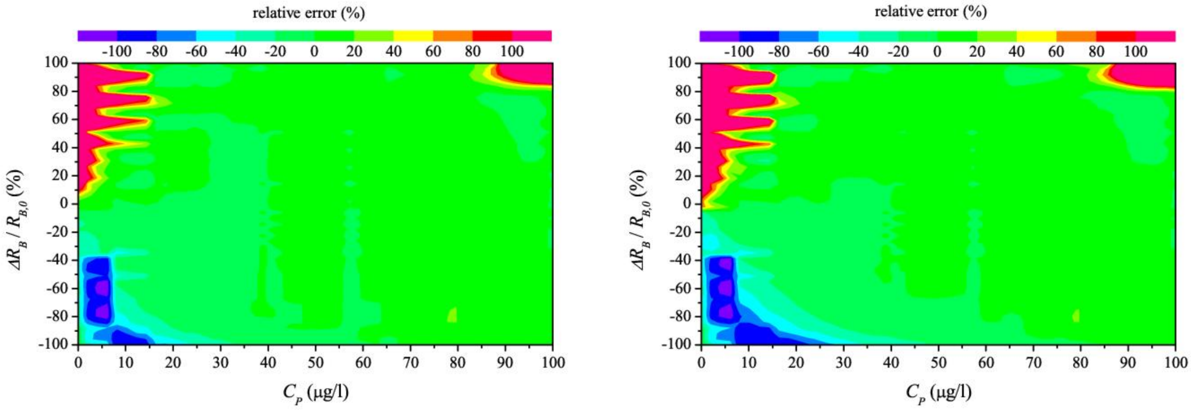

Figure 4.20: Relative error of the estimated concentration of phytoplankton for irradiance (left) and remote sensing reflectance (right) depending on the relative error of bottom albedo. A constant bottom albedo of 0.1 was used for forward calculations. The concentrations are $C_X = 2$ mg/l and $a_Y(440\text{nm}) = 0.3\ \text{m}^{-1}$. Subsurface solar zenith angle is 30° and subsurface viewing angle 0°. The bottom depth is 3 m.

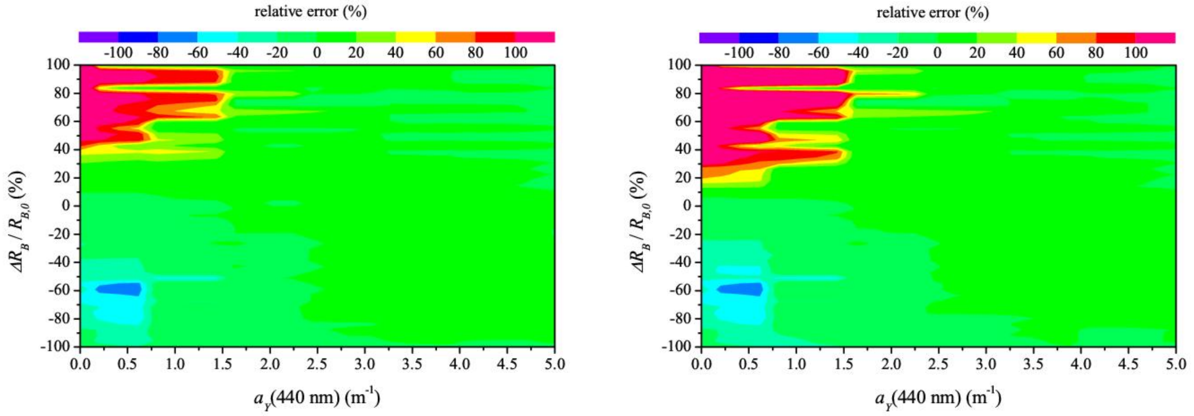

Figure 4.21: Relative error of the estimated absorption of gelbstoff at 440 nm for irradiance (left) and remote sensing reflectance (right) depending on the relative error of bottom albedo. A constant bottom albedo of 0.1 was used for forward calculations. The concentrations are $C_P = 2$ μg/l and $C_X = 2$ mg/l. Subsurface solar zenith angle is 30° and subsurface viewing angle 0°. The bottom depth is 3 m.

4.3 Pre-calculation and pre-fits

The previous chapter described the methods developed to derive initial values of z_B, C_X, C_P, and $a_Y(\lambda_0)$, $\lambda_0 = 440$ nm. The investigations show that the deviations between the initial and true values are usually around 20% and are higher for extreme situations with very high or very low concentrations. Thus, the initial values of all parameters have sufficient accuracy. The procedures were included in the software WASI (Gege, 2001; 2004). A short description of WASI is also presented in appendix B. Before the main fit starts, the initial value calculations and pre-fits have to be done in a certain order, as explained in the following, and the user has to select an input spectrum of R or R_{rs} and the fit parameters. For shallow water inversion it is also necessary to select the bottom types, represented by n bottom albedo spectra $R_{B,i}(\lambda)$ and their related areal fractions $f_{a,i}$. Six different bottom albedos can be chosen from a spectral library included in WASI, which can be edited by the user to define own spectra.

4.3.1 Steps of the initial value calculation

The estimate of the initial phytoplankton concentration and gelbstoff absorption needs knowledge about the bottom depth and the suspended matter concentration. Thus, this step is at the end, and the calculations of bottom depth and suspended matter concentration are at the beginning. The scheme of the steps is shown in figure 4.22. If z_B and C_X are fit parameters, then an additional loop is included to optimize the initial values of z_B and C_X before the initial values of C_P and $a_Y(\lambda_0)$ are derived.

This stepwise estimation of the initial values shows the best results.

4.3.2 Pre-fit in the blue and near infrared spectra

After the determination of all initial values, the input spectrum is fitted for infrared wavelengths from 700 to 800 nm and then for blue from 400 to 500 nm. The investigations to optimise between accuracy and computation time showed that a wavelength interval of 5 nm is sufficient here and also a maximum number of iterations of the Simplex of 100. This step improves the accuracy of the initial values of those parameters, which have a strong impact on specific spectral regions: suspended matter concentration in the infrared and gelbstoff absorption in the blue. Furthermore, the initial values of the phytoplankton concentration and the bottom depth are improved as well.

The pre-calculations and pre-fits are finished at this point and the main fit starts calculating all fit parameters selected by the user.

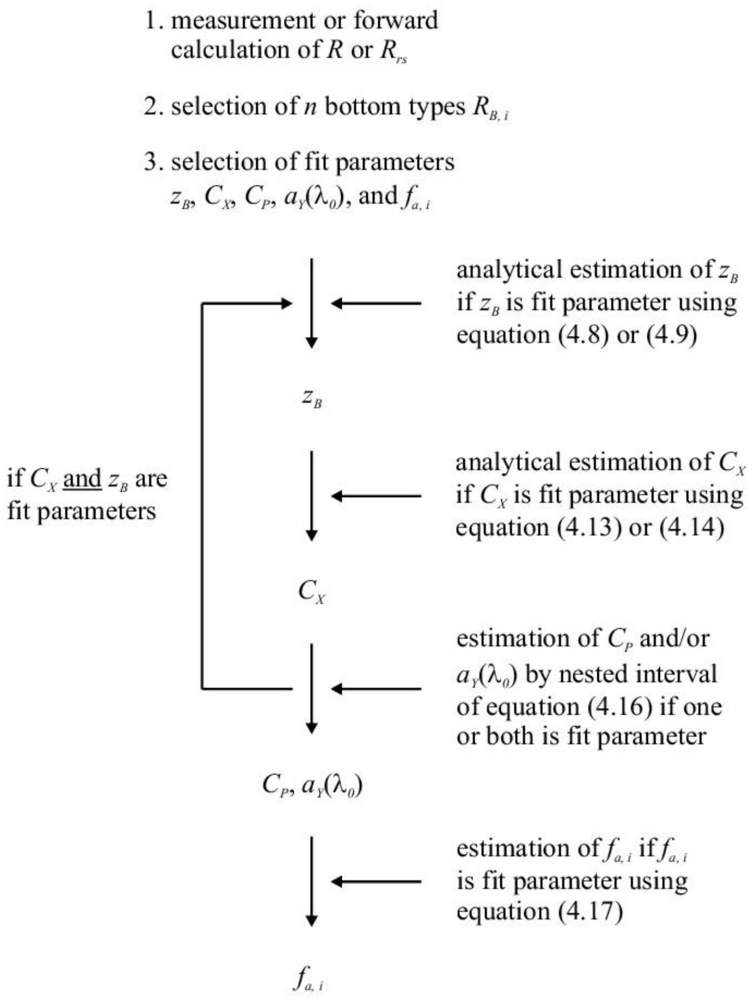

Figure 4.22: Scheme of the steps for the initial value calculation of water constituent concentrations, bottom depth, and areal fraction of the bottom types. Steps 1 to 3 have to be defined by the user.

4.4 Main fit

After the initial values are estimated and the pre-fits in the blue and infrared wavelengths are done, the main fit starts using the input spectrum of the irradiance or remote sensing reflectance. The user has to define in the software WASI (Gege, 2001; 2004) what spectral region is fitted and what spectral resolution is necessary. Here, the spectra are fitted by the Simplex algorithm from 400 to 800 nm and usually the wavelength interval is 1 nm. The Simplex is a set of $M+1$ vectors. Each vector contains the actual values of the M fit parameters and the corresponding residuum. When the fit routine is started, the $M+1$ vectors are initialized: the fit parameters' initial values and the corresponding residuum form one vector, the other M vectors are calculated using incremental changes of the initial values. These increments are set to 10% of the initial values. They cannot be changed by the user. The fit is stopped when either the termination criterion is fulfilled or the maximum number of iterations is reached. The termination criterion is: the differences between the actual parameter values must be less than a threshold for each parameter. Each parameter has its specific threshold, which is set to 10^{-5} times the initial value. It cannot be changed by the user. The user defines the maximum number of iterations, which should be set so high that a forced stop occurs only exceptionally. The scheme of the entire inversion procedure is shown in figure 4.23.

The accuracy of the inversion technique is described in the next chapters for the water constituents concentrations, bottom depth, and bottom coverage. During these inversions for error assessment only one parameter was fit parameter. All other parameters remained fixed. More realistic error estimates are obtained by fitting simultaneously more than one parameter. However, the obtained errors are a mixture of errors from the model and error propagation. A detailed analysis of these effects and the resulting errors is given in chapter 5.

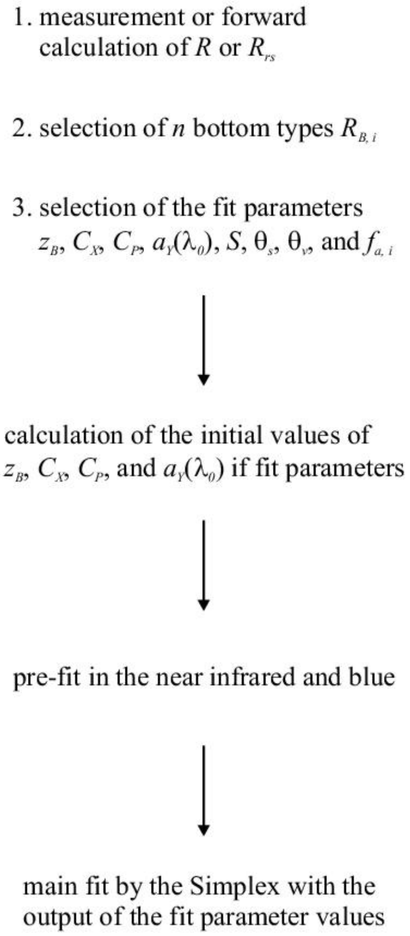

Figure 4.23: Scheme of the entire inversion procedure using the Simplex algorithm. The steps one to three have to be defined by the user.

4.4.1 Concentration of phytoplankton

The accuracy of the retrieved concentration of phytoplankton is determined by inversion of forward calculated spectra with concentrations ranging from 0.1 to 100.0 μg/l. The other parameters are fixed at $C_X = 2$ mg/l, $a_Y(\lambda_0) = 0.3$ m^{-1}, $\lambda_0 = 440$ nm, and $z_B = 3$ m for forward and inverse calculation. The accuracy of the inversion is shown in the figures 4.24 and 4.25. The relative error of C_P is plotted for the entire range of C_P depending on the other parameters and the bottom albedo of sediment and macrophytes. Additionally, the relative error of C_P is plotted, if the parameters z_B, C_X, $a_Y(\lambda_0)$, and R_B are set to a wrong value during the inversion procedure. The graphs show the results of the inversion of the remote sensing reflectance. The inversion of irradiance reflectance shows the same results and is not plotted.

The relative error of C_P is below 0.1% for the entire range, if the other parameters are fixed at their correct values. For $C_P < 5$ μg/l the relative error of C_P is 20% and higher, if the relative errors of z_B, C_X, $a_Y(\lambda_0)$, and R_B are 50% and higher. The error decreases for increasing concentration of phytoplankton except for erroneous C_X. The influence of a wrong value of C_X of 50% causes a relative error of C_P of more than 40% even for high concentrations of phytoplankton. The under- and overestimation of C_X has the effect of the under- and overestimation of C_P, respectively. The highest relative errors of C_P are for incorrect values of z_B. An underestimation of the bottom depth of 25% results in an overestimation of C_P of 40% and more for $C_P < 10$ μg/l. Overestimation of z_B of 50% yields an underestimation of C_P of about the same range. The influence of a wrong value of $a_Y(\lambda_0)$ is largest for concentrations of phytoplankton below 5 μg/l. C_P is underestimated, if $a_Y(\lambda_0)$ is overestimated and vice versa. The influence of the bottom albedo is shown in figure 4.25. A constant bottom albedo of 0.1 is used for the forward calculations. If R_B is underestimated, C_P is underestimated as well. The effect decreases for increasing concentration of phytoplankton.

4.4.2 Concentration of suspended matter

Figures 4.26 and 4.27 show the retrieved concentrations of suspended matter C_X for the range from 0.1 to 50.0 mg/l. The relative error of C_X is zero, if the other parameters are fixed at their correct values, $C_P = 2$ μg/l, $a_Y(\lambda_0) = 0.3$ m^{-1}, $\lambda_0 = 440$ nm, and $z_B = 3$ m. The figures show the curves above the bottom types sediment and macrophyte.

The influence of an inaccurate bottom depth is largest for $C_X < 5$ mg/l. The relative error of C_X reaches 50% and more. An under- or overestimation of bottom depth leads to an under- or overestimation of suspended matter concentration, respectively. Only for $C_X < 2$ mg/l at macrophyte and $C_X < 0.5$ mg/l at sediment bottom an underestimation of z_B results in an overestimation of C_X as well. For $C_X > 8$ mg/l the influence of z_B decreases and the relative error of C_X is below 5%. The effect of an incorrect phytoplankton concentration is nearly constant for $C_X > 7$ mg/l. An error of C_P of 50% causes a relative error of C_X of about 10%. For low concentrations of suspended matter the error of C_P affects the accuracy of C_X more and

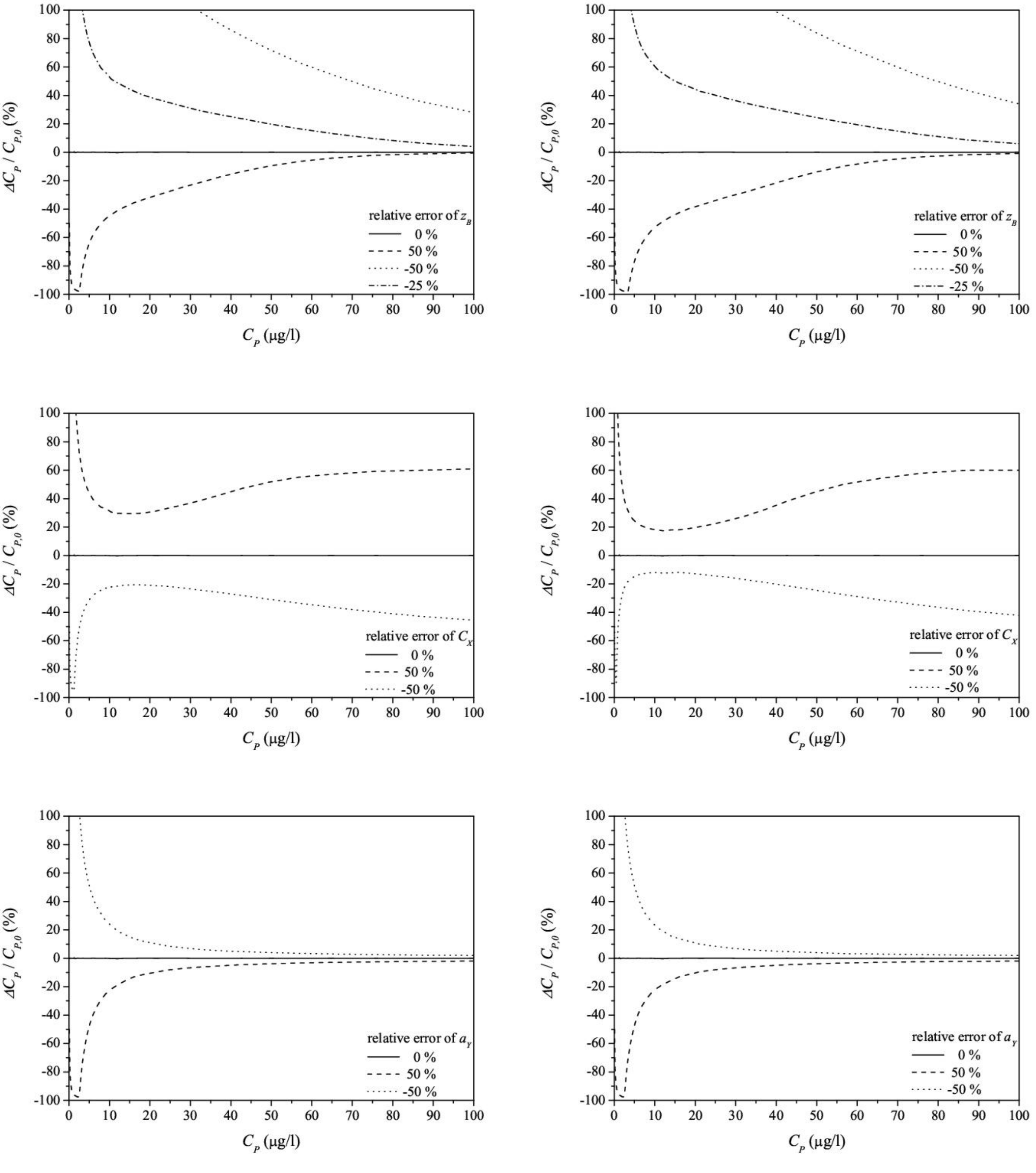

Figure 4.24: Relative error of retrieved phytoplankton concentration depending on the relative error of the concentrations of water constituents, bottom depth, and bottom types; left graphs are for sediment and right ones for macrophytes. The fixed concentrations are $C_X = 2$ mg/l and $a_Y(440\text{nm}) = 0.3$ m^{-1}. Subsurface solar zenith angle is 30° and subsurface viewing angle 0°. The bottom depth is 3 m.

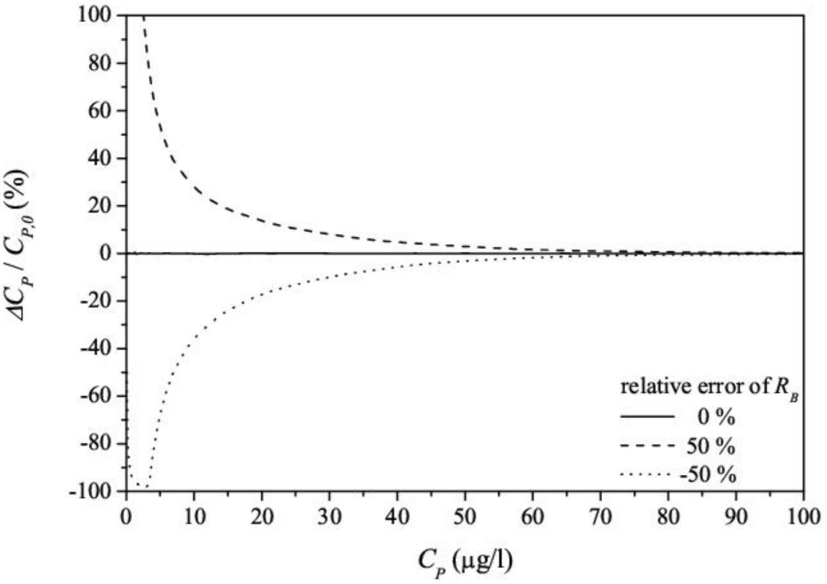

Figure 4.25: Relative error of the retrieved phytoplankton concentration depending on the relative error of bottom albedo. A constant bottom albedo of 0.1 was used for forward calculations. The fixed concentrations are $C_X = 2$ mg/l and $a_Y(440\text{nm}) = 0.3$ m^{-1}. Subsurface solar zenith angle is 30° and subsurface viewing angle 0°. The bottom depth is 3 m.

the relative error of C_X increases to 100% below 0.5 mg/l. An under- or overestimation of C_P results in an under- or overestimation of C_X, respectively. The influence of gelbstoff is similar to that of phytoplankton described before. The only difference is that the relative error of C_X reaches a constant value of about 20%, if the gelbstoff absorption error is 50% and $C_X > 10$ mg/l. For lower values of C_X the error increases rapidly to more than 100%. Figure 4.27 shows the influence of inaccurate bottom reflectance on C_X. For $C_X > 5$ mg/l the relative error of C_X is below 10% and vanishes for higher values of C_X. For concentrations of suspended matter $C_X < 5$ mg/l the relative error increases to 100% at about $C_X = 1$ mg/l. The underestimation of R_B causes an overestimation of C_X and vice versa.

4.4.3 Absorption of gelbstoff

The accuracy of the estimation of gelbstoff absorption $a_Y(\lambda_0)$, $\lambda_0 = 440$ nm, is shown in the figures 4.28 and 4.29. The range of $a_Y(\lambda_0)$ is from 0.01 to 5.00 m^{-1}. The gelbstoff absorption is calculated exactly by the inversion, if the other parameter are correct during the procedure at $C_P = 2$ μg/l, $C_X = 2$ mg/l, and $z_B = 3$ m at sediment and macrophyte.

The effect of an inaccurate bottom depth during the inversion decreases with increasing gelbstoff absorption. The relative error of $a_Y(\lambda_0)$ is below 50%, if the relative error of z_B is larger than 25%. Only if $a_Y(\lambda_0) < 0.1$ m^{-1} and the relative error of z_B is >25%, the relative error of $a_Y(\lambda_0)$ increases rapidly to more than 100%. An underestimation of z_B results in an overestimation of

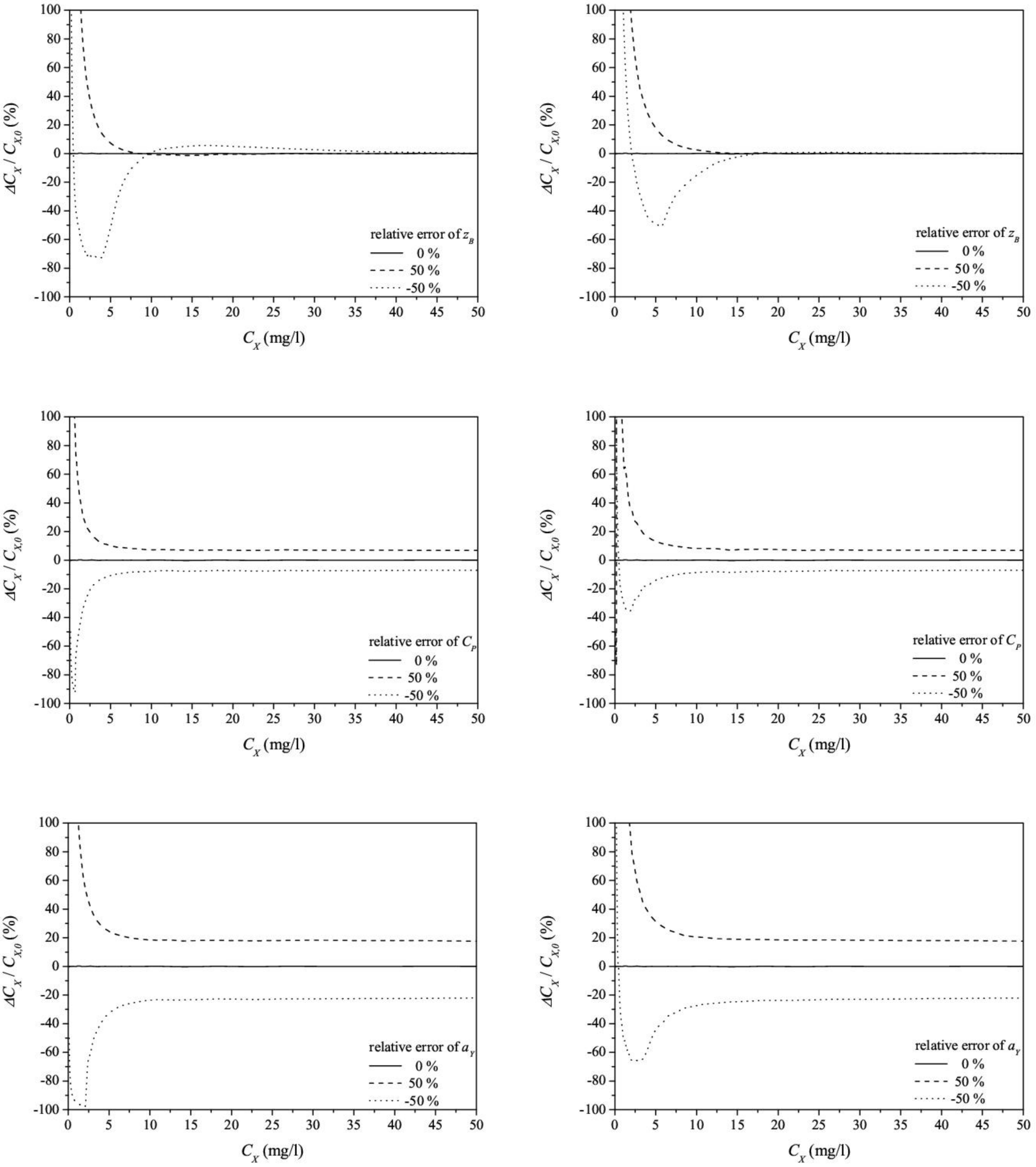

Figure 4.26: Relative error of retrieved suspended matter concentration depending on the relative error of the concentrations of water constituents, bottom depth, and bottom types; left graphs are for sediment and right ones for macrophytes. The fixed concentrations are $C_P = 2$ μg/l and $a_Y(440\text{nm}) = 0.3$ m^{-1}. Subsurface solar zenith angle is 30° and subsurface viewing angle 0°. The bottom depth is 3 m.

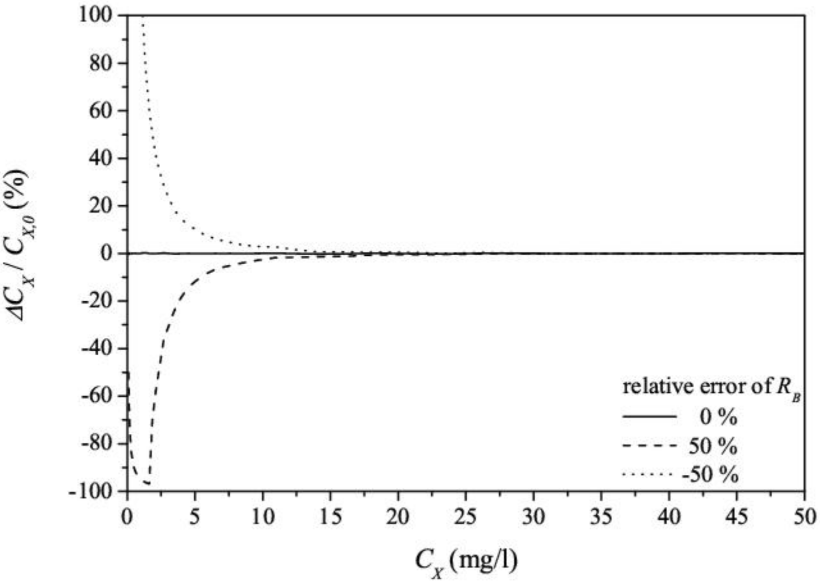

Figure 4.27: Relative error of retrieved suspended matter concentration depending on the relative error of bottom albedo. A constant bottom albedo of 0.1 was used for forward calculations. The concentrations are $C_P = 2$ μg/l and $a_Y(440\text{nm}) = 0.3$ m^{-1}. Subsurface solar zenith angle is 30° and subsurface viewing angle 0°. The bottom depth is 3 m.

$a_Y(\lambda_0)$ and vice versa. The overestimation of z_B causes a smaller relative error of $a_Y(\lambda_0)$ as the underestimation of z_B in the same order. The influence of an incorrect value of C_X on the accuracy of $a_Y(\lambda_0)$ is smallest between 0.5 and 1.0 m^{-1}. The relative error of $a_Y(\lambda_0)$ is about 15 to 25% for an error of C_X of 50%. Below 0.5 m^{-1} the relative error of $a_Y(\lambda_0)$ increases to more than 100%, if the relative error of C_X is larger than 50%. Above 1.0 m^{-1} the relative error of $a_Y(\lambda_0)$ increases only slowly. An under- or overestimation of C_X results in an under- or overestimation of $a_Y(\lambda_0)$, respectively. An error of C_P has the smallest impact on the accuracy of $a_Y(\lambda_0)$. The relative error of $a_Y(\lambda_0)$ is below 15% for $a_Y(\lambda_0) > 0.3$ m^{-1}, even if the error of the phytoplankton concentration is 50%. But at lower values of gelbstoff absorption the relative error increases to 100% and more. An overestimation of C_P causes an underestimation of $a_Y(\lambda_0)$ and vice versa. The influence of the relative error of R_B on the retrieved gelbstoff absorption is shown in figure 4.29. The influence of the bottom reflectance decreases with increasing gelbstoff absorption. For $a_Y(\lambda_0) < 0.3$ m^{-1} an error of 50% in R_B results in an error in $a_Y(\lambda_0)$ of more than 40%. An under- or overestimation of R_B yields an under- or overestimation of $a_Y(\lambda_0)$, respectively.

4.4.4 Bottom depth

The accuracy of the estimated bottom depth is shown in the figures 4.30 and 4.31 from 0.1 to 50.0 m depending on the relative error of the water constituent concentrations and bottom

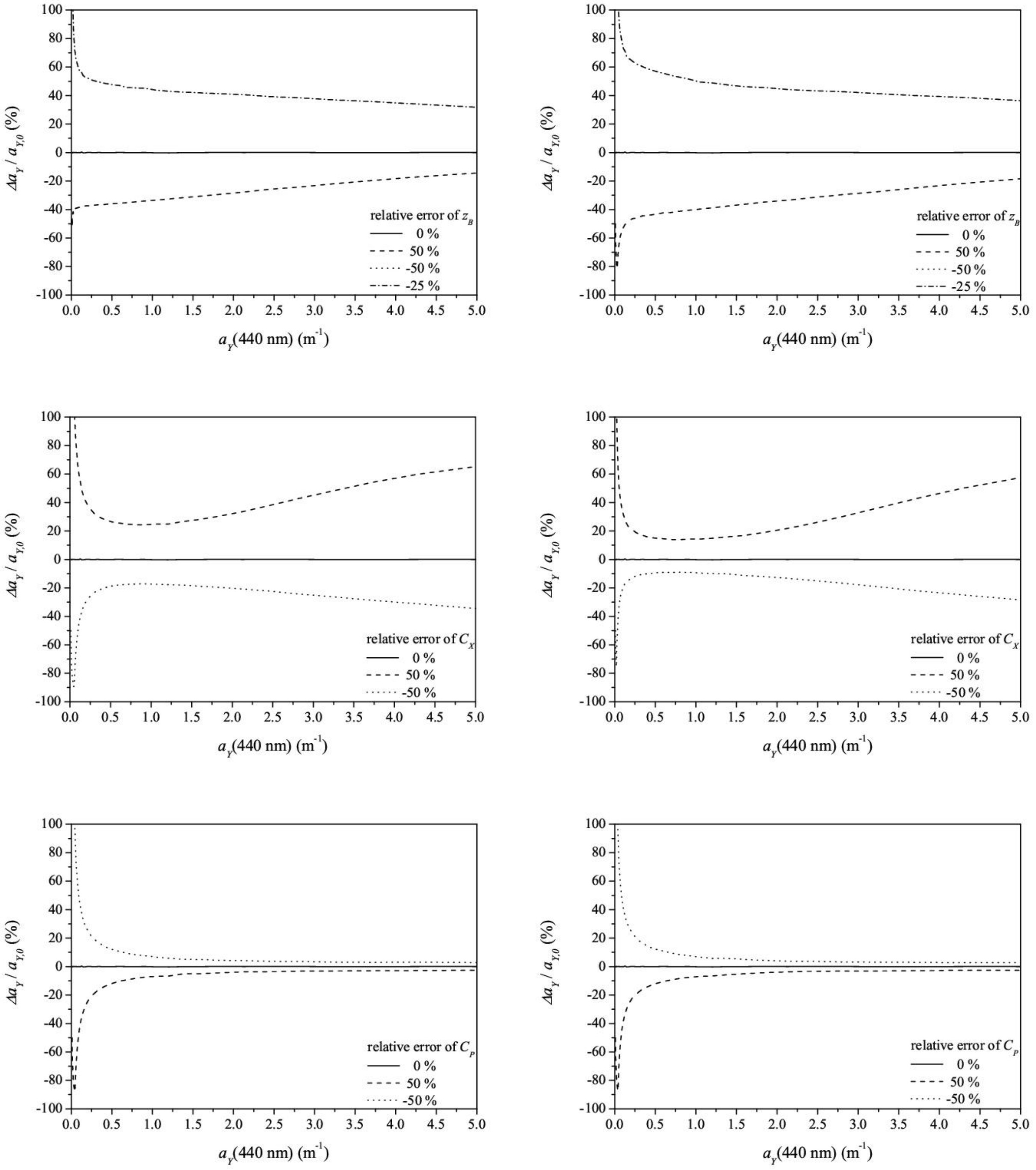

Figure 4.28: Relative error of retrieved gelbstoff absorption depending on the relative error of the concentrations of water constituents, bottom depth, and bottom types; left graphs are for sediment and right ones for macrophytes. The fixed concentrations are $C_P = 2$ μg/l and $C_X = 2$ mg/l. Subsurface solar zenith angle is 30° and subsurface viewing angle 0°. The bottom depth is 3 m.

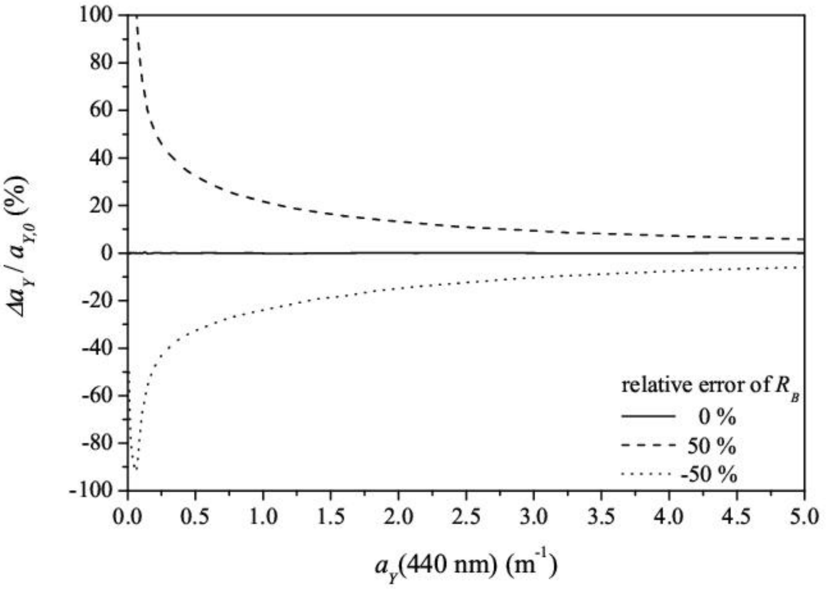

Figure 4.29: Relative error of retrieved gelbstoff absorption depending on the relative error of bottom albedo. A constant bottom albedo of 0.1 was used for forward calculations. The fixed concentrations are $C_P = 2$ μg/l and $C_X = 2$ mg/l. Subsurface solar zenith angle is 30° and subsurface viewing angle 0°. The bottom depth is 3 m.

reflectance. If the values of the non-fitted parameters are correct during the inversion at $C_P = 2$ μg/l, $C_X = 2$ mg/l, and $a_Y(\lambda_0) = 0.3$ m^{-1} at $\lambda_0 = 440$ nm, the bottom depth is derived without error. The analysis was done using the bottom albedo of both sediment and macrophyte.

Generally, the influence of an error in the water constituent concentrations increases with increasing bottom depth. In the first few meters the relative error of z_B is below 30%, even if C_P, C_X, and $a_Y(\lambda_0)$ are under- or overestimated by 50%. If the absorbing water constituents like phytoplankton and gelbstoff are overestimated, then the bottom depth is underestimated. For underestimated values of C_P and $a_Y(\lambda_0)$ the bottom depth is overestimated, but the relative error of z_B is higher than for an overestimation of C_P and $a_Y(\lambda_0)$ of the same order. This behaviour is different for scatterers like suspended matter. An under- or overestimation of C_X causes an under- or overestimation of z_B, respectively. The reason of the high relative error of z_B for increasing z_B is that the optical thickness of the water body makes it more and more difficult to detect the bottom. The influence of the relative error of bottom albedo is shown in figure 4.31. For increasing bottom depth the relative error of z_B decreases, if the bottom albedo is not correct. For $z_B < 5$ m and 50% relative error of R_B the relative error of z_B is about 50% and even higher for very small bottom depths. An under- or overestimation of R_B causes an under- or overestimation of z_B, respectively.

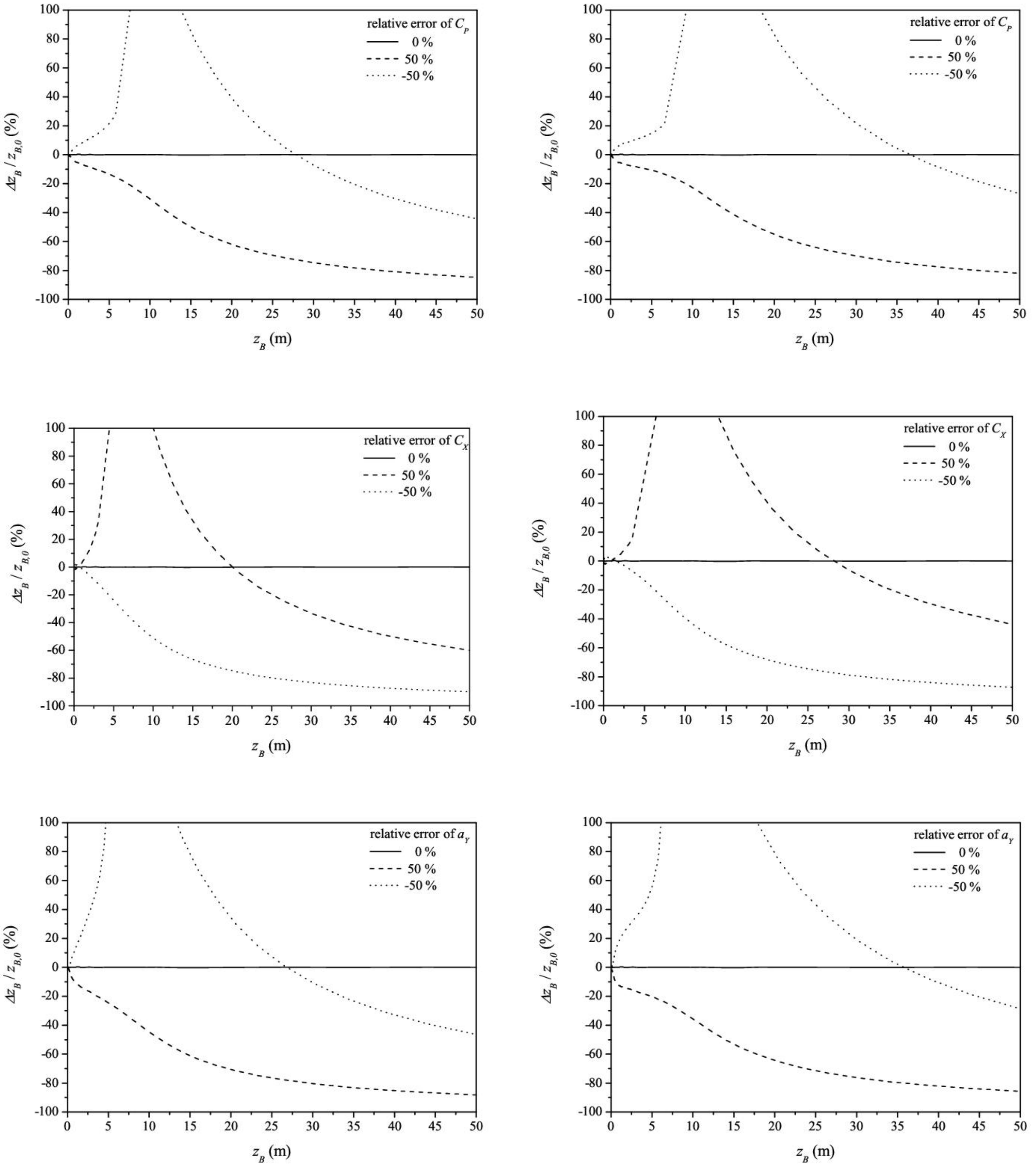

Figure 4.30: Relative error of retrieved bottom depth depending on the relative error of the concentrations of water constituents and bottom types; left graphs are for sediment and right ones for macrophytes. The fixed concentrations are $C_P = 2$ μg/l, $C_X = 2$ mg/l, and $a_Y(440\text{nm}) = 0.3$ m^{-1}. Subsurface solar zenith angle is 30° and subsurface viewing angle 0°.

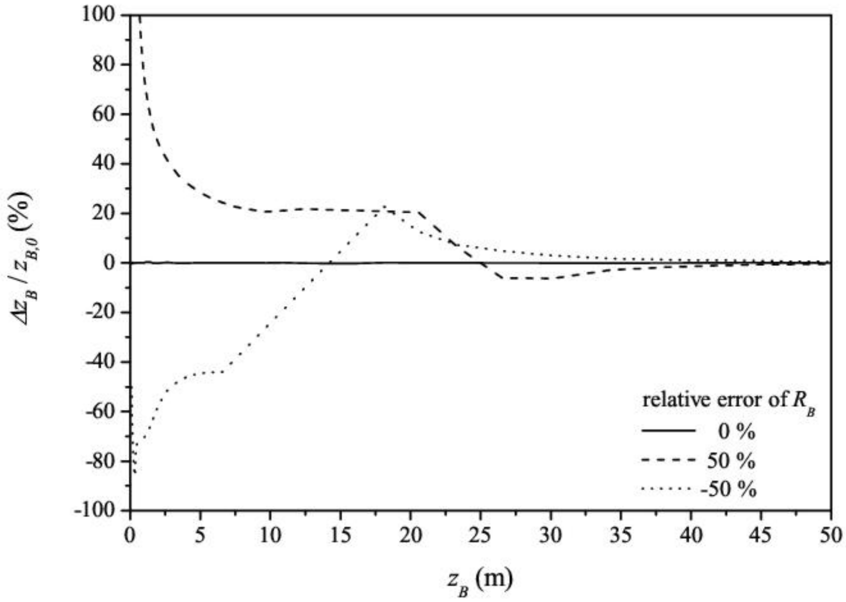

Figure 4.31: Relative error of retrieved bottom depth depending on the relative error of bottom albedo. A constant bottom albedo of 0.1 was used for forward calculations. The fixed concentrations are $C_P = 2$ μg/l, $C_X = 2$ mg/l, and $a_Y(440\text{nm}) = 0.3$ m^{-1}. Subsurface solar zenith angle is 30° and subsurface viewing angle 0°.

4.4.5 Areal fraction of bottom albedo

Figure 4.32 shows the accuracy of the retrieved areal fraction of bottom cover. Two bottom types are used, sediment and macrophyte, and their areal fraction, $f_{a,sed}$ and $f_{a,mac}$ respectively, are coupled as $f_{a,sed} + f_{a,mac} = 1$ to get 100% coverage with that bottom types. Their areal fractions vary between 0 and 1. The other parameters are fixed at $C_P = 2$ μg/l, $C_X = 2$ mg/l, $a_Y(\lambda_0) = 0.3$ m^{-1}, $\lambda_0 = 440$ nm, and $z_B = 3$ m. If these parameters are known, no errors of the areal fraction of sediment and macrophyte occur.

Generally, for both bottom types the error of other parameters affects the accuracy of $f_{a,sed}$ and $f_{a,mac}$ most for low values of the areal fraction and less for high values. The relative error of the areal fraction of sediment is more sensitive to errors of C_P, C_X, $a_Y(\lambda_0)$, and z_B. The relative error of bottom depth shows the strongest influence on relative errors of $f_{a,sed}$ and $f_{a,mac}$. An under- or overestimation of z_B of 25% results in an under- or overestimation of the areal fraction of sediment of 50% and more, but does not affect the areal fraction of macrophyte for $f_{a,mac} > 0.4$. The same effect is seen for a relative error of C_P of 50%, but with a lower relative error in the areal fractions. The relative errors of $f_{a,sed}$ and $f_{a,mac}$ due to incorrect suspended matter concentration of 50% is higher than 40%, if the values of the areal fractions are below 0.5. An overestimation of C_X underestimates the areal fraction of sediment, but overestimates that of macrophyte. It is vice versa for an underestimation of C_X. The influence of the error

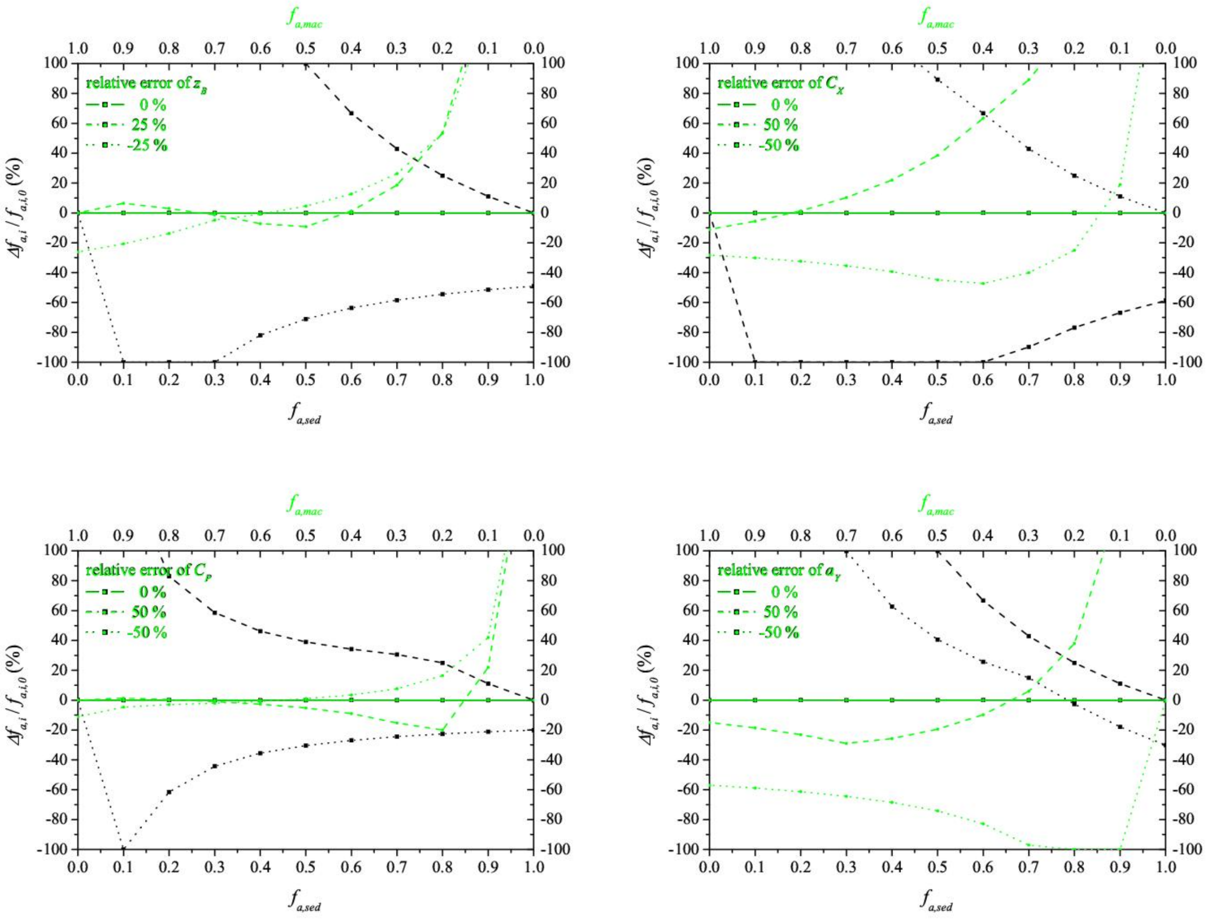

Figure 4.32: Relative error of the retrieved areal fraction of sediment (black) and macrophyte (green) bottom cover depending on the relative error of the concentrations of water constituents and bottom depth. The concentrations are $C_P = 2$ μg/l, $C_X = 2$ mg/l, and $a_Y(440\text{nm}) = 0.3$ m^{-1}. Subsurface solar zenith angle is 30° and subsurface viewing angle 0°. The bottom depth is 3 m.

of $a_Y(\lambda_0)$ is strong for both, $f_{a,sed}$ and $f_{a,mac}$. If the values of the areal fractions are below 0.3 the relative error of $f_{a,sed}$ and $f_{a,mac}$ increases rapidly to more than 100%. For $f_{a,sed} < 0.8$ and $f_{a,mac} > 0.3$ an under- or overestimation of $a_Y(\lambda_0)$ results in an overestimation of $f_{a,sed}$ and an underestimation of $f_{a,mac}$.

Especially for low values the relative errors of $f_{a,sed}$ and $f_{a,mac}$ are high, if water constituents concentrations and bottom depth are inaccurately known. To put this into perspective, the absolute errors of the areal fractions are shown in figure 4.33. The error of $f_{a,mac}$ is usually below 20% with the exception for an underestimation of $a_Y(\lambda_0)$, where the error can reach 50%. The absolute error of $f_{a,sed}$ is normally higher with a value between 30 to 50%. For erroneous concentrations of suspended matter and gelbstoff, the value can be higher than 50%. The lowest impact on the error of $f_{a,sed}$ and $f_{a,mac}$ has an inaccurate phytoplankton concentration.

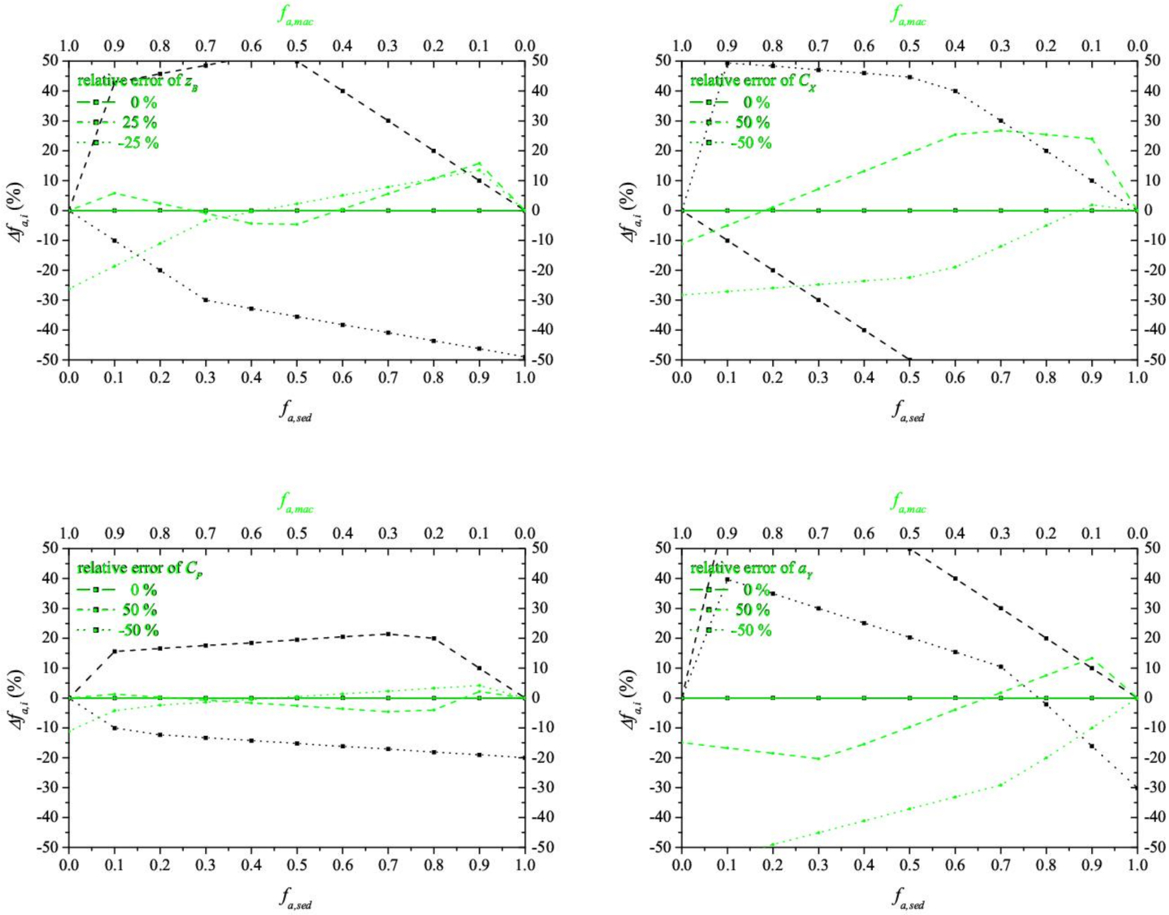

Figure 4.33: Absolute error of the retrieved areal fraction of sediment (black) and macrophytes (green) at the bottom depending on the relative error of the concentrations of water constituents and bottom depth. The concentrations are $C_P = 2$ μg/l, $C_X = 2$ mg/l, and $a_Y(440\text{nm}) = 0.3$ m^{-1}. Subsurface solar zenith angle is 30° and subsurface viewing angle 0°. The bottom depth is 3 m.

Chapter 5

Analysis of inversion accuracy

Chapter 4 explained the inversion technique for the new parameterisations of the irradiance and remote sensing reflectance in shallow water, R and R_{rs}. The parameters, which are retrieved by inversion, are the concentration of phytoplankton C_P, of suspended matter C_X, the absorption of gelbstoff $a_Y(\lambda_0)$, $\lambda_0 = 440$ nm, the bottom depth z_B, and the fraction f_a of up to six bottom types in the sensor's field of view. The inversion procedure is implemented in the Windows-based software tool WASI (Gege, 2001; 2004), which is briefly explained in appendix B. The software allows detailed analysis of R and R_{rs} in forward and inverse simulations. Convergence and usefullness of the inversion method were shown at the end of chapter 4. This chapter discusses the accuracy of the new inversion in shallow water under the influence of the model error itself, the error propagation using different fit parameters, and of sensor characteristics like signal noise, radiometric and spectral resolution. Finally, measurements are inverted and the results are compared to those derived from in-situ observations.

5.1 Model error

Chapter 4 showed the accuracy of the inversion technique using the new parameterisations of R and R_{rs} developed in chapter 3. Due to the differences between the reference model Hydrolight and the analytical shallow water parameterisations, a model inversion error exists, which can be quantified by the retrieval of the input parameters with Hydrolight. To show that, spectra of irradiance and remote sensing reflectance calculated with Hydrolight are taken as input for the inversion procedure. The wavelengths from 660 to 715 nm are excluded during the inversion, to avoid effects due to the fluorescence of chlorophyll, which is included in the Hydrolight simulations. The relative errors of the fit parameters C_P, C_X, $a_Y(\lambda_0)$, $\lambda_0 = 440$ nm, and z_B are estimated using the values listed in table 5.1 for the bottom type sediment. Each fit parameter is analysed separately, while the other parameters are fixed at the correct values during the inversion. If not varied, $C_P = 2.0$ μg/l, $C_X = 2.0$ mg/l, $a_Y(\lambda_0) = 0.3$ m^{-1}, and $z_B = 3$ m.
The accuracy of the retrieved suspended matter concentration is shown in figure 5.1 as a function of C_X and z_B. The relative error of C_X lies between 0 and 10%, whereby C_X is generally

C_P (μg/l)	1.0	2.0	3.0	4.0	5.0	6.0	7.0	8.0	9.0	10.0
C_X (mg/l)	1.0	2.0	3.0	4.0	5.0	6.0	7.0	8.0	9.0	10.0
$a_Y(\lambda_0)(\mathrm{m}^{-1})$	0.10	0.20	0.30	0.40	0.50	0.60	0.70	0.80	0.90	1.00
z_B (m)	0.5	1.0	2.0	4.0	6.0	10.0				

Table 5.1: Concentrations of the water constituents and bottom depths used for the simulations with Hydrolight and the following inversion.

underestimated. For a bottom depth below 2 m and $C_X < 2.0$ mg/l the relative error is above 10%: more than 20% overestimation for the remote sensing reflectance and about 50% underestimation for the irradiance reflectance. Figure 5.2 shows the relative error of C_P depending on the bottom depth estimated by the inversion of Hydrolight spectra. The relative error is below 15% for $C_P > 2$ μg/l except for $z_B = 10$ m, where the relative error of C_P is 20% for R and 30% for R_{rs}. For lower concentrations and increasing z_B the relative error increases to -40% for R and -50% for R_{rs}. This is due to the influence of gelbstoff fluorescence considered for the Hydrolight simulations but not for the analytical model: the relative contribution of gelbstoff fluorescence increases for increasing depth. Thus, the higher reflectance is compensated during the inversion by decreasing the concentrations. Simulations of R_{rs} for varying gelbstoff absorption and $C_P = 1$ μg/l result in a relative error of C_P of 50% and higher for $a_Y(\lambda_0) \geq 0.6$ m^{-1} and of 24% for $a_Y(\lambda_0) = 0.1$ m^{-1}. Simulations of R show the same behaviour. For increasing concentrations of C_P the relative error is about 0 to 5% for all values of z_B. The relative error of $a_Y(\lambda_0)$ is shown in figure 5.3. The deviation of $a_Y(\lambda_0)$ between the input value of Hydrolight and the retrieved value by inversion is lower than 5% for $a_Y(\lambda_0) > 0.2$ m^{-1} slightly increasing with the bottom depth. Only the estimations of $a_Y(\lambda_0)$ using R_{rs} at $z_B = 10$ m result in an higher relative error up to 10%. If the gelbstoff absorption is below 0.2 m^{-1}, the relative error increases to about 10% for R and 15% for R_{rs}.

Figure 5.4 shows the accuracy of the bottom depth. The relative error of z_B is plotted from 1 to 10 m depending on the concentration of phytoplankton, suspended matter, and the absorption of gelbstoff. The graphs show clearly the limitations of the possibility of detecting the bottom characteristics. The influence of the bottom decreases with increasing optical thickness of the water body, which is coupled with absorption and scattering. In the range of C_P and $a_Y(\lambda_0)$ during the estimations, the relative error of z_B is about 5% for $z_B < 5$ m. The strongest impact is due to the amount of suspended matter in the water. Even below $z_B = 5$ m and $C_X \leq 5$ mg/l the relative error increases to 25% for R and 15% for R_{rs}. The influence of phytoplankton and gelbstoff is lower than that of suspended matter. Below 5 m the relative error of z_B is between 0 and 5% and increases for greater bottom depths to 25% and more.

The reason for the differences between the Hydrolight input and the retrieved value is that the analytical parameterisations deviate from the simulations. This is due to the analytical equations themselves, because they are approximations of the ratiative transfer equations. Additional

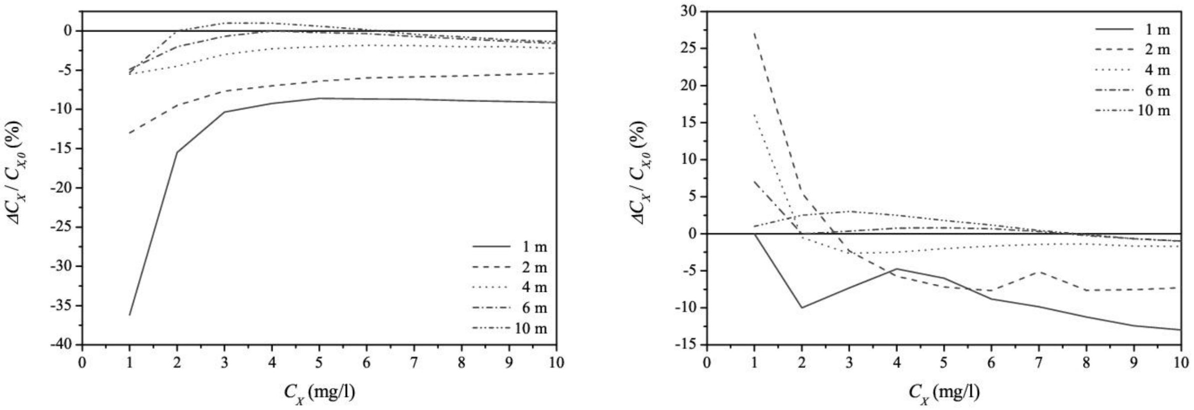

Figure 5.1: Relative error of the retrieved suspended matter concentration using Hydrolight spectra, for different values of the bottom depth. Left graphs are valid for the inversion of irradiance reflectance and right ones for remote sensing reflectance. The bottom type is sediment.

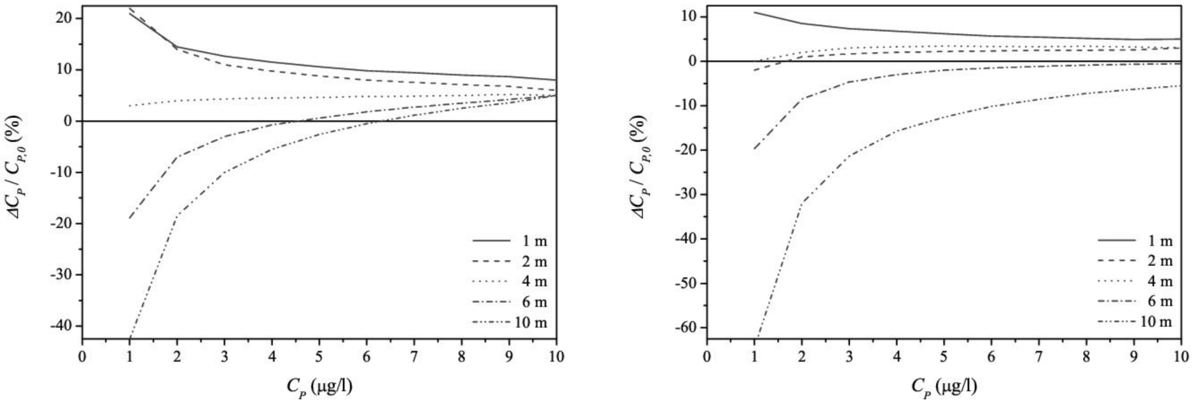

Figure 5.2: Relative error of the retrieved phytoplankton concentration using Hydrolight spectra, for different values of the bottom depth. Left graphs are valid for the inversion of irradiance reflectance and right ones for remote sensing reflectance. The bottom type is sediment.

errors are due to the missing fluorescence parameterisation in the analytical model.

5.2 Error propagation

The paragraphs before have described the inversion of one parameter. But in reality there exists more than one unknown parameter, which has to be determined. In the case of shallow water remote sensing, the concentration of phytoplankton C_P, suspended matter C_X, the gelbstoff absorption $a_Y(\lambda_0)$ at $\lambda_0 = 440$ nm, the bottom depth z_B, and the fractional bottom coverage $f_{a,i}$ of $i = 1, ..., n$ bottom types are the unknown parameters. This chapter describes the influence on the accuracy of the fit parameters, if two and more parameters are determined at once by the

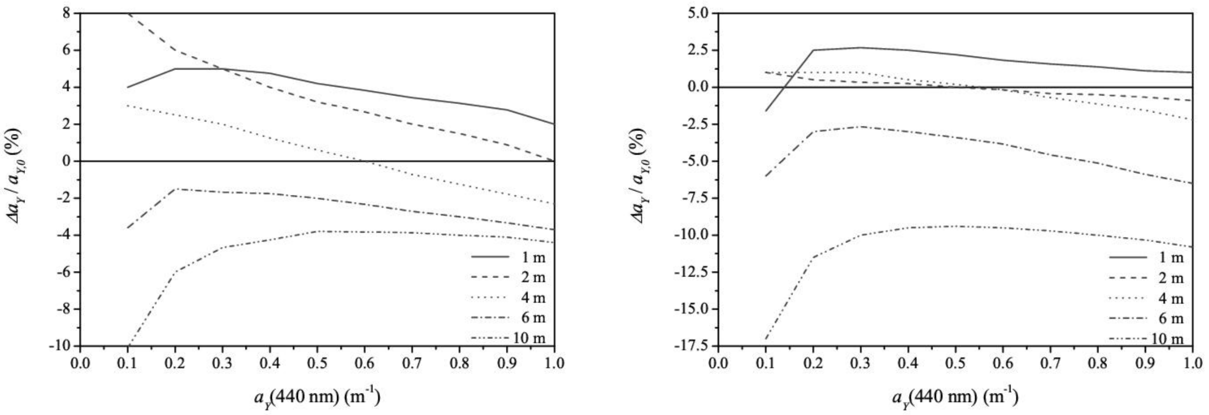

Figure 5.3: Relative error of the retrieved gelbstoff absorption using Hydrolight spectra, for different values of the bottom depth. Left graphs are valid for the inversion of irradiance reflectance and right ones for remote sensing reflectance. The bottom type is sediment.

inversion technique in shallow water. Detailed investigations for deep water are also explained in Gege (2002).

Figures 5.5 and 5.6 show the relative error of C_P, C_X, $a_Y(\lambda_0)$, and z_B, if two parameters are retrieved simultaneously. The relative error corresponds to the parameter of the x-axis and the second fit parameter is given along the y-axis. Parameters not retrieved are kept constant at their correct values during the inversion: $C_P = 2.0$ μg/l, $C_X = 2.0$ mg/l, $a_Y(\lambda_0) = 0.3$ m^{-1}, and $z_B = 3$ m. The figures are calculated with sediment as bottom type. The results of calculations with a bottom albedo of macrophytes show very similar features and are not plotted.

The relative error of C_P in figure 5.5 (left) is below 5% for $C_P > 1.0$ μg/l, independent of the second fit parameter. The error increases to 50% and more for lower phytoplankton concentrations and for $C_X < 0.2$ mg/l and $a_Y(\lambda_0) < 0.1$ m^{-1}. This is due to the low optical thickness of the water body and therefore the domination of bottom reflectance. Thus, low values of C_P, C_X, and $a_Y(\lambda_0)$ do not change the spectral shape of R and R_{rs} and are hard to estimate by inversion. The relative error of C_P increases below 1 μg/l and for C_X between 3 to 10 mg/l, and decreases for higher suspended matter concentrations. This can be explained by the influence of the bottom. If the water contains high amounts of suspended matter, the water becomes opaque and the bottom invisible. But the suspended matter concentration dominates the optical properties of the water and the very low amount of C_P does not affect the spectral shape very much.

The relative error of C_X is shown in figure 5.5 at the right and has generally very low values from 0 to 5%. Only for low concentrations of phytoplankton and suspended matter below 0.2 μg/l and 0.2 mg/l, respectively, the underestimation of C_X is larger than 20%. The strongest influence is due to bottom depth. For extremely low values of $z_B < 0.2$ m the relative error of C_X is higher than 100%. Figure 5.6 shows the relative error of $a_Y(\lambda_0)$ (left) and z_B (right). The relative error of $a_Y(\lambda_0)$ is generally below 5%. The exceptions are for a phytoplankton

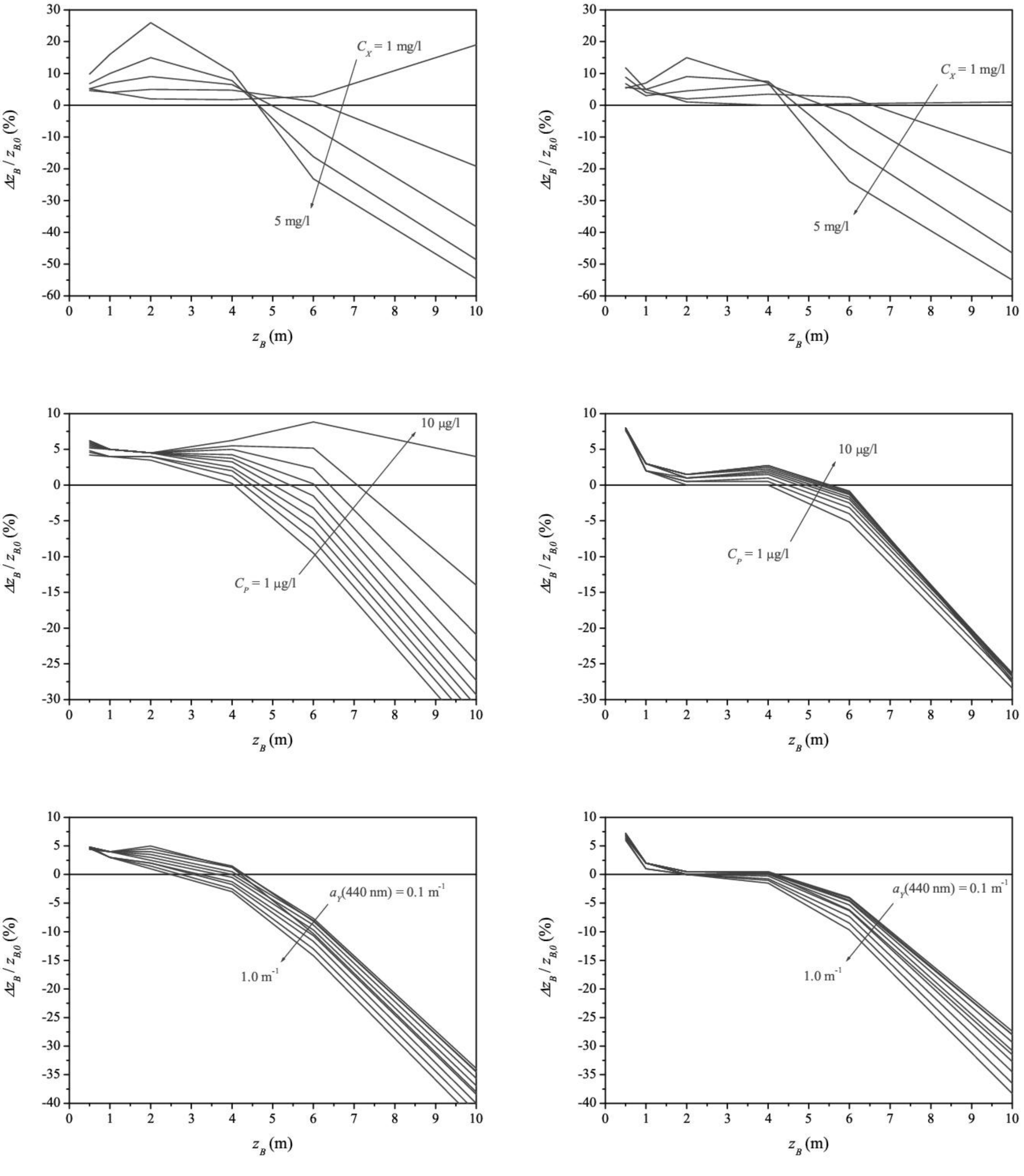

Figure 5.4: Relative error of retrieved bottom depth using Hydrolight spectra, depending on suspended matter (top), phytoplankton (centre), and absorption of gelbstoff (bottom). Left graphs are valid for the inversion of irradiance reflectance and right ones for remote sensing reflectance. The bottom type is sediment.

concentrations below 1 μg/l in combination with very low gelbstoff absorption below 0.05 m^{-1} and for a bottom depth $z_B < 0.2$ m. The reason is the high influence of bottom reflectance. The relative error of z_B is high correlated with the optical thickness of the water body. Thus, the accuracy of the bottom depth decreases for increasing concentrations of phytoplankton and suspended matter and for increasing gelbstoff absorption. If the bottom depth is detectable, the relative error of z_B is below 5%. For $C_X > 10$ mg/l and $z_B > 10$ m the error increases to more than 100%. Also for $C_P > 10$ μg/l or $a_Y(\lambda_0) > 0.3$ m^{-1} in combination with $z_B > 10$ m the relative error of z_B is greater than 50%.

After the fit of two parameters, the accuracy of the inversion technique is estimated for three fit parameters. If the water constituent values C_P, C_X, and $a_Y(\lambda_0)$ are determined simultaneously at a given bottom depth, the corresponding relative errors show very low values of 0 to 5% generally. The plots are not shown, because the same features can be seen as explained before in the figures 5.5 and 5.6 of two fit parameters. The relative errors decrease with increasing amount of water constituents.

The situation is nearly the same, if the bottom depth is fit parameter together with the water constituent concentrations. The relative errors of z_B and C_X show the same behaviour during the fit of three parameters as before during the fit of two parameters. The higher the concentration of C_X the higher the error of z_B, and the lower the bottom depth the higher the error of C_X. The third fit parameter does not affect the accuracy of z_B and C_X compared to the fit of only z_B and C_X. The only effect of fitting three parameters simultaneously can be seen for the accuracy of the phytoplankton concentration. The relative error of C_P is shown in figure 5.7. For increasing concentration of suspended matter the relative error of C_P increases. The values are larger than 50% for $C_X = 6$ mg/l and $z_B = 0.5$ m. The influence of suspended matter on the phytoplankton concentration decreases, if the bottom depth or the concentration of phytoplankton increases.

The accuracy of the determination of the areal fraction of the two bottom types sediment and macrophyte together with the bottom depth is shown in figure 5.8. The relative error of z_B is below 5% until that bottom depth, where the bottom is detectable, and does not depend on the areal fraction (figure 5.8 left). The relative error of the areal fraction of sediment $f_{a,sed}$ is shown on the right of figure 5.8. The error is also below 5%, if bottom reflectance contributes to the signal at the water surface. The graph of the areal fraction of macrophyte $f_{a,mac}$ shows the same results and is not plotted.

Finally, the error propagation is investigated for the inversion of the four parameter C_P, C_X, $a_Y(\lambda_0)$, and z_B simultaneously in combination with the Hydrolight model error. 488 Hydrolight spectra are calculated using the range of the water constituent concentrations and bottom depths listed in table 5.1 for both bottom types sediment and macrophyte. The mean relative errors are listed in table 5.2. The mean values are low with a maximum of only 8 to 12% for the concentration of suspended matter above macrophytes, for the concentration of phytoplankton above both bottom types, and for the depth of the bottom covered with macrophytes. The mean

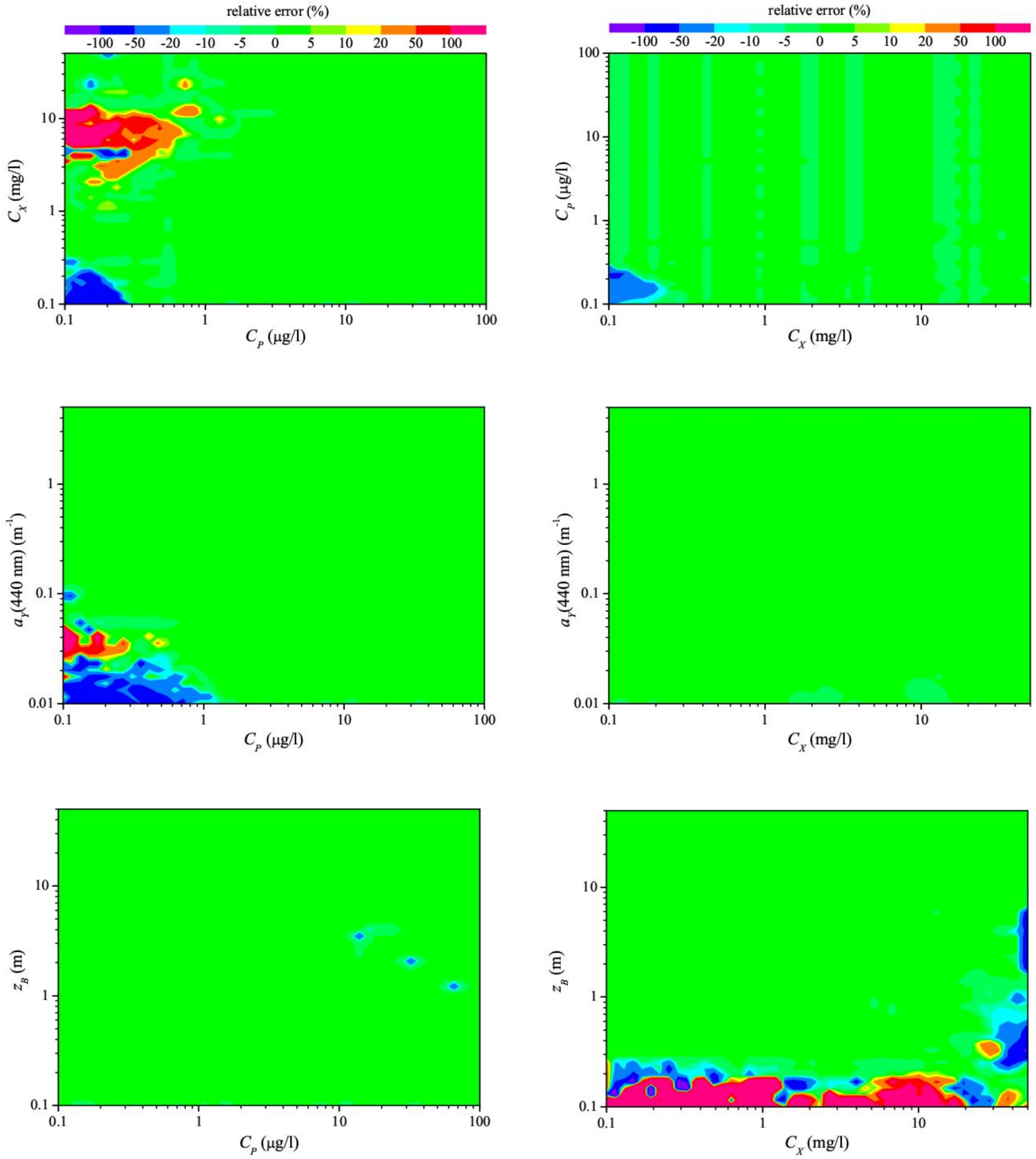

Figure 5.5: Relative error of the simultaneously retrieved concentrations of phytoplankton (left) and suspended matter (right). The second fit parameter is given along the y-axis. If not fitted, $C_P = 2.0$ μg/l, $C_X = 2.0$ mg/l, $a_Y(440\text{nm}) = 0.3$ m^{-1}, and $z_B = 3$ m. The bottom type is sediment.

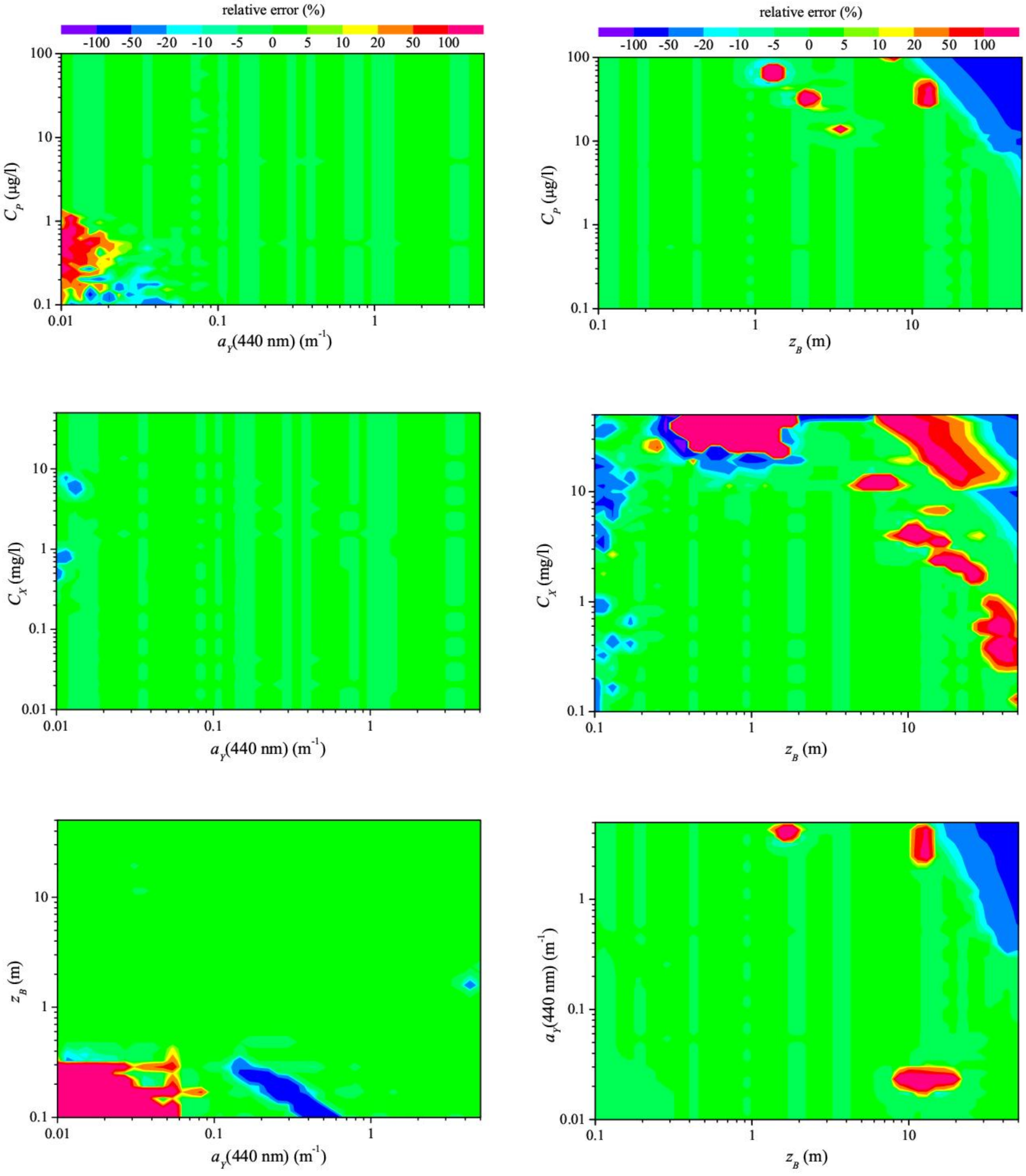

Figure 5.6: Relative error of the simultaneously retrieved gelbstoff absorption (left) and bottom depth (right). The second fit parameter is given along the y-axis. If not fitted, $C_P = 2.0$ μg/l, $C_X = 2.0$ mg/l, $a_Y(440\text{nm}) = 0.3$ m^{-1}, and $z_B = 3$ m. The bottom type is sediment.

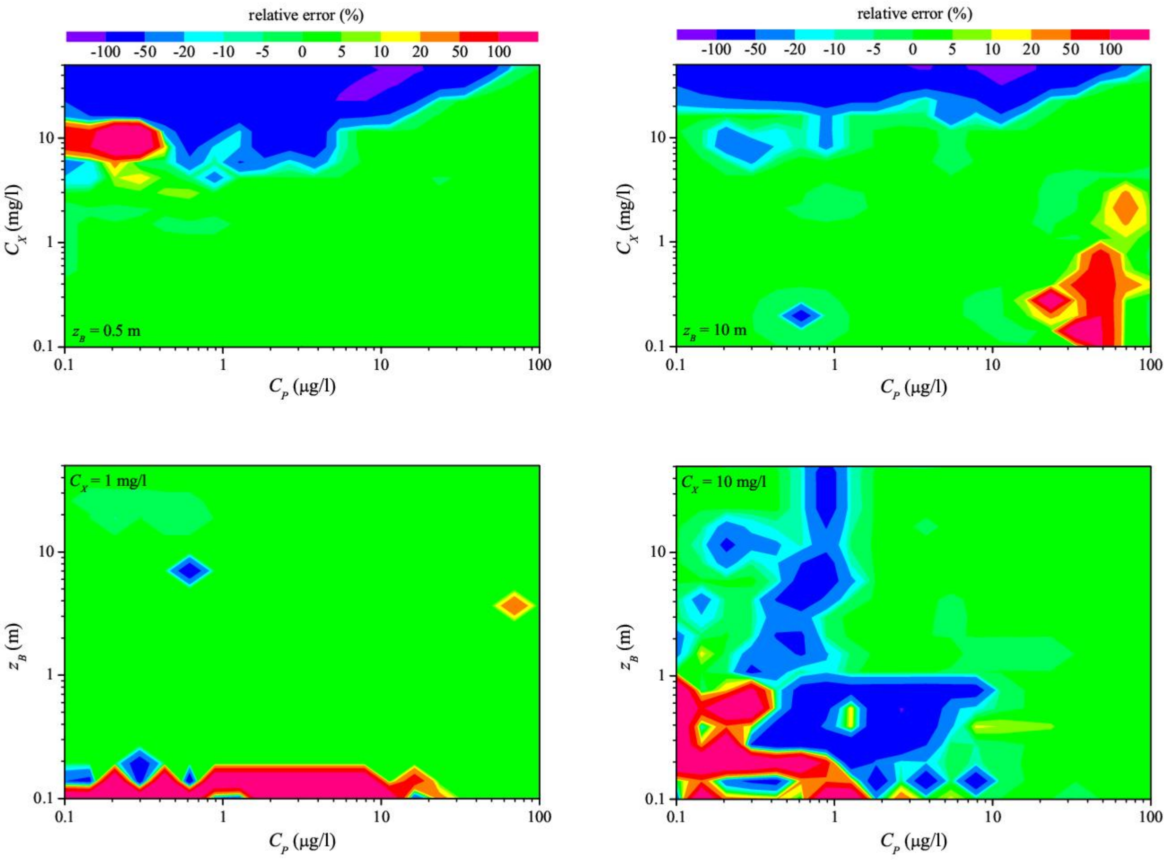

Figure 5.7: Relative error of the retrieved phytoplankton concentration fitting the three parameters C_P, C_X, and z_B simultaneously. The bottom type is sediment.

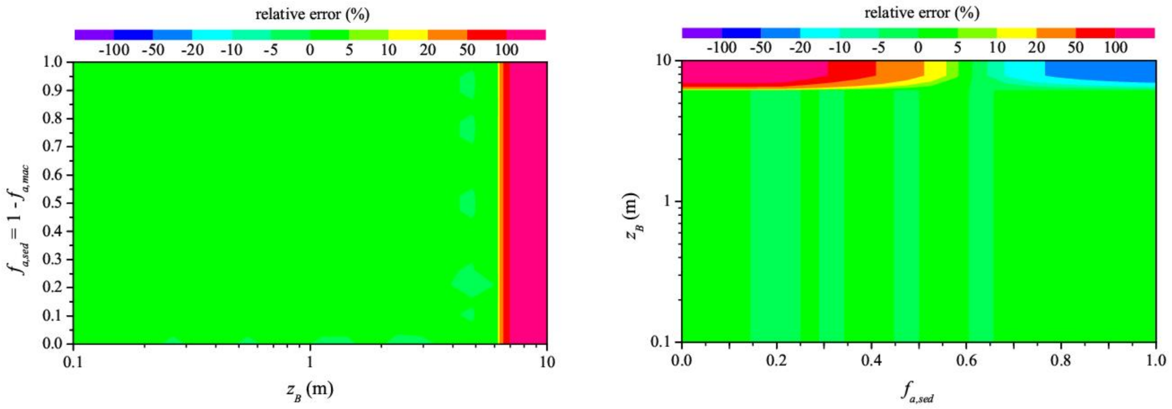

Figure 5.8: Relative error of the retrieved bottom depth (left) and areal fraction of sediment (right) fitting the three parameters z_B, $f_{a,sed}$, and $f_{a,mac}$ simultaneously.

	macrophytes	sediment
$\overline{\delta}_P$ (%)	-7.55	-9.59
$\overline{\delta}_X$ (%)	-10.26	-0.38
$\overline{\delta}_Y$ (%)	1.52	-1.58
$\overline{\delta}_z$ (%)	-11.78	-5.34

Table 5.2: Mean relative error of the phytoplankton concentration $\overline{\delta}_P$, suspended matter concentration $\overline{\delta}_X$, gelbstoff absorption $\overline{\delta}_Y$, and bottom depth $\overline{\delta}_z$ estimated by inversion of Hydrolight spectra for the bottom types sediment and macrophytes. All four parameters are fitted simultaneously.

relative error of $a_Y(\lambda_0)$ is about 2%.

The frequency distribution of the relative errors is shown in figures 5.9 and 5.10. The shape shows a strongly peaked normal distribution around the corresponding mean values listed in table 5.2. Exceptions are the distributions of the relative error of C_P, especially above sediment. Its broad distribution is due to the fact that the retrieval of C_P is very sensitive and strongly affected by the other parameters and their errors as analysed in the error propagation study above. Even for the inversion in deep water without the influence of the bottom, the phytoplankton concentration is very susceptible to errors in the suspended matter concentration and gelbstoff absorption as shown in Gege (2002). Outliers can also be seen for the distribution of the relative error of z_B. They appear at high concentrations of water constituents as explained above.

The error propagation analysis shows the feasibility to estimate water constituent concentrations and bottom characteristics in shallow water by remote sensing. The mean errors of the retrieved parameters are below 10%. Limitations of the water constituent calculation occur for very low bottom depth z_B, and for bottom depth at high optical thickness of water constituents. The results of the error analysis are promising the feasibility to derive water constituent concentration, bottom depth, and bottom type simultaneously in shallow waters.

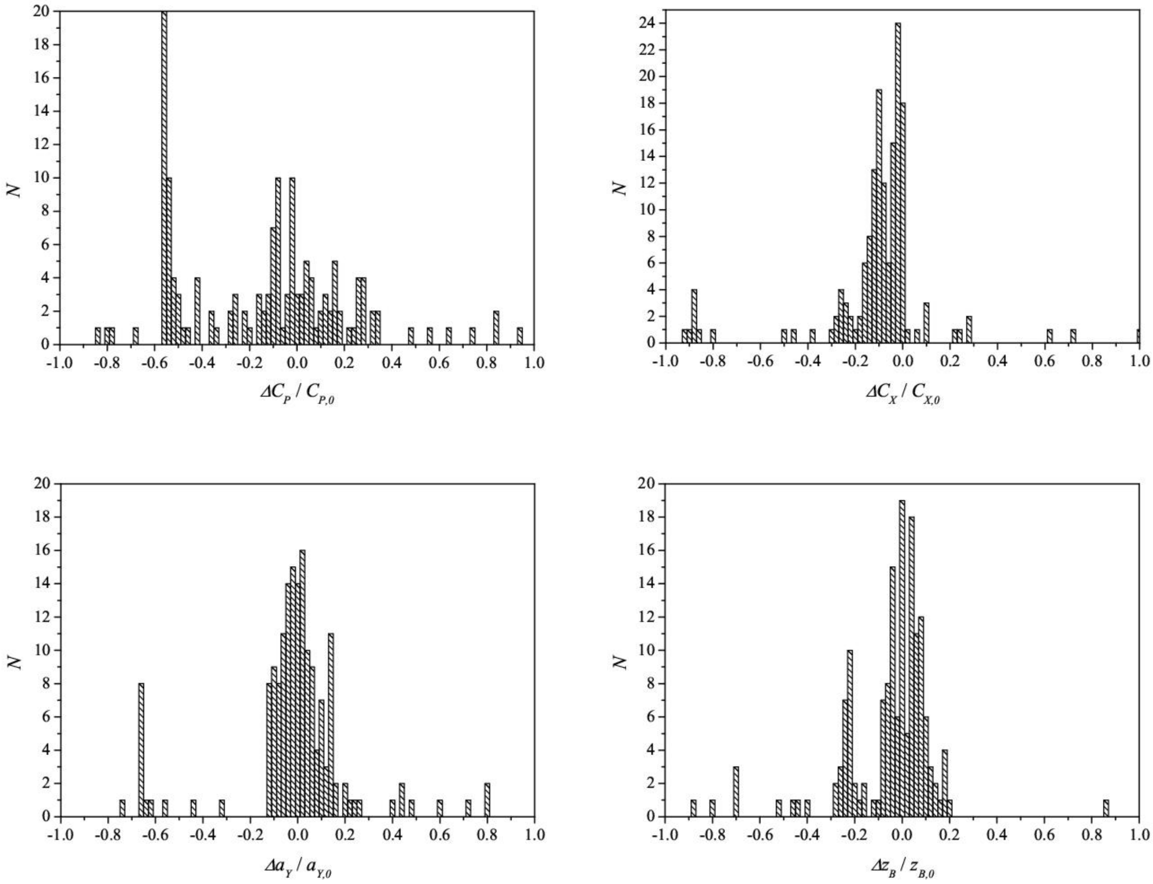

Figure 5.9: Relative error frequency distributions for the concentration of phytoplankton (top left), suspended matter (top right), gelbstoff absorption (bottom left), and bottom depth (bottom right) using Hydrolight spectra of the remote sensing reflectance and fitting all four parameters simultaneously. The bottom type is sediment.

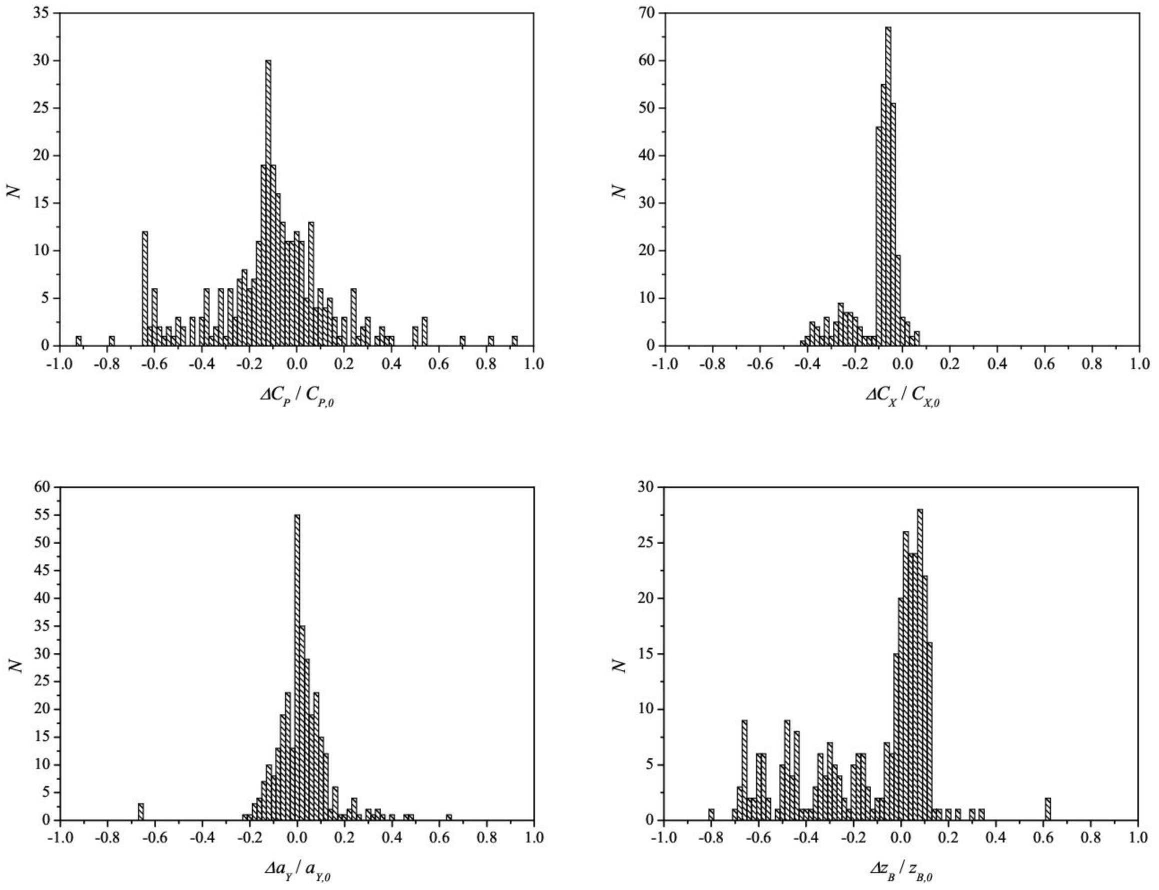

Figure 5.10: Relative error frequency distributions for the concentration of phytoplankton (top left), suspended matter (top right), gelbstoff absorption (bottom left), and bottom depth (bottom right) using Hydrolight spectra of the remote sensing reflectance and fitting all four parameters simultaneously. The bottom type is macrophyte.

5.3 Signal noise, radiometric and spectral resolution

This chapter describes the effect of instrument characteristics on the accuracy of the parameter retrievals. A sensor, which detects irradiance or remote sensing reflectance, R or R_{rs}, is characterised by its signal noise δ, radiometric resolution ΔR, and spectral resolution $\delta\lambda$. The software WASI is able to account for and simulate these effects.

For the simulations, the spectral resolution $\Delta\lambda$ was set to 1, 5, 10, and 20 nm. The radiometric resolution was treated as an irrelevant error source ($\Delta R < 10^{-8}$) and additionally introduced as a reduced dynamics of $\Delta R = 10^{-3}$. This value is the minimum requirement for ocean colour remote sensing and is realistic for airborne and spaceborne systems (Schulz, 1997). The simulations including signal noise consider its dependence on spectral resolution: the higher the spectral resolution, the higher the signal noise and vice versa. Thus, following investigations of Schulz (1997) and Heege (2000), the signal noise δ was set to is $5 \cdot 10^{-4}$, $3 \cdot 10^{-4}$, $2 \cdot 10^{-4}$, and $1 \cdot 10^{-4}$, for spectral resolutions of 1, 5, 10, and 20 nm, respectively. Since signal noise disturbs statistically the spectrum, ten calculations were made for each combination. For comparison, calculations with $\Delta\lambda = 1$ nm, $\delta = 0$, $\Delta R = 0$ and $\Delta\lambda = 1$ nm, $\delta = 5 \cdot 10^{-4}$, $\Delta R = 0$ were done additionally. The influence of $\delta = 5 \cdot 10^{-4}$ and $\Delta R = 10^{-3}$ on the remote sensing reflectance spectrum is graphically shown in figure 5.11 for $C_P = 2$ μg/l, $C_X = 2$ mg/l, $a_Y(\lambda_0) = 0.3$ m^{-1}, and the bottom type sediment at $z_B = 3$ m.

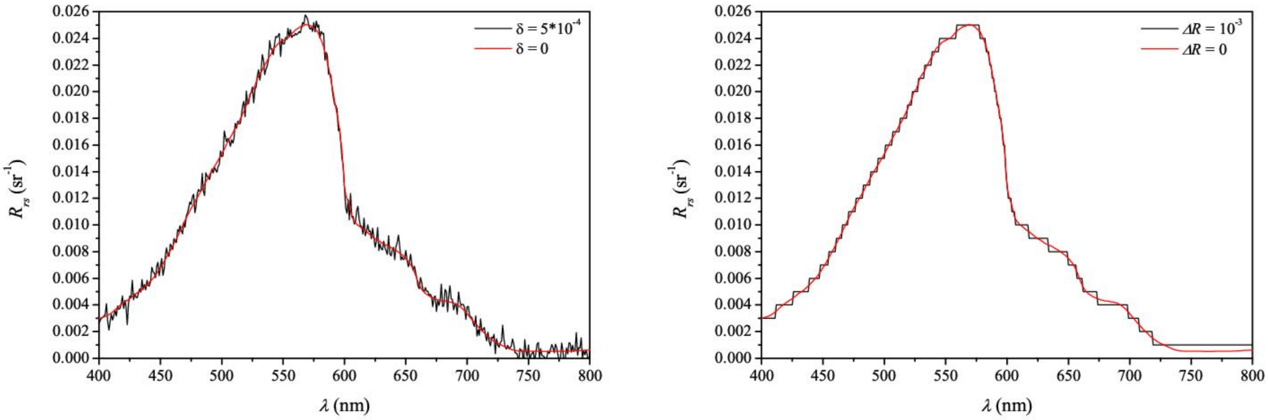

Figure 5.11: Influence of signal noise δ (left) and radiometric resolution ΔR (right) on the spectrum of the remote sensing reflectance calculated for $C_P = 2$ μg/l, $C_X = 2$ mg/l, $a_Y(440\text{nm}) = 0.3$ m^{-1}, and $z_B = 3$ m. The bottom type is sediment.

The results are shown in the figures 5.12 to 5.16 for the water constituent concentrations, bottom depth, and the areal fraction using the two bottom types sediment and macrophytes. The mean relative errors of C_P, C_X, $a_Y(\lambda_0)$, $\lambda_0 = 440$ nm, and z_B are listed in table 5.3. For areal fraction of sediment $f_{a,sed}$ and macrophytes $f_{a,mac}$ they are given in table 5.4. If not fitted during the inversion, the parameters are fixed at their correct values $C_P = 2$ μg/l, $C_X = 2$ mg/l,

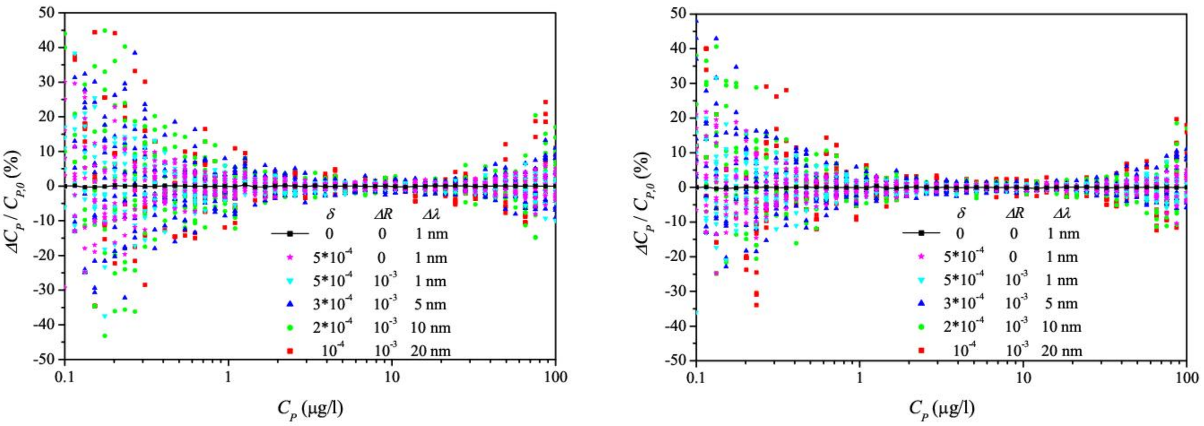

Figure 5.12: Relative error of retrieved phytoplankton concentration estimated by inversion depending on signal noise δ, radiometric and spectral resolution, ΔR and $\Delta\lambda$, respectively. The other parameters are fixed at $C_X = 2$ mg/l, $a_Y(440\text{nm}) = 0.3$ m^{-1}, and $z_B = 3$ m. The bottom types are sediment (left) and macrophytes (right).

$a_Y(\lambda_0) = 0.3$ m^{-1}, and $z_B = 3$ m. The results are shown only for inverting remote sensing reflectances. Similar results are obtained for the irradiance reflectance.

The relative error of all parameters is negligible ($< 1\%$), if the signal includes no noise, full radiometric resolution, and spectral resolution of 1 nm. When adding statistical signal noise, most of all bottom depth is affected. The maximum detectable bottom depth $z_{B,max}$ decreases, depending on the bottom type, from $\sim 20 - 22$ m to $\sim 11 - 12$ m. The relative error of z_B increases rapidly to more than 100% for greater depth. This is due to the fact that the signal noise reduces the spectral differences between 600 and 700 nm. The mean relative error of z_B is below 1% in the detectable range. The influence of noise, radiometric and spectral resolution on the concentration of phytoplankton and suspended matter is low for concentrations above 1 μg/l and 1 mg/l, respectively. The relative error is below 10% and increases with increasing noise and decreasing radiometric and spectral resolution especially for concentrations below 0.5 μg/l and 0.5 mg/l, respectively. The relative error of $a_Y(\lambda_0)$ is below 5% and increases for decreasing spectral resolution to about 10% over the entire range from 0.01 to 5.00 m^{-1}. The accuracy of the estimated areal fractions of sediment and macrophyte are strongly affected by the sensor characteristics. Especially if the areal fraction is below 0.5, the relative error of $f_{a,sed}$ and $f_{a,mac}$ is larger than 50%. The relative error of $f_{a,sed}$ is a little bit higher than for $f_{a,mac}$, because bottom reflectance of macrophytes used here has more spectral features. Thus, the influence of macrophytes is detectable over a wider spectral range than for sediment.

	$\delta = 0$ $\Delta R = 0$ $\Delta\lambda = 1$ nm	$\delta = 5 \cdot 10^{-4}$ $\Delta R = 0$ $\Delta\lambda = 1$ nm	$\delta = 5 \cdot 10^{-4}$ $\Delta R = 10^{-3}$ $\Delta\lambda = 1$ nm	$\delta = 3 \cdot 10^{-4}$ $\Delta R = 10^{-3}$ $\Delta\lambda = 5$ nm	$\delta = 2 \cdot 10^{-4}$ $\Delta R = 10^{-3}$ $\Delta\lambda = 10$ nm	$\delta = 10^{-4}$ $\Delta R = 10^{-3}$ $\Delta\lambda = 20$ nm
sediment						
$\overline{\delta}_P$ (%)	<1	2.87	3.03	4.69	5.69	6.13
$\overline{\delta}_X$ (%)	<1	3.57	4.33	6.33	7.40	7.69
$\overline{\delta}_Y$ (%)	<1	1.09	1.30	1.81	2.35	2.65
$\overline{\delta}_z$ (%)	<1	<1	<1	<1	<1	<1
$z_{B,max}$ (m)	20.5	17.0	16.0	14.5	12.5	11.5
macrophytes						
$\overline{\delta}_P$ (%)	<1	2.26	2.37	3.65	3.85	5.07
$\overline{\delta}_X$ (%)	<1	3.82	5.32	6.52	6.71	8.17
$\overline{\delta}_Y$ (%)	<1	<1	<1	1.47	1.62	1.88
$\overline{\delta}_z$ (%)	<1	<1	<1	<1	<1	<1
$z_{B,max}$ (m)	21.5	16.5	15.5	15.0	14.0	13.0

Table 5.3: Mean relative error of retrievals of phytoplankton concentration $\overline{\delta}_P$, suspended matter concentration $\overline{\delta}_X$, gelbstoff absorption $\overline{\delta}_Y$, and bottom depth $\overline{\delta}_z$ depending on signal noise δ, radiometric and spectral resolution, ΔR and $\Delta\lambda$, respectively. Each combination is calculated ten times. The ranges of the parameters are $0.1 \leq C_P \leq 100.0$ μg/l, $0.1 \leq C_X \leq 50.0$ mg/l, $0.01 \leq a_Y(440\text{nm}) \leq 5.00$ m^{-1}, and 0.1m $\leq z_B \leq z_{B,max}$. $z_{B,max}$ denotes the maximum detectable bottom depth. If not fitted, the parameters are fixed at $C_P = 2$ μg/l, $C_X = 2$ mg/l, $a_Y(440\text{nm}) = 0.3$ m^{-1}, and $z_B = 3$ m. The bottom types are sediment and macrophytes.

	$\delta = 0$ $\Delta R = 0$ $\Delta\lambda = 1$ nm	$\delta = 5 \cdot 10^{-4}$ $\Delta R = 0$ $\Delta\lambda = 1$ nm	$\delta = 5 \cdot 10^{-4}$ $\Delta R = 10^{-3}$ $\Delta\lambda = 1$ nm	$\delta = 3 \cdot 10^{-4}$ $\Delta R = 10^{-3}$ $\Delta\lambda = 5$ nm	$\delta = 2 \cdot 10^{-4}$ $\Delta R = 10^{-3}$ $\Delta\lambda = 10$ nm	$\delta = 10^{-4}$ $\Delta R = 10^{-3}$ $\Delta\lambda = 20$ nm
$\overline{\delta}_{sed}$ (%)	<1	3.52	3.57	8.36	5.94	3.44
$\overline{\delta}_{mac}$ (%)	<1	2.75	3.94	5.65	3.53	3.15

Table 5.4: Mean relative error of the retrieved fraction of sediment $\overline{\delta}_{sed}$ and macrophytes $\overline{\delta}_{mac}$ depending on signal noise δ, radiometric and spectral resolution, ΔR and $\Delta\lambda$, respectively. Each combination is calculated ten times. The areal fractions range from 0 to 1, whereby the sum is always 1. The other parameters are fixed at $C_P = 2$ μg/l, $C_X = 2$ mg/l, $a_Y(440\text{nm}) = 0.3$ m^{-1}, and $z_B = 3$ m.

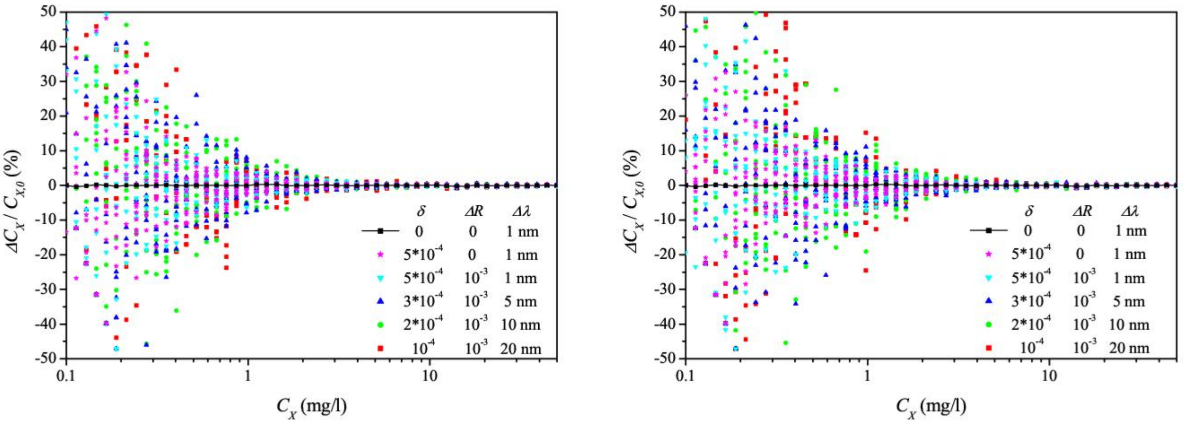

Figure 5.13: Relative error of retrieved suspended matter concentration depending on signal noise δ, radiometric and spectral resolution, ΔR and $\Delta\lambda$, respectively. The other parameters are fixed at $C_P = 2$ μg/l, $a_Y(440\text{nm}) = 0.3$ m^{-1}, and $z_B = 3$ m. The bottom types are sediment (left) and macrophytes (right).

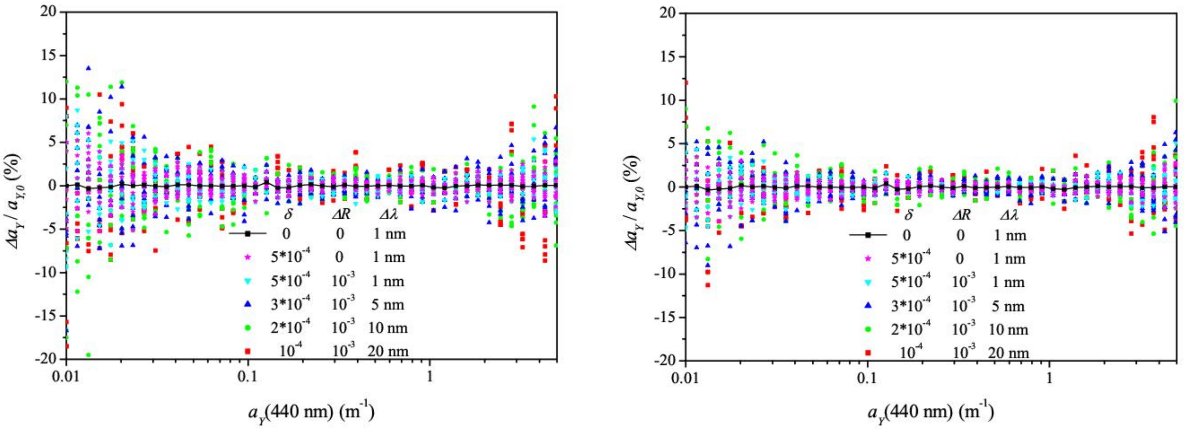

Figure 5.14: Relative error of retrieved gelbstoff absorption depending on signal noise δ, radiometric and spectral resolution, ΔR and $\Delta\lambda$, respectively. The other parameters are fixed at $C_P = 2$ μg/l, $C_X = 2$ mg/l, and $z_B = 3$ m. The bottom types are sediment (left) and macrophytes (right).

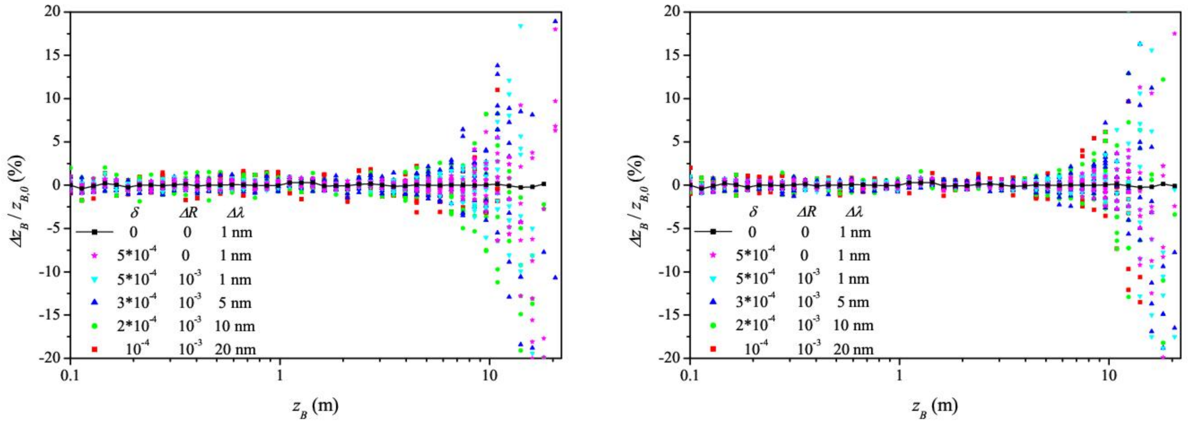

Figure 5.15: Relative error of retrieved bottom depth depending on signal noise δ, radiometric and spectral resolution, ΔR and $\Delta\lambda$, respectively. The other parameters are fixed at $C_P = 2$ μg/l, $C_X = 2$ mg/l, and $a_Y(440\text{nm}) = 0.3$ m^{-1}. The bottom types are sediment (left) and macrophytes (right).

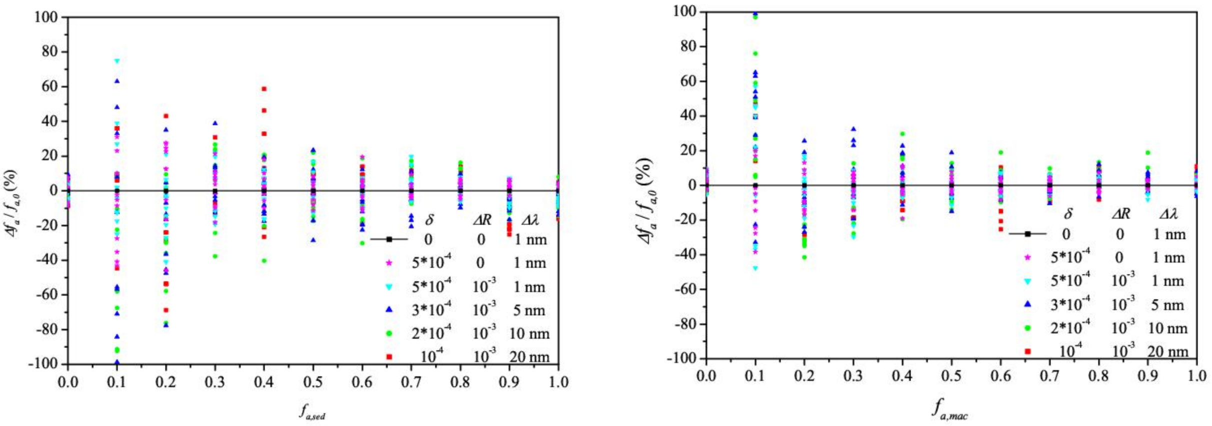

Figure 5.16: Relative error of retrieved areal fraction of sediment (left) and macrophytes (right) depending on signal noise δ, radiometric and spectral resolution, ΔR and $\Delta\lambda$, respectively. The other parameters are fixed at $C_P = 2$ μg/l, $C_X = 2$ mg/l, $a_Y(440\text{nm}) = 0.3$ m^{-1}, and $z_B = 3$ m.

5.4 Inversion of measurements

After the description of model errors, error propagation, and the influence of sensor characteristics on the accuracy of the inversion procedure in the last paragraphs, this part of chapter 5 shows the results of the inversion of in-situ measurements made in Lake Constance at the 51 stations shown in the map of figure 5.17. The optical measurements were made during campaigns from 1998 to 2002 in deep and shallow water using the instruments HYDRA (1998 to 2000) and RAMSES (2001 to 2002). The water constituent concentrations were determined by analysing water samples. A detailed description of the in-situ instruments and methods is given in appendix A.

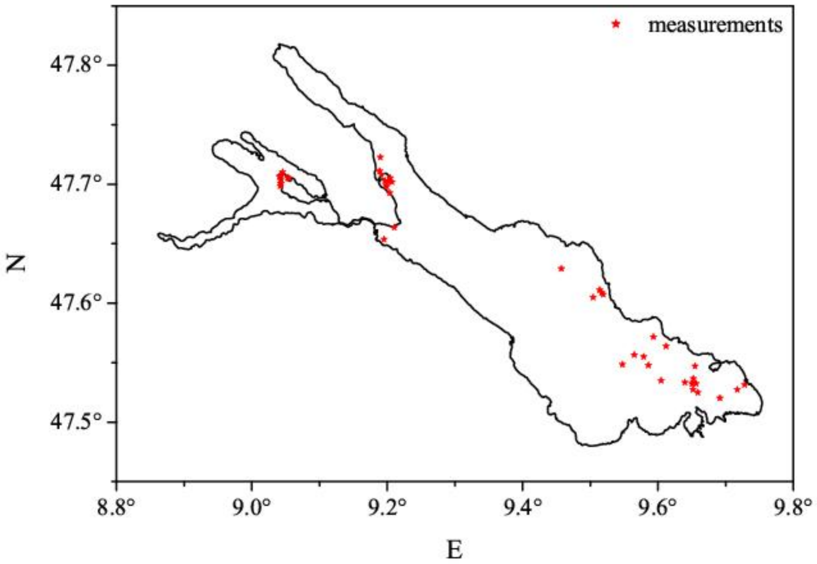

Figure 5.17: Map of Lake Constance with 51 in-situ stations.

The figures 5.18 and 5.19 show the comparisons between water constituent concentrations plus bottom depth derived from in-situ measurements and the inversion of remote sensing and irradiance reflectances measured just below the water surface. Wavelengths from 660 to 715 nm were excluded during the fits due to the neglection of chlorophyll fluorescence in the parameterisations. The values of the in-situ concentrations are plotted including error bars assuming an uncertainty of 10% for $C_{P,0}$, $C_{X,0}$, and $a_{Y,0}(\lambda_0)$ at $\lambda_0 = 440$ nm, but this can be higher (see appendix A). For the in-situ bottom depth $z_{B,0}$ the error bar depends on the situation: estimations before 2000 were made without sonar altimeter and therefore have a higher variability than 10%; also measurements within macrophytes resulted in higher fluctuations due to varying growing height of the plants in an observed patch. For the discussion of the scatter plots it is important to remember the influence of different error sources. A detailed description of possible error sources was given in chapter 3.3. A brief summary is listed below:

- Optical in-situ data are taken at variable depth of 10 to 100 cm below the water surface, due to waves and ship movements.
- Low sensitivity of the optical sensors in the blue part of the spectrum due to the decreasing quantum efficiency of the detector material silicon.
- Scattered light in the spectrometer unit of the instrument affects the signal mainly in the blue.
- Sensor characteristics like non-linearity, temperature dependence, and dark current have a direct influence on the signal.
- Changes of the specific optical properties of phytoplankton and suspended matter are not considered.
- Phytoplankton and suspended matter with sizes $< 1\ \mu$m are not considered.
- The phytoplankton concentration is determined from chlorophyll-a and pheophytin concentration, but there are additional components like for example chlorophyll-b, phycocyanin, phycoerythrin, and carotenoids, which have an influence on the remote sensing signal.
- The optical measurements and the water samples were not taken simultaneously, and not exactly at the same location.
- During the optical measurements, a spectral mismatch of L_u and E_u to E_d leads to spectral noise in the calculated reflectance spectra.
- Errors in phytoplankton and suspended matter concentration caused by a wrong handling during filtering, extraction, and weighing.
- The bottom albedo used for the calculation may be different to the actual one, due to different composition and a sloping bottom.
- The accuracy of the bottom depth value can be low due to a sloping bottom and the movement of the ship.
- The near shore specific optical properties of suspended matter can vary due to the resuspension of all kinds of particles by waves.

The calibration of the instruments is difficult in the blue spectrum. This affects mainly the determination of gelbstoff absorption and phytoplankton concentration. An underestimation of gelbstoff yields an overestimation of phytoplankton concentration and vice versa. Especially early HYDRA measurements in 1998 show calibration problems and high noise for wavelengths below 450 nm (red points in figures 5.18 and 5.19).

Despite all these potential error sources the phytoplankton concentrations determined by inversion using the remote sensing reflectance are mainly within the 10% error range of the in-situ determined values. Only few outliers show a higher deviation. The estimations of C_P using the irradiance reflectance show differences above 10%. Even deviations of 30% and more exist.

Similar results are obtained for gelbstoff. The distribution of the differences varies from 10% to more than 50%. But only a small range of $a_Y(\lambda_0)$ was observed: most measured values of gelbstoff are between 0.2 and 0.3 m^{-1}. To get a more reliable conclusion, further investigations for a wider range of gelbstoff absorption have to be made in the future.

The mean value of gelbstoff absorption is 0.28 m^{-1} with a standard deviation of 0.06 m^{-1}. This mean value of gelbstoff was used to investigate if the outliers of C_P are the result of gelbstoff errors (see figure 5.20). The inversion was performed first using the fixed gelbstoff absorption of 0.28 m^{-1}. To get the variations of the values determined by inversion, additional calculations were made with $a_Y(\lambda_0) = 0.22\ \mathrm{m}^{-1}$ and 0.34 m^{-1}. These small variations of gelbstoff absorption cause deviations of phytoplankton concentration of up to 100% bringing the outliers into the range of the 1:1-line. Thus, as already described in section 5.2, the concentration of phytoplankton is the most sensitive parameter during the inversion.

This is also obvious in figure 5.21. The simultaneous inversion of all parameters leads to an almost perfect fit of the spectrum, but underestimates gelbstoff by 56% and overestimates the phytoplankton concentration by 88% (red line). If the gelbstoff absorption is fixed during the inversion, the fit differs up to about 10% in the blue part of the spectrum (400 to 450 nm), but all parameters are estimated correctly. Thus, small errors can cause great errors in the calculation of the water constituent concentrations, especially of phytoplankton concentration.

For suspended matter, the results of the inversion show the same behaviour for remote sensing and irradiance reflectance: the linear correlation between in-situ and retrieved values is good (correlation coefficient $r > 0.7$), but the values calculated by inversion are systematically higher than the in-situ estimates. This indicates that the specific backscattering coefficient of suspended matter of 0.0086 m^2/g is too low. An increase of 30% for R_{rs} and 60% for R would yield a better correlation (blue dotted lines of the graph of C_X in figures 5.18 and 5.19). This can be due to variations of the particle size distribution and the scattering phase function.

One example of failing the determination of water constituent concentrations and bottom depth by inversion is illustrated in figure 5.22. The fit of the measurement (red line) matches indeed between 450 and 600 nm, but the spectrum of R_{rs} calculated using the in-situ estimated parameters (green line) is 30 to 50% lower compared to the measured spectrum. This systematic difference can be due to problems during the measurement, for example a sloping position of the instrument. Thus, to investigate the scaling problem, a second fit (blue line) was performed using the remote sensing reflectance of water parameterised by $R_{rs,\infty} = f^\circ/Q \cdot \omega_b$ instead of the new parameterisation. A constant f-factor of $f^\circ = 0.50$ was used according to the results about the f-factor described in chapter 3.2.1 and plotted in figure 4.2. The Q-factor was also fitted and a value of $Q = 1.92$ sr was estimated, and the results of the water constituents and the bottom depth match much better. An additional problem occurs due to missing values in the blue and infrared part of the spectrum, which makes the inversion more difficult.

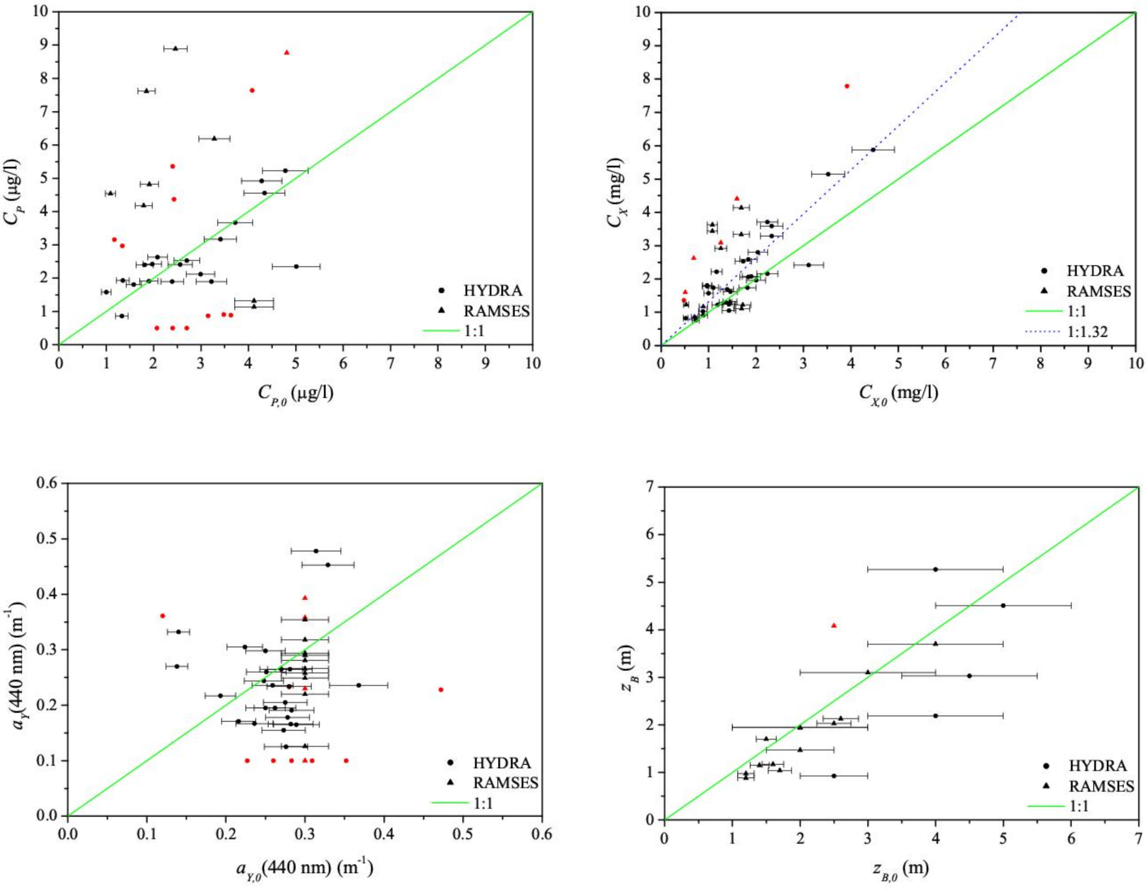

Figure 5.18: Comparisons between retrieved and in-situ (index 0) concentration of phytoplankton, suspended matter, gelbstoff absorption, and bottom depth using remote sensing reflectance measured by the HYDRA and RAMSES instruments in Lake Constance. The red points signal missing values: (1) in the blue part of the spectra leading to errors in phytoplankton and gelbstoff estimates; (2) in the red and near infrared part leading to errors in suspended matter and bottom depth estimates. The blue dotted line in the graph of C_X (top right) indicates the regression line of all values.

The calculations of bottom depth from remote sensing reflectance measurements correlate well with the in-situ values of the bottom depth in view of the mentioned error sources. The observed bottom depths range from 1 to 5 m. The majority of the in-situ values are underestimated by the inversion of the in-situ spectra. The retrievals using the irradiance reflectance show larger deviations. One reason could be that variations of the environment affect more the upwelling irradiance than the upwelling radiance due to hemispherical view of the sensor. More simulations and observations in a wider range of z_B have to be made in the future to ensure this assumption.

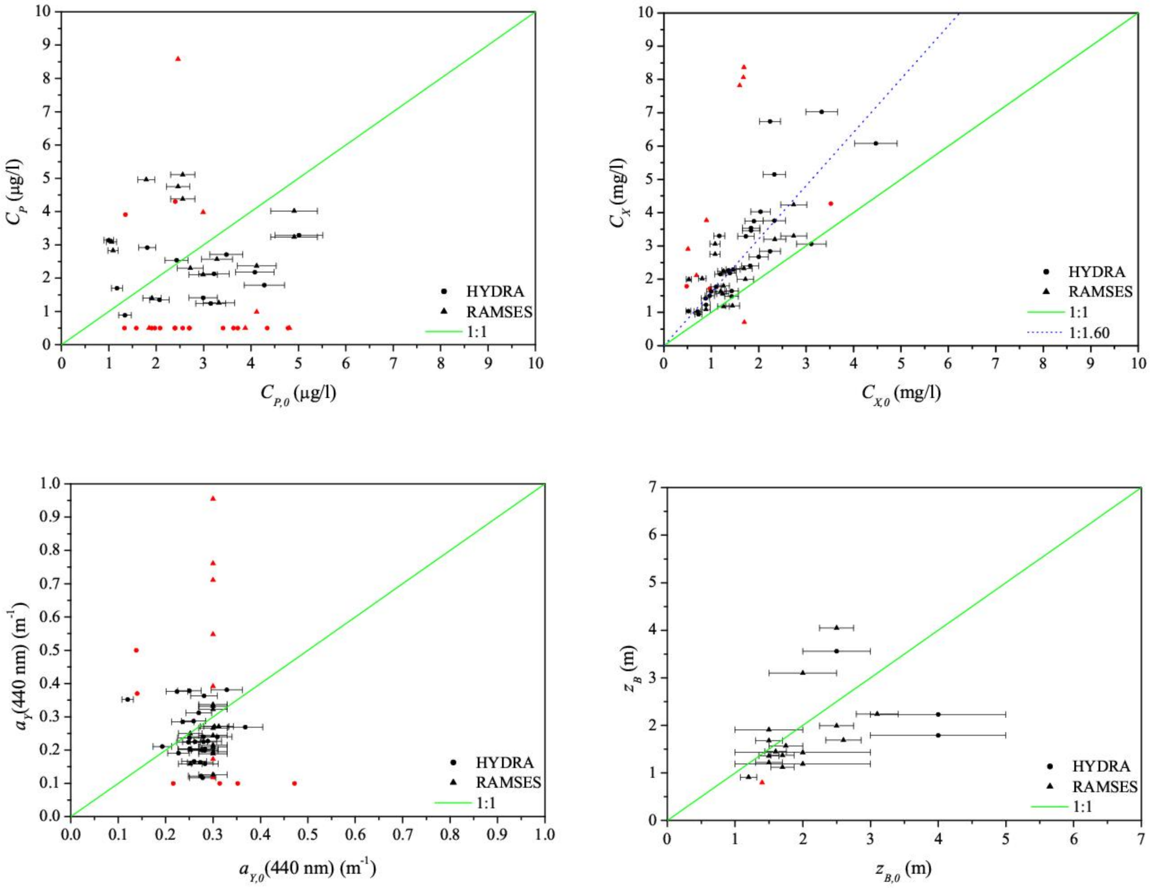

Figure 5.19: Comparisons between retrieved and in-situ (index 0) concentration of phytoplankton, suspended matter, gelbstoff absorption, and bottom depth using irradiance reflectance measured by the HYDRA and RAMSES instruments in Lake Constance. The red points mark incomplete measurements: (1) in the blue part of the spectra leading to erroneous phytoplankton and gelbstoff estimates; (2) in the red and near infrared part leading to erroneous suspended matter and bottom depth estimates. The blue dotted line in the graph of C_X (top right) indicates the regression line of all values.

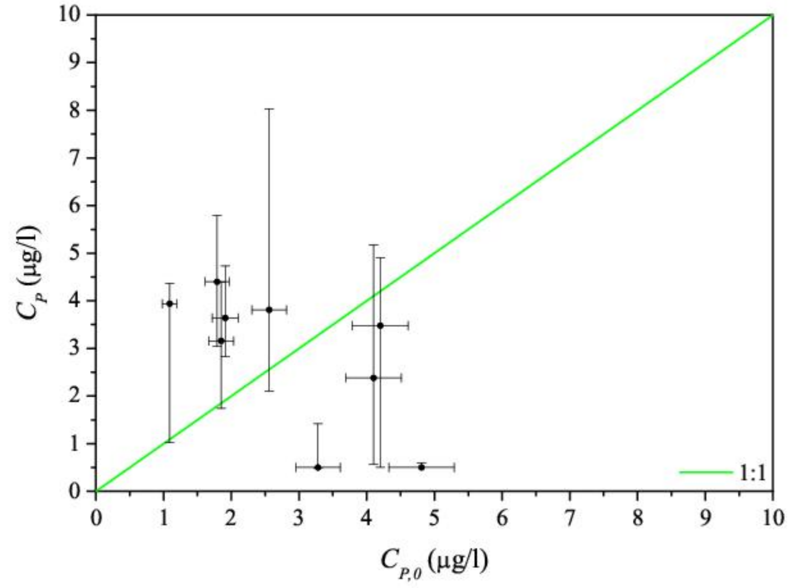

Figure 5.20: Reanalysis of outliers of the phytoplankton concentration retrieval using fixed gelbstoff absorption $a_Y(440\text{nm}) = 0.28\ \text{m}^{-1}$. The error bars of the retrieved values are calculated assuming a standard deviation of gelbstoff absorption of $0.06\ \text{m}^{-1}$.

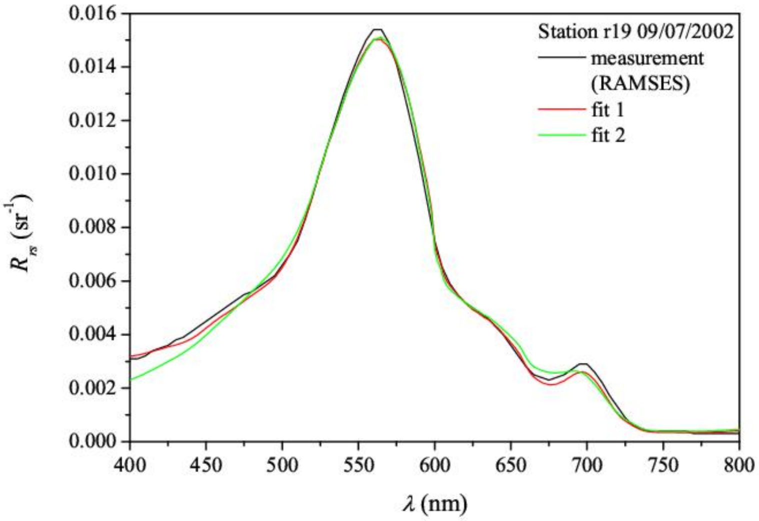

Figure 5.21: Inversion of the in-situ measurement (black) in Lake Constance of station "r19" from 09/07/2002. The bottom at depth 2.6 m was covered by *Characeae*; the analysis of the water samples resulted in $C_P = 3.3\ \mu$g/l, $C_X = 1.5$ mg/l, $a_Y(440\text{nm}) = 0.30\ \text{m}^{-1}$. The bottom type was fixed during the inversion. Fit 1 (red) shows the curve for the simultaneous retrieval of $C_P = 6.2$ μg/l, $C_X = 1.3$ mg/l, $a_Y(440\text{nm}) = 0.13\ \text{m}^{-1}$, and $z_B = 2.1$ m. During fit 2 (green) the gelbstoff absorption at 440 nm was fixed at $0.30\ \text{m}^{-1}$, and the inversion changed to $C_P = 2.6\ \mu$g/l, $C_X = 1.5$ mg/l, and $z_B = 2.6$ m.

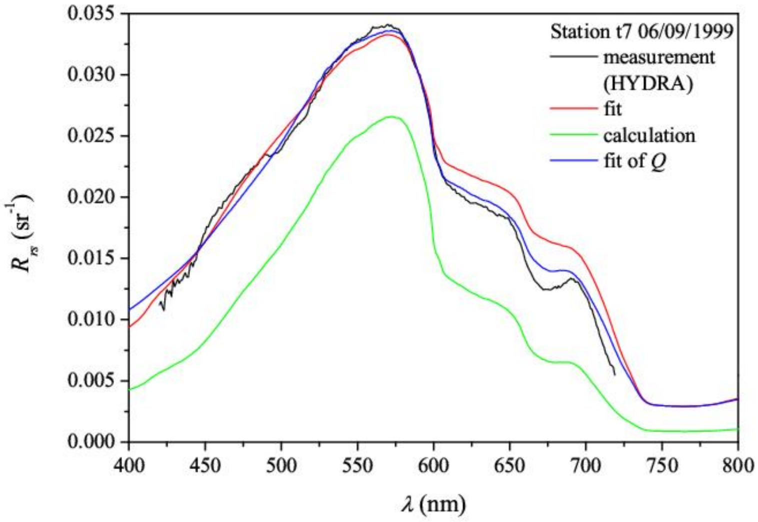

Figure 5.22: Inversion of the in-situ measurement (black) in Lake Constance of station “t7” from 06/09/1999. The forward calculation (green) is also plotted, using the in-situ data: $C_P = 3.5$ μg/l, $C_X = 3.3$ mg/l, $a_Y(440\text{nm}) = 0.33$ m^{-1}, and sediment at $z_B = 2.4$ m. The fit (red) gave $C_P = 0.91$ μg/l, $C_X = 10.5$ mg/l, $a_Y(440\text{nm}) = 0.45$ m^{-1}, and $z_B = 0.9$ m. The second fit (blue) was performed assuming a scaling error, hence the remote sensing reflectance of water was parameterised as $R_{rs,\infty} = 0.50/Q \cdot \omega_b$, and Q was additional fit parameter. The results then are $C_P = 5.62$ μg/l, $C_X = 3.62$ mg/l, $a_Y(440\text{nm}) = 0.34$ m^{-1}, $z_B = 4.7$ m, and $Q = 1.92$ sr. The bottom type was fixed during the inversion.

Finally, the accuracy of the inversion technique concerning the estimation of the bottom type and the areal fractions of different bottom types within the field of view was assessed. The bottom type was determined from the ship by direct observation and/or photographs. Table 5.5 lists the results of the differentiation between sediment and macrophytes. The water constituent concentrations C_P, C_X, and $a_Y(\lambda_0)$, the bottom depth z_B and the areal fractions $f_{a,sed}$ and $f_{a,mac}$ were determined simultaneously. The values of the areal fraction vary between 0 and 1 and were rounded to the first decimal place, because the in-situ observation did not lead to higher accuracy. The errors are below 20% for most cases. The maximum error of 60% occured for a mixed bottom type. These high discrepancies occur, if the real bottom reflectance differs much from the bottom reflectances used for the inversion. This can be due to varying species of macrophytes or changes of epiphytes on macrophytes and sediment in the sensor's field of view as described in chapter 2.5.

Summarising, the inversion technique was tested for measurements in Lake Constance. The results for suspended matter concentration and bottom depth are promising. Also the determination of areal fractions of different bottom types makes hope for good results from remote sensing data. Further investigations especially on instrument calibration are needed to reduce the errors in retrievals of phytoplankton concentration and gelbstoff absorption. To test the new method for a wider range of water constituent concentrations, bottom types, and bottom depths, waters with different trophical state have to be investigated in the future.

	observation		inversion		error
station	$f_{a,sed}$	$f_{a,mac}$	$f_{a,sed}$	$f_{a,mac}$	$\Delta f_{a,i}$ (%)
r7	1	0	0.8	0.2	20
r10	0.3	0.7	0.2	0.8	10
r11	0	1	0.1	0.9	10
r12	0	1	0.4	0.6	40
r13	1	0	1	0	0
r14	1	0	1	0	0
r15	0	1	0	1	0
r16	0	1	0	1	0
r19	0	1	0	1	0
r21	1	0	1	0	0
r22	0.6	0.4	0	1	60
r23	0	1	0.2	0.8	20

Table 5.5: Retrieval of bottom coverage from in-situ measured remote sensing reflectance for stations in Lake Constance from 09/07/2002. The concentrations C_P, C_X, and a_Y(440nm) as well as the bottom depth were fitted simultaneously. Predetermined bottom reflectances of sediment and macrophytes were chosen to estimate the areal fraction $f_{a,sed}$ and $f_{a,mac}$.

Chapter 6

Conclusion and outlook

This study describes the development and sensitivity analysis of an inversion technique for optical remote sensing (400 to 800 nm) in shallow water, based on radiative transfer and the comparison with in-situ measurements made in Lake Constance.
New analytical parameterisations of the irradiance reflectance and the remote sensing reflectance in deep and shallow case-2 waters were developed using only the inherent optical properties of the water, the bottom albedo, the water depth, the viewing and solar zenith angle, and the surface wind speed. Additionally, new parameterisations for the up- and downward attenuation coefficients were developed (Albert and Mobley, 2003). For the forward simulation of the underwater light field the well-established and validated radiative transfer program Hydrolight (version 3.1) (Mobley et al., 1993; Mobley, 1994) was applied, using specific optical properties of water and bottom measured in Lake Constance. The values of the water constituent concentrations - and therefore the optical properties - were varied over a wide range in order to cover a great variety of waters (see table 3.1). The new model separates the dependencies on inherent optical properties, wind speed, viewing, and solar zenith angle. Thus, their influences can be analysed very easily. The irradiance reflectance and remote sensing reflectance can be calculated about 10^6 times faster using the analytical equations than with Hydrolight or Monte Carlo methods and can be inverted. The set of equations is implemented in the Windows-based software WASI (Gege, 2001; 2004) to provide a user-friendly tool for forward and invers modelling.
Irradiance and remote sensing reflectances agree significantly better with the simulations of Hydrolight than calculations with existing equations, both of deep water (Gordon et al., 1975; Kirk, 1984; Sathyendranath and Platt, 1997) and of shallow water (Maritorena et al., 1994; Lee et al., 1998; Pozdnyakov et al., 2002b). The mean error is about 2 to 3%. A maximum error of about 15% occurs at wavelengths around 685 nm owing to the fluorescence of chlorophyll, which is not included in the system of equations presented here. The spectral shape of the calculations using the new parameterisations fits very well to the Hydrolight simulations. The relative error at a given wavelength is below 5% for the irradiance reflectance and below 10% for the remote sensing reflectance from 400 to 800 nm except around 685 nm. Main error sources are the fluorescence

	$\overline{\delta}$ (%)	σ (%)
C_P	7–9	40
C_X	1–3	10
a_Y	1–2	15
z_B	5–10	10

Table 6.1: Mean relative error $\overline{\delta}$ and standard deviation σ of the phytoplankton concentration C_P, suspended matter concentration C_X, gelbstoff absorption a_Y, and bottom depth z_B estimated by inversion of more than 400 spectra simulated by Hydrolight for the bottom types sediment and macrophytes. All four parameters are fitted simultaneously.

of chlorophyll and gelbstoff. Considering the different error sources of the parameterisation and the in-situ measurements, the comparisons of calculations with in-situ measurements in Lake Constance show good agreement.

Based on the new parameterisations, a new inversion procedure for shallow water applications was developed and included in the software tool WASI using the method of nonlinear curve fitting by means of the search algorithm Simplex (Nelder and Mead, 1965; Caceci and Cacheris, 1984). The iteration starts using an automatical determination of the initial values of the fit parameters. A new and robust methodology was developed for shallow water to find the initial values of water constituent concentrations, bottom depth, and fractions of up to six different bottom types. The performance of the initial value determination was analysed in detail for the relevant parameters. The bottom depth and suspended matter concentration can be estimated analytically at the beginning with an accuracy of about 20 to 40%. Phytoplankton concentration and gelbstoff absorption are initially calculated by the method of nested intervals with an accuracy of about 60 to 80%. The investigations showed that this is sufficient for the following main fit by the search algorithm Simplex. A sensivity analysis was made to estimate the accuracy of the entire inversion procedure including model error, error propagation, and influence of instrument characteristics like noise, radiometric, and spectral resolution. Table 6.1 lists the mean relative errors and standard deviations of the water constituent concentrations and the bottom depth achievable considering model errors and error propagation. Bottom depth and suspended matter concentration can be estimated most exactly, followed by gelbstoff absorption. The determination of phytoplankton concentration is most sensitive.

The mean relative error of z_B is calculated using only the cases where the bottom can be detected. For increasing bottom depth the relative error increases with higher concentrations of the water constituents. The influence of signal noise, reduced radiometric and spectral resolution increases the errors of the water constituent concentrations and the bottom depth to values of 10% and more and restricts the estimation of low water constituent concentrations as well as the detection of the bottom. The inversion technique was tested for measurements in Lake Constance considering different bottom types. Previous studies, for example of Lee et al. (1999) and

Ohde and Siegel (2001), were only made for one type like sandy bottom. Taking into account several error sources, which affect the accuracy of in-situ measurements, the results are consistent. High discrepancies are obvious for phytoplankton due to its high sensitivity to all error sources. Systematic differences of the suspended matter concentration are due to variations of the specific backscattering coefficient and the phase function.

The results for suspended matter concentration and bottom depth are promising. Also the determination of fractions of different bottom types gives hope for good results from remote sensing data. First investigations on the classification of submersed vegetation at Lake Constance by means of the new analytical model and linear spectral unmixing were done by Bogner (2003) and Heege et al. (2003) using multispectral data of the airborne scanner DAEDALUS AADS1268 in Airborne Thematic Mapper (ATM) mode. The scanner has 11 channels in the visible and near-infrared part of the spectrum, a field of view (FOV) of ±43° with an Instantaneous FOV (IFOV) of 2.5 mrad, and was flown at an altitude of about 500 m above ground to get 1 m spatial resolution. The channels 2 to 5 at centre wavelenghts of 485, 560, 615, and 660 nm with Full Width at Half Maximum (FWHM) of 56, 85, 33, and 71 nm, respectively, were used during the thematic processing (atmosphere, water surface, water constituents) in the modular inversion program MIP (Heege et al., 2003; Heege and Fischer, 2004; Heege, 2004). Preprocessing (calibration, masking, georeferencing) was performed using the image analysis software XDibias (Müller et al., 1992; 2002). An example of the results is shown in figure 6.1. Classes of low growing (*Characeae*) and high growing macrophytes (*P. perfoliatus* and *P. pectinatus*) as well as uncovered sediment are distinguished quantitatively. The calculated patterns are in very good agreement with in-situ observations from ship. The influence of the water body was corrected by means of in-situ determined concentrations, and the bottom depth was taken from bathymetry data of Lake Constance measured by the IGKB[1] in 1994 and processed by Christoph Wittkugel at the University of Konstanz. Due to the spectral limitations of the DAEDALUS scanner, it was not possible to calculate these parameters from the remote sensing data in shallow water areas. These remote sensing images provide useful information and are used by biologists and limnologists within the Collaborative Research Centre SFB 454 "Littoral zone of Lake Constance"[2] funded by the German Research Foundation DFG[3].

Further investigations have to be done also on the calibration of the in-situ instruments HYDRA and RAMSES to reduce the error of the phytoplankton concentration and gelbstoff absorption. Due to the implementation into the software WASI, the developed forward and inverse models provide an excellent and fast tool for sensitivity studies, for example investigations on the influence of instrument calibration.

The variability of specific optical properties of phytoplankton and suspended particles have to be analysed carefully in the future to improve the model. Influences of particle size distributions may play an important role especially in shallow water areas. Investigations on the specific

---

[1] Internationale Gewässerschutzkommission für den Bodensee, `http://www.igkb.de`

[2] `http://www.uni-konstanz.de/sfb454`

[3] Kennedyallee 40, 53175 Bonn, Germany, `http://www.dfg.de`

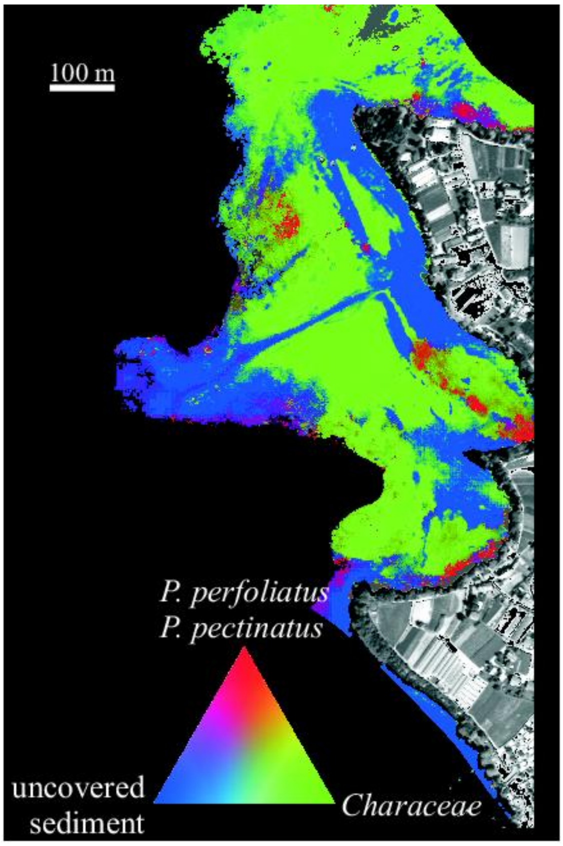

Figure 6.1: Classification of bottom types in the littoral zone of Reichenau island (9.040°E, 47.706°N) at Lake Constance by Bogner (2003) using multispectral airborne remote sensing data of 1 m spatial resolution for an overflight from 11/08/2000 processed by the modular inversion program (Heege et al., 2003; Heege and Fischer, 2004; Heege, 2004). The bottom coverage is distinguished between uncovered sediment and submersed vegetation, which is further divided into low growing macrophytes like *Characeae* and high growing like *P. perfoliatus* and *P. pectinatus*. The new shallow water parameterisations explained in chapter 3.2 were used for the estimation. Black areas assign optically deep water, where the bottom is not detectable.

optical properties (Gege, 2000; Schwarz et al., 2002) of gelbstoff may improve the results as well. To test the new method for a wider range of water constituent concentrations, bottom types, and bottom depths, other water types of different trophical states have to be investigated in the future. Although the initial value determination and inversion procedure was developed and tested for conditions in Lake Constance, the technique can be easily adjusted by changing coefficients, specific optical properties, and bottom conditions. The implementation of an analytical model of chlorophyll and gelbstoff fluorescence, as for example done by Pozdnyakov et al. (2002b), is also expected to improve the accuracy.

The method shall be applied to hyperspectral remote sensing data measured by airborne and spaceborne sensors. Thus, effects of the atmosphere and the water surface on the accuracy of shallow water parameters have to be investigated, for example by the integration of the inversion technique into MIP.

Appendix A

In-situ measurements

This part of the appendix describes the in-situ methods of estimating water constituents concentrations and of optical measurements by shipborne instruments. The water samples were collected in deep water using a Ruttner bottle of 1 m length in 0.5 m depth, i.e. the average concentrations of the depth range from 0 to 1 m were obtained and in shallow water using a opaque plastic bottle in about 0.5 m depth. The biochemical analysis for phytoplankton concentration C_P were done by B. Beese[1] and M. Weyhmüller[2] and for total suspended matter concentration C_X by C. Gebauer[3] and M. Weyhmüller[2].
The optical in-situ measurements were made just below the water surface in about 0.5 to 2 m depth to get irradiance and remote sensing reflectance. The instruments were placed at a distance of 3 to 4 m from the ship's bow which was oriented into the direction of the sun. The bottom albedo was measured by placing the optical sensors about 0 to 30 cm above the different bottom types. Measurements were made during campaigns from 1999 to 2002 with assistance of K. Bochter[4] and T. Heege[5]. Additional data were measured in 1998 by K. Bochter[4].

A.1 Phytoplankton

The concentration of phytoplankton C_P was determined as the sum of the concentration of chlorophyll-a and pheophytin. The chlorophyll-a and pheophytin content was measured photometrically. Depending on the concentration of particulate matter, a volume of 0.5 to 3.0 l of water was filtered through a glass fibre filter (Schleicher & Schuell No. 6 VG[6] or Whatman

---

[1] University of Konstanz, Limnological Institute, Mainaustr. 252, 78464 Konstanz, Germany, `mailto:baerbel.beese@uni-konstanz.de`

[2] Biologiebüro Weyhmüller, Am Königsbühl 15, 88147 Achberg, Germany, `mailto:bbw_weyhmueller@t-online.de`

[3] University of Konstanz, Limnological Institute, Mainaustr. 252, 78464 Konstanz, Germany, `mailto:christine.gebauer@uni-konstanz.de`

[4] Dr. Johannes Heidenhain GmbH, Dr.-Johannes-Heidenhain-Str. 5, 83301 Traunreut, Germany, `mailto:bochter@heidenhain.de`

[5] DLR German Aerospace Center, Remote Sensing Technology Institute, Marine Remote Sensing, Muenchener Str. 20, 82234 Wessling, Germany, `mailto:thomas.heege@dlr.de`

[6] Schleicher & Schuell, Hahnestr. 3, 37582 Dassel, Germany, `http://www.schleicher-schuell.de`

GF/F[7]). The minimum size of particles retained by the glass fibre filters is about 1 μm. The filters were stored after filtration in darkened and cooled boxes to avoid light impact on the pigments. If the filters were not analysed immediately after the collection, they were placed in a refrigerator at about -18°C. The pigments on the filters were extracted with hot ethanol (90%) in the laboratory after the method of Nusch (1980), which is shortly described in the following. Particulate matter was separated by centrifugation. The transmission of the solution containing the pigments was measured at 665 and 750 nm using a photometer. The value at 750 nm is for the correction of the value at 665 nm due to turbidity. The correction of pheophytin was determined by a second photometric measurement after the treatment of the sample by hydrochloric acid (2 mol/l HCl). The concentration of chlorophyll-a C_{chl} in μg/l is given by

$$C_{chl} = (c_{665}^{b} - c_{665}^{a}) \cdot \frac{c_{665}^{b}/c_{665}^{a}}{c_{665}^{b}/c_{665}^{a} - 1} \cdot \frac{v \cdot 10^{3}}{V \cdot l \cdot a_{chl}^{*}} \tag{A.1}$$

with the extinction at 665 nm before and after the acidification, c_{665}^{b} and c_{665}^{a}, respectively. v is the extracted volume in ml, V the volume of filtered water in l, l the length of the cuvette in the photometer in cm, and a_{chl}^{*} the specific absorption coefficient of chlorophyll-a in l g^{-1}cm^{-1}. In ethanol (90%) is $a_{chl}^{*} = 82$ l g^{-1}cm^{-1} and $c_{665}^{b}/c_{665}^{a} = 1.7$. Thus, the concentration of chlorophyll-a and pheophytin, C_{chl} and C_{pheo}, in μg/l is given by

$$C_{chl} = 29.6 \cdot (c_{665}^{b} - c_{665}^{a}) \cdot \frac{v}{V \cdot l} \tag{A.2}$$

$$C_{pheo} = 20.8 \cdot c_{665}^{a} \cdot \frac{v}{V \cdot l} - C_{chl} \tag{A.3}$$

The standard deviation of this method is about 3% for chlorophyll-a concentrations below 5 μg/l and is below 1% for higher concentrations. The accuracy of the estimated concentrations is lower and is assumed to be about 10% due to the impact of the following error sources: (a) inaccuracy in estimating the volume of water during the filtration, (b) light influence and storage time leads to reduction of chlorophyll after the filtration, (c) inaccuracy of the specific chlorophyll-a absorption at 665 nm. These effects may cause higher errors. The intercomparison of 44 water samples from Lake Constance in 2003 analysed by two laboratories resulted in a standard deviation of 19% (Miksa et al., 2004). Gege (1994) investigated the different estimates of the method explained here and the High Performance Liquid Chromatography (HPLC). The comparison of 132 water samples from Lake Constance yielded that the differences of the photometrically estimated chlorophyll-a values and those obtained by HPLC vary about 22% on average. Similar results were found by Van Heukelem et al. (2002) and Zibordi et al. (2002) in coastal and oceanic waters.

An additional error arises due to the fact that the phytoplankton concentration is determined by adding the chlorophyll-a and pheophytin concentration. There are additional components like for example chlorophyll-b, phycocyanin, phycoerythrin, and carotenoids, which have an influence

---

[7] Whatman International Ltd., Whatman House, St Leonard's Road, 20/20 Maidstone, Kent, ME16 0LS, United Kingdom, `http://www.whatman.com`

on the remote sensing signal and are not considered. Besides, the specific optical properties of chlorophyll-a and pheophytin are different. Thus, the physically correct absorption has to be determined by a spectrally weighed sum of both absorptions. No investigations are known, which quantify this influence. Furthermore, pigment bearing particles smaller than 1 μm, for example bacterioplankton, are not considered for the estimation due to the retention efficiency of the filters. The error depends on the observed water body, especially the total amount of these particles. The impact on total absorption is low due to very low values of the absorption efficiency (Morel and Ahn, 1990; Stramski and Mobley, 1997), but the contribution of very small particles on the total scattering can be 50% and more (Babin et al., 2003).

A.2 Suspended matter

The total content of suspended matter - sometimes called seston - is the sum of organic and inorganic particles and was measured gravimetrically by weighing the dry residuum on the filters. As described for the determination of the phytoplankton concentration, a defined volume of water (0.5 to 3.0 l) was filtered through a glass fibre filter (Schleicher & Schuell No. 6 VG[6] or Whatman GF/F[7]). The minimum size of particles retained by the glass fibre filters is about 1 μm. The filters were transported in a cooling box after the filtration to the laboratory and stored in a refrigerator at about -18°C before analysing. The dry weight of the filters was measured before in the laboratory. The weight of total suspended matter was derived as the difference between the dry weight of the filters after and before filtering. The filters were dried in an oven for about two hours at a temperature of 105°C. To estimate the concentration of inorganic particles, the filters were combusted for about four hours at 550°C to remove organic particles. At this temperature the organic connective material contained in the filters is also destroyed. To correct this effect, the weight of the organic substances of the filters was determined by weighing three blank filters before and after combusting. The correction factor was the mean of the three singular results and was derived on every day of a campaign.

The accuracy of the estimated concentration is about 10% due to the following error sources: (a) inaccuracy in estimating the volume of water during the filtration, (b) inaccuracy during the weighing of the filters before and after filtering and drying. The error increases, if the filters were damaged not visibly by improper treatment during filtration, transport, and storage. This impact can not be quantified afterwards. These effects may cause higher errors. The intercomparison of 43 water samples from Lake Constance in 2003 analysed by two laboratories resulted in a standard deviation of 15% (Miksa et al., 2004). Similar standard deviations by comparison of duplicates were obtained by Zibordi et al. (2002) and Ferrari et al. (2003). An additional error source is due to the fact that suspended particles of a size smaller than 1 μm are not considered due to the retention efficiency of the used filters. The effect depends on the observed water body, namely the fraction and size distribution of mineral and algal particles. Theoretical investigations of Babin et al. (2003) showed that mineral particles smaller than 2

μm contribute about 80% to the scattering at 555 nm, and particles smaller than 1 μm about 50%. Algal particles smaller than 1 and 2 μm account about 15 and 30% to the scattering, respectively.

A.3 Gelbstoff

After sampling the water from a depth range of 0 to 1 m, it was filtered on board the ship in two steps: (a) filtering with glass fibre filters retaining particles, which are larger than about 1 μm (Schleicher & Schuell No. 6 VG[6] or Whatman GF/F[7]), to remove particulate material; (b) filtering with membran filters of 0.2 μm pore size (Sartorius Type 11307[8] or Isopore GTTP[9]). The filtered water was filled into small bottles of PVC or glass and stored cool before analysing. Spectral measurements were made onboard the ship within one hour or in the laboratory one or two days later using an ultraviolet-visible double beam spectrometer of the type Varian CARY-1[10] or Perkin-Elmer Lambda-2[11]. The scanning wavelengths are between 190 and 900 nm in 1 nm steps. The instruments detect the transmission of the filtered water sample filled in a quartz cell of the length l. The measured transmission t depends on the wavelength and the temperature T and is a combination of the transmission of the quartz cell $t_c(\lambda)$, pure water $t_W(\lambda, T)$, and gelbstoff $t_Y(\lambda)$:

$$\begin{aligned} t^l(\lambda, T) &= t_c(\lambda) \cdot t_W^l(\lambda, T) \cdot t_Y^l(\lambda) \\ &= t_c(\lambda) \cdot \mathrm{e}^{-[a_W(\lambda,T)+a_Y(\lambda)]\cdot l} \end{aligned} \tag{A.4}$$

The absorption of gelbstoff $a_Y(\lambda)$ is then derived by

$$a_Y(\lambda) = -\frac{1}{l} \ln \left[\frac{t^l(\lambda, T)}{t_c(\lambda)} \right] - a_W(\lambda, T) \tag{A.5}$$

A quartz cell of $l = 10$ cm was used. The influence of the temperature is included in the water absorption. Its correction was estimated by comparing the total absorption at two wavelengths. Thus, the absorption difference at these two wavelengths divided by the difference of the corresponding temperature gradients yields the correction factor. The temperature gradient of water is known from measurements by Gege (1999). Reference measurements of purified water were made separately to account for the transmission of the cuvette and the absorption of pure water. Since 1999, additional measurements by a quartz cell of $l = 5$ cm were made. By comparing the transmission measurements of two different quartz cells of the lengths l_1 and l_2, the effect of the transmission of the quartz cell was removed, and the absorption of gelbstoff can be estimated by

$$a_Y(\lambda) = \frac{1}{l_2 - l_1} \ln \left[\frac{t^{l_1}(\lambda, T)}{t^{l_2}(\lambda, T)} \right] - a_W(\lambda, T) \tag{A.6}$$

---

[8] Sartorius AG, Weender Landstr. 94-108, 37075 Goettingen, Germany, `http://www.sartorius.com`

[9] Millipore Corporation, 290 Concord Rd., Billerica, MA 01821, USA, `http://www.millipore.com`

[10] Varian Inc., 3120 Hansen Way, Palo Alto, CA 94304-1030, USA, `http://www.varianinc.com`

[11] Perkin-Elmer, 45 William Street, Wellesley, MA 02481-4078, USA, `http://www.perkinelmer.com`

The absorption of pure water was considered by means of the spectrum measured by Buiteveld et al. (1994). This avoids problems of varying properties of purified water as a reference, and the gelbstoff absorption is determined consistently as implemented in the radiative transfer modelling. The result of the equations (A.5) and (A.6) were expressed by means of the exponential approximation of the gelbstoff absorption spectrum (Bricaud et al., 1981).

$$a_Y(\lambda) = a_Y(\lambda_0) \cdot \mathrm{e}^{-s_Y(\lambda-\lambda_0)} \tag{A.7}$$

The reference wavelength was chosen at $\lambda_0 = 440$ nm. The values representing the spectral shape of the gelbstoff absorption, $a_Y(\lambda_0)$ and s_Y, were determined by linear regression of the logarithmised equation (A.7).

First systematic optical gelbstoff measurements at Lake Constance were made by Heege et al. (1998) followed by investigations of Gege (1999). Typical values of $a_Y(\lambda_0) = 0.3$ m^{-1} and $s_Y = 0.014$ nm^{-1} were found within the range from 0.2 to 0.5 m^{-1} in deep and shallow water. Gelbstoff absorption greater 1 m^{-1} was found only at the inflow of the river Schussen. The accuracy of the estimated gelbstoff absorption is about 10% due to instrument noise, mechanical alignment of the cuvette, and effects of small bubbles in the water sample. Similar uncertainties were found by Zibordi et al. (2002) through duplicate analysis.

A.4 HYDRA

The Hydrological Spectral Radiometer HYDRA is a spectral multi-beam radiometer and was developed at the Remote Sensing Technology Institute (former Institute of Optoelectronics) of the German Aerospace Center DLR, Wessling (Wallhäußer, 1995; Bochter and Wallhäußer, 1997; Bochter, 2000). The instrument was designed to measure in-situ optical properties of the water body from ship. It consists of two measuring units, one above the water surface with two sensors and one below with seven sensors. The nine signals are recorded simultaneously. The underwater sensors are attached at two levels in depths z_1 and z_2. The distance $\Delta z = z_2 - z_1$ between the working planes of the submersible unit is variable from 30 cm to 150 cm. For the shallow water applications conducted during this study, the sonar altimeter PSA-916[12] and the pressure transmitter PA-27W/8763[13] was attached to provide informations about the distance to the bottom and the measuring depth. A schematic overview of the instrument design is shown in figure A.1.

The incident radiation is detected by four types of light collectors and then transmitted by glass fibres to a spectrometer. The present length of the fiber cable is 40 m. The glass fibres of the nine sensors are arranged in a stack one upon the other. The sensor signals are dispersed by an imaging grating and focused onto a charge-coupled device (CCD) detector array. The CCD

---

[12] Benthos Inc., Undersea Systems Including Datasonics Inc., 49 Edgerton Drive, North Falmouth, MA 02556, USA, `http://www.benthos.com`

[13] Keller Druckmesstechnik GmbH, Schwarzwaldstr. 17, 79798 Jestetten, Germany, `http://www.keller-druck.com`

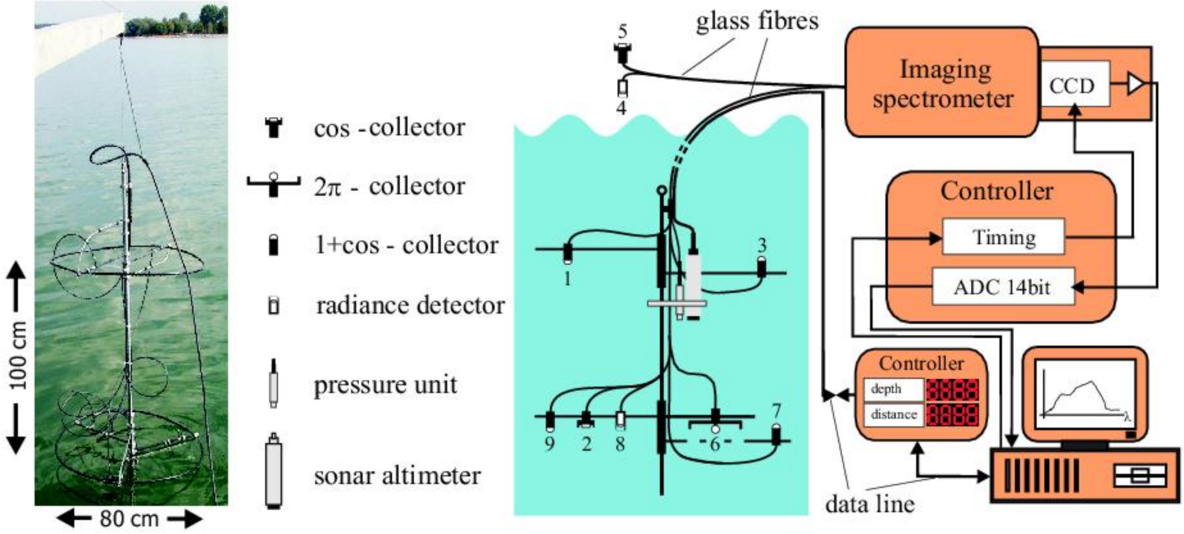

Figure A.1: Photograph and scheme of the optical in-situ instrument HYDRA with nine sensors.

array has 512 by 512 pixels illuminated by nine sensor signals in the rows and spectral channels in the columns (see figure A.2). The signals are digitised with 14 bit resolution. The measured wavelength interval ranges from 400 to 850 nm. The pressure transmitter yields data from 0 to 10 bar with an accuracy of 0.08% to derive the working plane depth. The sonar altimeter has a working frequency of 200 kHz and provides depth data ranging from 0.3 to 100 m with a resolution of 1 cm. Both digital signals are transfered by the RS232 interface. The combination of the signals results the bottom depth z_B.

Four different types of light collectors were built to measure radiance and irradiances. The sensors' diameters are minimised to avoid self-shading. Diagrams of the detectors are shown in figure A.3.

radiance detector A collimated beam is generated by a non-spherical lens of a focal length of 7.8 mm. The radiance is detected within an angle of 2.2° due to the glass fibre diameter of 300 μm. A downward looking radiance detector is mounted at the submersible unit to measure the upwelling radiance L_u (sensor 8) and at the above water unit to get the upwelling radiance in air L_u^+ (sensor 4).

cos-collector The incident radiation is weighted by the cosine of the zenith angle due to the shape of the sensor. The measured signal is the integrated radiance over the hemisphere to supply the upwelling irradiance E_u (sensor 2) and the downwelling irradiance in air E_d^+ (sensor 5). The accuracy of the angular response function is better than 2% compared to the cosine for incident angles between 0 an 70°.

2π-collector The radiation of the hemisphere is detected equally weighted for all incident angles to get the upwelling scalar irradiance E_{0u} (sensor 6). The accuracy of the angular response function is better than 1% for angles between 0 and 75°.

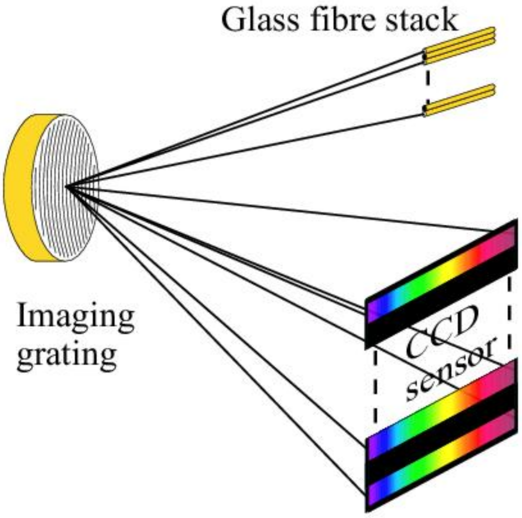

Figure A.2: Schematic diagram of the spectrometer unit of the HYDRA.

1+cos-collector The incident radiation of the angle θ is weighted due to the shape of the sensor by a function $\frac{1}{2}(1+\cos\theta)$. The sensitivity is within angles ranging from -180° to 180° (Højerslev, 1975). The scalar and vector irradiance, E_0 and E, are obtained at the two underwater levels by adding and subtracting the signals of the sensors 1 and 3 as well as 7 and 9.

From the measured signals the inherent and apparent optical properties of the water listed in table A.1 are derived. The simultaneous measurement of all spectra makes the derived optical properties insensitive to changes in the illumination conditions. The recorded spectra at two levels under water allows to calculate the absorption and attenuation for the depth $z_m = \frac{1}{2}(z_1 + z_2)$ using Gershun's law (equation (2.23)).

The spectral calibration of HYDRA was done using spectral lamps with defined emission wavelength at 435.7 and 546.1 nm of mercury (Hg) and at 826.5 nm of argon (Ar). The correlation between wavelength and CCD channel was made by linear regression and has an accuracy of 0.5 nm. Due to aberration of the imaging grating the spectral resolution, given by the Full Width at Half Maximum (FWHM), depends on the position of the sensor signal on the CCD array and is between 2.5 nm for sensor 4 and 5 in the centre and 12 nm for sensor 1 and 9 on top and bottom.

The radiometric calibration of the above water radiance detector was done using a irradiance standard calibrated by the Physikalisch-Technische Bundesanstalt[14] with an uncertainty of 4%. Then the radiance detector was combined with a white reflectance standard to get the cosine weighted irradiance, which was the reference for the cos-collectors. Then, the underwater sensors were intercalibrated under water including the wavelenght dependend immersion factor. The collectors were lowered twice to the same depth, first all looking upward and then all looking

---

[14] Bundesallee 100, 38116 Braunschweig, Germany, `http://www.ptb.de`

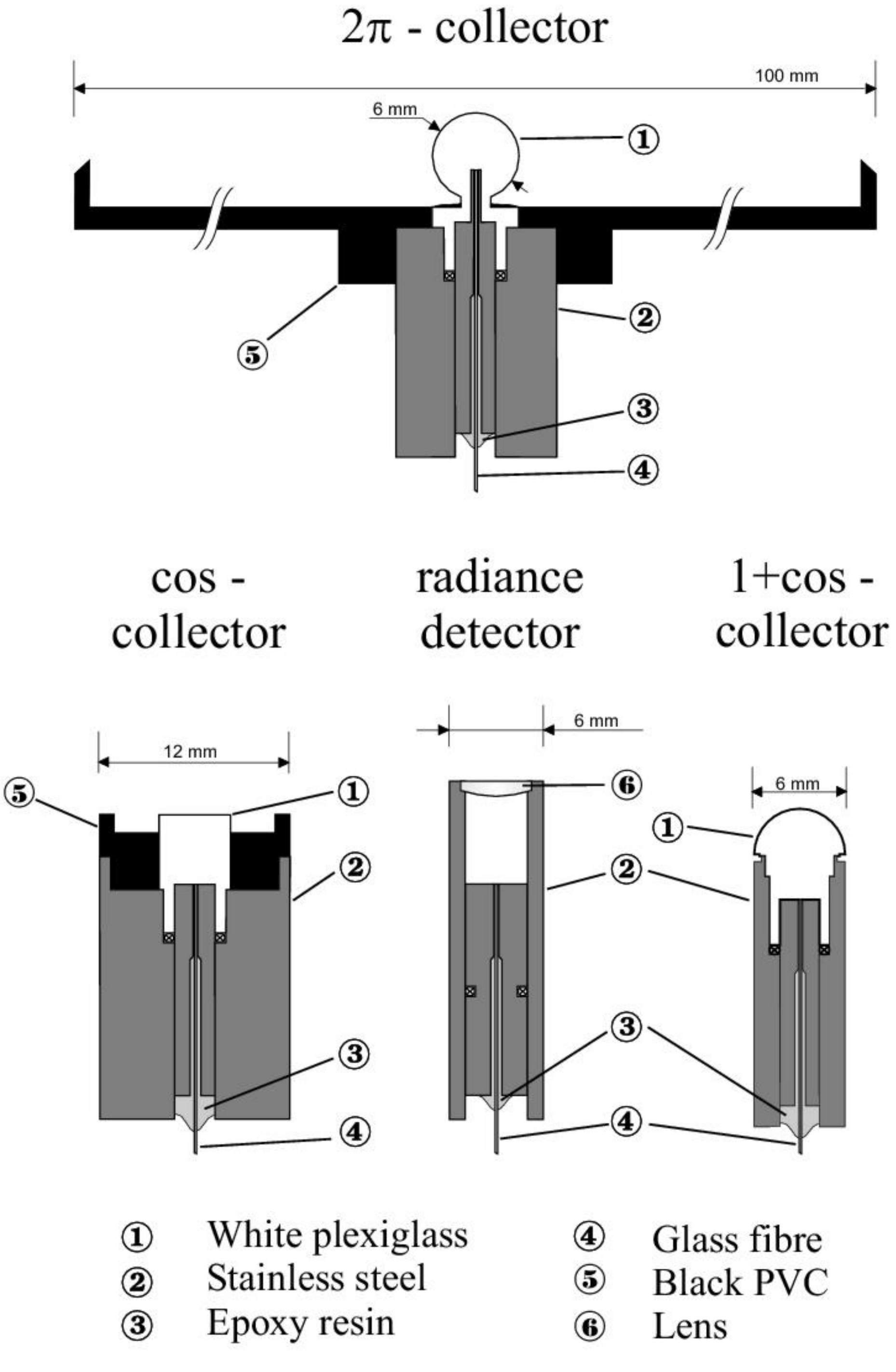

Figure A.3: Four different light collectors of HYDRA to measure irradiance and radiance.

Remote sensing reflectance in air	R_{rs}^{+}	=	L_u^{+}/E_d^{+}
at depht z_2	R_{rs}	=	L_u/E_d
Irradiance reflectance at z_2	R	=	E_u/E_d
Q-factor at z_2	Q	=	E_u/L_u
Mean cosine at z_1 and z_2	$\bar{\mu}$	=	E/E_0
Mean cosine of upwelling irradiance at z_2	$\bar{\mu}_u$	=	E_u/E_{0u}
downwelling irrradiance at z_2	$\bar{\mu}_d$	=	E_d/E_{0d}
Absorption coefficient	a	=	$-\frac{1}{E_0(z_m)}\left[\frac{\mathrm{d}E(z)}{\mathrm{d}z}\right]_{z_m}$
Attenuation coefficient of vector irradiance	K	=	$-\frac{1}{E(z_m)}\left[\frac{\mathrm{d}E(z)}{\mathrm{d}z}\right]_{z_m}$
scalar irradiance	K_0	=	$-\frac{1}{E_0(z_m)}\left[\frac{\mathrm{d}E_0(z)}{\mathrm{d}z}\right]_{z_m}$

Table A.1: Inherent and apparent optical properties of the water, which can be derived from HYDRA measurements.

downward. For the calibration of the underwater radiance detector a reflectance standard of white teflon disk was placed in the sensor's field of view. The noise equivalent radiance is about $2 \cdot 10^{-6}$ W m^{-2}nm^{-1}sr^{-1} at 488 nm and for an integration time of 5 s.

A.5 RAMSES

The Radiation Measurement Sensor with Enhanced Spectral Resolution RAMSES[15] is a commercially available system of submersible radiance and irradiance sensors for optical measurements in the water. The system used for campaigns at Lake Constance consists of one sensor for measuring upwellig radiance spectra L_u, one for upwelling irradiance E_u, and one for downwelling irradiance E_d. The detected signal is transmitted in each sensor unit to the built-in spectrometer MMS[16] consisting of a 256 channel silicon photodiode array. The optics of the spectrometer allows the use of 190 channels from 320 to 950 nm, i.e. the spectral sampling interval is 3.3 nm. The accuracy of the wavelength position is 0.3 nm. The radiance detector has a field of view of 7° in air. The irradiance detector has a cosine response function with an accuracy better than 10%. The three sensors are mounted on a frame such that their optical axes are aligned parallel to each other and the three entrance optics are on the same level as shown in figure A.4. The irradiance and radiance sensors have a length of about 30 cm and a diameter of 5 cm. Photographs are shown in figure A.5. The radiance sensor contains a tilt sensor to measure the inclination. The sonar altimeter PSA-916[12] and the pressure transmitter PA-27W/8763[13] as described in section A.4 can be also attached to the frame in order to measure the depth. All devices are connected to a control unit by the RS232 interface, which ensures that all measurements are made simultaneously. The data are tranfered to the computer by a cable of 25 m

---

[15] TriOS Optical Sensors, Werftweg 15, 26135 Oldenburg, Germany, `http://www.trios.de`

[16] Carl Zeiss Jena GmbH, Carl-Zeiss-Promenade 10, 07745 Jena, Germany, `http://www.zeiss.de`

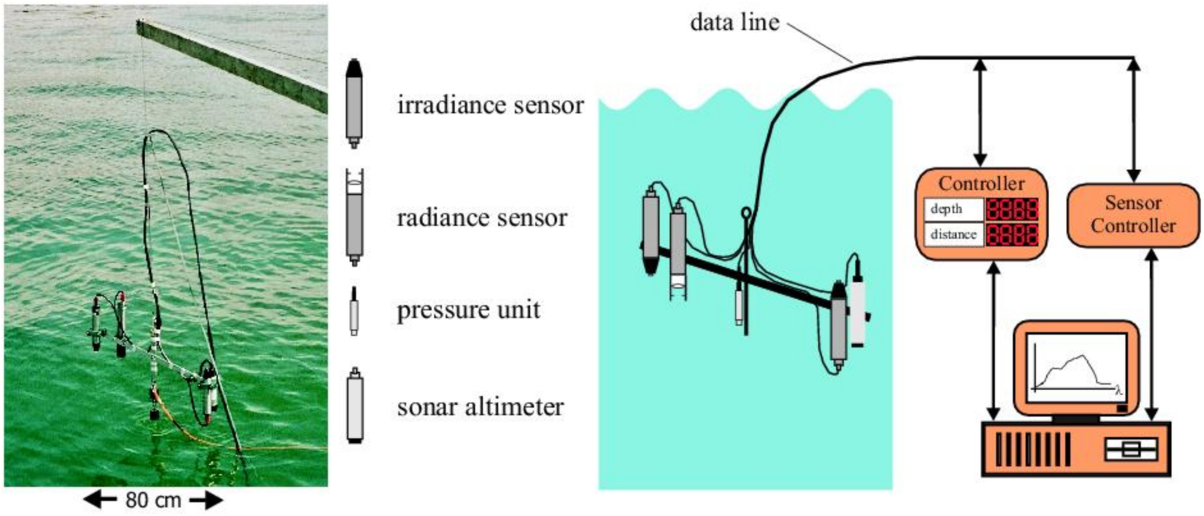

Figure A.4: Photograph and scheme of the optical in-situ instrument RAMSES.

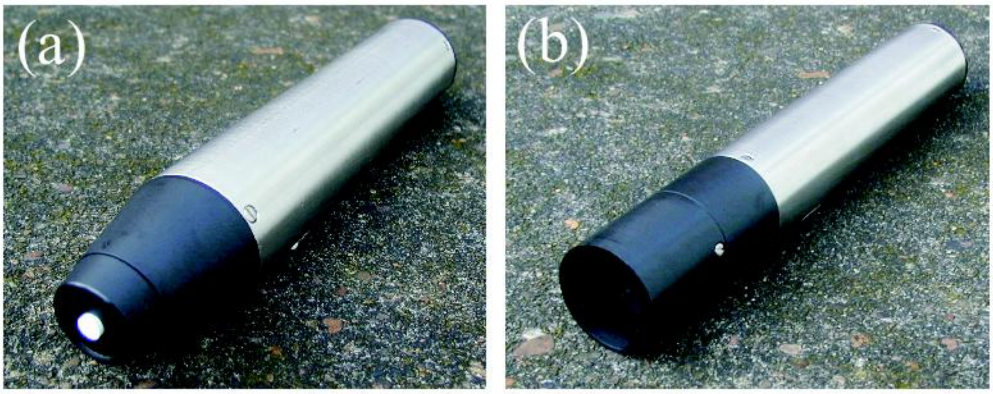

Figure A.5: Photographs of the irradiance (a) and radiance (b) sensors of RAMSES.

length and the RS232 interface. The irradiance reflectance R, remote sensing reflectance R_{rs}, and the Q-factor can be derived from the recorded signals. The noise equivalent radiance is about $0.3 \cdot 10^{-6}$ W m^{-2}nm^{-1}sr^{-1} at 500 nm and for an integration time of 8 s.

Appendix B

WASI: water colour simulator

The Water Colour Simulator WASI is a comfortable Microsoft® Windows-based software tool programmed in Borland® Delphi 6.0 for forward and inverse modeling and analysing of optical in-situ data in aquatic environments. WASI was developed by P. Gege[1] and is described in Gege (2001; 2004). The program is free of charge and the actual version can be downloaded from an anonymous ftp server[2] together with the user manual.

B.1 Concept

WASI is designed as a sensor independent spectra generator and spectra analyzer with well documented calculation steps and automatic result visualization by a graphical user interface. A screenshot is shown in figure B.1. The supported spectrum types are listed in table B.1. The default data provided with WASI were determined at Lake Constance (Gege, 1994; Heege, 2000) and are suited for calculating all spectra types at least from 390 to 800 nm at a spectral resolution of 1 nm. All input and output files are in text format (ASCII), making it easy to adapt the calculations to regional specifics by replacing some default input spectra and changing the provided specific optical properties or bottom characteristics. Spectral resolution, wavelength interval as well as number and position of spectral channels are arbitrary and can be chosen by the user. WASI can also be operated in a background mode where all actions are controlled by an input file so that other programs can utilize WASI as a slave to generate or analyze data according to their demands. This input file, WASI.INI, is also used to initialize and document all program settings. It is automatically read during program start and a copy with the actual settings is automatically stored in the relevant directory whenever outputs from calculations are saved.

---

[1] DLR German Aerospace Center, Remote Sensing Technology Institute, Marine Remote Sensing, Muenchener Str. 20, 82234 Wessling, Germany, `mailto:peter.gege@dlr.de`

[2] `ftp://ftp.dfd.dlr.de/pub/WASI`

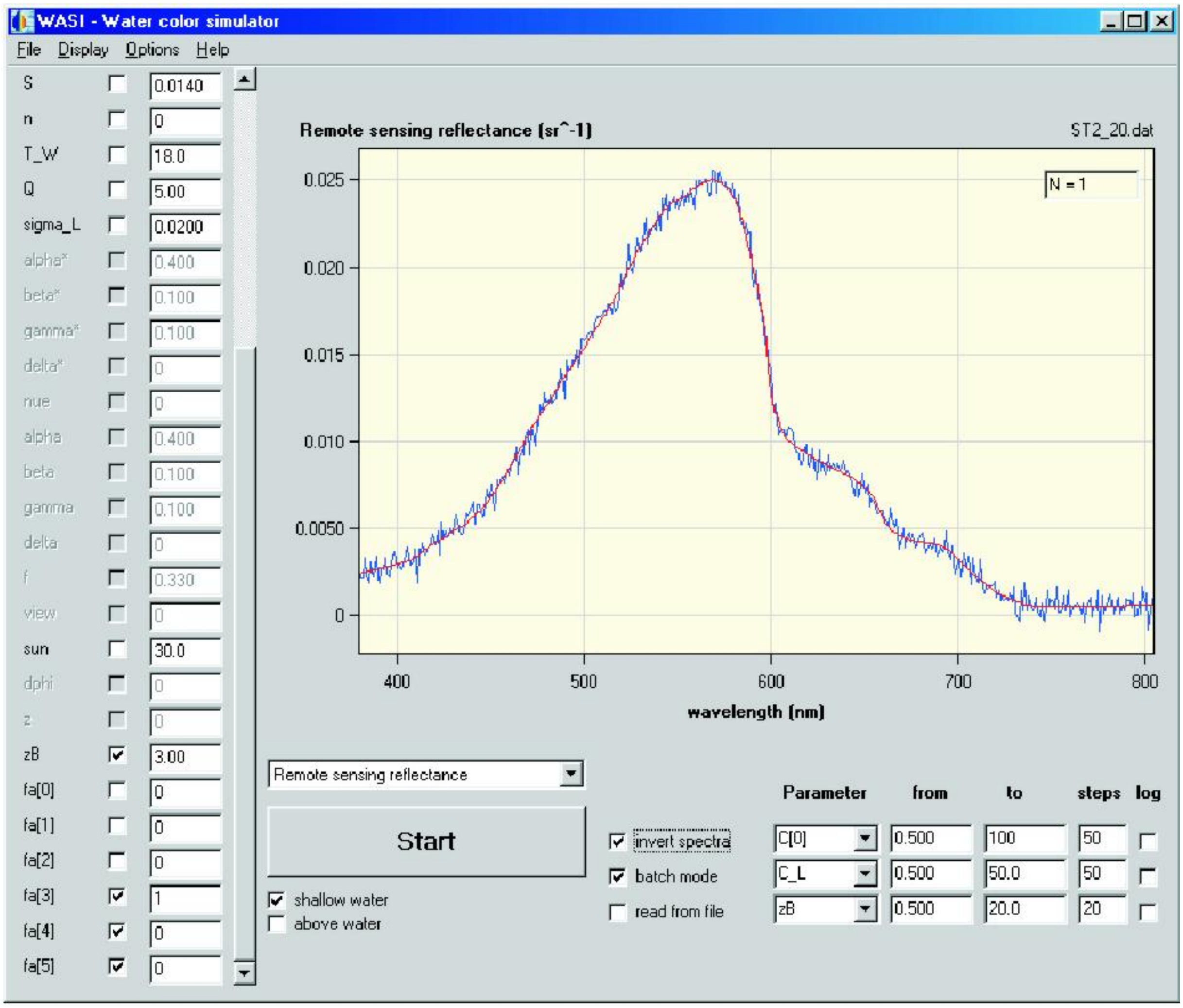

S ☐ 0.0140
n ☐ 0
T_W ☐ 18.0
Q ☐ 5.00
sigma_L ☐ 0.0200
alpha* ☐ 0.400
beta* ☐ 0.100
gamma* ☐ 0.100
delta* ☐ 0
nue ☐ 0
alpha ☐ 0.400
beta ☐ 0.100
gamma ☐ 0.100
delta ☐ 0
f ☐ 0.330
view ☐ 0
sun ☐ 30.0
dphi ☐ 0
z ☐ 0
zB ☑ 3.00
fa[0] ☐ 0
fa[1] ☐ 0
fa[2] ☐ 0
fa[3] ☑ 1
fa[4] ☑ 0
fa[5] ☑ 0

Remote sensing reflectance

☑ shallow water
☐ above water

☑ invert spectra
☑ batch mode
☐ read from file

Parameter	from	to	steps	log
C[0]	0.500	100	50	☐
C_L	0.500	50.0	50	☐
zB	0.500	20.0	20	☐

Figure B.1: Graphical user interface of WASI.

B.2 Models

All calculations of WASI are based on analytical models. The advantage of analytical equations is that they require little computing time, can be used for inversion, and need input parameters, which can be relatively easily measured. The disadvantage of analytical models compared to numerically exact methods is the accuracy. But the development of an analytical equation system based on an exact reference model improves the accuracy significantly, as shown in this study. Compared to Hydrolight (version 3.1) (Mobley et al., 1993; Mobley, 1994), the calculations by WASI are typically faster by a factor of 10^6. In WASI the user can chose from different implemented parameterisations to calculate and analyse the spectra types listed in table B.1. An example of a user interface is shown in figure B.2 for the model selection of irradiance reflectance. Different widely-used models for the absorption, backscattering, remote sensing reflectance, and above surface reflectance are included (Gordon et al., 1975; Morel, 1974; Prieur, 1976; Bricaud et al., 1981; Prieur and Sathyendranath, 1981; Kirk, 1984; Morel and Gentili, 1991; Ahn et al.,

Absorption excluding pure water including pure water	$a_{WC}(\lambda)$ $a(\lambda)$
Attenuation for downwelling irradiance	$K_d(\lambda)$
Specular reflectance wavelength dependent constant	$\sigma_E^+(\lambda)$ σ_E^+
Irradiance reflectance for deep and shallow water	$R(\lambda)$
Remote sensing reflectance for deep and shallow water (below and above the surface)	$R_{rs}(\lambda)$
Bottom reflectance for irradiance sensors for radiance sensors	$R_B(\lambda)$ $\tilde{B}(\lambda, \theta_i, \phi_i, 0, 0)$
Downwelling irradiance below surface above surface	$E_d(\lambda)$ $E_d^+(\lambda)$
Upwelling radiance below surface above surface	$L_u(\lambda)$ $L_u^+(\lambda)$

Table B.1: Types of spectral measurements for which inverse modeling is implemented in WASI.

1992; Sathyendranath and Platt, 1997). New analytical parameterisations for shallow water by Albert and Mobley (2003) are also implemented. The sky radiance and irradiance model of Gege (1994) is used for the linkage of subsurface and above surface reflectances. The list of parameters, which are used in WASI, is given in table B.2. Depending on the spectrum type selected by the user, relevant parameters are visible and non-relevant are hidden.

B.3 Forward calculation

In the forward mode a spectrum or a series of spectra is calculated according to user-specified parameter values using a selected model. The spectra are automatically plotted on screen and can also be saved as text files. In order to generate effectively a large number of spectra, which cover a wide range of natural aquatic situations, up to three parameters can be iterated simultaneously. For example in figure B.1 down right, the user has selected that phytoplankton concentration (C[0]) shall be iterated from 0.5 to 100 μg/l in 50 steps, suspended matter concentration (C_L) from 0.5 to 50 mg/l in 50 steps, and bottom depth (zB) from 0.5 to 20 m in 20 steps. Thus, $50^2 \cdot 20 = 50000$ calculations will be performed altogether after the "Start" button is pressed. A personal computer (Microsoft® Windows NT 4.0) with a 550 MHz Intel® Pentium III-MMX processor required 73.5 minutes to calculate and save these 50000 spectra, where each spectrum consisted of 601 data points in 1 nm steps from 300 to 900 nm. The time of one single spectrum is about 0.1 second.

Main applications of the forward mode are generation of spectra for sensitivity studies and visualisation of spectral changes upon altered conditions. For example, WASI and 6S, a radiative

Algorithm

● R = f * bb / (a + bb) Gordon et al. (1975)

○ R = f * bb / a Prieur (1976)

f factor

○ f = constant Gordon et al. (1975)

○ f = 0.975 - 0.629 * cos(sun_w) Kirk (1984)

○ f = 0.6279-0.2227*n-0.0513*n^2 + (-0.3119+0.2465n) * cos(sun) Morel & Gentili (1991)

○ f = 0.5 / (0.5 + cos(sun_w)) Sathyendranath & Platt (1997)

● f = p1 * (1 + p2*x - p3*x^2 + p4*x^3) * (1 + p5 / cos(sun_w)) Albert & Mobley (2003)

n = bb_W / b
sun = sun zenith angle above water surface
sun_w = sun zenith angle below water surface

Figure B.2: Graphical user interface of WASI for the selection of irradiance reflectance models.

transfer simulation program for the atmosphere, were used together to estimate the influence of errors in atmospheric correction on the retrieval of phytoplankton, gelbstoff, and suspended matter from MERIS and MODIS data (Pyhälahti and Gege, 2001). Two features are implemented which are useful to study the sensitivity of a sensor: statistical noise with user-defined standard deviation can be added, and the radiometric resolution can be defined arbitrarily.

B.4 Invers modeling

Invers modeling is the determination of model parameters for a given spectrum, which can be a measurement or a forward simulation. Table B.2 summarises all parameters, whose values can principally be determined via fit. The actual number of fit parameters depends on the spectrum type, on model options, and on the user's choice, which parameters to fit and which to fix during inversion. The actual values of model parameters are determined iteratively from a given spectrum or a series of spectra. In the first iteration a spectrum is calculated using initial values for the model parameters. This model spectrum is compared with the measured one by calculating the residual, which is a number that characterises the degree of correspondence. Several methods for calculating the residual are implemented, for example a spectral weighting function can be used. Then, in the further iterations, the parameter values are altered, resulting in altered model curves and altered residuals. The selection of the new parameter values in each step is done by the Simplex algorithm (Nelder and Mead, 1965; Caceci and Cacheris, 1984), which is briefly explained in chapter 4.1. The procedure is stopped after the best fit between calculated and measured spectrum, or the minimum residual, has been found. The parameters

Symbol	WASI	Units	Description
$C_{P,i}$	C[i]	μg/l	Concentration of i^{th} phytoplankton class, $i = 0, ..., 5$
$C_{X,l}$	C_L	mg/l	Concentration of large suspended particles
$C_{X,s}$	C_S	mg/l	Concentration of small suspended particles
a_T	C_X	m^{-1}	Concentration of non-chlorophyllous particles
a_Y	C_Y	m^{-1}	Concentration of gelbstoff
s_Y	S	nm^{-1}	Exponent of gelbstoff absorption
n_s	n	-	Exponent of backscattering by small particles
T	T_W	°C	Water temperature
f	f	-	Proportionality factor of reflectance (f-factor)
Q	Q	sr	Anisotropy factor (Q-factor)
θ_s	sun	°	Sun zenith angle in air
θ_v	view	°	Viewing angle in air ($0 =$ nadir)
σ_L^+	sigma_L	-	Reflection factor of sky radiance
z_B	zB	m	Bottom depth
ν	nue	-	Exponent of aerosol scattering
α	alpha	-	Weight of directly transmitted solar irradiance
β	beta	-	Weight of diffuse irradiance by molecule scattering
γ	gamma	-	Weight of diffuse irradiance by aerosol scattering
δ	delta	-	Weight of diffuse irradiance by cloud scattering
α^*	alpha*	sr^{-1}	Reflection factor of direct solar radiation
β^*	beta*	sr^{-1}	Reflection factor of molecule scattering
γ^*	gamma*	sr^{-1}	Reflection factor of aerosol scattering
δ^*	delta*	sr^{-1}	Reflection factor of cloud scattering
$f_{a,i}$	fa[i]	-	Areal fraction of i^{th} bottom type, $i = 0, ..., 5$

Table B.2: Parameter list of WASI.

that were used in the step with the smallest residual are the results.

If the solution of the inversion problem is ambiguous, the inversion algorithm may not find the correct values of the fit parameters. The problem occurs when different sets of model parameters yield similar spectra, i.e. the problem is model specific. Measures are implemented in WASI to handle the ambiguity problem. The most effective measure to obtain reliable results is the usage of “realistic” values of all fit parameters as initial values when inversion is started. Methods, which provide usually good results, are implemented to determine automatically start values of most important fit parameters. Finetuning of these methods by the user is supported. An example of the graphical user interface for fit tuning is shown in figure B.3. The figure displays the implemented methods of this study to calculate the initial values in shallow water.

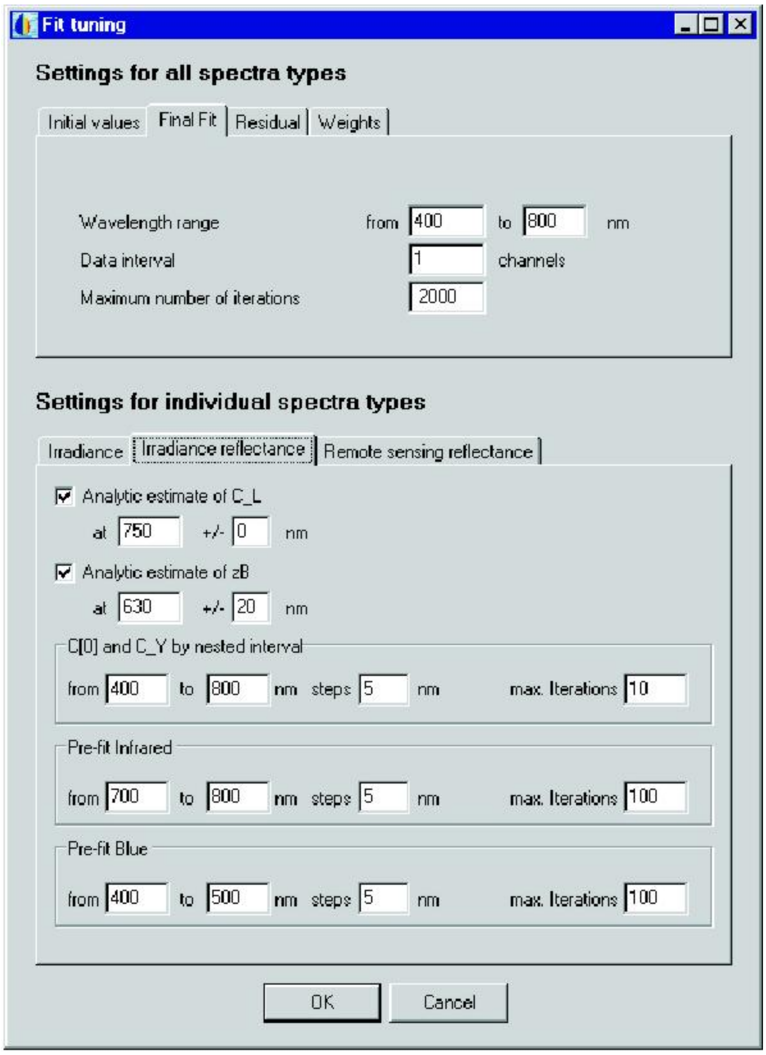

Settings for all spectra types

Wavelength range from 400 to 800 nm
Data interval 1 channels
Maximum number of iterations 2000

Settings for individual spectra types

☑ Analytic estimate of C_L
at 750 +/- 0 nm
☑ Analytic estimate of zB
at 630 +/- 20 nm

C[0] and C_Y by nested interval
from 400 to 800 nm steps 5 nm max. Iterations 10

Pre-fit Infrared
from 700 to 800 nm steps 5 nm max. Iterations 100

Pre-fit Blue
from 400 to 500 nm steps 5 nm max. Iterations 100

Figure B.3: Graphical user interface of WASI for the fit tuning.

Acknowledgement

I would like to thank everybody who encouraged me during this work. Special thanks go to

Prof. Dr. Hartmut Graßl for supervising this work at the Department of Earth Sciences of the University of Hamburg,

Dr. Peter Gege for extremely fruitful discussions and excellent support,

Dr. Heinz van der Piepen and Dr. Thomas Heege for making available the topic of the work in the Collaborative Research Centre SFB 454 “Littoral zone of Lake Constance” funded by the German Research Foundation (DFG),

Prof. Dr. Richard Bamler, Prof. Dr. Manfred Schroeder, Dr. Andreas Neumann, and Hans-Henning Voß for providing the place of employment at the Remote Sensing Technology Institute (former Institute of Optoelectronics) of the German Aerospace Center (DLR) in Oberpfaffenhofen,

Dr. Curtis D. Mobley for supplying the source code of the radiative transfer program “Hydrolight 3.1”,

Dr. Kurt Bochter for getting me aquainted with the instrument “HYDRA” and the support during further developments,

Erich Bogner and Jürgen Wörishofer for the technical assistance in the laboratory,

The staff at the Limnological Institute of the University of Konstanz, particularly Alfred Sulger, Susanne Wolfer, Bärbel Beese, and Christine Gebauer, as well as Michael Weyhmüller of the Biologiebüro Weyhmüller for the support during the campaigns at Lake Constance,

My colleagues at the institute, particularly Dr. Clivia Häse, Dr. Sabine Thiemann, Sabine Miksa, and Anke Bogner for useful advices and innumerable discussions,

and last but not least

My parents, Hildegard and Helmut Albert, for giving me the opportunity and the support to pursue my study,

and Katja Müller-Koch for her endless patience and love.

References

Y.-H. Ahn, A. Bricaud, and A. Morel. Light backscattering efficiency and related properties of some phytoplankters. *Deep-Sea Research*, 39 (11/12):1835–1855, 1992.

A. Albert and C.D. Mobley. An analytical model for subsurface irradiance and remote sensing reflectance in deep and shallow case-2 waters. *Optics Express*, 11 (22):2873–2890, 2003. `http://www.opticsexpress.org/abstract.cfm?URI=OPEX-11-22-2873`.

M. Babin, A. Morel, V. Fournier-Sicre, F. Fell, and D. Stramski. Light scattering properties of marine particles in coastal and open ocean waters as related to the particle mass concentration. *Limnology and Oceanography*, 48 (2):843–859, 2003.

M. Babin and D. Stramski. Light absorption by aquatic particles in the near-infrared spectral region. *Limnology and Oceanography*, 47 (3):911–915, 2002.

T.T. Bannister. Model of the mean cosine of underwater radiance and estimation of underwater scalar irradiance. *Limnology and Oceanography*, 37 (4):773–780, 1992.

J. Berwald, D. Stramski, C.D. Mobley, and D.A. Kiefer. Effect of Raman scattering on the average cosine and diffuse attenuation coefficient of irradiance in the ocean. *Limnology and Oceanography*, 43 (4):564–576, 1998.

K. Bochter. *Das Mehrstrahl-Spektralradiometer HYDRA: Entwicklung und Einsatz zur Charakterisierung des natürlichen Lichtfeldes unter und über Wasser und zur Bestimmung von Wasserqualitätsparametern.* PhD thesis, Institut für Methodik der Fernerkundung, Deutsches Zentrum für Luft- und Raumfahrt Oberpfaffenhofen, 2000. ISSN 1434-8454.

K. Bochter and C. Wallhäußer. New instrument for simultaneous measurement of the daylight field's optical properties above and under water. *Proceedings of SPIE "Ocean Optics XIII"*, 2963:631–636, 1997.

A. Bogner. Prozesskette zur Kartierung submerser Makrophyten mit dem Multispektralscanner DAEDALUS. Master's thesis, Fachhochschule München, Vermessungswesen und Kartographie, 2003.

A. Bricaud, M. Babin, A. Morel, and H. Claustre. Variability in the chlorophyll-specific absorption coefficients of natural phytoplankton: analysis and parameterization. *Journal of Geophysical Research*, 100 (C7):13321–13332, 1995.

A. Bricaud, A. Morel, and L. Prieur. Absorption by dissolved organic matter of the sea (yellow substance) in the UV and visible domains. *Limnology and Oceanography*, 26 (1):43–53, 1981.

H. Buiteveld, J.H.M. Hakvoort, and M. Donze. The optical properties of pure water. *Proceedings of SPIE "Ocean Optics XII"*, 2258:174–183, 1994.

R.P. Bukata, J.H. Jerome, K.Y. Kondratyev, and D.V. Pozdnyakov. *Optical properties and remote sensing of inland and coastal waters.* CRC Press, Boca Raton, 1995.

B. Bulgarelli, V.B. Kisselev, and L. Roberti. Radiative transfer in the atmosphere-ocean system: the finite-element method. *Applied Optics*, 38 (9):1530–1542, 1999.

M.S. Caceci and W.P. Cacheris. Fitting curves to data - the simplex algorithm is the answer. *Byte Magazine*, May:340–362, 1984.

R.E. Carlson. A trophic state index for lakes. *Limnology and Oceanography*, 22 (2):361–369, 1977.

G.K. Clarke, G.C. Ewing, and C.J. Lorenzen. Spectra of backscattered light from the sea obtained from aircraft as a measure of chlorophyll concentration. *Science*, 167:1119–1121, 1970.

C. Cox and W. Munk. Statistics of the sea surface derived from sun glitter. *Journal of Marine Research*, 13 (2):198–227, 1954a.

C. Cox and W. Munk. Measurement of the roughness of the sea surface from photographs of the sun's glitter. *Journal of the Optical Society of America*, 44 (11):838–850, 1954b.

M.E. Culver and M.J. Perry. Calculation of solar-induced fluorescence in the surface and subsurface waters. *Journal of Geophysical Research*, 102 (C5):10563–10572, 1997.

A.W. Decho, T. Kawaguchi, M.A. Allison, E.M. Louchard, R.P. Reid, F.C. Stephens, K.J. Voss, R.A. Wheatcroft, and B.B. Taylor. Sediment properties influencing upwelling spectral reflectance signatures: the "biofilm gel effect". *Limnology and Oceanography, Light in Shallow Waters*, 48 (1, part 2):431–443, 2003.

A.G. Dekker. *Detection of optical water quality parameters for eutrophic waters by high resolution remote sensing.* PhD thesis, Vrije Universiteit Amsterdam, 1993. ISBN 90-9006234-3.

A.G. Dekker, H.J. Hoogenboom, L.M. Goddijn, and T.J.M. Malthus. The relation between inherent optical properties and reflectance spectra in turbid inland waters. *Remote Sensing Reviews*, 15:59–74, 1997.

A. Dekker, S. Peters, R. Vos, and M. Rijkeboer. *Remote sensing for inland water quality detection and monitoring: state-of-the-art application in Friesland waters*, pages 17–38. GIS and Remote Sensing Techniques in Land- and Water-management, chapter 3. Kluwer Academic Publishers, the Netherlands, 2001.

R. Doerffer and H. Schiller. Determination of case 2 water constituents using radiative transfer simulation and its inversion by neural network. *Proceedings of Ocean Optics XIV, Hawaii, USA, Nov 10-13*, 1998.

L.A. Drake, F.C. Dobbs, and R.C. Zimmerman. Effects of epiphyte load on optical properties and photosynthetic potential of the seagrasses Thalassia testudinum Banks ex König and Zostera marina L. *Limnology and Oceanography, Light in Shallow Waters*, 48 (1, part 2): 456–463, 2003.

D. Durand, J. Bijaoui, and F. Cauneau. Optical remote sensing of shallow-water environmental parameters: a feasibility study. *Remote Sensing of Environment*, 73:152–161, 2000.

EC. Directive 2000/60/EC of the European Parliament and of the Council of 23 October 2000 establishing a framework for Community action in the field of water policy. *Official Journal of the European Communities*, L327:1–72, 2000.

A. Einstein. Theorie der Opaleszenz von homogenen Flüssigkeiten und Flüssigkeitsgemischen in der Nähe des kritischen Zustandes. *Annalen der Physik*, 33:1275–1298, 1910.

F. Fell and J. Fischer. Numerical simulation of the light field in the atmosphere-ocean system using the matrix-operator method. *Journal of Quantitative Spectroscopy & Radiative Transfer*, 69:351–388, 2001.

G.M. Ferrari, F.G. Bo, and M. Babin. Geo-chemical and optical characterizations of suspended matter in European coastal waters. *Estuarine, Coastal and Shelf Science*, 57:17–24, 2003.

J. Fischer and H. Grassl. Radiative transfer in an atmosphere-ocean system: an azimuthally dependent matrix-operator approach. *Applied Optics*, 23 (7):1032–1039, 1984.

J. Fischer, R. Doerffer, and H. Grassl. Factor analysis of multispectral radiances over coastal and open ocean water based on radiative transfer calculations. *Applied Optics*, 25 (3):448–456, 1986.

S.K. Fyfe. Spatial and temporal variation in spectral reflectance: are seagrass species spectrally distinct? *Limnology and Oceanography, Light in Shallow Waters*, 48 (1, part 2):464–479, 2003.

P. Gege. *Gewässeranalyse mit passiver Fernerkundung: Ein Modell zur Interpretation optischer Spektralmessungen.* PhD thesis, Institut für Optoelektronik, Deutsche Forschungsanstalt für Luft- und Raumfahrt Oberpfaffenhofen, 1994. ISSN 0939-2963.

P. Gege. Characterization of the phytoplankton in Lake Constance for classification by remote sensing. *Archiv für Hydrobiologie, Special issues: Advances in Limnology*, 53:179–193, 1998.

P. Gege. Lake Constance: yellow substance measurements in 1998. Internal Report 552-9/99, Institut für Optoelektronik, Deutsches Zentrum für Luft- und Raumfahrt, Oberpfaffenhofen, 1999.

P. Gege. Gaussian model for yellow substance absorption spectra. *Proceedings of Ocean Optics XV, Monaco, 16-20 October*, 2000.

P. Gege. The water colour simulator WASI: a software tool for forward and inverse modeling of optical in-situ spectra. *Proceedings of IGARSS, Sydney, Australia, July 9-13*, 2001.

P. Gege. Error propagation at inversion of irradiance reflectance spectra in case-2 waters. *Proceedings of Ocean Optics XVI, Santa Fe (NM), USA, 18-22 November*, 2002.

P. Gege. The water colour simulator WASI: an integrating software tool for analysis and simulation of optical in-situ spectra. *Computers and Geosciences*, 30:523–532, 2004.

H.R. Gordon. Can the Lambert-Beer law be applied to the diffuse attenuation coefficient of ocean water? *Limnology and Oceanography*, 34 (8):1389–1409, 1989.

H.R. Gordon and O.B. Brown. Irradiance reflectivity of a flat ocean as a function of its optical properties. *Applied Optics*, 12 (7):1549–1551, 1973.

H.R. Gordon and A.Y. Morel. *Remote assessment of ocean color for interpretation of satellite visible imagery: a review*, volume 4 of *Lecture Notes on Coastal and Estuarine Studies.* Springer Verlag, New York, 1983.

H.J. Gordon, O.B. Brown, and M.M. Jacobs. Computed relationships between the inherent and apparent optical properties of a flat homogeneous ocean. *Applied Optics*, 14 (2):417–427, 1975.

H.R. Gordon, O.B. Brown, R.H. Evans, J.W. Brown, R.C. Smith, K.S. Baker, and D.K Clark. A semianalytic radiance model of ocean color. *Journal of Geophysical Research*, 93 (D9): 10909–10924, 1988.

W.W. Gregg and K.L. Carder. A simple spectral solar irradiance model for cloudless maritime atmospheres. *Limnology and Oceanography*, 35 (8):1657–1675, 1990.

K.P. Günther, A. Neumann, P. Gege, R. Doerffer, J. Fischer, and C. Brockmann. MERIS - value added products for land-, water-, and atmospheric applications. *Proceedings of the 19th DFD User Workshop, Oberpfaffenhofen, Germany, October 15-16*, pages 37–51, 2002.

J.H.M. Hakvoort. *Absorption of light by surface water.* PhD thesis, Delft University of Technology, 1994. ISBN 90-407-1023-6.

V.I. Haltrin and G.W. Kattawar. Self-consistent solutions to the equation of transfer with elastic and inelastic scattering in oceanic optics: I. model. *Applied Optics*, 32 (27):5356–5367, 1993.

C. Häse and T. Heege. A remote sensing algorithm for primary production in Lake Constance with special emphasis on the integration level. *Final report of the HGF Strategy Fonds Project "ENVISAT Oceanography ENVOC"*, 2003.

C. Häse, U. Gaedke, A. Seifried, B. Beese, and M.M. Tilzer. Phytoplankton response to re-oligotrophication in large and deep Lake Constance: photosynthetic rates and chlorophyll concentration. *Archiv für Hydrobiologie, Special issues: Advances in Limnology*, 53:159–178, 1998.

S.K. Hawes, K.L. Carder, and G.R. Harvey. Quantum fluorescence efficiencies of fulvic and humic acids: effects on ocean color and fluorometric detection. *Proceedings of SPIE "Ocean Optics XI"*, 1750:212–223, 1992.

T. Heege. *Flugzeuggestützte Fernerkundung von Wasserinhaltsstoffen im Bodensee.* PhD thesis, Institut für Methodik der Fernerkundung, Deutsches Zentrum für Luft- und Raumfahrt Oberpfaffenhofen, 2000. ISSN 1434-8454.

T. Heege. Remote sensing of shallow water areas in Lake Constance. Collaborative Research Centre 454 of the German Research Foundation DFG: Littoral zone of Lake Constance, Report of the Working Period 2001–2004, University of Konstanz, 2004.

T. Heege and J. Fischer. Mapping of water constituents in Lake Constance using multispectral airborne scanner data and a physically based processing scheme. *Canadian Journal of Remote Sensing*, 30 (1):77–86, 2004.

T. Heege, H. van der Piepen, J. Fischer, and V. Amann. Gewässerfernerkundung am Bodensee: Verfahren und Anwendungsbeispiele. DLR-Forschungsbericht 98-22, Institut für Optoelektronik, Deutsches Zentrum für Luft- und Raumfahrt, Institut für Optoelektronik Oberpfaffenhofen, 1998. ISSN 1434-8454.

T. Heege, A. Bogner, C. Häse, A. Albert, N. Pinnel, and S. Zimmermann. Mapping aquatic systems with a physically based process chain. *Proceedings of the 3rd EARSeL Workshop on Imaging Spectroscopy, Herrsching, Germany, 13-16 May*, pages 415–422, 2003. ISBN 2-908885-26-3.

N.K. Højerslev. A spectral light absorption meter for measurements in the sea. *Limnology and Oceanography*, 20 (6):1024–1034, 1975.

W.A. Hovis, D.K. Clark, F. Anderson, R.W. Austin, W.H. Wilson, E.T. Baker, D. Ball, H.R. Gordon, J.L. Mueller, S.J. El Sayed, B. Sturm, R.C. Wrigley, and C.S. Yentsch. Nimbus-7 coastal zone color scanner: system description and initial imagery. *Science*, 210:60–63, 1980.

B. Ibelings, R. Vos, P. Boderie, H. Hakvoort, and E. Hoogenboom. The RALLY project: remote sensing of algal blooms in Lake IJssel - integration with in situ data and computational modelling. RIZA rapport 2001.036, RIZA Institute for Inland Water Management and Waste Water Treatment, 2001. ISBN 9036953901.

IGKB. Limnologischer Zustand des Bodensees - Jahresbericht Januar 2001 bis März 2002. IGKB Bericht 29, Internationale Gewässerschutzkommission für den Bodensee, 2002. ISSN 1011-1271.

S. Illert, H. Fries, E. Hollan, H. Müller, F. Osterkorn, R. Ott, W. Sanzin, B. Wagner, and C. Steinberg. Zur Bedeutung der Flachwasserzone des Bodensees. IGKB Bericht 35, Internationale Gewässerschutzkommission für den Bodensee, 1987.

IOCCG. *Remote sensing of ocean colour in coastal, and other optically-complex, waters*, volume 3 of *Reports of the International Ocean-Colour Coordinating Group*. IOCCG, Dartmouth, Canada, 2000.

N.G. Jerlov. *Marine optics*. Optical Oceanography, Elsevier Oceanography Series 5. Elsevier Scientific Publishing Company, Amsterdam, 1976. 2nd revised and enlarged edition.

J.H. Jerome, R.P. Bukata, and J.E. Bruton. Determination of available subsurface light for photochemical and photobiological activity. *Journal of Great Lakes Research*, 16 (3):436–443, 1990.

J. Joseph. Untersuchungen über Ober- und Unterlichtmessungen im Meere und über ihren Zusammenhang mit Durchsichtigkeitsmessungen. *Deutsche Hydrographische Zeitschrift*, 3 (5/6):324–335, 1950.

K. Kalle. Meereskundliche chemische Untersuchungen mit Hilfe des Zeissschen Pulfrich Photometers. *Annalen der Hydrographie, Berlin*, 65:276–282, 1937.

K. Kalle. The problem of the gelbstoff in the sea. *Oceanography and Marine Biology Annual Review*, 4:91–104, 1966.

G.W. Kattawar and G.N. Plass. Radiative transfer in the earth's atmosphere-ocean system: II. Radiance in the atmosphere and ocean. *Journal of Physical Oceanography*, 2 (2):148–156, 1972.

J.T.O. Kirk. Monte Carlo procedure for simulating the penetration of light into natural waters. *CSIRO Division of Plant Industry, Technical Paper*, 36:1–16, 1981.

J.T.O. Kirk. *Light and photosynthesis in aquatic ecosystems*. Cambridge University Press, 1983.

J.T.O. Kirk. Dependence of relationship between inherent and apparent optical properties of water on solar altitude. *Limnology and Oceanography*, 29 (2):350–356, 1984.

J.T.O. Kirk. The upwelling light stream in natural waters. *Limnology and Oceanography*, 34 (8):1410–1425, 1989.

V.B. Kisselev, L. Roberti, and G. Perona. Finite-element algorithm for radiative transfer in vertically inhomogeneous media: numerical scheme and applications. *Applied Optics*, 34 (36): 8460–8471, 1995.

P. Koepke. Effective reflectance of oceanic whitecaps. *Applied Optics*, 23 (11):1816–1824, 1984.

H. Krawczyk, A. Neumann, T. Walzel, and G. Zimmermann. Investigation of interpretation possibilities of spectral high-dimensional measurements by means of principle component analysis: a concept for physical interpretation of those measurements. *Proceedings of SPIE "Recent Advances in Sensors, Radiometric Calibration, and Processing of Remotely Sensed Data"*, 1938: 401–411, 1993.

B. Kunkel, F. Blechinger, D. Viehmann, H. van der Piepen, and R. Doerffer. ROSIS imaging spectrometer and its potential for ocean parameter measurements (airborne and space-borne). *International Journal of Remote Sensing*, 12 (4):753–761, 1991.

V. Lafon, J.M. Froidefond, F. Lahet, and P. Castaing. SPOT shallow water bathymetry of a moderately turbid tidal inlet based on field measurements. *Remote Sensing of Environment*, 81:136–148, 2002.

Z. Lee, K.L. Carder, C.D. Mobley, R.G. Steward, and J.S. Patch. Hyperspectral remote sensing for shallow waters. 1. A semianalytical model. *Applied Optics*, 37 (27):6329–6338, 1998.

Z. Lee, K.L. Carder, C.D. Mobley, R.G. Steward, and J.S. Patch. Hyperspectral remote sensing for shallow waters: 2. Deriving bottom depths and water properties by optimization. *Applied Optics*, 38 (18):3831–3843, 1999.

R.V. Lynch. *The occurence and distribution of surface bioluminescence in the oceans during 1966 through 1977*, volume 8210 of *NRL report*. Naval Research Laboratory, Marine Biology and Biochemistry Branch, 1978.

D.R. Lyzenga. Passive remote sensing techniques for mapping water depth and bottom features. *Applied Optics*, 17 (3):379–383, 1978.

S. Maritorena, A. Morel, and B. Gentili. Diffuse reflectance of oceanic shallow waters: influence of water depth and bottom albedo. *Limnology and Oceanography*, 39 (7):1689–1703, 1994.

A. Melzer. Aquatic macrophytes as tools for lake management. *Hydrobiologia*, 395/396:181–190, 1999.

S. Miksa, P. Gege, and T. Heege. Investigations on the capability of CHRIS-Proba for monitoring of water constituents in Lake Constance compared to MERIS. *Proceedings of the* 2^{nd} *ESA CHRIS-Proba Workshop, Frascati, Italy, 28-30 April*, ESA SP-578, 2004.

C.D. Mobley. *Light and water - radiative transfer in natural waters.* Academic Press, San Diego, 1994.

C.D. Mobley. Hydrolight 3.0 users' guide. Final Report, SRI Project 5632, Office of Naval Research, Environmental Optics, Arlington (VA), USA, 1995.

C.D. Mobley. Hydrolight 3.1 users' guide. Final Report, SRI Project 6583, Office of Naval Research, Environmental Optics, Arlington (VA), USA, 1996.

C.D. Mobley. Estimation of the remote-sensing reflectance from above-surface measurements. *Applied Optics*, 38 (36):7442–7455, 1999.

C.D. Mobley and L.K. Sundman. Effects of optically shallow bottoms on upwelling radiances: inhomogeneous and sloping bottoms. *Limnology and Oceanography, Light in Shallow Waters*, 48 (1, part 2):329–336, 2003.

C.D. Mobley, B. Gentili, H.R. Gordon, Z. Jin, G.W. Kattawar, Á. Morel, P. Reinersman, K. Stamnes, and R.H. Stavn. Comparison of numerical models for computing underwater light fields. *Applied Optics*, 32 (36):7484–7504, 1993.

C.D. Mobley, H. Zhang, and K.J. Voss. Effects of optically shallow bottoms on upwelling radiances: bidirectional reflectance distribution function effects. *Limnology and Oceanography, Light in Shallow Waters*, 48 (1, part 2):337–345, 2003.

E.C. Monohan and I.G. O'Muircheartaigh. Whitecaps and the passive remote sensing of the ocean surface. *International Journal of Remote Sensing*, 7 (5):627–642, 1986.

A. Morel. *Optical properties of pure water and pure sea water*, pages 1–24. Optical Aspects of Oceanography. Academic Press, London, 1974.

A. Morel. Optical modeling of the upper ocean in relation to its biogenous matter content (case I waters). *Journal of Geophysical Research*, 93 (C9):10749–10768, 1988.

A. Morel. Light and marine photosynthesis: a spectral model with geochemical and climatological implications. *Progress in Oceanography*, 26:263–306, 1991.

A. Morel and Y.-H. Ahn. Optical efficiency factors of free-living marine bacteria: influence of bacterioplankton upon the optical properties and particulate organic carbon in oceanic waters. *Journal of Marine Research*, 48:145–175, 1990.

A. Morel and B. Gentili. Diffuse reflectance of oceanic waters: its dependence on sun angle as influenced by molecular scattering contribution. *Applied Optics*, 30 (30):4427–4438, 1991.

A. Morel and L. Prieur. Analyse spectrale de l'absorption per les substances dissoutes (substances jaunes). *Publ. CNEXO*, 10 (Sect. 1.1.11):1–9, 1976.

A. Morel and L. Prieur. Analysis of variations in ocean color. *Limnology and Oceanography*, 22 (4):709–722, 1977.

R. Müller, P. Reinartz, G. Kritikos, and M. Schroeder. Image processing in a network environment. *Proceedings of the ISPRS Commission II Symposium: International Archives of Photogrammetry and Remote Sensing, Washington DC, USA, 2-14 August*, 29 (B2):289–293, 1992.

Ru. Müller, M. Lehner, Ra. Müller, P. Reinartz, M. Schroeder, and B. Vollmer. A program for direct georeferencing of airborne and spaceborne line scanner images. *Proceedings of the ISPRS Commission I Symposium: Integrating Remote Sensing at the Global, Regional and Local Scale, Denver (CO), USA, 10-15 November*, 2002. `http://www.isprs.org/commission1/proceedings/contents_isprs.html`.

J.A. Nelder and R. Mead. A simplex method for function minimization. *Computer Journal*, 7: 308–313, 1965.

A. Neumann, M. Hetscher, H. Krawczyk, and C. Tschentscher. Methodological aspects of principal component inversion for case-II applications. *Second International Workshop on MOS-IRS and Ocean Colour, Berlin, Germany, June 10-12*, pages 163–170, 1998. ISBN 3-89685-559-X.

E.A. Nusch. Comparison of different methods for chlorophyll and phaeopigment determination. *Archiv für Hydrobiologie, Special issues: Advances in Limnology*, 14:14–36, 1980.

T. Ohde and H. Siegel. Correction of bottom influence in ocean colour satellite images of shallow water areas of the Baltic Sea. *International Journal of Remote Sensing*, 22 (2&3):297–313, 2001.

W.S. Pegau and J.R.V. Zaneveld. Temperature-dependent absorption of water in the red and near-infrared portions of the spectrum. *Limnology and Oceanography*, 38 (1):188–192, 1993.

T.J. Petzold. *Volume scattering functions for selected ocean waters*, pages 152–174. Light in the sea. Dowden, Hutchinson & Ross, Strouddberg, 1977.

W.D. Philpot and S.G. Ackleson. Remote sensing of optically shallow, vertically inhomogeneous waters: a mathematical model. *Delaware Sea Grant Collage Program*, pages 283–299, 1981. DEL-SG-12-81.

G.N. Plass and G.W. Kattawar. Monte Carlo calculations of radiative transfer in the earth's atmosphere-ocean system: I. Flux in the atmosphere and ocean. *Journal of Physical Oceanography*, 2 (2):139–147, 1972.

S. Porto. Angular dependence and depolarization ratio of the Raman effect. *Journal of the Optical Society of America*, 56 (11):1585–1589, 1966.

D. Pozdnyakov and H. Grassl. *Colour of inland and coastal waters - a methodology for its interpretation.* Springer Verlag Berlin/Heidelberg/New York, Praxis Publishing Ltd. Chichester, 2003.

D. Pozdnyakov, A. Lyaskovsky, H. Grassl, and L. Pettersson. Numerical modelling of transspectral processes in natural waters: implications for remote sensing. *International Journal of Remote Sensing*, 23 (8):1581–1607, 2002a.

D. Pozdnyakov, A. Lyaskovsky, H. Grassl, L. Pettersson, and F. Tanis. Optically shallow waters: modelling of radiometric colour and development of water quality retrieval algorithms. *Proceedings of the 7th International Conference on Remote Sensing for Marine and Coastal Environments, Miami/Florida, USA, 20-22 May*, 2002b.

R.W. Preisendorfer. *Hydrologic optics.* U.S. Department of Commerce, National Oceanic and Atmospheric Administration, Environmental Research Laboratories, Pacific Marine Environmental Laboratory, 1976. CDROM.

L. Prieur. *Transfers radiatifs dans les eaux de mer.* PhD thesis, Doctorat d'Etat, Univ. Pierre et Marie Curie, Paris, 1976.

L. Prieur and S. Sathyendranath. An optical classification of coastal and oceanic waters based on the specific spectral absorption curves of phytoplankton pigments, dissolved organic matter, and other particulate materials. *Limnology and Oceanography*, 26 (4):671–689, 1981.

A.G. Pulvermüller, J. Kleiner, and W. Mauser. Calcite patchiness in Lake Constance as viewed by LANDSAT-TM. *Aquatic Sciences*, 57 (4):338–349, 1995.

T. Pyhälahti and P. Gege. Retrieval of water quality parameters using different channel configurations. *Proceedings of the ISPRS symposium "Physical measurements and signatures in remote sensing", Aussois, France, Jan 8-12*, 2001.

X. Quan and E.S. Fry. Empirical equation for the index of refraction of seawater. *Applied Optics*, 34 (18):3477–3480, 1995.

R. Reuter, D. Diebel-Langohr, R. Doerffer, F. Dörre, H. Haardt, and T. Hengstermann. Optical properties of gelbstoff. *The influence of gelbstoff on remote sensing of sea-water constituents from space*, 2, Appendix 3:1–58, 1986. GKSS Contract No. V 8547, ESA Contract No. RFQ 3-5060/84/NL/MD.

C.S. Roesler, M.J. Perry, and K.L. Carder. Modeling in situ phytoplankton absorption from total absorption spectra in productive inland marine waters. *Limnology and Oceanography*, 34 (8):1510–1523, 1989.

S. Sathyendranath and T. Platt. Analytic model of ocean color. *Applied Optics*, 36 (12):2620–2629, 1997.

S. Sathyendranath, L. Lazzara, and L. Prieur. Variations in the spectral values of specific absorption of phytoplankton. *Limnology and Oceanography*, 32 (2):403–415, 1987.

S. Sathyendranath, L. Prieur, and A. Morel. A three-component model of ocean colour and its application to remote sensing of phytoplankton pigments in coastal waters. *International Journal of Remote Sensing*, 10 (8):1373–1394, 1989.

H. Schiller and R. Doerffer. Neural network for emulation of an inverse model - operational derivation of case II water properties from MERIS data. *International Journal of Remote Sensing*, 20 (9):1735–1746, 1999.

K. Schmieder. Submerse Makrophyten der Litoralzone des Bodensees 1993 im Vergleich mit 1978 und 1967. IGKB Bericht 46, Internationale Gewässerschutzkommission für den Bodensee, 1998. ISSN 1011-1263.

K. Schneider. Spatial heterogeneity of pigment concentration and water surface temperature determined from satellite data. *Archiv für Hydrobiologie, Special issues: Advances in Limnology*, 53:451–488, 1998.

J. Schulz. *Systemtechnische Untersuchungen an dem abbildenden Spektrometer ROSIS-01 zur Erfassung und Interpretation der Meeresfarbe.* PhD thesis, Institut für Optoelektronik, Deutsche Forschungsanstalt für Luft- und Raumfahrt Oberpfaffenhofen, 1997. ISSN 0939-2963.

J.N. Schwarz, P. Kowalczuk, S. Kaczmarek, G.F. Cota, B.G. Mitchell, M. Kahru, F.P. Chavez, A. Cunningham, D. McKee, P. Gege, M. Kishino, D.A. Phinney, and R. Raine. Two models for absorption by coloured dissolved organic matter (CDOM). *Oceanologia*, 44 (2):209–241, 2002.

R.C. Smith and K.S. Baker. Optical properties of the clearest natural waters (200-800nm). *Applied Optics*, 20 (2):177–184, 1981.

R.C. Smith and J.E. Tyler. *Transmission of solar radiation into natural waters*, chapter 1, pages 117–155. Photochemical and Photobiological Reviews. Plenum Press, New York, 1976.

M. Smoluchowski. Molekular-kinetische Theorie der Opaleszenz von Gasen im kritischen Zustande, sowie einiger verwandter Erscheinungen. *Annalen der Physik*, 25:205–226, 1908.

R.H. Stavn and A.D. Weidemann. Shape factors, two-flow models, and the problem of irradiance inversion in estimating optical parameters. *Limnology and Oceanography*, 34 (8):1426–1441, 1989.

F.C. Stephens, E.M. Louchard, R.P. Reid, and R.A. Maffione. Effects of microalgal communities on reflectance spectra of carbonate sediments in subtidal optically shallow marine environments. *Limnology and Oceanography, Light in Shallow Waters*, 48 (1, part 2):535–546, 2003.

M. Stramska, D. Stramski, B.G. Mitchell, and C.D. Mobley. Estimation of the absorption and backscattering coefficients from in-water radiometric measurements. *Limnology and Oceanography*, 45 (3):628–641, 2000.

D. Stramski and C.D. Mobley. Effects of microbial particles on oceanic optics: a database of single-particle optical properties. *Limnology and Oceanography*, 42 (3):538–549, 1997.

S. Sugihara, M. Kishino, and N. Okami. Contribution of Raman scattering to upward irradiance in the sea. *Journal of the Oceanographical Society of Japan*, 40:397–404, 1984.

M.M. Tilzer and P. Hartig. Produktivität und Bilanzierung des Phytoplanktons. DFG-Sonderforschungsbereich 248: Stoffhaushalt des Bodensees, Bericht über den Bewilligungszeitraum 1992–1994, Universität Konstanz, 1994.

H.C. van de Hulst. *Light scattering by small particles.* Dover Publications Inc. New York, 1981. unabridged and corrected republication of the work originally published in 1957 by John Wiley & Sons Inc. New York.

H. van der Piepen. Nutzung und Anwendung des abbildenden Spektrometers Rosis - Vorbereitungen für einen neuen Erdbeobachtungssensor. *DLR-Nachrichten*, 77:11–14, 1995.

H. van der Piepen and T. Heege. Verteilung allochthoner und autochthoner Wasserinhaltsstoffe zwischen Uferzone und angrenzendem Freiwasserbereich. DFG-Sonderforschungsbereich 454: Bodenseelittoral, Bericht über den Bewilligungszeitraum 1998–2001, Universität Konstanz, 2001.

L. Van Heukelem, C.S. Thomas, and P.M. Glibert. Sources of variability in chlorophyll analysis by fluorometry and high performance liquid chromatography in a SIMBIOS inter-calibration exercise. Technical report, NASA, Goodard Space Flight Center, Greenbelt, Maryland, USA, 2002. NASA/TM-2002-02338-0.

B. Wagner, H.G. Schröder, H. Güde, W. Sanzin, and U. Engler. Zustand des Seebodens 1992 - 1994, Sedimentinventare - Phosphor - Oligochaeten. IGKB Bericht 47, Internationale Gewässerschutzkommission für den Bodensee, 1998. ISSN 1011-1263.

C. Wallhäußer. Mehrkanalspektrometer zur Messung der Lichtabsorption in Binnen- und Küstengewässern. Master's thesis, Technische Universität München, 1995.

R.G. Wetzel. *Limnology - lake and river ecosystems.* Academic Press, San Diego, 2001. 3rd edition.

R. Zahner, J. Florin, A. Meier-Schlegel, W. Dütschler, H. Löffel, E. Amann, B. Wagner, U. Jaquemar, W. Immler, L. Probst, D. Volk, and U. Huber. Zum biologischen Zustand des Seebodens des Bodensees in den Jahren 1972 bis 1978. IGKB Bericht 25, Internationale Gewässerschutzkommission für den Bodensee, 1981.

H. Zhang, K.J. Voss, R.P. Reid, and E.M. Louchard. Bidirectional reflectance measurements of sediments in the vicinity of Lee Stocking Island, Bahamas. *Limnology and Oceanography, Light in Shallow Waters*, 48 (1, part 2):380–389, 2003.

G. Zibordi, J.-F. Berthon, J.P. Doyle, S. Grossi, D. van der Linde, and C. Targa. Coastal Atmosphere and Sea Time Series (CoASTS), Part 1: a tower-based, long-term measurement program. SeaWiFS Postlaunch Technical Report Series 19, NASA, Goodard Space Flight Center, Greenbelt, Maryland, USA, 2002. NASA/TM 2002-206892.

G. Zimmermann. *Fernerkundung des Ozeans.* Akademie Verlag, Berlin, 1991.

G. Zimmermann and A. Neumann. The imaging spectrometer experiment MOS on IRS-P3 - three years of experience. *Journal of Spacecraft Technology*, 10 (1):1–9, 2000.

G. Zimmermann, A. Neumann, H. Sümnich, and H. Schwarzer. MOS/PRIRODA - an imaging VIS/NIR spectrometer for ocean remote sensing. *Proceedings of SPIE "Imaging Spectrometry of Terrestrial Environment"*, 1937:201–206, 1993.